

# **Illuminating the tau lepton with the ATLAS detector:**

A study of  $\gamma\gamma \rightarrow \tau^+\tau^-$  scattering in ultra-peripheral  
Pb+Pb collisions, and constraints on the tau lepton  
electromagnetic dipole moments

Dissertation zur Erlangung des Doktorgrades  
der Fakultät für Mathematik und Physik  
der Albert-Ludwigs-Universität Freiburg

Vorgelegt von  
**Kartik Deepak Bhide**  
July, 2025



# **Illuminating the tau lepton with the ATLAS detector:**

A study of  $\gamma\gamma \rightarrow \tau^+\tau^-$  scattering in ultra-peripheral  
Pb+Pb collisions, and constraints on the tau lepton  
electromagnetic dipole moments

Dissertation zur Erlangung des Doktorgrades  
der Fakultät für Mathematik und Physik  
der Albert-Ludwigs-Universität Freiburg

Vorgelegt von  
**Kartik Deepak Bhide**  
July, 2025

<b>Dean</b>	Prof. Dr. Annette Huber-Klawitter
<b>Supervisor</b>	Dr. Valerie Lang
<b>Dissertation examiners</b>	Dr. Valerie Lang Prof. Dr. Karl Jakobs
<b>Defense examiners</b>	Dr. Valerie Lang Prof. Dr. Marco Gersabeck Prof. Dr. Stefan Dittmaier
<b>Date of defense</b>	20 October 2025



# Abstract

Lead ions accelerated to ultra-relativistic energies at the Large Hadron Collider are accompanied by a strong flux of quasi-real photons. These photons can interact and produce pairs of tau leptons, via the  $\gamma\gamma \rightarrow \tau^+\tau^-$  scattering process, at an enhanced rate in ultra-peripheral Pb+Pb collisions. This process can be used to investigate the physics of the photon-tau lepton coupling. This thesis presents the first measurement of the  $\gamma\gamma \rightarrow \tau^+\tau^-$  scattering cross-section in ultra-peripheral Pb+Pb collisions at  $\sqrt{s_{\text{NN}}} = 5.02$  TeV, recorded by the ATLAS detector in Run 2 of the Large Hadron Collider. The cross-sections are measured for 21 kinematic observables of the tau lepton decay products across three fiducial regions, and are found to agree well with the available theoretical predictions. The measured cross-sections are used to constrain the anomalous magnetic dipole moment and the electric dipole moment of the tau lepton. The obtained constraints are expected to be the most stringent results using  $\sqrt{s_{\text{NN}}} = 5.02$  TeV Pb+Pb collisions at the Large Hadron Collider.

# Zusammenfassung

Bleiionen, die im Large Hadron Collider auf ultra-relativistische Energien beschleunigt werden, sind von einem starken Fluss quasi-realer Photonen umgeben. Diese Photonen können interagieren und über den  $\gamma\gamma \rightarrow \tau^+\tau^-$ -Streuprozess Paare von Tau-Leptonen erzeugen. Dieser Prozess tritt in ultra-peripheren Pb+Pb Kollisionen im Vergleich zu Proton-Kollisionen mit erhöhter Rate auf und erlaubt es, die Physik der Photon-Tau-Lepton-Kopplung untersuchen. Diese Arbeit präsentiert die erste Messung des  $\gamma\gamma \rightarrow \tau^+\tau^-$  Wirkungsquerschnitts in ultra-peripheren Pb+Pb Kollisionen bei  $\sqrt{s_{\text{NN}}} = 5.02$  TeV, aufgezeichnet mit dem ATLAS-Detektor in der zweiten Datennahmeperiode des Large Hadron Collider. Differentielle Wirkungsquerschnitte wurden für insgesamt 21 kinematische Observablen der Tau-Lepton-Zerfallsprodukte in drei fiduziellen Regionen gemessen und stimmen gut mit den verfügbaren theoretischen Vorhersagen überein. Die gemessenen Wirkungsquerschnitte werden verwendet, um das anomale magnetische Dipolmoment und das elektrische Dipolmoment des Tau-Leptons zu bestimmen. Die erhaltenen erwarteten Grenzen stellen die genauesten Ergebnisse bei der Verwendung von  $\sqrt{s_{\text{NN}}} = 5.02$  TeV Pb+Pb Kollisionen am Large Hadron Collider dar.



# Table of Contents

<b>Abstract</b>	<b>iii</b>
<b>Table of Contents</b>	<b>iv</b>
<b>1 Introduction</b>	<b>1</b>
<b>2 Theoretical and phenomenological background</b>	<b>5</b>
2.1 Standard Model of particle physics . . . . .	5
2.1.1 Theoretical framework . . . . .	6
2.1.2 Fundamental particles and their interactions . . . . .	10
2.1.3 Beyond the Standard Model . . . . .	15
2.2 Electromagnetic dipole moments . . . . .	18
2.2.1 Contributions to the EMDMs of the tau lepton . . . . .	20
2.2.2 Experimental measurements . . . . .	22
2.3 Tau lepton pair production in ultra-peripheral Pb+Pb collisions . . . . .	27
2.3.1 Photon flux . . . . .	28
2.3.2 Survival factor . . . . .	30
2.3.3 Hard scattering . . . . .	31
2.3.4 Tau lepton decay and spin correlations . . . . .	32
<b>3 The ATLAS detector at the Large Hadron Collider</b>	<b>35</b>
3.1 The Large Hadron Collider . . . . .	35
3.1.1 Particle acceleration . . . . .	37
3.1.2 LHC operation . . . . .	39
3.1.3 LHC instrumentation . . . . .	41
3.2 The ATLAS detector . . . . .	42
3.2.1 The ATLAS coordinate system . . . . .	42
3.2.2 Inner Detector . . . . .	44
3.2.3 Calorimeters . . . . .	46

3.2.4	Muon System . . . . .	48
3.2.5	Forward detectors . . . . .	50
3.2.6	Magnet system . . . . .	52
3.2.7	Trigger and Data Acquisition . . . . .	53
3.3	Object reconstruction . . . . .	55
3.3.1	Tracks . . . . .	56
3.3.2	Vertices . . . . .	59
3.3.3	Topoclusters . . . . .	60
3.3.4	Electrons and photons . . . . .	60
3.3.5	Muons . . . . .	63
3.3.6	Other objects . . . . .	66
<b>4</b>	<b>Luminosity measurement</b>	<b>69</b>
4.1	Introduction . . . . .	69
4.1.1	Concept of luminosity . . . . .	69
4.1.2	Luminosity measurement in ATLAS . . . . .	71
4.1.3	Absolute calibration . . . . .	73
4.2	Track-based luminosity measurement . . . . .	77
4.2.1	Track selection . . . . .	77
4.2.2	Track-based luminosity algorithms . . . . .	78
4.2.3	Algorithm performance . . . . .	79
4.3	Luminosity calibration of the 2023 Pb+Pb dataset . . . . .	81
4.3.1	Scan sequence . . . . .	81
4.3.2	Bunch population measurement . . . . .	83
4.3.3	Background subtraction . . . . .	85
4.3.4	Bunch current offset correction . . . . .	87
4.3.5	Fit model . . . . .	88
4.3.6	Specific luminosity . . . . .	88
4.3.7	Orbit drift correction . . . . .	89
4.3.8	Length scale calibration . . . . .	91
4.3.9	Beam-beam effects . . . . .	93
4.3.10	Emittance change . . . . .	94
4.3.11	Non-factorization . . . . .	95
4.3.12	Reproducibility and consistency . . . . .	99
4.3.13	Long term stability . . . . .	100
4.3.14	Results of the preliminary 2023 Pb+Pb calibration . . . . .	101

<b>5</b>	<b>Measurement of <math>\gamma\gamma \rightarrow \tau^+\tau^-</math> scattering cross-sections and constraints on tau lepton electromagnetic dipole moments</b>	<b>105</b>
5.1	Analysis strategy	105
5.2	Data collection	108
5.2.1	Trigger in 2015	108
5.2.2	Trigger in 2018	109
5.3	Monte Carlo simulations and modeling	110
5.3.1	Samples	110
5.3.2	Theoretical modeling	111
5.3.3	Detector performance modeling	115
5.3.4	Spin correlation effects	116
5.4	Object and event selections	119
5.4.1	Tracks and vertices	119
5.4.2	Topoclusters	119
5.4.3	Electrons	120
5.4.4	Photons	121
5.4.5	Muons	122
5.4.6	Event selections	122
5.5	Background estimation	123
5.5.1	Exclusive muon pair production	124
5.5.2	Diffraction photonuclear processes	125
5.5.3	Multiple UPC scattering	126
5.6	Reconstruction-level distributions	128
5.7	Unfolding	132
5.7.1	Fiducial object and region definitions	132
5.7.2	Binning and weights	133
5.7.3	Unfolding methods	134
5.7.4	Unfolding inputs	137
5.7.5	Monte Carlo closure test	137
5.7.6	Number of iterations	137
5.7.7	Statistical uncertainties and correlations	140
5.8	Systematic uncertainties	143
5.8.1	Object calibration and performance	143
5.8.2	Trigger	144
5.8.3	Monte Carlo modeling	145
5.8.4	Other	148
5.8.5	Impact of systematic uncertainties	150
5.9	Measured differential fiducial cross-sections	156
5.10	Constraints on tau lepton electromagnetic dipole moments	161

5.10.1	Modeling of non-zero dipole moments . . . . .	161
5.10.2	Statistical framework . . . . .	163
5.10.3	Effect of statistical combination . . . . .	167
5.10.4	Constraints on anomalous magnetic dipole moment . . . . .	169
5.10.5	Constraints on electric dipole moment . . . . .	171
<b>6</b>	<b>Summary and outlook</b>	<b>173</b>
	<b>References</b>	<b>176</b>
	<b>Appendices</b>	<b>195</b>
<b>A</b>	<b>Supplementary material for Chapter 5</b>	<b>197</b>
A.1	Monte Carlo samples . . . . .	197
A.2	Unfolding inputs . . . . .	199
A.3	Monte Carlo closure test . . . . .	209
A.4	Number of iterations for unfolding . . . . .	213
A.5	Data-driven closure test . . . . .	217
A.6	Impact of tau lepton EMDM's on truth-level observables . . . . .	224
A.7	Fit diagnostics for $a_\tau$ extraction . . . . .	231
A.8	Fit diagnostics for $d_\tau$ extraction . . . . .	236

# Chapter 1

## Introduction

Over the last century, progress in the field of elementary particle physics has followed two paths. The first path is where *discoveries* occur, i.e. the direct experimental observation of hitherto unknown or unobserved particles. The second path is where *measurements* are performed, i.e. the characterization of the properties of particles, both new and old. The two paths are intertwined: new discoveries warrant new measurements, while measurements that cannot be explained by the best available theories, may hint at future discoveries.

This thesis is concerned with the measurement of the interaction between two elementary particles, namely the *photon*  $\gamma$  and the *tau lepton*  $\tau^-$ . The photon is the familiar quantum of light, and is responsible for mediating electromagnetic interactions between charged particles. The tau lepton is a heavier copy of the well known electron  $e^-$ . It was discovered in the 1970s in a *search* for heavy electron cousins, i.e. *leptons*, using  $e^+e^-$  collisions recorded by the Mark I experiment at SLAC [1, 2].

The Standard Model of particle physics provides the best description of the observed behaviors of elementary particles. It posits that to first order, the photon-tau lepton interaction is identical to the photon-electron interaction, given that electrons and tau leptons are copies of each other (albeit with different masses). Thus, by measuring the photon-tau lepton *coupling*, it is possible to gather evidence that either supports the Standard Model, or hints at physics Beyond the Standard Model. The photon-tau lepton coupling contains two physically observable quantities, called the *anomalous magnetic dipole moment* (AMDM) and *electric dipole moment* (EDM) of the tau lepton, which are inherently related to how the spin of the tau lepton affects its interaction with the photon. These observables, which are together called the *electromagnetic dipole moments* (EMDMs) of the tau lepton are therefore at the core of the photon-tau lepton coupling analysis. Even though the tau lepton was discovered nearly fifty years ago, high precision measurements of the tau lepton EDMs have only become possible in the last twenty years, due to significant improvements in the available experimental facilities.

The tau lepton is not found freely in nature, as it is an unstable particle. It decays to lighter (and stable) elementary particles with a mean lifetime of less than one picosecond.

The measurement of the tau lepton EDMs requires the production of tau leptons, where the production mechanism includes the photon-tau lepton coupling. For this reason, this thesis explores photon-initiated tau lepton pair production, i.e. the  $\gamma\gamma \rightarrow \tau^+\tau^-$  scattering process.

This process is realized in high energy particle collisions, such as those delivered by the *Large Hadron Collider* (LHC), located at the *Conseil Européen pour la Recherche Nucléaire* (CERN) in Geneva, Switzerland. Since quantum mechanics, the framework underlying the Standard Model, is inherently probabilistic, not every high energy particle collision can result in  $\gamma\gamma \rightarrow \tau^+\tau^-$  scattering. However, the probability can be significantly enhanced by colliding highly charged particles. Thus, this thesis focuses on  $\gamma\gamma \rightarrow \tau^+\tau^-$  scattering in lead (Pb) ion collisions delivered by the LHC. In particular, this thesis investigates *ultra-peripheral* Pb+Pb collisions, where the nuclei interact at distances larger than twice their radii. In such collisions, the probability of electromagnetic interactions is significantly enhanced, compared to those of the strong and weak nuclear interactions.

The Pb+Pb collisions were recorded by the ATLAS experiment in 2015 and 2018, and constitute the data that were analyzed in this thesis. The probability, or *cross-section*, of  $\gamma\gamma \rightarrow \tau^+\tau^-$  scattering is measured with this data, using various decay processes of the tau lepton. In fact, this is the first *differential* measurement of  $\gamma\gamma \rightarrow \tau^+\tau^-$  scattering at the LHC. The measured cross-sections are then used to set constraints on the tau lepton EDMs.

As the impact of the results of this analysis is limited by the size of the available dataset, it is natural to expect that the constraints on the tau lepton EDMs will improve as more Pb+Pb collision data is collected. Such new datasets need to be *calibrated*, in order to reduce uncertainties due to experimental sources. In this direction, this thesis presents a preliminary calibration of the *luminosity*, or “brightness”, of Pb+Pb collisions, delivered to and recorded by the ATLAS experiment in 2023.

## Overview

This thesis is organized as follows. In Chapter 2, the Standard Model of particle physics, the electromagnetic dipole moments of leptons, and the details of  $\gamma\gamma \rightarrow \tau^+\tau^-$  scattering in ultra-peripheral Pb+Pb collisions are described, thereby providing an overview of the theoretical and phenomenological framework necessary for this thesis. The experimental methods relevant to this thesis are presented in Chapter 3. This includes a description of LHC, the ATLAS experiment, and the analysis techniques used to infer the presence of particles produced in high energy collisions, using the data recorded by the ATLAS experiment. A calibration of the luminosity of the 2023 Pb+Pb collision dataset recorded by ATLAS is discussed in Chapter 4. In Chapter 5, the first experimental measurement of the differential cross-section of  $\gamma\gamma \rightarrow \tau^+\tau^-$  scattering in ultra-peripheral Pb+Pb collisions is presented. Further, Chapter 5 describes the expected constraints on the electromagnetic dipole moments of the tau lepton, using the measured differential cross-sections. Finally, a summary of the thesis, as well as an outlook on the future of the reported measurements, is given in Chapter 6.



---

## Statement on author's contribution

Given the substantial scale and complexity of modern high energy particle physics, conducting successful experiments requires large collaborations of physicists, technicians and engineers. This is certainly true for the ATLAS experiment, and for the other major experiments at the Large Hadron Collider.

The work presented in this thesis was conducted within the ATLAS collaboration, of which the author is a member. It has relied on the efforts of thousands of people, in the areas of detector construction, operations, data-taking, performance and calibration, event simulation, computing, etc. The publications related to these efforts have therefore been properly cited, wherever this thesis makes reference to work that was not explicitly done by the author.

The measurement of the  $\gamma\gamma \rightarrow \tau^+\tau^-$  scattering cross-section, which is the main physics measurement presented in this thesis, was performed within a team of roughly 15 people. As this analysis is an extension of the studies performed in Ref. [3], several inputs from the previous analysis, based on the work of the associated analysis team, were re-used for this thesis. This included the Monte Carlo samples and modeling, object calibration, signal region selections, background estimation, systematic uncertainty evaluation etc. The author was one of two main analyzers of the updated analysis along with W. Stanek-Maslouska (PhD student, DESY). The author was responsible for the following components of the analysis:

- Investigation of the effect of spin correlations in the tau lepton production and decay.
- Revised treatment of the photon flux uncertainty.
- Study of background contribution of simultaneous ultra-peripheral scattering processes.
- Running the unfolding procedure. This includes the determination of:
  - the statistical correlations between the measured cross-section bins.
  - the impact of systematic uncertainties on the measured cross-sections.
  - the systematic uncertainties due to the unfolding bias, response matrix statistics, and background statistics.
- Determination of the final differential cross-sections and comparison to available theory predictions.
- Determination of constraints on the tau lepton electromagnetic dipole moments using the measured differential cross-sections. This includes:
  - the development of the event-by-event reweighting procedure for non-zero tau lepton electromagnetic dipole moments.
  - the development of the statistical framework used in the analysis.

A preliminary result of the  $\gamma\gamma \rightarrow \tau^+\tau^-$  cross-section measurement based on the author's contributions was presented in Ref. [4]. Since then, several improvements were made to the analysis. This includes a revised treatment of the 0n0n weights (i.e. deriving weights for the combined Run 2 dataset, as opposed to separate weights for the two data-taking years), and the revised treatment of the photon flux uncertainty. The results of Ref. [4] therefore differ slightly from those presented in this thesis, which used the resources of the ATLAS collaboration, but was not “approved” by it.

Further, the author made significant contributions to the calibration of the luminosity of the 2023 Pb+Pb dataset recorded by ATLAS. The author was the main analyzer of this calibration, where the methodology was based on previous luminosity calibration strategies by ATLAS. The author was responsible for developing an alternate beam-gas background subtraction method, and for identifying and fixing an error within the standard calibration framework, pertaining to the application of the orbit drift correction. In the course of the analysis, the author relied on the (unpublished) efforts of the following people: the ghost and satellite charge fractions were determined by A. Jury (PhD student, University of Liverpool / CERN), and the length scale calibration was performed by R. Hawkings (staff physicist, CERN). For his ATLAS Authorship Qualification Project, the author developed a new track-based event counting algorithm, which was used in the estimation of the long term stability of the luminosity calibration. Two sets of public figures related to heavy ion luminosity calibration released by the ATLAS collaboration were a result of the author's work [5, 6]. These figures have been cited in this thesis wherever appropriate.

# Chapter 2

## Theoretical and phenomenological background

This chapter summarizes the theoretical and phenomenological aspects of the experimental measurement pursued in this thesis. The Standard Model of particle physics is presented in Sec. 2.1. The underlying physical theories, particle content, and the limitations of the Standard Model, are also discussed. The electromagnetic dipole moments of leptons, one of which is measured in this thesis, are introduced in Sec. 2.2. The high energy scattering process through which the measurement presented in this thesis is performed is discussed in Sec. 2.3.

The notation and conventions followed in this chapter are borrowed from Ref. [7].

### 2.1 Standard Model of particle physics

The Standard Model (SM) of particle physics refers to a number of theories grouped into one overarching model. It explains the behavior and interactions of a set of elementary particles, i.e. physical objects which cannot be subdivided further. The SM provides a description of three of the four known fundamental interactions in nature (i.e. excluding gravity):

- **Quantum electrodynamics (QED):** describes the quantum nature of electromagnetic (EM) phenomena. The EM fields themselves, as well as their interactions with both elementary particles and macroscopic materials, are modeled by QED.
- **Weak interaction:** gives a particle description of the weak nuclear interaction. It is required to understand the decays of elementary particles, and of unstable nuclei.
- **Quantum chromodynamics (QCD):** describes the strong nuclear interaction at microscopic scales. The interactions of nuclei, their constituent nucleons, and even sub-nucleon phenomena, cannot be modeled without QCD.

Like most modern physical theories, the Standard Model rests on the shoulders of giants. Describing the particle content of the SM and their interactions, without understanding the

underlying physics, would do a great injustice to the theoretical developments of the last two centuries. Thus, this section begins with an overview of the theoretical tools required to build the Standard Model.

### 2.1.1 Theoretical framework

According to special relativity, spacetime can be modeled by the  $\mathbb{R}^4$  manifold endowed with the metric tensor  $\eta_{\mu\nu} = \text{diag}(+1, -1, -1, -1)$ . Spacetime rotations of a system are described by *Lorentz transformations*; the collection of all possible transformations constitutes a mathematical *group* called the Lorentz group.

Particles can be described using wave-functions, which may transform in different ways under Lorentz transformations. This is connected to the concept of *spin*, which is an intrinsic, quantized type of angular momentum not related to physical rotation. Particles can be categorized based on their spin quantum number:

- **Bosons:** have integer spin quantum number, i.e. 0, 1, 2 etc., and obey Bose-Einstein statistics. There is only one fundamental spin-0 particle in the Standard Model, called the Higgs boson, while the spin-1 particles in the SM mediate the fundamental interactions. Spin-0 particles are invariant under Lorentz transformations and are called *scalar* particles. Spin-1 particles obey the Lorentz transformation property  $A^\mu \rightarrow \Lambda^\mu_\nu A^\nu$ , where  $\Lambda^\mu_\nu$  is an element of the Lorentz group. Since this is the same transformation rule as, for example, a four-momentum, spin-1 particles are also called *vector* particles.
- **Fermions:** have half-integer spin quantum number, i.e. 1/2, 3/2, 5/2 etc., and obey Fermi-Dirac statistics. They constitute the known *matter particles* in the SM, and are represented by four-component Dirac spinors. Under Lorentz transformations, they obey the rule  $\psi \rightarrow \exp\left(\frac{1}{8}\omega_{\mu\nu}[\gamma^\mu, \gamma^\nu]\right)\psi$ , where  $\gamma^\mu$  are the  $4 \times 4$  *gamma matrices*,  $[\cdot, \cdot]$  is the commutator, and  $\omega_{\mu\nu}$  is an antisymmetric  $4 \times 4$  matrix which parameterizes the transformation. Four-component Dirac spinors consist of two *left-* and *right-* chiral Weyl spinors, which transform under different representations of the Lorentz group.

Spacetime is a stage upon which the dynamics and interactions of particles play out. In classical mechanics, this can be described using the Lagrangian formalism. For a classical system with discrete degrees of freedom, the Lagrangian is defined as the difference between the kinetic energy  $T$  and potential energy  $V$ , i.e.  $L = T - V$ . For classical *fields*  $\phi(x)$ , which are objects that return a value at all points in spacetime, the Lagrangian takes the form

$$L(t) = \int d^3x \mathcal{L}(\phi(x), \partial_\mu \phi(x)). \quad (2.1)$$

Here,  $\mathcal{L}$  is called the *Lagrangian density*<sup>1</sup> of the system, and  $\partial_\mu$  represents the gradient (or

---

<sup>1</sup>The Lagrangian density is often simply called the Lagrangian. Exactly which quantity is being discussed, is inferred from context, convention and notation.

momentum) of the field. The *action*, which is the time integral of the Lagrangian, is defined as

$$\mathcal{S} = \int L dt = \int \mathcal{L}(\phi(x), \partial_\mu \phi(x)) d^4x. \quad (2.2)$$

As a system evolves through time, it traces out a path in its phase space. Each path that can be taken corresponds to a given value of the action. The *principle of least action* states that variations of the action along the “most physical” path are zero. Imposing this condition, i.e.  $\delta \mathcal{S} = 0$ , gives the classical equation of motion of the system,

$$\partial_\mu \left( \frac{\partial \mathcal{L}}{\partial (\partial_\mu \phi(x))} \right) - \frac{\partial \mathcal{L}}{\partial \phi(x)} = 0. \quad (2.3)$$

If different field configurations result in the same equation of motion, the Lagrangian is said to possess a *symmetry*. All physical theories are required to be symmetric, or *invariant*, under Lorentz transformations. There are additional symmetries relevant to the Standard Model called *local gauge symmetries*, which are *internal*, i.e. not related to spacetime.

The construction of field theories obeying such symmetries can best be understood with the Lagrangian of a free fermionic field  $\psi$  with mass  $m$ , given by<sup>2</sup>

$$\mathcal{L} = i\bar{\psi}\gamma^\mu \partial_\mu \psi - m\bar{\psi}\psi. \quad (2.4)$$

This equation, also known as the Dirac Lagrangian, is invariant under a global rotation of  $\psi \rightarrow e^{ig\alpha}\psi$ , where  $\alpha$  is a real number and  $g$  quantifies the strength of the rotation. To construct local gauge field theories,  $\alpha$  is allowed to depend on spacetime, i.e. the transformation becomes

$$\psi \rightarrow e^{ig\alpha(x)}\psi. \quad (2.5)$$

For the Dirac Lagrangian above to be invariant under this *gauge transformation*, a *covariant derivative*  $D_\mu$  defined by

$$D_\mu = \partial_\mu - igA_\mu \quad (2.6)$$

is introduced, where  $A_\mu$  is a vector field known as the *gauge field*, and  $g$ , now called the *coupling strength*, quantifies the strength of the interaction between  $\psi$  and  $A_\mu$ . The gauge field transforms under the gauge transformation as

$$A_\mu \rightarrow A_\mu + \frac{1}{g}\partial_\mu \alpha(x). \quad (2.7)$$

Invariance under gauge transformations is guaranteed if the gauge field is assigned a kinetic term in the Lagrangian. Then, the total Lagrangian takes the form

---

<sup>2</sup>The spacetime arguments of  $\psi$  and all other fields will be subsequently dropped for brevity.

$$\mathcal{L} = i\bar{\psi}\gamma^\mu D_\mu\psi - m\bar{\psi}\psi - \frac{1}{4}F_{\mu\nu}F^{\mu\nu}, \quad (2.8)$$

where  $F_{\mu\nu} = \partial_\mu A_\nu - \partial_\nu A_\mu$  is the *field strength tensor* of the gauge field. Eq. 2.8 thus describes a theory involving a fermion and a massless vector boson, along with their interactions.

The gauge transformation in Eq. 2.5 is a representation of the  $U(1)$  symmetry group, which defines rotations along a unit circle. It is also possible to construct field theories for other groups. Of particular importance to the Standard Model are the  $SU(N)$  groups, which are the Lie groups of  $N \times N$  unitary matrices with unit determinant (in the fundamental representation). Elements of these groups act on multiplets of fermions  $\Psi \equiv (\psi_1, \psi_2, \dots, \psi_N)$  as

$$\Psi \rightarrow U\Psi = \exp(iT^a\alpha^a(x))\Psi, \quad (2.9)$$

where  $U$  is an element of the  $SU(N)$  group, defined using the generators  $T^a$  and angles  $\alpha^a(x)$ . The sum runs over the  $N^2 - 1$  generators of the  $SU(N)$  group. The generators define a *Lie algebra* given by

$$[T^a, T^b] = if^{abc}T^c, \quad (2.10)$$

where  $f^{abc}$  are called the structure constants.

The covariant derivative of a theory obeying  $SU(N)$  symmetry is given by

$$D_\mu = \partial_\mu - igA_\mu^a T^a, \quad (2.11)$$

where the partial derivative  $\partial_\mu$  is the usual partial derivative embedded in the  $N$ -dimensional identity matrix, and  $A_\mu^a$  are the  $N^2 - 1$  gauge fields associated with the symmetry. Analogous to Eq. 2.5, the Lagrangian of a  $SU(N)$  symmetric field theory is written as

$$\mathcal{L} = i\bar{\Psi}\gamma^\mu D_\mu\Psi - m\bar{\Psi}\Psi - \frac{1}{4}F_{\mu\nu}^a F^{\mu\nu,a}, \quad (2.12)$$

where the field strength tensor is given by

$$F_{\mu\nu}^a = \partial_\mu A_\nu^a - \partial_\nu A_\mu^a + gf^{abc}A_\mu^b A_\nu^c. \quad (2.13)$$

This equation says that the gauge fields of an  $SU(N)$  symmetric theory can interact with each other if the structure constants allow it. This fact has enormous implications on the phenomenology of the Standard Model, particularly in the description of the strong interaction.

Besides symmetries under continuous transformations, the gauge field theories relevant to the Standard Model also possess discrete symmetries: charge conjugation  $\mathcal{C}$ , where the signs of all quantum numbers are flipped; parity  $\mathcal{P}$ , where the spatial coordinates are inverted, i.e.  $\mathbf{x} \rightarrow -\mathbf{x}$ ; time reversal  $\mathcal{T}$ , where time evolution is reversed, i.e.  $t \rightarrow -t$ . The operators corresponding to these transformations can be combined, e.g. in the case of  $\mathcal{CP}$  transformations.

Elementary particles can be modeled by wave packets in their corresponding fields, but this is still a classical description. In order to describe physics at microscopic scales, it is necessary to quantize the field theory. In the canonical quantization of *quantum field theories* (QFTs), the classical fields are promoted to quantum operators which contain *creation* and *annihilation* operators that increase or decrease the number of quanta in a system. This leads to the notion of *particles* and *anti-particles*, which have the same mass and spin, but opposite gauge quantum numbers. Another approach to quantizing a field theory is the path integral formalism, which is manifestly Lorentz covariant, and offers a more intuitive connection between classical and quantum physics. It posits that the evolution of a system can proceed through all possible field configurations, weighted by  $e^{iS}$ , where  $S$  is the action.

Quantum field theories are used to compute the evolution of a system from an *initial state*  $|i\rangle$  to a *final state*  $|f\rangle$ . This transition is given by the *scattering matrix*, defined by

$$\langle f | S - \mathbb{1} | i \rangle = i (2\pi)^4 \delta^4 \left( \sum p \right) \langle f | \mathcal{M} | i \rangle, \quad (2.14)$$

where the  $\mathbb{1}$  is the identity matrix, i.e. no interactions occur. On the right hand side, momentum conservation between the incoming and outgoing states is guaranteed by the  $\delta^4(\sum p)$ , and  $\langle f | \mathcal{M} | i \rangle$  is known as the *matrix element*<sup>3</sup>. The objects in this equation are vectors and matrices in the Fock space of the system.

Matrix elements are evaluated using  $n$ -point Greens functions. A more intuitive and less cumbersome approach to these computations is offered by *Feynman diagrams*, which are diagrammatic representations of the underlying mathematics. Within such diagrams, scalar particles are represented by dashed lines, vector bosons by wiggly lines, and fermions by solid lines. Feynman diagrams are also used to define *Feynman rules*, which provide a recipe to easily compute matrix elements.

The matrix elements  $\mathcal{M}$  of scattering processes are connected to experimentally observable quantities through *cross-sections*. In the crossing of two volumes of particles, such as in collider experiments, the cross-section essentially gives the fraction of particle-particle interactions that result in the final state of interest, within the transverse area common to the interacting volumes. Cross-sections have units of area, and can be differential in the kinematic phase space variables of the process. For  $2 \rightarrow N$  scattering, the differential cross-section  $d\sigma$  is given by

$$d\sigma = \frac{(2\pi)^4 \delta^4(\sum p)}{(2E_1)(2E_2) |\mathbf{v}_1 - \mathbf{v}_2|} |\mathcal{M}|^2 \prod_{j \in \text{final}} \frac{d^3 p_j}{(2\pi)^3 2E_j}, \quad (2.15)$$

where  $E_{1,2}$  and  $\mathbf{v}_{1,2}$  are the energies and velocities of the initial state particles, and the final state particles  $j$  have energy and momentum  $E_j$  and  $p_j$  respectively.

The gauge QFTs discussed so far involve parameters like  $g$  which quantify the strength of

---

<sup>3</sup>Conventionally, the quantity  $\mathcal{M}$  is referred to as the matrix element, rather than  $\langle f | \mathcal{M} | i \rangle$ .

particle interactions. These coupling parameters are typically small, so it is convenient to use *perturbation theory* to enable the computation of scattering cross-sections. Here, the cross-section, differential in a phase space variable  $\Omega$ , can be written in powers of  $g$  like

$$\frac{d\sigma}{d\Omega} = \frac{d\sigma^{(0)}}{d\Omega} + \left(\frac{g^2}{4\pi}\right) \frac{d\sigma^{(1)}}{d\Omega} + \left(\frac{g^2}{4\pi}\right)^2 \frac{d\sigma^{(2)}}{d\Omega} + \dots \quad (2.16)$$

The first term is called the *Born* or *leading-order* (LO) term, the second is called the *next-to-leading-order* (NLO) term, and so on. Adding more terms to a cross-section computation generally improves the difference between predictions and observations. However, the computational complexity grows dramatically as higher order terms are included, due to the number of Feynman diagrams that need to be evaluated.

Higher order Feynman diagrams often involve closed loops of *virtual* particles, which are not included in the initial or final state, so they have to be integrated over. Depending on the structure of the loops, these integrals can diverge with the momenta of the virtual particles. This is known as an ultraviolet (i.e. high energy) divergence. On the other hand, infrared (i.e. low energy) divergences can occur if massless particles are present in the loops. Infrared divergences also occur in the case of bremsstrahlung-like radiation processes. As a consequence, QFT predictions can yield infinite results, even though observable quantities are finite.

This *problem of infinities* is addressed using the process of *renormalization*, which recognizes that observables like scattering cross-sections do not depend on the same parameters that enter a Lagrangian. Instead, what is observed are *renormalized* versions of the *bare* parameters of the theory, which are allowed to be divergent. The divergences in the bare quantities are cancelled by the divergent loop diagrams, resulting in finite *physical* observables and parameters.

### 2.1.2 Fundamental particles and their interactions

With the relevant theoretical tools at hand, the Standard Model of particle physics can be described. The physics of the Standard Model evolved over the history of the universe, so a proper introduction should begin with the high temperature early universe, when the gauge group structure of the Standard Model took the form

$$\text{SU}(3)_C \times \text{SU}(2)_L \times \text{U}(1)_Y. \quad (2.17)$$

Here, the subscripts denote the conserved gauge charges:  $C$  is the *color* charge,  $L$  is the *weak isospin* charge, and  $Y$  is the *hypercharge*.

The SM particle spectrum, as shown in Fig. 2.1 (albeit after spontaneous electroweak symmetry breaking), consists of the gauge bosons of these gauge groups, and fermions with which they interact. The *quarks* possess charges under all gauge groups; *leptons* have hypercharge and weak isospin quantum numbers, but no color charges. The fermions are grouped into three *families* or *generations*. The left-chiral up- and down- type quarks form doublets under the



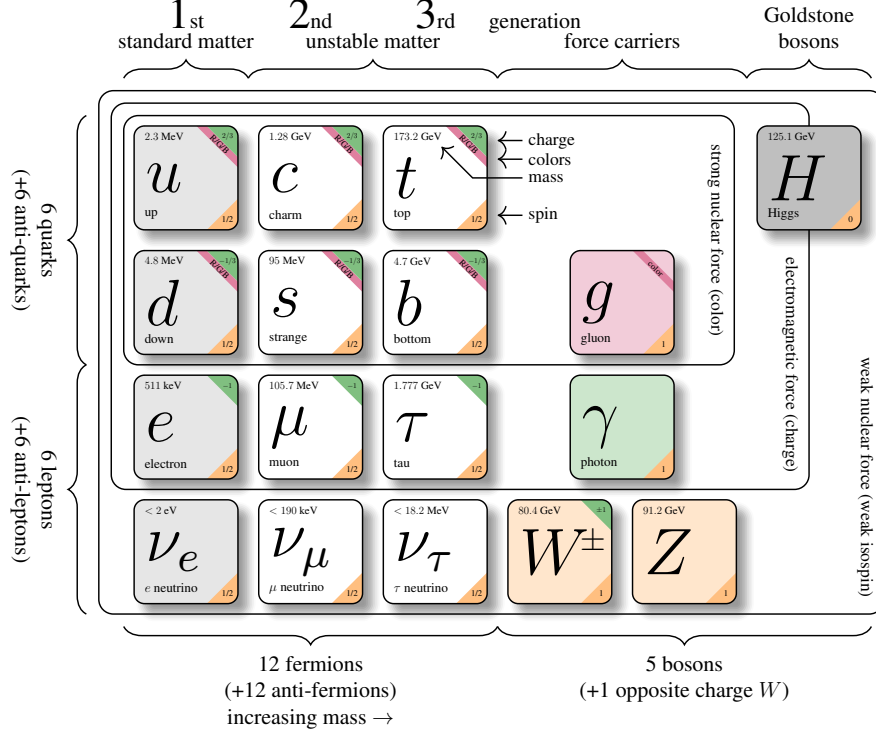


**Figure 2.1:** Particle content of the Standard Model after spontaneous electroweak symmetry breaking. Figure adapted from Ref. [8].

weak isospin group, while the left-chiral charged leptons and their corresponding neutrinos form the doublets in the lepton sector. All right-chiral fermions are singlets under the weak isospin group, with the exception of the right-chiral neutrinos, which are decoupled from their left-chiral counterparts.

The pieces of the SM Lagrangian that describe the dynamics and interactions of the aforementioned particles are given by

$$\mathcal{L}_{\text{SM}} \supset \mathcal{L}_{\text{gauge bosons}} + \mathcal{L}_{\text{fermions}}, \quad (2.18)$$

where

$$\mathcal{L}_{\text{gauge bosons}} = -\frac{1}{4}B_{\mu\nu}B^{\mu\nu} - \frac{1}{4}W_{\mu\nu}^i W^{\mu\nu,i} - \frac{1}{4}G_{\mu\nu}^a G^{\mu\nu,a}, \quad (2.19)$$

$$\mathcal{L}_{\text{fermions}} = \sum_{\psi} i\bar{\psi}\gamma^{\mu}D_{\mu}\psi. \quad (2.20)$$

The gauge boson Lagrangian contains the field strength tensors of the  $B_{\mu}$ ,  $W_{\mu}^i$  and  $G_{\mu}^a$  fields, which are the gauge bosons of the  $U(1)_Y$ ,  $SU(2)_L$  and  $SU(3)_C$  groups respectively. The covariant derivative acting on the fermions  $\psi$  is given by

$$D_{\mu} = \partial_{\mu} - \frac{1}{2}ig'B_{\mu} - \frac{1}{2}ig\sigma^a W_{\mu}^a - \frac{1}{2}ig_s T^a G_{\mu}^a, \quad (2.21)$$

where  $\sigma^i$  are the Pauli matrices,  $T^a$  are the Gell-Mann matrices, and  $g, g'$  and  $g_s$  are the charges of the associated gauge groups.

Some of the particles in the SM particle spectrum are known to be massive. However, Eq. 2.18 does not contain any mass terms for the fermions and gauge bosons. In fact, such mass terms are forbidden by the gauge symmetry of Eq. 2.17. In order to accommodate particle masses into the SM, the Brout-Englert-Higgs mechanism, also simply called the *Higgs mechanism*, was proposed in 1964 [9, 10].

The Higgs mechanism introduces a complex scalar field  $\Phi$ , called the *Higgs field*, which is a doublet under  $SU(2)_L$  transformations. The Lagrangian of the Higgs field is given by

$$\mathcal{L}_{\text{Higgs}} = (D_\mu \Phi)^\dagger (D^\mu \Phi) - V(\Phi). \quad (2.22)$$

In the high temperature environment of the early universe, the Higgs potential  $V(\Phi)$  is believed to be quadratic in  $\Phi$ . As the universe expanded and cooled down, an *electroweak phase transition* occurred around the Curie temperature of the Higgs field, which changed the shape of the Higgs potential, resulting in the *spontaneous breaking* of the  $SU(2)_L \times U(1)_Y$  gauge symmetry. Today, the shape of the Higgs potential, constrained by renormalizability and gauge invariance, is given by

$$V(\Phi) = -\mu^2 \Phi^\dagger \Phi + \frac{\lambda}{4} (\Phi^\dagger \Phi)^2, \quad (2.23)$$

such that  $-\mu^2, \lambda > 0$ . The potential is minimized for the field configurations

$$\Phi = \frac{1}{\sqrt{2}} e^{i\pi^a \sigma^a} \begin{pmatrix} 0 \\ v + h \end{pmatrix}, \quad (2.24)$$

where the *Higgs boson*  $h$  is a real scalar field that is a singlet under the electroweak gauge group,  $v = \sqrt{-\mu^2/\lambda}$  is the *vacuum expectation value* (vev) of the Higgs field, and  $\pi^a$  are the massless (to be-)Goldstone bosons associated with the spontaneous symmetry breaking (SSB) mechanism. The physics of the Higgs mechanism is independent of the choice of Goldstone bosons, so it is customary to work in the *unitary gauge* where  $\pi^a = 0$  is chosen.

Inserting this into Eq. 2.22, the kinetic term becomes

$$(D_\mu \Phi)^\dagger (D^\mu \Phi) = \frac{g^2 v^2}{8} \left[ W_\mu^1 W^{\mu 1} + W_\mu^2 W^{\mu 2} + \left( \frac{g'}{g} B_\mu - W_\mu^3 \right)^2 \right]. \quad (2.25)$$

This equation describes the mass terms for three vector bosons, which is made apparent by the following rotations

$$W_\mu^\pm = \frac{1}{\sqrt{2}} (W_\mu^1 \mp iW_\mu^2), \quad (2.26)$$

$$\begin{pmatrix} Z_\mu \\ A_\mu \end{pmatrix} = \begin{pmatrix} \cos \theta_W & -\sin \theta_W \\ \sin \theta_W & \cos \theta_W \end{pmatrix} \begin{pmatrix} W_\mu^3 \\ B_\mu \end{pmatrix}, \quad (2.27)$$

where  $\theta_W$  is the Weinberg angle, defined as  $\tan \theta_W = g'/g$ . These rotations inserted in Eq. 2.25 allow the definition of the charged  $W^\pm$  bosons with mass  $m_W = gv/2$ , the neutral  $Z$  boson with mass  $m_Z = m_W/\cos \theta_W$ , and a massless boson  $A$ . The kinetic terms of these fields are obtained by applying the same rotations shown above to the  $W_\mu^a$  and  $B_\mu$  kinetic terms in Eq. 2.19.

By inspecting the symmetries of the Lagrangian after SSB, a new  $U(1)$  gauge symmetry is found. The conserved charge is

$$e = g \sin \theta_W, \quad (2.28)$$

which is found by using Eq. 2.27 in the gauge transformation rules for the  $W_\mu^a$  bosons. This is the electric charge that is conserved in quantum electrodynamics. The associated gauge boson is  $A_\mu$ , which is the familiar photon. Thus, the SSB mechanism resulted in a change of the gauge group structure of the SM Lagrangian,

$$SU(3)_C \times SU(2)_L \times U(1)_Y \rightarrow SU(3)_C \times U(1)_{EM}, \quad (2.29)$$

where  $U(1)_{EM}$  is the electromagnetic gauge symmetry. The relation between the electric charge  $Q$ , weak isospin quantum number  $T_3$ , and hypercharge  $Y$  of a particular field, is given by  $Q = T_3 + \frac{Y}{2}$  [11, 12].

Applying Eq. 2.27 to the Higgs potential in Eq. 2.23, the self-interactions of the post-SSB vector bosons are found, which are the triple gauge interactions ( $W^\pm W^\mp A$  and  $W^\pm W^\mp Z$ ) and the quartic gauge interactions ( $W^\pm W^\mp AA$ ,  $W^\pm W^\mp ZZ$ ,  $W^\pm W^\mp AZ$  and  $W^\pm W^\mp W^\pm W^\mp$ ).

The Higgs field is also responsible for generating fermion masses through Yukawa couplings to the quarks and leptons. Prior to SSB, the Higgs field couples to the quarks like

$$\mathcal{L}_{\text{Yukawa,quark}} = -Y_{ij}^d \bar{Q}^i \Phi d_R^j - Y_{ij}^u \bar{Q}^i \tilde{\Phi} u_R^j + \text{h.c.}, \quad (2.30)$$

where  $i, j$  run over the three generations of up-type ( $u$ ) and down-type ( $d$ ) quarks,  $Q^i$  are the  $SU(2)_L$  doublets of left-chiral quarks,  $Y^{u,d}$  are  $3 \times 3$  complex matrices that encode the Yukawa couplings, and  $\tilde{\Phi} = i\sigma_2 \Phi$ . Expanding the Higgs field around its vev according to Eq. 2.24, the above terms after SSB become

$$\mathcal{L}_{\text{Yukawa,quark}} = -\left(\frac{v}{\sqrt{2}} + \frac{h}{\sqrt{2}}\right) (\bar{\mathbf{d}}_L Y^d \mathbf{d}_R + \bar{\mathbf{u}}_L Y^u \mathbf{u}_R), \quad (2.31)$$

where matrix notation has been used. This term describes the coupling of the Higgs boson to the quarks, as well as the quark masses. Through a series of matrix rotations via unitary matrices  $U_{u,d}$  and  $K_{u,d}$ , the terms above are diagonalized and the quark masses are obtained. The matrix  $V = U_u^\dagger U_d$ , called the Cabibbo-Kobayashi-Maskawa (CKM) matrix, describes how the quark flavours “mix” in the electroweak interactions. The CKM matrix contains a complex parameter (with one real and imaginary component) that is responsible for  $\mathcal{CP}$  violating effects in the quark sector [13, 14].

A similar mass generation mechanism exists for the charged leptons. Before SSB, the Higgs field coupling to charged leptons is described by the Lagrangian

$$\mathcal{L}_{\text{Yukawa,lepton}} = -y_i \bar{L}^i \Phi \ell_R^j + \text{h.c.}, \quad (2.32)$$

where  $i, j$  run over the three generations of leptons,  $L^i$  are the  $\text{SU}(2)_L$  doublets of left-chiral leptons,  $\ell_R$  refers to the right-chiral charged leptons and  $y_i$  are the Yukawa couplings. After SSB, the above Lagrangian term becomes

$$\mathcal{L}_{\text{Yukawa,lepton}} = -\sum_{\ell} m_{\ell} \bar{\ell}_R \ell_L + \text{h.c.}, \quad (2.33)$$

where  $m_{\ell} = y_{\ell} v / \sqrt{2}$  are the masses of the charged leptons. The above mass generation mechanism cannot be applied to the neutrinos, since their right-chiral components are not present in the particle spectrum. Thus, neutrinos remain massless in the Standard Model.

After SSB, the three generations of quarks and leptons are found to have a mass hierarchy, due to the structure of the corresponding Yukawa couplings. In units of the fundamental electric charge  $e$ , the up-type and down-type quarks possess charges of  $+2/3$  and  $-1/3$  respectively. The charged leptons, i.e. the electron, muon and tau, have charges of  $-1$ , while their corresponding neutrinos are electrically neutral. The anti-particles of the quarks and leptons are also present in the SM particle spectrum.

The  $W^{\pm}$  and  $Z$  bosons, which are obtained only after SSB, mediate the weak nuclear interaction. It is a short range interaction since the  $W^{\pm}$  and  $Z$  bosons have  $\mathcal{O}(100)$  GeV mass. On the other hand, the fact that the photon is massless implies that the electromagnetic interaction has infinite range. The gluon, which mediates the strong nuclear interaction, is also massless since it is left untouched by the SSB mechanism. The range of the strong interaction is energy-dependent, despite the gluon being massless, due to the phenomenon of *asymptotic freedom* in quantum chromodynamics [15, 16]. The photon, gluon and  $Z$  boson are their own anti-particles, while the  $W^{\pm}$  bosons are particle-anti-particle counterparts.

Putting all the pieces together, the Lagrangian of the Standard Model of particle physics can be written as

$$\mathcal{L}_{\text{SM}} = \mathcal{L}_{\text{gauge bosons}} + \mathcal{L}_{\text{fermions}} + \mathcal{L}_{\text{Higgs}} + \mathcal{L}_{\text{Yukawa, quark}} + \mathcal{L}_{\text{Yukawa, lepton}}. \quad (2.34)$$

This thesis focuses on the physics of the tau lepton. The electroweak sector of the above Lagrangian can be used to derive the following Feynman rules for electroweak interactions involving the tau lepton,

$$\begin{aligned}
 & \underbrace{\text{Diagram 1}}_{= -ie\gamma^\mu} \quad \underbrace{\text{Diagram 2}}_{= -i\frac{g}{\cos\theta_W}\gamma^\mu (c_V^\tau - c_A^\tau\gamma^5)} \quad \underbrace{\text{Diagram 3}}_{= -i\frac{g}{\sqrt{2}}\gamma^\mu \frac{1-\gamma^5}{2}}. \quad (2.35)
 \end{aligned}$$

In the coupling to the  $Z$  boson, the parameters  $c_V^\tau = -\frac{1}{4} + \frac{1}{2}\sin^2\theta_W$  and  $c_A^\tau = -\frac{1}{4}$  highlight the chiral nature of the electroweak interaction. The coupling to the  $W$  boson is only present for the left-chiral tau lepton (and for all fermions in general), due to the presence of the  $1 - \gamma^5$  in the interaction vertex.

### 2.1.3 Beyond the Standard Model

It is not an understatement to claim that the Standard Model of particle physics provides an excellent description of elementary particle physics. One of the best laboratories to test the predictions of the SM is the Large Hadron Collider at CERN (see Chapter 3). In particular, scattering processes in high energy proton-proton collisions involving the SM particles have been studied extensively with the ATLAS experiment. A summary of the experimental measurements of the cross-sections of such processes, confronted with the corresponding SM predictions, is shown in Fig. 2.2. Remarkable agreement has been observed for numerous processes across fifteen orders of magnitude in the production cross-section.

Despite its many accolades, there are still some observations about nature for which the Standard Model offers no explanation, such as:

- **Neutrino masses:** Experimental measurements have shown that neutrinos change flavour as they propagate through spacetime [17, 18]. Assuming that relativity holds, this can only occur if the neutrino flavour and mass eigenstates are not the same, which implies that neutrinos must have mass. This breaks the Standard Model assumption that the neutrinos are massless.
- **Cosmology:** Observations like the rotation curves of spiral galaxies, gravitational lensing etc. point to the existence of an unknown kind of matter, called *dark matter*. The observation of the accelerated expansion of the universe hints at an unknown kind of energy, called *dark energy*, existing homogeneously throughout space. The Standard Model does not contain particles describing dark matter and dark energy, even though they account for around 25% and 70% of the matter-energy budget of the universe respectively [19].

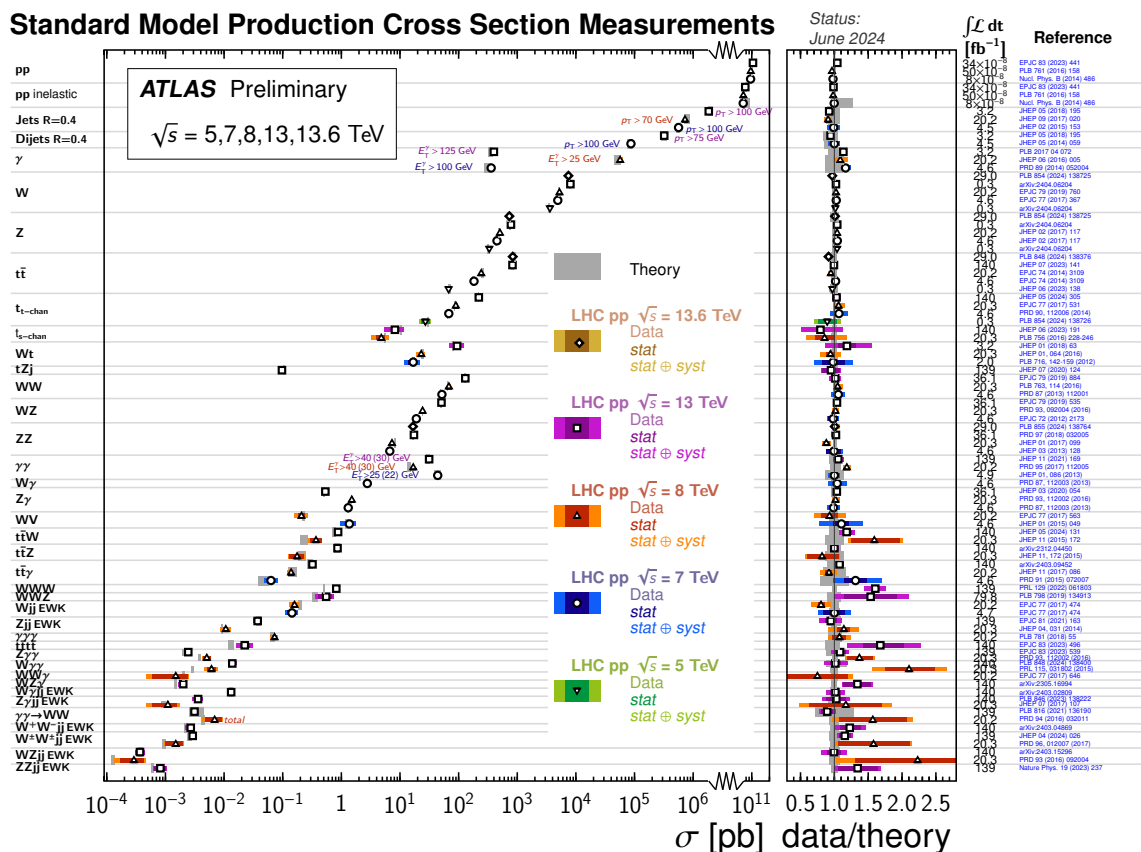


**Figure 2.2:** Summary of total and fiducial cross-section measurements of various “Standard Model production processes” (i.e. excluding Higgs production processes) measured in proton-proton collisions at different center of mass energies by the ATLAS experiment [22]. Total cross-section measurements are corrected by the branching ratios of the relevant signal regions. Comparisons to theoretical predictions are shown in the right panel. Status as of June 2024.

- **Matter anti-matter asymmetry** [20]: It is thought that matter and anti-matter were present in equal amounts during the first instants of the universe. However, in the present day, the universe is matter dominated, particularly in the baryon sector. The idea of *baryogenesis*, which is a mechanism that requires the three Sakharov conditions to be satisfied [21], may explain this asymmetry. One of these conditions is for  $\mathcal{C}$  and  $\mathcal{CP}$  violation to be present in the model.
- **Gravity**: Unlike the electromagnetic, strong and weak interactions, the SM fails to provide a particle explanation for the gravitational interaction. General relativity, our best description of gravity so far, is a purely classical theory. Since the gravitational constant  $G$  has a mass dimension of  $-2$  in natural units, general relativity by itself is not renormalizable due to power-counting, so it cannot be included in the Standard Model. This is undoubtedly the SM's biggest drawback.

It is thought that there may be theories Beyond the Standard Model (BSM), also called *new physics* theories, which may resolve these open questions. It is important to note that

some observations could be resolved by modifications to the analogous “Standard Models” of astrophysics and cosmology. Since this thesis lies in the realm of particle physics, these ideas are not discussed further.

There are generally two approaches to constructing BSM theories. In the *top-down* approach, a theory of nature with more fundamental assumptions than the SM is constructed, e.g. with additional gauge symmetries, different spacetime structures, etc. Through mechanisms like spontaneous symmetry breaking, the Standard Model manifests as a low-energy version of this higher theory. In contrast, in the *bottom-up* approach, the Standard Model is extended by a small number of interactions and particles.

Both approaches typically predict a large number of new particles and couplings, so falsifying their existence through indirect measurements alone is not scientifically sound. In other words, only the *direct discovery* of new particles, e.g. through the discovery of new resonances, can be used to prove or disprove the existence of top-down theories. This has not happened to date. Thus, both direct searches and indirect measurements have been used to set limits on BSM physics, e.g. on the masses and coupling strengths of the predicted new particles.

Experimental studies of BSM physics are inherently model-dependent, since statistical analyses have to be performed with a particular model as one of the hypotheses. Effective Field Theories (EFTs) are therefore often considered instead of specific BSM theories, as they offer a model agnostic framework for statistical interpretations. The working principle of EFTs is the separation of scales: if a theory predicts physics at microscopic scales (or high energies), a corresponding *effective* version is observable at macroscopic scales (or low energies). In particle physics, Fermi’s four-fermion interaction being an effective theory of the weak interaction is a classic historical example.

Effective Field Theories are constructed as extensions of the Standard Model. The Lagrangian of a generic EFT can be written as

$$\mathcal{L}_{\text{EFT}} = \mathcal{L}_{\text{SM}} + \sum_{d>4} \sum_i \frac{c_i^{(d)}}{\Lambda^{d-4}} \mathcal{O}_i^{(d)}, \quad (2.36)$$

where  $d$  runs over all mass dimensions greater than four,  $\mathcal{O}_i^{(d)}$  are higher dimensional operators with associated couplings or *Wilson coefficients*  $c_i^{(d)}$ , and  $\Lambda$  is interpreted as the scale of new physics. Using a *matching* procedure, experimental observables predicted by the EFT are equated to those predicted by any BSM theory. This allows constraints on the EFT couplings  $c_i^{(d)}$  to be interpreted as constraints on the free parameters of specific BSM theories.

The underlying (gauge) symmetries and particle spectrum dictate the available operators  $\mathcal{O}_i^{(d)}$  in an EFT. If only the Standard Model fields and interactions are considered, the theory is referred to as SMEFT [23]. Other EFTs can be constructed with additional assumptions depending on the use case. It is even possible to construct EFTs using BSM fields and interactions, but this is generally not done. Within the SMEFT, odd-dimension operators are not



considered, as they are shown to violate lepton and/or baryon conservation. Since higher dimensional operators are suppressed by powers of  $\Lambda$ , the majority of SMEFT interpretations only investigate dimension-6 operators.

## 2.2 Electromagnetic dipole moments

Spin is one of the more interesting aspects of quantum physics, since it has no classical counterpart. As mentioned in Sec. 2.1.1, it is an intrinsic property that has no effect on the trajectories of free particles. However, the spins of particles can be studied through interactions with other particles. In particular, Lagrangians like Eq. 2.8 show that gauge bosons are good candidates for probes of fermion spins. Among the Standard Model gauge bosons, the photon is the best candidate, since it is a stable particle.

To see how the spins of fermions couple to photons, it is useful to consider the QED equation of motion for a fermion  $\psi$  with mass  $m$ , given by

$$(D_\mu \gamma^\mu - m) \psi = 0. \quad (2.37)$$

Multiplying both sides by  $(D_\mu \gamma^\mu + m)$  results in

$$\left( D_\mu D^\mu + \frac{e}{2} F_{\mu\nu} \sigma^{\mu\nu} + m^2 \right) \psi = 0, \quad (2.38)$$

where the factor of  $1/2$  in the second term cancels the double counting implied by the Einstein summation convention in the product of  $F_{\mu\nu}$  with  $\sigma^{\mu\nu} = \frac{i}{2} [\gamma^\mu, \gamma^\nu]$ . It is practical to use the Weyl basis for the gamma matrices, where  $\gamma^0 = \text{antidiag}(1, 1)$  and  $\gamma^i = \text{antidiag}(\sigma^i, -\sigma^i)$ , with  $i = 1, 2, 3$  and  $\sigma^i$  being the Pauli matrices. With this, along with the fact that the spin vector of the fermion is given by  $\mathbf{S} \equiv \boldsymbol{\sigma}/2$ , the equation of motion becomes

$$\frac{(\mathcal{H} - eA_0)^2}{2m} \psi = \left( \frac{m}{2} + \frac{1}{2} (\mathbf{p} - e\mathbf{A})^2 - 2\frac{e}{2m} \mathbf{B} \cdot \mathbf{S} \pm i\frac{e}{m} \mathbf{E} \cdot \mathbf{S} \right) \psi, \quad (2.39)$$

where the photon field is defined by  $A_\mu \equiv (A_0, \mathbf{A})$  with associated electric and magnetic fields  $\mathbf{E}$  and  $\mathbf{B}$ ,  $\mathcal{H}$  is the Hamiltonian of the system, and  $\mathbf{p}$  is the momentum of the fermion. The  $\pm$  is related to the two spinor components of the fermion field.

The  $\mathbf{B} \cdot \mathbf{S}$  term is related to the intrinsic magnetic dipole moment  $\boldsymbol{\mu}$  of the fermion. The name comes from the classical picture of a magnetic dipole with moment  $\mathbf{m}$ , in a uniform magnetic field  $\mathbf{B}$ , whose potential energy is  $-\mathbf{m} \cdot \mathbf{B}$ . In fact, Eq. 2.39 contains such a potential energy term, where  $\mathbf{m} \sim \mathbf{S}$ . The magnetic dipole moment of  $\psi$  is defined as

$$\boldsymbol{\mu} = -g\mu\mathbf{S}, \quad (2.40)$$

where the strength of the magnetic dipole moment is quantified in units of  $\mu = e/2m$  (i.e. the Bohr magneton if  $\psi$  is the electron). In general, all elementary fermions have a magnetic



dipole moment with a strength of  $g\mu$ , where the  $g$ -factor is simply  $g = 2$ . Unlike the classical case where the dipole simply aligns with the external field, the quantum dipole (i.e. the spin vector) undergoes *Larmor precession* about the direction of the external field, with a frequency  $\omega_S = g\mu B$  (neglecting relativistic corrections).

This prescription applies to on-shell photons, but similar definitions can be made for off-shell photons with virtuality  $q^2 > 0$ . Consider an on-shell fermion interacting with an off-shell photon. Let  $p_1$  and  $p_2$  be the initial and final four-momenta of the fermion, such that  $q = p_1 - p_2$  is the momentum transfer of the photon. The most general vertex between the photon and the fermion obeying gauge and Lorentz symmetries is given by

$$i\Gamma^\mu(p_1, p_2) = -ie \left[ \gamma^\mu F_1(q^2) + \frac{i\sigma^{\mu\nu} q_\nu}{2m} F_2(q^2) + \frac{\gamma^5 \sigma^{\mu\nu} q_\nu}{2m} F_3(q^2) \right], \quad (2.41)$$

where  $F_{1,2,3}(q^2)$  are the *form factors* associated with the Lorentz structures in the vertex. Their physical interpretations are:

- The term associated with the  $F_1$  form factor is spin-independent, and modifies the overall coupling strength. Thus, it is responsible for renormalizing the charge  $e$ . When  $q^2 \rightarrow 0$ , i.e. when the photon is on-shell,  $F_1$  takes the value

$$F_1(0) = 1. \quad (2.42)$$

- The term associated with the  $F_2$  form factor is spin-dependent through  $\sigma^{\mu\nu}$ . This term has the same structure as the magnetic dipole moment, which is most readily seen when Eq. 2.38 is taken to the momentum space. When  $q^2 \rightarrow 0$ , the  $F_2$  form factor becomes

$$F_2(0) = \frac{g-2}{2}. \quad (2.43)$$

The  $g$  appearing in this expression is the same as the  $g$ -factor introduced earlier. It is convenient to define an *anomalous magnetic dipole moment* (AMDM),

$$a = \frac{g-2}{2}, \quad (2.44)$$

which simply gives the deviation of the  $g$ -factor from two.

- The term associated with the  $F_3$  form factor is also spin-dependent. Due to the presence of the  $\gamma^5$ , this term has the opposite eigenvalue under  $\mathcal{CP}$  transformations as the first two terms, which have even eigenvalues. As such, a non-zero  $F_3$  implies that the interaction violates the  $\mathcal{CP}$  symmetry of the theory. When  $q^2 \rightarrow 0$ ,  $F_3$  takes the value

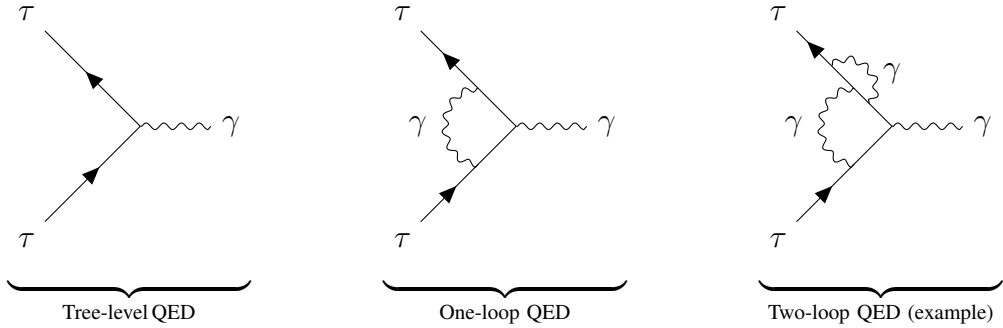
$$F_3(0) = d \cdot \frac{2m}{e}. \quad (2.45)$$

Here, the quantity  $d$  is called the *electric dipole moment* (EDM) of the fermion, which gives the strength of a  $\mathbf{E} \cdot \mathbf{S}$  coupling in the Hamiltonian. Note that in Eq. 2.39, the  $\mathbf{E} \cdot \mathbf{S}$  term is not related to the electric dipole moment, but is rather the Lorentz invariant completion of the  $\mathbf{B} \cdot \mathbf{S}$  term.

In this thesis, the AMDM and EDM are collectively referred to as the *electromagnetic dipole moments* (EMDMs) of a given fermion. EDMs are powerful probes of the internal structure of particles. For example, a non-zero EDM – which can be understood through its classical counterpart, i.e. two charges separated by a distance – may hint at possible internal electric structure. The same argument can be made for the magnetic dipole moment. Since the proton has the same spin quantum number and charge magnitude as the electron, it is reasonable to expect that their  $g$ -factors are equal (i.e. 2). However, the measured  $g$ -factor of the proton is 5.5856946893(16) [24]. This relatively large measurement provided the first hints of the existence of quarks.

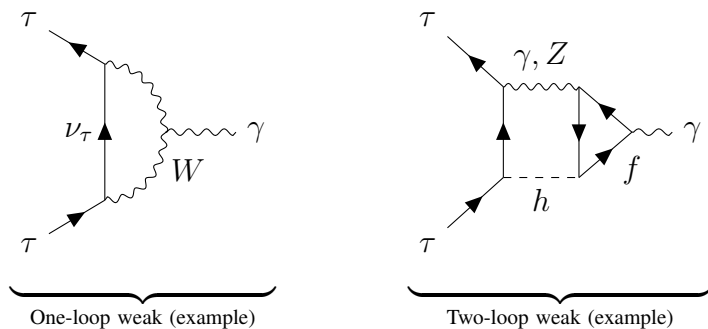
### 2.2.1 Contributions to the EDMs of the tau lepton

The preceding discussion only related to the leading order QED prediction of the EDMs of elementary fermions. However, these quantities receive corrections from all possible loop diagrams within a given theory. Examples of such diagrams in QED, for the tau lepton, are



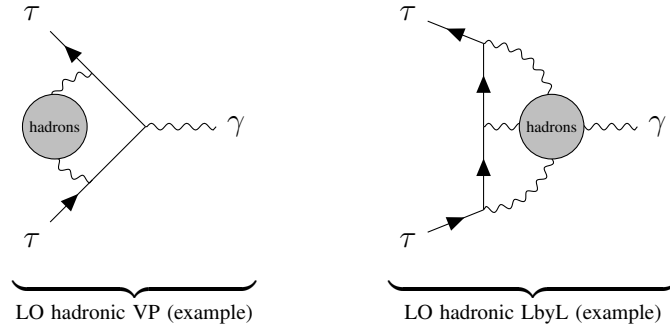
Here, the tree-level diagram predicts  $a = 0$ , as given by Eq. 2.39. The second diagram predicts  $a = \alpha_{\text{EM}}/2\pi$ , where  $\alpha_{\text{EM}} = e^2/4\pi$ , which is the famous Schwinger calculation [25].

Corrections to the EDMs are also possible due to the presence of weak interactions in the loop diagrams. For example, higher order corrections to the  $\gamma\tau\tau$  vertex involve diagrams like



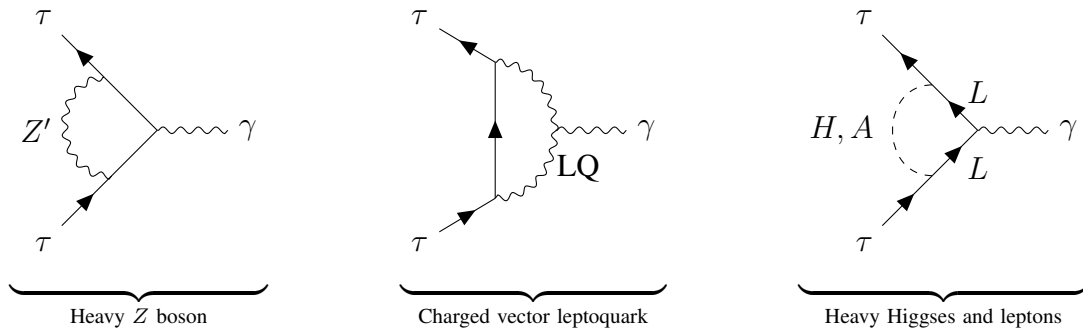
Since the weak interaction is  $\mathcal{CP}$  violating in the quark sector (by way of the CKM matrix) elementary particles can possess a non-zero (but very small) electric dipole moment, arising from higher order weak corrections to their coupling to the photon.

The QED and weak corrections to EMDMs can be calculated using perturbative techniques, since the related coupling constants are small. The same cannot be said for QCD corrections, since the strong coupling constant diverges at low energy. Thus, QCD corrections involve loop diagrams with hadrons rather than quarks and gluons. Examples of the most pertinent hadronic corrections, namely the vacuum polarization (VP) and the light-by-light (LbyL) diagrams, for the tau lepton look like



The hadronic VP contribution can be measured experimentally using the ratio of hadron to lepton production in  $e^+e^-$  collisions, while the LbyL contribution is not directly measurable. However, both parts can, in principle, be determined using lattice QCD.

If Beyond Standard Model physics exists, new particles can also contribute to the EMDMs of elementary particles via loop diagrams. Some examples include



The first diagram shows a heavy neutral  $Z$  boson, which can arise in models with more than four spacetime dimensions, additional  $U(1)$  symmetries etc. In the middle, a charged vector leptoquark is present in the loop, which typically arises in models where higher order gauge transformations like  $SU(5)$  act on multiplets containing both leptons and quarks. On the right, new heavy (pseudo)-scalar Higgs bosons and leptons are shown, which manifest in models with additional scalar doublets, in the seesaw mechanism for neutrino mass generation etc.

Generic new physics contributions to the EMDMs of elementary fermions can be captured using effective field theories; the SMEFT is best suited for this task. In the Warsaw basis [26], the SMEFT operators that contribute to the EMDMs of fermions at tree level are

$$\mathcal{L}_{\text{SMEFT}} = \frac{1}{\Lambda^2} \bar{L}_\tau \sigma^{\mu\nu} \tau_R \Phi (C_{\tau B} B_{\mu\nu} + C_{\tau W} \sigma^i W_{\mu\nu}^i), \quad (2.46)$$

where  $\Lambda$  is the scale of the new physics,  $L_\tau \equiv (\bar{\nu}_{\tau,L}, \bar{\tau}_L)$  is the tau lepton doublet under  $\text{SU}(2)_L$ ,  $\Phi$  is the Higgs field, and  $C_{\tau B}, C_{\tau W}$  are the free SMEFT parameters. After spontaneous electroweak symmetry breaking, the Higgs field can be replaced with Eq. 2.24, and the  $B_\mu$  and  $W_\mu^3$  fields can be rotated according to Eq. 2.27. The above Lagrangian then becomes

$$\mathcal{L}_{\text{SMEFT}} = \frac{v}{\sqrt{2}\Lambda^2} \bar{\tau}_L \sigma^{\mu\nu} F_{\mu\nu} \tau_R (C_{\tau B} \cos \theta_W - C_{\tau W} \sin \theta_W). \quad (2.47)$$

Without loss of generality,  $C_{\tau W} = 0$  can be assumed, as only the combination of  $C_{\tau B}$  and  $C_{\tau W}$  can be measured experimentally. From this, a Feynman rule for the  $\gamma\tau\tau$  vertex can be extracted, resulting in

$$\begin{aligned} \delta a_\tau &= \frac{2m_\tau}{e} \frac{\text{Re}[C_{\tau B}]}{M}, \\ \delta d_\tau &= \frac{\text{Im}[C_{\tau B}]}{M}. \end{aligned} \quad (2.48)$$

Here,  $M = \Lambda^2/\sqrt{2}v \cos \theta_W$ , and  $\delta$  denotes the addition of the SMEFT contribution to the EMDMs, i.e. the *total* tau lepton AMDM, for example, is given by  $a_\tau = a_\tau^{\text{SM}} + \delta a_\tau$ . The Lagrangian term associated with the imaginary part of  $C_{\tau B}$  has the opposite  $\mathcal{CP}$  eigenvalue compared to the real part, so it can be identified with the electric dipole moment.

## 2.2.2 Experimental measurements

The strategies that are used to measure the EMDMs of the Standard Model fermions depend strongly on their mass, lifetime and interactions. Experimental measurements of the EMDMs of quarks are complicated by confinement in QCD, but there has been phenomenological work related to the EMDMs of heavy quarks ( $c, b, t$ ) [27–29]. In contrast, measurements of the EMDMs of the charged leptons are much easier; the status of these measurements is described below.

### Electron

Since the electron is stable, individual electrons can be manipulated for the measurement of the electron AMDM  $a_e$ . High precision measurements can be achieved using the *Penning trap* apparatus, where single electrons can be isolated using a homogeneous axial  $\mathbf{B}$ -field and quadrupolar  $\mathbf{E}$ -field. The apparatus also includes a magnetic bottle near the center of the trap, which introduces a quadratic axial  $\mathbf{B}$ -field along with a radial component.

In such an environment, electrons undergo cyclotron motion with frequency  $\omega_C$  and Larmor precession with frequency  $\omega_S$ . If no further external fields are applied, they are in the ground state of the cyclotron orbit (i.e. first Landau level), with an equal probability of being in either the spin-up or spin-down states. Transitions between the spin states can be induced by applying an external radio-frequency field, while excitations to higher Landau levels are induced by an applied microwave field.

By measuring the shift in the axial frequency of the electron motion due to the state transitions,  $\omega_C$  and  $\omega_S$  are inferred. With this, the electron AMDM can be measured using

$$1 + a_e = \frac{\omega_S}{\omega_C}. \quad (2.49)$$

The current best experimental measurement of  $a_e$  used the Penning trap technique, with the obtained result being [30]

$$a_e = 0.00115965218059(13). \quad (2.50)$$

The precision of this measurement is at the level of 0.1 parts per trillion, so a direct comparison to the Standard Model prediction of  $a_e$  becomes sensitive to the details of other experimental inputs. In particular, an apparent tension in the measurement of  $\alpha_{\text{EM}}$  based on rubidium (Rb) and cesium (Cs) atomic interferometry, has resulted in two predictions [31]

$$a_e^{\text{SM}}(\text{Rb}) = 0.001159652182042(720) \quad (2.51)$$

$$a_e^{\text{SM}}(\text{Cs}) = 0.001159652181620(230). \quad (2.52)$$

These predictions include  $\mathcal{O}(\alpha_{\text{EM}}^5)$  contributions (which is where the  $\alpha_{\text{EM}}$  tension enters), two loops with electroweak interactions, NNLO hadronic VP, and NLO LbyL contributions. Depending on the  $\alpha_{\text{EM}}$  input, a  $2.1\sigma$  or  $3.8\sigma$  deviation can be observed.

The electron EDM  $d_e$  has been measured using  $\text{HfF}^+$  (hafnium fluoride) ions, which were chosen due to the large internal  $\mathbf{E}$ -field of around 23 GV/cm experienced by the valence electrons [32]. If a non-zero  $d_e$  existed, there would be a shift in the energy difference between the spin-up and spin-down states of the valence electron, as a consequence of the  $\mathbf{E} \cdot \mathbf{S}$  coupling. In the experimental setup of Refs. [33, 34], the  $\text{HfF}^+$  ions were confined in a radio-frequency ion trap. Using Ramsey spectroscopy, the population of spin-up and spin-down states was allowed to evolve over time, and then measured using state-selective photo-dissociation induced by lasers. The obtained constraint on  $d_e$  was

$$d_e < 4.1 \times 10^{-30} e \cdot \text{cm} \text{ (90\% CL)}, \quad (2.53)$$

which can be compared to the Standard Model prediction of [35]

$$d_e^{\text{SM}} \lesssim 10^{-40} e \cdot \text{cm}. \quad (2.54)$$

This tiny prediction arises due to three-loop and four-loop diagrams involving quark loops and a minimum of four  $W$  boson vertices, such that the  $\mathcal{CP}$  violating phase in the CKM matrix can be realized. Enhancements due to loops with virtual hadrons are also included in the prediction. Despite the ten orders of magnitude difference between experiment and theory, it is expected that measurements of  $d_e$  will reach the  $10^{-35} - 10^{-37} e \cdot \text{cm}$  range in the future [36], so there is some hope of testing the validity of the SM prediction.

## Muon

The muon has a lifetime of  $2.2 \mu\text{s}$  in the rest frame [37], so the muon EDMs cannot be measured in tabletop experiments. However, the lifetime can be increased by boosting them, thanks to special relativity. Modern measurements of the muon EDMs have therefore relied on cyclotron storage rings, where the properties of circulating muon beams are investigated.

The best measurements of  $a_\mu$  in recent years have come from the Muon  $g - 2$  experiment at Fermilab [38]. In the experimental setup, a beam of protons is made to collide with a fixed target, resulting in the production of pions and other hadrons. The  $\pi^+$ 's decay into anti-muons, whose spins are preferentially aligned with their momentum in the lab frame. The longitudinally polarized  $\mu^+$ 's are then transferred into a storage ring at an energy of 3.09 GeV. At this energy, the lifetime of the anti-muons is boosted to around  $65 \mu\text{s}$ .

Calorimeters placed along the inside of the storage ring detect the energy of positrons from the  $\mu^+ \rightarrow e^+ \nu_e \bar{\nu}_\mu$  decay. Since this decay proceeds via the weak interaction, the kinematics of the positrons depend on the  $\mu^+$  spin. In particular, the positrons have higher energy when the anti-muon spin is aligned with the momentum, as opposed to when it is anti-parallel. Due to the applied magnetic field  $\mathbf{B}$  in the storage ring, the  $\mu^+$ 's undergo Larmor precession in the plane of the ring. Thus, the energy of the detected decay positrons oscillates with a frequency  $\omega_a$  given by

$$\omega_a = \omega_S - \omega_C = a_\mu \frac{e}{m_\mu} B. \quad (2.55)$$

This equation (including relativistic corrections) can be used to measure  $a_\mu$ , but it requires a precise measurement of the magnetic field, which is difficult to achieve in a cyclotron. In practice, the Fermilab experiment calibrates  $\mathbf{B}$  using nuclear magnetic resonance (NMR) in petroleum jelly, and measures  $a_\mu$  using

$$a_\mu = \frac{\omega_a}{\omega_p} \frac{\mu_p}{\mu_e} \frac{m_\mu}{m_e} \frac{g_e}{2}, \quad (2.56)$$

where  $\omega_p$  is the proton Larmor precession frequency in the same magnetic field  $B$ ,  $\mu_{p,e}$  are the magnetic moments of the proton and electron, and  $g_e$  is the  $g$ -factor of the electron.

The 2025 Fermilab measurement of  $a_\mu$  is [39]

$$a_\mu = 0.001165920715(145), \quad (2.57)$$

which is the current world average, combining the latest Fermilab data with the previous Brookhaven measurement [40]. The most recent Standard Model prediction for  $a_\mu$  is [41]

$$a_\mu = 0.00116592033(62), \quad (2.58)$$

which includes  $\mathcal{O}(\alpha_{EM}^5)$  corrections, weak interactions up to two loops (and three loop leading logarithms), and NNLO hadronic VP and NLO hadronic LbyL contributions. This new prediction appears to have resolved a long standing 3-5 $\sigma$  tension between previous measurements and predictions [42], which was used to set constraints on a plethora of BSM scenarios (see Ref. [43] for a review). The 2025 measurement and prediction of  $a_\mu$  agree within one standard deviation of each other.

The storage ring at the Fermilab Muon  $g - 2$  experiment was reused from its precursor, the Brookhaven Muon  $g - 2$  experiment. Data from the Brookhaven experiment was used to set the most stringent limits on the muon EDM  $d_\mu$ . The analysis made use of the fact that in the muon rest frame, the  $\mathbf{B}$ -field in the storage ring looks like an  $\mathbf{E}$ -field. As a consequence, the muon spin vector rotates out of the plane of the ring, thereby affecting the kinematics of the decay positrons. The obtained limit on  $d_\mu$  was [44]

$$d_\mu < 1.9 \times 10^{-19} e \cdot \text{cm} \text{ (95\% CL)}, \quad (2.59)$$

which can be compared to the Standard Model prediction of [35]

$$d_\mu^{\text{SM}} \lesssim 10^{-40} e \cdot \text{cm}. \quad (2.60)$$

Unlike the AMDM, the experimental limit and theoretical prediction of  $d_\mu$  are orders of magnitude away from each other. However, the Fermilab Muon  $g - 2$  experiment has not published its own  $d_\mu$  measurement yet, so there is scope for future improvements.

## Tau

The tau lepton has a mean lifetime of 0.29 ps and a mass of around 1.776 GeV [37]. Accelerating tau leptons to energies where their lifetimes are in the microsecond range, such that spin precession techniques can be used to measure their EMDM's, is far beyond the capabilities of current particle accelerators. Instead, recent measurements have used high energy scattering processes with  $\gamma\tau\tau$  vertices to measure the tau lepton EMDMs, using the parameterizations given in Eq. 2.41 and Eq. 2.47.

The EMDMs of elementary fermions are formally defined in the limit where the photon becomes real. Drell-Yan processes like  $e^+e^- \rightarrow \gamma^* \rightarrow \tau^+\tau^-$  are thus not ideal, since the  $s$ -channel photons have a large non-zero virtuality. *Photon initiated* scattering processes at high energy colliders, where the colliding particles radiate photons with very low virtuality, resulting in  $\gamma\gamma \rightarrow \tau^+\tau^-$  scattering, have instead been the preferred probe in recent years. The

phenomenological aspects of this reaction, in the context of tau EDM measurements, have been extensively studied in the literature [45–59]. It has been investigated in  $e^+e^-$  collisions at the Large Electron Positron collider [60–62], as well as in proton-proton [63] and Pb+Pb [3, 64] collisions at the Large Hadron Collider; the latter will be discussed in more detail in Sec. 2.3. Other processes, like radiative tau decays, were investigated at the Large Electron Positron collider [65, 66].  $D_s \rightarrow \tau \nu_\tau$  decays in fixed target collisions have also been proposed for the measurement of the tau lepton EDMs [67, 68], but have not been realized in experiment.

The Standard Model prediction for the tau lepton AMDM  $a_\tau$  has been computed with  $\mathcal{O}(\alpha_{EM}^3)$  corrections, two loops with electroweak interactions, and contains contributions from leading order hadronic VP and LbyL scattering. Its value is [31]

$$a_\tau^{\text{SM}} = 0.001177171(39). \quad (2.61)$$

This prediction is not as precise as those for the electron and muon, partially because experimental measurements of  $a_\tau$  have not yet reached its level of precision. The most precise measurement of  $a_\tau$  was obtained by the CMS experiment at the Large Hadron Collider, by analyzing the  $\gamma\gamma \rightarrow \tau^+\tau^-$  process in proton-proton collisions. The obtained result is [63]

$$a_\tau = 0.0009^{+0.0032}_{-0.0031} \text{ (68\% CL) }, \quad (2.62)$$

which is still a factor of three away from testing even the Schwinger term. The same publication also yielded an upper bound on  $d_\tau$ ,

$$d_\tau < 1.7 \times 10^{-17} e \cdot \text{cm} \text{ (68\% CL) }. \quad (2.63)$$

It should be noted that a measurement of  $d_\tau$  by the Belle experiment in  $e^+e^- \rightarrow \gamma^* \rightarrow \tau^+\tau^-$  scattering exists in the literature, with the obtained result being [69]

$$\begin{aligned} -1.85 \times 10^{-17} &< \text{Re} \{d_\tau\} < 0.61 \times 10^{-17} e \cdot \text{cm}, \\ -1.03 \times 10^{-17} &< \text{Im} \{d_\tau\} < 0.23 \times 10^{-17} e \cdot \text{cm}. \end{aligned} \quad (2.64)$$

This measurement was performed at  $\sqrt{s} = 10.58 \text{ GeV}$ , so according to the definitions in Eq. 2.41 it is not a true measurement of the tau EDM. However, both the CMS and Belle results are many orders of magnitude away from the Standard Model prediction of [35]

$$d_\tau^{\text{SM}} \lesssim 10^{-34} e \cdot \text{cm}, \quad (2.65)$$

which, like the electron and muon, includes three-loop and four-loop contributions from electroweak and strong interactions, as well as enhancements due to hadronic loops.

It may seem that the current constraints on  $a_\tau$  and  $d_\tau$  are not exciting for SM and BSM phe-



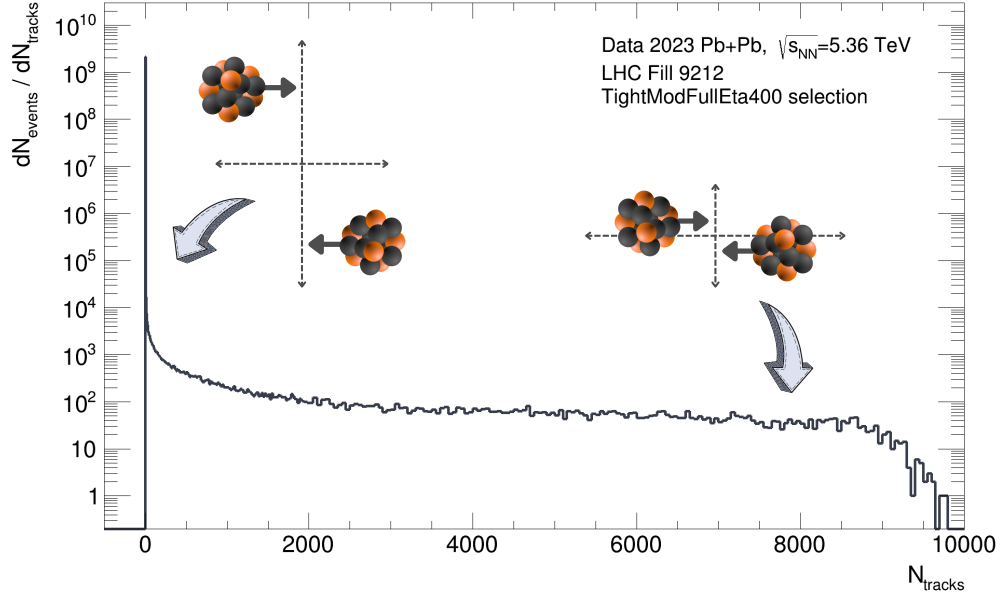


**Figure 2.3:** Multiplicity of tracks reconstructed in the ATLAS Inner Detector in randomly triggered Pb+Pb collisions in one LHC fill (see Sec. 3.3.1 and 4.2 for further details on the data collection, track reconstruction and selection). Cartoons correlating the impact parameter between the colliding ions to the track multiplicity are also shown. Arrows with solid lines denote the direction of propagation of the ions, while arrows with dashed lines represent the collision plane.

nomenology, when compared to the electron and muon EMDMs. However, as a consequence of the structure of BSM loop contributions to the  $\gamma\ell\ell$  vertex, new physics effects are expected to scale with  $m_\ell^2$  [70]. Thus, experimental measurements of these parameters are crucial in the quest for new physics, especially considering that the majority of the collision data at the LHC is yet to be recorded and analyzed.

### 2.3 Tau lepton pair production in ultra-peripheral Pb+Pb collisions

In heavy ion collisions, the *impact parameter*  $|b|$ , i.e. the distance between the “centers” of the two colliding nuclei, governs the multiplicity of the final state. In *central* collisions, where a small impact parameter implies a large overlap between the nuclei,  $\mathcal{O}(10^3)$  particles can be produced in the final state. As the impact parameter increases, the final state particle multiplicity drops. *Ultra-peripheral* collisions (UPCs) refer to those collisions with  $|b| \gtrsim 2R_A$ , where  $R_A$  is the nuclear radius. Since the overlap between the colliding nuclei is minimal (or zero), the final state particle multiplicity can be  $\mathcal{O}(10^1)$  or less. These differences are highlighted in Fig. 2.3, which shows ultra-peripheral and central collisions on the left and right of the figure respectively. In central collisions, where nucleons and partons (quarks and gluons) are close to each other, all possible interactions, i.e. strong, weak and electromagnetic, can occur. Long-range interactions like the electromagnetic force dominate in UPCs, which can cause photon-photon and photon-nucleus scattering processes to occur.

The total cross-section of  $A_1 A_2 \xrightarrow{\gamma\gamma} A_1 A_2 + X$  scattering, where a photon-photon interaction between two colliding nuclei  $A_{1,2}$  produces a generic system  $X$ , can be expressed using a master equation of the form

$$\sigma \left( A_1 A_2 \xrightarrow{\gamma\gamma} A_1 A_2 + X \right) = \int dk_1 dk_2 \frac{d^2 N_{\gamma\gamma}}{dk_1 dk_2} \hat{\sigma}_{\gamma\gamma \rightarrow X}, \quad (2.66)$$

where  $k_{1,2}$  are the energies of the photons emitted by the nuclei and  $\hat{\sigma}_{\gamma\gamma \rightarrow X}$  is the *partonic* cross-section for the hard scattering. The *two photon luminosity* is given by

$$\frac{d^2 N_{\gamma\gamma}}{dk_1 dk_2} = \int d\mathbf{b}_1 d\mathbf{b}_2 P_{\text{surv}}(\mathbf{b}) N_{A_1}(k_1, \mathbf{b}_1) N_{A_2}(k_2, \mathbf{b}_2). \quad (2.67)$$

Here,  $\mathbf{b}_{1,2}$  are the impact parameters of the two ions in the lab frame, such that the ion-ion impact parameter is  $\mathbf{b} = \mathbf{b}_1 - \mathbf{b}_2$ ,  $P_{\text{surv}}(\mathbf{b})$  is the *survival factor*, and  $N_{A_{1,2}}(k_{1,2}, \mathbf{b}_{1,2})$  are the *photon fluxes* of the two ions.

This master equation is used to model photon-induced scattering processes in ultra-peripheral heavy ion collisions, so that data from experiments can be compared to different theoretical predictions. It is not practical to derive predictions analytically due to the complexity of the computations. Instead, numerical tools called *event generators* are used, which use Monte Carlo (MC) methods to perform multidimensional phase space integrations. In the process, they create a discrete set of phase space points corresponding to simulated scattering events, along with their *weights*, or probabilities, of being observed.

In the remainder of this section, the pieces of Eq. 2.66 relevant to  $\gamma\gamma \rightarrow \tau^+ \tau^-$  scattering in ultra-peripheral Pb+Pb collisions are discussed. The details of the different MC event generators used in this thesis are also highlighted.

### 2.3.1 Photon flux

When a charged particle moves at ultra-relativistic velocities, the flux of electromagnetic fields produced by it becomes concentrated along the plane transverse to the direction of motion. The *equivalent photon approximation* (EPA), originally proposed by Fermi [71], and later adapted to the ultra-relativistic case by Weizsäcker and Williams [72, 73], equates the intensity of the EM fields to the energy carried by a flux of quasi-real (i.e. almost on-shell) photons. It is a semi-classical method, and is best suited for the computation of *coherent* photon emission, where the photons “see” the total electric charge of the emitter, rather than that of its constituents.

Following the arguments of the EPA, the photon flux of an ultra-relativistic extended charged object, such as a nucleus, is given by [74, 75]

$$N_{A_i}(k_i, \mathbf{b}_i) = \frac{Z_i^2 \alpha}{\pi^2} \frac{1}{k_i} \left| \int_0^\infty \frac{dk_T k_T^2}{k_T^2 + k_i^2 / \gamma_L^2} F \left( \sqrt{k_T^2 + k_i^2 / \gamma_L^2} \right) J_1(k_T b_i) \right|^2, \quad (2.68)$$

where  $Z_i$  is the atomic number of the nucleus  $A_i$ ,  $k_T$  is the transverse momentum of the photon,  $b_i = |\mathbf{b}_i|$  is the impact parameter in the lab frame,  $\gamma_L$  is the Lorentz factor of the ion, and  $J_1$  is

a Bessel function of the first kind. The virtuality of the photons is given by  $q_i^2 = k_T^2 + k_i^2/\gamma_L^2$ . Under the condition of coherent emission, the photons should not be able to “resolve” the ion, so the virtuality is limited to  $q_i^2 < 1/R_A^2$ , which is  $\mathcal{O}(10^{-3})$  GeV<sup>2</sup> for large nuclei like lead.

The quantity  $F$  is the nuclear form factor, which is related to the nuclear density  $\rho_A(\mathbf{r})$  of the ion via a Fourier transform, i.e.

$$F(q) = \int d^3\mathbf{r} \cdot e^{i\mathbf{q}\cdot\mathbf{r}} \rho_A(\mathbf{r}) = \frac{4\pi}{q} \int_0^{+\infty} dr \rho_A(r) r \sin(qr). \quad (2.69)$$

In the second equality, it is assumed that the charge distribution is radially symmetric. The nuclear density is usually normalized in such a way that the above integrals are equal to unity, which implies  $F(0) = 1$ .

A realistic model of the nuclear density, particularly for radially symmetric nuclei like Pb, is the Woods-Saxon (WS) distribution

$$\rho_A^{\text{WS}}(r) = \frac{\rho_{0,A}}{1 + \exp\left(\frac{r-R_A}{a_A}\right)}, \quad (2.70)$$

where  $\rho_{0,A}$  is the normalization factor (fixed by the  $F(0) = 1$  condition),  $R_A$  is a radius-like parameter that describes the mean nuclear density, and  $a_A$  is referred to as the skin depth. For <sup>208</sup>Pb, these parameters are  $\rho_{\text{Pb}} = 6.62$  fm and  $a_{\text{Pb}} = 0.549$  fm [76]. This form of the WS nuclear density distribution is used by the SuperChic [77] and gammaUPC [78] MC event generators.

Two other common models for the nuclear density are the hard sphere (HS) model

$$\rho_A^{\text{HS}}(r) = \frac{3}{4\pi R_A^3} \Theta(R_A - r), \quad (2.71)$$

where  $\Theta$  is the Heaviside step function, and the Yukawa model

$$\rho_A^{\text{Yukawa}}(r) = \frac{a^2 e^{-ar}}{4\pi r}, \quad (2.72)$$

where  $a = 0.7$  fm. The STARlight MC event generator [79] uses a combination of these models to define the nuclear form factor, i.e.

$$F(q) = F^{\text{HS}}(q) F^{\text{Yukawa}}(q) \quad (2.73)$$

$$= \left[ \frac{3}{(qR_A)^3} (\sin qR_A - qR_A \cos qR_A) \right] \left[ \frac{a^2}{a^2 + q^2} \right], \quad (2.74)$$

which is found to approximate the WS model reasonably well.

A key difference between MC event generators pertaining to the photon flux is the choice of impact parameter integration range in Eq. 2.67. In STARlight, the integration range is

restricted to the  $|\mathbf{b}_{1,2}| > R_{\text{Pb}}$  and  $|\mathbf{b}| > 2R_{\text{Pb}}$  region, so that  $\gamma\gamma \rightarrow X$  production is not permitted from “inside” the colliding nuclei. This condition is justified in the sense that it forces the hard scattering to be ultra-peripheral, but it results in predicted cross-sections that are generally lower than the data. On the other hand, the photon flux calculations within `SuperChic` and `gammaUPC` are performed over the entire impact parameter range. As a consequence, the predicted cross-sections are generally higher than that of `STARlight`, and tend to agree better with the data. These observations are made more apparent in Chapter 5.

The emission and absorption of quasi-real photons in ultra-peripheral heavy ion collisions often leads to nuclear excitation and subsequent de-excitation [80]. Several low energy (i.e.  $\mathcal{O}(10)$  MeV) mechanisms, such as electromagnetic dissociation and the giant dipole resonance<sup>4</sup>, result in the emission of nuclear fragments during the de-excitation process. Of importance are the neutral fragments, particularly neutrons, since they are not bent away by the beam steering magnets in a collider. The emitted neutrons can be detected in zero degree calorimeters, and used to *tag* UPC processes through vetoes. The probability of *nuclear breakup* is impact parameter-dependent, and is typically not included in the two-photon luminosity, so Eq. 2.66 actually represents the cross-section of the  $A_1 A_2 \xrightarrow{\gamma\gamma} A_1 A_2 + X$  process inclusive in nuclear breakup. The probability of nuclear breakup increases with the virtuality of the exchanged photons, i.e. in UPCs, where the exchanged photons are almost on-shell, the interacting ions have a high probability of remaining intact.

### 2.3.2 Survival factor

Photon-induced scattering processes are typically very clean, i.e. are associated with almost no other particles in the final state besides the  $\gamma\gamma \rightarrow X$  production. These processes are associated with large gaps in the distribution of final state particles as a function of rapidity (or longitudinal angle), particularly in the forward (i.e. high rapidity) regions. However, at small impact parameters ( $b \sim 2R_A$ ), QCD interactions may occur along with the electromagnetic interaction, resulting in additional final state particles. The *survival factor* represents the probability that the rapidity gaps in  $\gamma\gamma \rightarrow X$  production survive the nucleus-nucleus collision. It can also be seen as the probability for no hadronic interactions to occur between the two colliding nuclei.

The survival factor can be written as a suppression factor,

$$P_{\text{surv}}(\mathbf{b}) = e^{-\Omega(\mathbf{b})}, \quad (2.75)$$

where the nuclear opacity  $\Omega(\mathbf{b})$  can be interpreted as the probability of inelastic ion-ion interactions having occurred. It is given by [81]

$$\Omega(\mathbf{b}) = \int d^2\mathbf{b}_1 d^2\mathbf{b}_2 T_{A_1}(\mathbf{b}_1) T_{A_2}(\mathbf{b}_2) A_{nn}(\mathbf{b} - \mathbf{b}_1 + \mathbf{b}_2). \quad (2.76)$$

---

<sup>4</sup>The giant dipole resonance refers to a collective oscillation of all protons and neutrons in a nucleus out of phase with respect to each other.

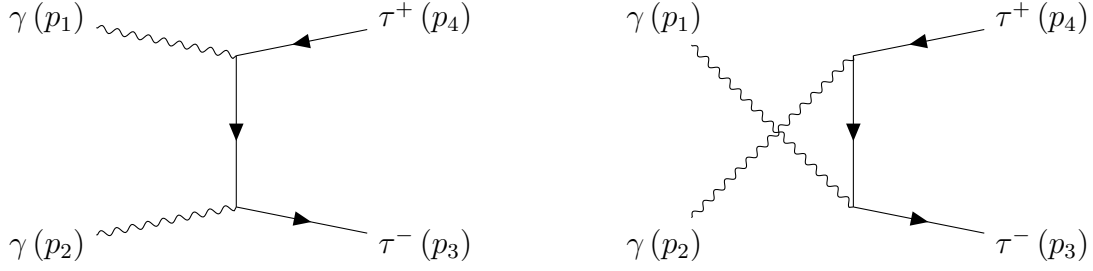


**Figure 2.4:** Feynman diagrams for  $\gamma\gamma \rightarrow \tau^+\tau^-$  scattering at leading order in QED. In terms of Mandelstam variables  $t, u$ , these are the  $t$ -channel and  $u$ -channel diagrams on the left and right respectively. The  $p_i$  are the four-momenta of the involved particles.

In this equation, the nuclear thickness function, defined as

$$T_{A_i}(\mathbf{b}) = \int dz \rho_i(\mathbf{b}_i + z\hat{\mathbf{z}}), \quad (2.77)$$

gives the amount of nuclear matter from the nucleus  $A_i$  at the given transverse position  $\mathbf{b}$ , integrated over all longitudinal positions  $z$ .  $A_{nn}$  is the amplitude of nucleon-nucleon scattering, which in `SuperChic`, depends on the nucleon opacity via the eikonal approximation (see, e.g. Ref [82]). In the `gammaUPC` and `STARlight` generators,  $A_{nn}$  is taken to be independent of  $\mathbf{b}$ , so it is effectively the nucleon-nucleon inelastic cross-section  $\sigma_{\text{inel}}^{\text{nn}}$ .

In `SuperChic`, the survival factor depends the details of the central  $\gamma\gamma \rightarrow X$  process. Thus, for  $\gamma\gamma \rightarrow \tau^+\tau^-$  scattering, it can also depend on the tau lepton EMDMs. This effect was studied recently in Ref. [59] and was found to be very small, so it is neglected in this thesis.

### 2.3.3 Hard scattering

The hard scattering process of interest in this thesis is the  $\gamma\gamma \rightarrow \tau^+\tau^-$  process. At leading order in QED, there are two Feynman diagrams that contribute, which are shown in Fig. 2.4. The matrix element of  $\gamma\gamma \rightarrow \tau^+\tau^-$  is given by

$$i\mathcal{M} = \epsilon_{1\mu}\epsilon_{2\nu}\bar{u}(p_3) \left[ i\Gamma^\mu(p_3, p_t) \frac{i(\not{p}_t + m_\tau)}{p_t^2 - m_\tau^2} i\Gamma^\nu(p_t, -p_4) \right. \\ \left. + i\Gamma^\nu(p_3, p_u) \frac{i(\not{p}_u + m_\tau)}{p_u^2 - m_\tau^2} i\Gamma^\mu(p_u, -p_4) \right] v(p_4), \quad (2.78)$$

where  $p_t = p_3 - p_1 = p_2 - p_4$  and  $p_u = p_1 - p_4 = p_3 - p_2$  are the momenta of the internal taus,  $\epsilon_{1\mu}$  and  $\epsilon_{2\nu}$  are the polarization four-vectors of the incoming photons,  $\bar{u}(p_3)$  and  $v(p_4)$  are the Dirac spinors of the outgoing taus, and  $\Gamma^\mu$  is the generalized  $\gamma\tau\tau$  vertex with electromagnetic form factors, introduced in Eq. 2.41.

In ultra-peripheral heavy ion collisions, the initial state photons have transverse momenta  $k_T$  in the  $\mathcal{O}(10)$  MeV range, so the  $p_T$  of a system produced in  $\gamma\gamma$  collisions can be non-

zero. In fact, the photon  $k_T$  spectrum can be derived from Eq. 2.68 by fixing  $k$  and integrating over  $b$ . However, the photon energy and longitudinal momentum spectra are many orders of magnitude higher than the  $k_T$  spectrum, so the photon  $k_T$  is often assumed to be zero<sup>5</sup>. Thus, only the longitudinal polarizations, i.e. *helicities*, of the photons can be considered as degrees of freedom. The Dirac spinors  $\bar{u}(p_3)$  and  $v(p_4)$  are, in general, functions of the full tau spin vectors, although they can also be reduced to helicity-dependent wave functions.

The unpolarized cross-section for  $\gamma\gamma \rightarrow \tau^+\tau^-$  scattering is obtained using Eq. 2.15 for the matrix element in Eq. 2.78, along with the usual average over photon polarizations and sum over tau spins. After integrating over the phase space, the total cross-section at a given center of mass energy  $s$ , with the EMDMs set to zero, is [83]

$$\begin{aligned} \hat{\sigma}_{\gamma\gamma \rightarrow \tau^+\tau^-}(s) = \frac{4\pi\alpha^2}{s^2} & \left[ \left( 2 + \frac{8m_\tau^2}{s^2} - \frac{16m_\tau^4}{s^4} \right) \log \left( \frac{s + \sqrt{s^2 - 4m_\tau^2}}{2m_\tau} \right) \right. \\ & \left. - \sqrt{1 - \frac{4m_\tau^2}{s^2}} \left( 1 + \frac{4m_\tau^2}{s^2} \right) \right]. \end{aligned} \quad (2.79)$$

The MC event generators considered in this thesis employ different techniques when simulating the  $\gamma\gamma \rightarrow \tau^+\tau^-$  process: STARlight simply samples the above equation during the event generation process, while SuperChic and MadGraph5\_aMC@NLO [84] include the helicity degrees of freedom in the matrix element calculations.

### 2.3.4 Tau lepton decay and spin correlations

The decays of tau leptons proceed via the chiral weak interaction, through the coupling of the tau lepton to  $W$  bosons. *Leptonic tau decays* refer to the  $\tau^- \rightarrow \nu_\tau \mu^- \bar{\nu}_\mu$  and  $\tau^- \rightarrow \nu_\tau e^- \bar{\nu}_e$  final states, and *hadronic tau decays* refer to the  $\tau^- \rightarrow \nu_\tau X$  final states, where  $X$  includes stable hadrons (mostly pions and kaons at relativistic energies). The ratio of the *partial width* of a given final state, to the *total width* of the tau lepton, is called the *branching fraction* or *branching ratio*. The decays to electrons and muons have a branching ratio of around 17% each, while the hadronic decays have a total branching ratio of around 65%. An overview of the tau lepton branching ratios is shown in Fig. 2.5.

Due to the chiral nature of the weak interaction, the kinematics of the tau decay products depend on the tau spin. For a generic  $\tau \rightarrow \nu_\tau X$  decay, the partial width  $\Gamma$  is given by [85, 86]

$$d\Gamma_{\tau \rightarrow \nu_\tau X} = \frac{1}{2m_\tau} |\mathcal{M}_{\text{unpol}}|^2 (1 + h_\mu s^\mu) dS, \quad (2.80)$$

where  $\mathcal{M}_{\text{unpol}}$  is the unpolarized matrix element for the given decay,  $dS$  is the Lorentz invariant

---

<sup>5</sup>This assumption is not appropriate for the  $\gamma\gamma \rightarrow e^+e^-, \mu^+\mu^-$  processes, since the photon  $k_T$  leads to a small but observable acoplanarity between the leptons. For  $\tau^+\tau^-$  pair production, this has no observable effect, since the neutrinos from the tau decay prevent the full reconstruction of the  $\tau^+\tau^-$  system four-momentum.

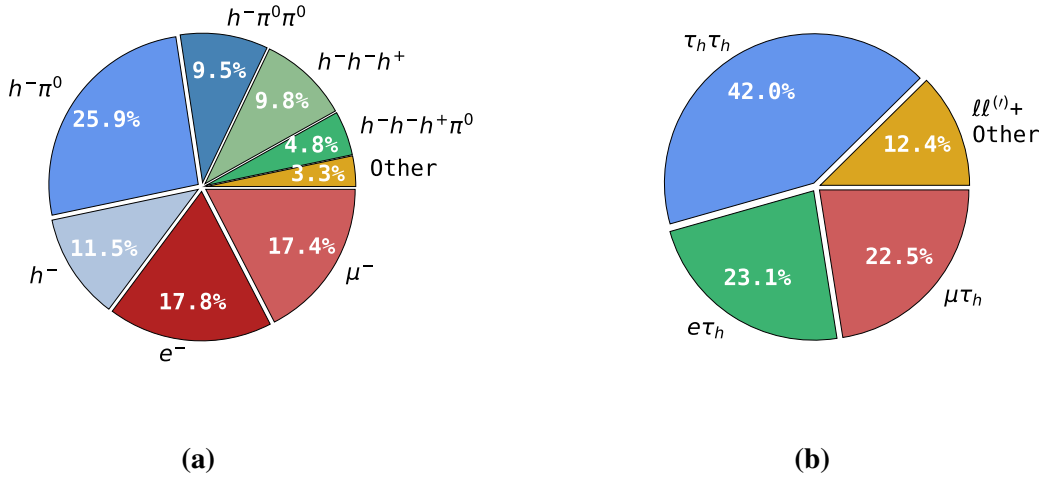


**Figure 2.5:** Branching fractions of (a) single  $\tau^-$  decays, and (b)  $\tau^+\tau^-$  pair decays. Here,  $h^\pm$  refers to stable charged hadrons (pions and kaons),  $\tau_h$  refers to hadronic tau decays, and  $\ell, \ell'$  refers to electrons and muons. The “Other” category includes radiative leptonic decays, hadronic decays with more than one  $\pi^0$  and more than three stable charged hadrons. The neutrinos have been omitted for brevity. Numbers taken from Ref. [37].

phase space element,  $s^\mu$  is the spin four-vector of the tau<sup>6</sup>, and  $h_\mu$  is called the *polarimetric vector* for the given decay. The polarimetric vector can be interpreted as the most probable direction of the tau spin, and can be calculated using [87]

$$h^\mu = \sum_{\lambda, \bar{\lambda}} \sigma^\mu_{\lambda, \bar{\lambda}} \mathcal{M}_\lambda \mathcal{M}_{\bar{\lambda}}^\dagger \quad (2.81)$$

where  $\sigma^\mu = (\mathbb{1}, \sigma^i)$ , and  $\lambda, \bar{\lambda}$  run over the spin projections of  $\mathcal{M}$  for the given decay. The polarimetric vector is normalized such that the time-like component  $h^0$  is unity.

The files created by the STARlight and SuperChic MC event generators do not store information on the tau spin vectors, so it is not possible to perform tau decay simulations with full spin dependence. However, the effect of including the spin information in the event generator can be restored through *spin weights*. In this approach, the differential cross-section for  $\tau^+\tau^-$  production can be written like [87]

$$d\sigma = \left( \sum_{\lambda_1, \lambda_2} |\mathcal{M}_{\lambda_1, \lambda_2}^{\text{prod}}|^2 \right) \left( \sum_{\lambda_1} |\mathcal{M}_{\lambda_1}^{\tau^+}|^2 \right) \left( \sum_{\lambda_2} |\mathcal{M}_{\lambda_2}^{\tau^-}|^2 \right) w_{\text{spin}} d\Omega_{\text{prod}} d\Omega_{\tau^+} d\Omega_{\tau^-}, \quad (2.82)$$

where  $\lambda_{1,2}$  are the spin projections of  $\tau^\pm$  on unspecified axes,  $\mathcal{M}_{\lambda_1, \lambda_2}^{\text{prod}}$  is the matrix element associated with the  $\tau^+\tau^-$  production with phase space element  $d\Omega_{\text{prod}}$ , and  $\mathcal{M}_{\lambda_1}^{\tau^+}$  and  $\mathcal{M}_{\lambda_2}^{\tau^-}$  are the matrix elements of the  $\tau^\pm$  decay with the phase space elements  $d\Omega_{\tau^\pm}$ . In essence, the first three factors give the unpolarized squared matrix element for the given process. The effects of

<sup>6</sup>The spin-four vector is equal to  $(0, \mathbf{s})$  in the rest frame of the tau lepton, with  $\mathbf{s}$  being the spin three-vector.

spin correlations in the complete process are recovered through the spin weight  $w_{\text{spin}}$ , which is given by

$$w_{\text{spin}} = \sum_{i=0}^4 R_{ij} h_{\tau^+}^i h_{\tau^-}^j. \quad (2.83)$$

Here,  $R_{ij}$  is the spin correlation matrix for the  $\tau^+\tau^-$  production,

$$R_{ij} = \sum_{\lambda_1, \bar{\lambda}_1, \lambda_2, \bar{\lambda}_2} \sigma_{\lambda_1, \bar{\lambda}_1}^i \sigma_{\lambda_2, \bar{\lambda}_2}^j \mathcal{M}_{\lambda_1, \lambda_2}^{\text{prod}} \mathcal{M}_{\bar{\lambda}_1, \bar{\lambda}_2}^{\text{prod} \dagger}, \quad (2.84)$$

and  $h_{\tau^\pm}^i$  are the polarimetric vectors.

In this thesis, tau decays have been implemented in simulated  $\gamma\gamma \rightarrow \tau^+\tau^-$  datasets using the Pythia8 [88] and Tauola [86] generators. In Pythia8, only the longitudinal spin correlations in the tau production and decay are included for the  $\gamma\gamma \rightarrow \tau^+\tau^-$  process, while the full spin correlation is included in Tauola by way of the TauSpinner package [89]. In a recent update of TauSpinner [90, 91], the electromagnetic dipole moments of the tau lepton have been included in the  $R_{ij}$  matrix of the  $\gamma\gamma \rightarrow \tau^+\tau^-$  process. Since EMDMs are fundamentally tied to the spins of fermions, this has enabled the investigation of the impact of non-zero tau EMDMs, together with full spin correlations, on the kinematic distributions of the decay products.



# Chapter 3

## The ATLAS detector at the Large Hadron Collider

In this chapter, the experimental methods relevant to this thesis are presented. In Sec. 3.1 the principles of particle acceleration and the Large Hadron Collider are introduced. The ATLAS experiment and its sub-detectors are described in Sec. 3.2. The techniques used in the processing and reconstruction of the data recorded by the ATLAS experiment are discussed in Sec. 3.3. Since this thesis makes use of data from collisions delivered by the LHC in the years 2015 and 2018, the layout of the LHC and the ATLAS detector in these years are presented.

### 3.1 The Large Hadron Collider

The Large Hadron Collider (LHC) [93] is an approximately circular hadron accelerator and collider, located at a mean depth of 100 m below the France-Switzerland border near Geneva. It is the worlds largest and most powerful accelerator (to date), with a circumference of around 27 km.

The LHC is the most complex scientific machine in the world, and requires a concerted effort from many different systems (cryogenics, vacuum, etc.) to deliver high energy collisions. There are eight *insertion points* along the LHC ring that house different facilities and services, as shown in Fig 3.1. At Point 3 and Point 7, collimation systems clean the beams of stray particles, ensuring the safe operation of the LHC. The radio frequency acceleration systems are located at Point 4, along with critical LHC instrumentation (see Sec. 3.1.3). The beams are dumped at Point 6 into a water-cooled graphite block, which is surrounded by a steel casing.

At the other insertion points, the LHC hosts four major particle physics experiments:

- **ATLAS** (A Toroidal Lhc ApparatuS) [94], situated at Point 1, is one of two general purpose detectors at the LHC, and performs precision measurements of the Standard Model and searches for Beyond Standard Model physics. It is also used to study heavy ion collisions, such as in this thesis.
- **CMS** (Compact Muon Solenoid) [95], located at Point 5, is the second general purpose

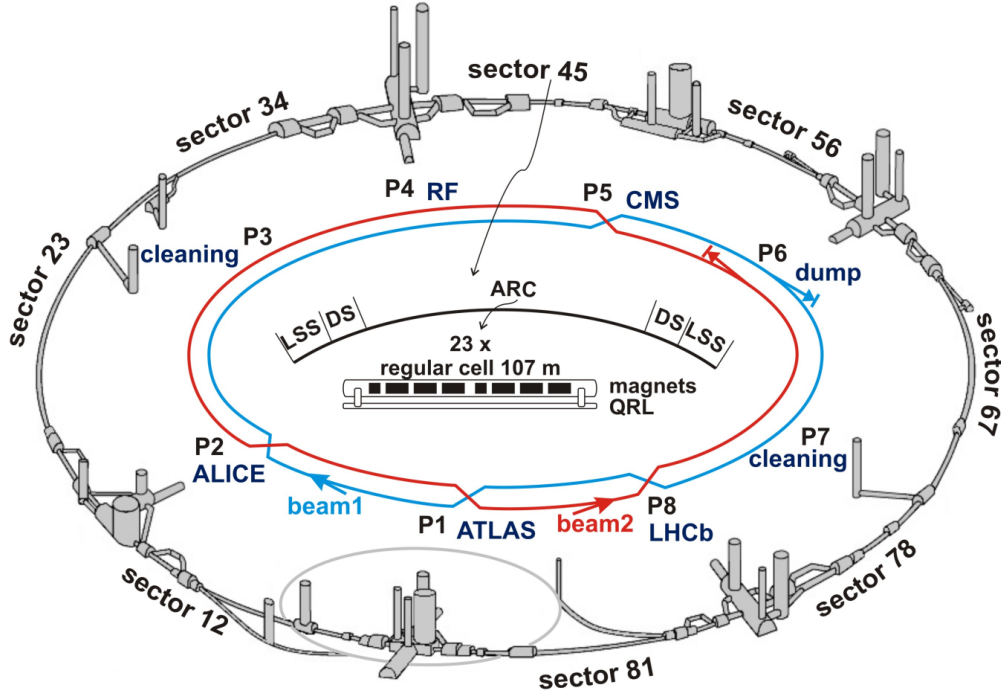


**Figure 3.1:** Illustration of the LHC underground complex [92]. The eight sectors and insertion regions are highlighted, along with facilities they host. The direction of propagation of the two beams is shown in the center of the figure, along with a breakdown of the magnet arrangement in one sector.

detector at the LHC, with similar physics goals as ATLAS, but constructed with complementary detector technologies.

- **ALICE** (A Large Ion Collider Experiment) [96], located at Point 2, is the only dedicated heavy ion detector at the LHC. It focuses on studies of QCD and the quark gluon plasma (QGP), through observables like particle correlations, flow coefficients and jet quenching. The detector is optimized for particle identification, and for track reconstruction in high multiplicity heavy ion collisions.
- **LHCb** (Large Hadron Collider Beauty) [97], situated at Point 8, is a single arm spectrometer designed to probe  $\mathcal{CP}$  violation through the physics of heavy quark hadrons (eg.  $B$  and  $D$  mesons). Using its particle identification capabilities, LHCb can perform precision SM measurements which indirectly test BSM physics.

The sections of the LHC ring between two insertion points are called *sectors*. Each sector consists of an *arc* with 23 *arc cells*, which house the main bending dipoles, (de)focusing quadrupoles and higher order corrector magnets. The arcs are bookended by *dispersion suppressors*, which adapt the beam orbit to the tunnel geometry and ensure that the beam optics are matched during insertion, and the *long straight sections*, which house the experimental halls and other utilities discussed above. In total, the LHC uses 9593 magnets in its ring, of which

1232 are the main dipoles with field strengths of 8.3 T, and 392 are the main (de)focusing quadrupoles with field strengths of 6.8 T. The magnets and other components of the LHC accommodate two counter-rotating beams, which are brought into collision at *interaction points* (IPs) within the experiments.

### 3.1.1 Particle acceleration

Particle accelerators, like those at CERN, rely on the principle of synchronous acceleration. The most common accelerator types at CERN are *linear accelerators* and *synchrotrons*. In these machines, periodically oscillating electric fields, typically in the radio-frequency (RF) range, are used to accelerate particles to very high energies.

At the LHC, which is a synchrotron, the RF fields are produced at a frequency of 400 MHz by high power vacuum tubes called *klystrons* [93]. The fields are fed into superconducting resonating cavities called *RF cavities*, eight of which are used per beam. As particles travel through the cavities, the phase difference between their revolution frequency and the RF frequency dictates the acceleration experienced by them. In particular, particles which enter the cavities at the peak of the RF field experience the largest acceleration, compared to those that arrive before or after the peak.

If particles enter the RF cavities during the negative half of the oscillation, they experience deceleration. Thus, the RF fields *bunch* the particles into small groups that reside in *buckets* within the positive half of the RF oscillation. The RF system at the LHC creates 35,640 buckets, which are grouped into 3564 *bunch slots*, each consisting of ten consecutive buckets. The middle bucket in a bunch slot, called the *nominal* bucket, is usually where the particles intended to be collided are found. Due to imperfections or inefficiencies in the beam manipulation along the injector chain, a small fraction of the charges in a bunch slot may be found in the remaining nine buckets. These are called *satellite charges*. On the other hand, charges present in RF buckets not in the filled bunch slots are called *ghost charges* [98].

Ghost and satellite charges are undesirable since they pose a risk to the operational safety of the LHC. Moreover, collisions between ghost charges and those in the nominal bucket can create undesired backgrounds in the experiments. The contribution of such backgrounds are mitigated at the LHC by colliding the beams at the interaction points with a non-zero *crossing angle* between them, as opposed to the *head-on* configuration.

As the particles are being accelerated by the RF system, their trajectories need to be tuned so that they remain within the beampipe. This is achieved at the LHC using high field superconducting magnets, operating at temperatures below 2 K. Dipole magnets are used to bend the trajectories of particles, while quadrupole magnets change the transverse shape of the bunches<sup>1</sup>. Additional higher order magnets are also used to correct for non-linear effects and ensuring the stability of the beams.

---

<sup>1</sup>Quadrupoles focus the beam along one axis, while defocusing along the other axis, due to the  $\mathbf{v} \times \mathbf{B}$  term in the Lorentz force.

In a synchrotron like the LHC, the particles do not travel exactly on the orbit defined by the center of the ring. Instead, they undergo *betatron oscillations* in the plane transverse to the beam orbit [99]. The amplitude of the betatron oscillation is a function of the position  $s$  along the beam orbit, given by  $A(s) = \sqrt{\epsilon\beta(s)}$ . Here, the emittance  $\epsilon$  of the beams relates to the size of the phase space occupied by the particles, and  $\beta(s)$  is called the beta function. It is often useful to know the value of the beta function at a given point  $s_0$  along the orbit. This is given the name  $\beta^* \equiv \beta(s_0)$ , which together with the emittance, gives the transverse size of the beam at a location of interest, such as at an interaction point.

One key metric of the performance of a collider is the energy at which it delivers collisions. For ultra-relativistic ion collisions, the per-nucleon center of mass energy is [100]

$$\sqrt{s_{\text{NN}}} = \sqrt{s_{\text{pp}}} \sqrt{\frac{Z_1 Z_2}{A_1 A_2}}, \quad (3.1)$$

where  $Z_{1,2}$  and  $A_{1,2}$  are the atomic number and nuclear mass of the colliding ions, and  $\sqrt{s_{\text{pp}}}$  is the proton-proton center of mass energy under the same accelerator configuration.

Another equally important collider metric is the instantaneous luminosity  $\mathcal{L}_{\text{inst}}$ , which relates the event rate  $R$  of a scattering process of interest to its theoretical cross section  $\sigma$  as

$$R = \frac{dN}{dt} = \mathcal{L}_{\text{inst}} \sigma. \quad (3.2)$$

If the charge distribution of the colliding bunches can be described by equal Gaussians, the instantaneous luminosity is given by [101]

$$\mathcal{L}_{\text{inst}} = \frac{N_1 N_2 f_{\text{rev}} n_b}{4\pi\sigma_x\sigma_y} \mathcal{F}, \quad (3.3)$$

where  $N_{1,2}$  are the intensities of the two bunches,  $f_{\text{rev}}$  is the revolution frequency (11.245 kHz at the LHC),  $n_b$  is the number of colliding bunches,  $\sigma_{x,y}$  are the Gaussian beam widths in the  $x$  and  $y$  planes, and  $\mathcal{F}$  is a reduction factor due to effects like crossing angles and beam separations. In 2018, the LHC delivered proton beams with a maximum luminosity of  $\mathcal{L}_{\text{inst}} = 2 \times 10^{34} \text{ cm}^2/\text{s}$ , and Pb ion beams with a maximum luminosity of  $\mathcal{L}_{\text{inst}} = 6 \times 10^{27} \text{ cm}^2/\text{s}$ . The time integral of the instantaneous luminosity, given by

$$\mathcal{L}_{\text{int}} = \int \mathcal{L}_{\text{inst}} dt \quad (3.4)$$

defines the *integrated luminosity*, and is directly related to the total amount of collision data collected during the integration period. The concept of luminosity, including its measurement and calibration, is discussed in further detail in Chapter 4.

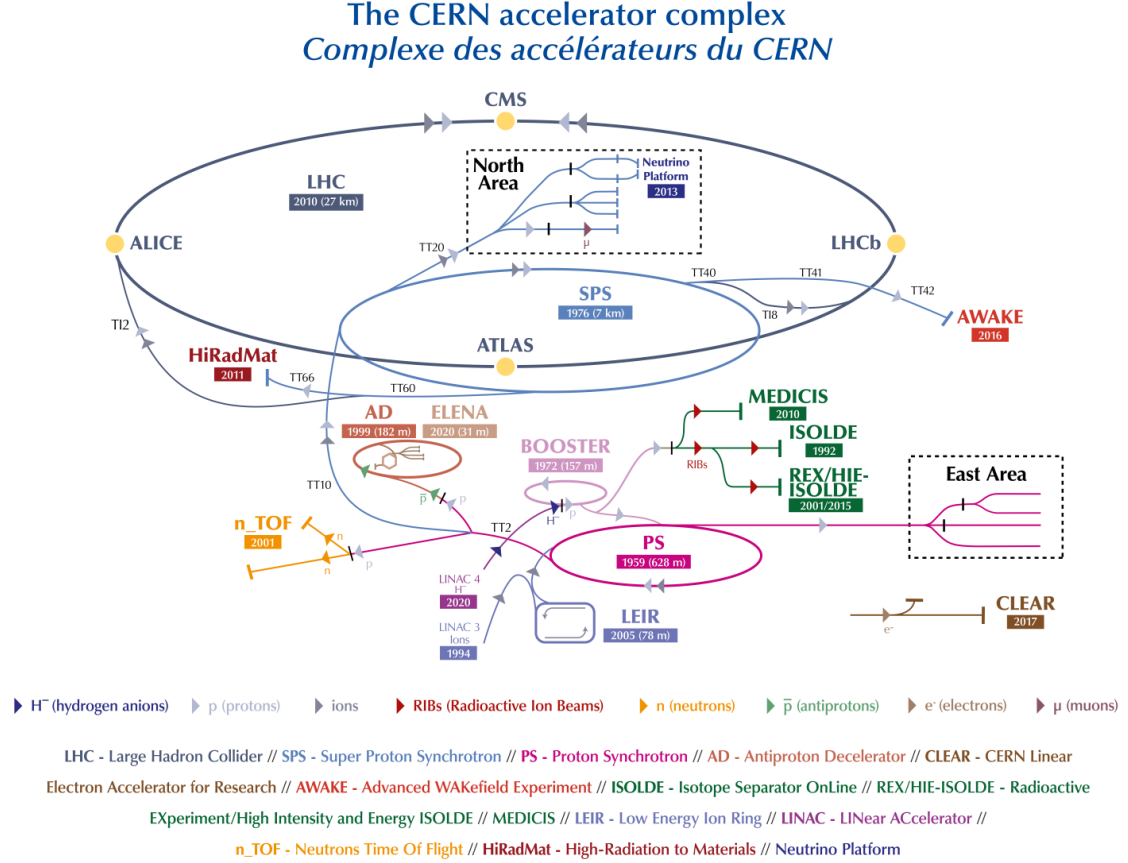


**Figure 3.2:** Layout of the CERN accelerator complex in the year 2022 [102]. The same layout and injector complex was used for ions during Run 2 of the LHC.

### 3.1.2 LHC operation

CERN operates the LHC for several years at a time in *Runs*, followed by *Long Shutdowns* (LSs) so that the LHC and the experiments can perform maintenance and upgrades. In the first run of the LHC (Run 1, from 2010-2013) the LHC delivered p+p collisions at 7 and 8 TeV center of mass energies. It was in this dataset that the ATLAS and CMS experiments discovered the Higgs boson [103, 104]. Additionally, Pb+Pb collisions at  $\sqrt{s_{\text{NN}}} = 2.76$  TeV and p+Pb collisions at  $\sqrt{s_{\text{NN}}} = 5.02$  TeV were also delivered. In Run 2 of the LHC (2015-2018), the p+p collision energy was upgraded to 13 TeV. Run 2 also featured many heavy ion collision datasets: Pb+Pb collisions at  $\sqrt{s_{\text{NN}}} = 5.02$  TeV in 2015 and 2018, p+Pb at  $\sqrt{s_{\text{NN}}} = 8.16$  TeV in 2016, and Xe+Xe collisions at  $\sqrt{s_{\text{NN}}} = 5.44$  TeV. At the time of writing this thesis, the LHC is in its third run (2022-present), where p+p collisions at  $\sqrt{s} = 13.6$  TeV and Pb+Pb collisions at  $\sqrt{s_{\text{NN}}} = 5.36$  TeV have been ongoing.

The preparation of proton and Pb ion beams at CERN share many components of the accelerator complex, as shown in Fig. 3.2. At the heavy ion source facility, partially stripped lead ions are created through the evaporation of an isotopically pure  $^{208}\text{Pb}_{82}$  block. The ions proceed

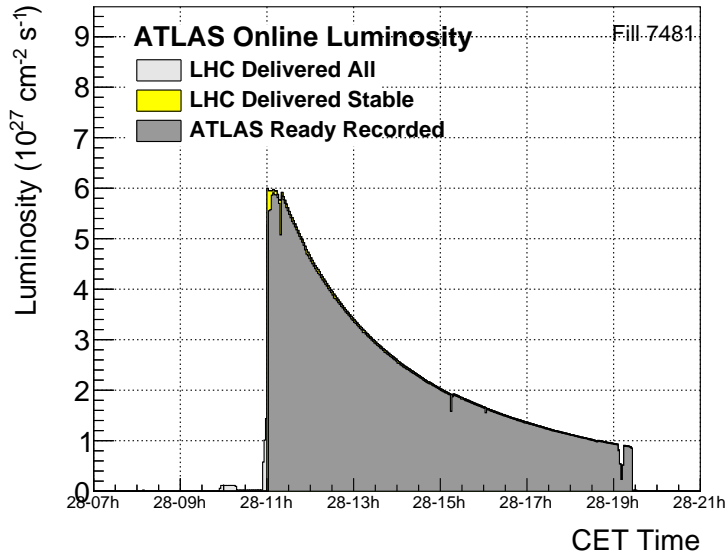


**Figure 3.3:** Instantaneous luminosity delivered to, and recorded by, the ATLAS experiment during a Pb+Pb fill in 2018. Separation levelling was used to limit the peak luminosity for the first few minutes of the fill.

through a series of injectors, where they are further stripped of their electrons, and accelerated to increasingly higher energies, until they are injected into the LHC. The path through the CERN injector complex followed by heavy ions, together with the maximum achieved energy per nucleon in Run 2 was [105]: LINAC3 (4.2 MeV/n), LEIR (72 MEV/n), PS (5.9 GeV/n), SPS (177 GeV/n), LHC (2.51 TeV/n).

Proton and ion beams at the LHC go through an operational cycle called the *fill cycle*. After the SPS injects the required bunches into the LHC, the LHC RF system accelerates the bunches to the top energy. At the same time, the field strength of the LHC magnets is increased, or *ramped*, so that the bunches are kept on orbit. Once the *flat top* energy is reached, the beams are focused or *squeezed*, and brought closer together by *adjusting* their transverse positions. *Stable beams* are declared when stable collisions are observed, which is when the experiments start recording collision data.

If the initial luminosity is too high for the experiments, the LHC performs *luminosity levelling*, either by first separating the beams and slowly bringing them closer (separation levelling), or by squeezing the beams in small increments as the luminosity reduces ( $\beta^*$  levelling). After some time the beam intensity reduces, partly due to the protons or ions being "consumed" in collisions. It then becomes more profitable to restart collisions with a fresh beam, so the original beam is dumped. The magnets are then ramped down, the LHC is refilled, and the fill cycle starts over. Figure 3.3 shows the luminosity profile for a Pb+Pb fill delivered to, and recorded by, ATLAS in 2018.

Heavy ion beams at the LHC typically have a lower intensity compared to proton beams due to the lower injection efficiency, increased probability of intra-beam scattering and space

charge effects, etc. As a consequence, the probability of multiple ion-ion collisions per bunch crossing, called *pileup*, is at the  $10^{-3}$  level, compared to a pileup of around 30 for p+p collisions in Run 2 (on average). Heavy ion beams also have a larger bunch spacing, compared to the 25 ns spacing of proton beams. The large signals produced by central heavy ion collisions can reduce the data-taking efficiency due to deadtime, so lower luminosity beams are somewhat beneficial.

The analysis presented in this thesis investigates Pb+Pb ion collisions in the LHC Run 2. Table 3.4 summarizes the key machine parameters for Pb ions collisions in 2015 and 2018.

Beam parameter	2015	2018
Max. colliding bunches in ATLAS	492	733
Min. bunch spacing (ns)	100	75
Max. ions per bunch ( $10^8$ )	2.0	2.2
$\beta^*$ (cm)	80	50
Crossing angle ( $\mu$ -rad)	-145	160

**Figure 3.4:** Key beam parameters during the best PbPb fills in 2015 and 2018 [106].

### 3.1.3 LHC instrumentation

Ensuring the smooth operation of the LHC requires knowing key parameters of the beams at all times. This includes, among other things, knowing the precise position of the beams within the ring, their intensity, energy, luminosity and emittance, and the charge distribution around the ring. The instrumentation relevant to this thesis are described below.

#### Ghost and satellite fraction measurements

At the LHC, the ghost and satellite charges are measured by the Beam Synchrotron Radiation Longitudinal (BSRL) system [107], also sometimes called the Longitudinal Density Monitor (LDM). The working principle of the BSRL is the detection of synchrotron radiation emitted by accelerating particles. In particular, the BSRL measures the intensity of synchrotron radiation, which gives access to the total charge in an RF bucket. The production of synchrotron radiation is enhanced by an undulator, which locally *wiggles* the beam without affecting the overall trajectory. The BSRL has a very large dynamic range, and following upgrades in Long Shutdown 2, a time resolution of 5 ps [108], which allows it to resolve satellite charges.

#### Bunch intensity measurement

Several systems are used to measure the beam intensity, which rely on transformers to convert the beam current into usable electronic signals. The Direct Current Current Transformer (DCCT) [109] and the Fast Beam Current Transformer (FBCT) [110, 111] are located at Point 4, and both consist of one system per beam. The DCCTs are high accuracy devices, and are used to measure the total intensity of the beams. The DCCT readings thus also contain the contribution of ghost and satellite charges to the total beam current. The FBCTs operate at 40 MHz, and are therefore capable of providing beam intensity measurements for all 25 ns



bunch slots. However, they cannot provide intensity measurements below a certain threshold, and as such, are not sensitive to ghost charges. The readings provided by the FBCTs include contributions from the satellite charges.

Additionally, the ATLAS Beam Pickup Timing system (BPTX) [112] provides a complementary measurement of bunch-by-bunch intensities. Although the BPTXs are provided by the LHC as button electrode-based beam position monitors, they are used by the experiments for timing and beam intensity measurement. Two stations, one for each beam, are located 175 m from the interaction point on both sides of ATLAS. With a timing resolution of less than 100 ps, the BPTX is also used to look for timing differences between the LHC clock signal and the actual timestamps at which collisions occur. The bunch intensity readings provided by the BPTX include the contributions of satellite charges.

### Beam position monitors

Beam Position Monitors (BPMs) are used to accurately determine the position of the beam at various points along the LHC orbit. BPMs work by measuring the charge induced on electrodes that are arranged symmetrically around the beampipe, as the beam passes through them. Any transverse offset of the beam with respect to the beamline then reflects as an asymmetry in the charges induced on diametrically opposite electrodes. The asymmetry then provides a measure of the beam position in the transverse plane. Two types of LHC BPMs are relevant to this thesis. The so-called *arc BPMs* [113, 114] are situated along the entire LHC ring, and use button electrodes. The Diode ORbit and OScillation (DOROS) BPMs [115] employ compensated diode detectors for precise measurements of the beam position in critical regions of the LHC ring, namely around the collimators and the interaction points.

## 3.2 The ATLAS detector

As mentioned in Sec. 3.1, the ATLAS (A Toroidal Lhc ApparatuS) experiment [94] is one of the two general purpose detectors at the LHC. It is a cylindrical detector, with a length of 45 m, a diameter of 25 m, and weighs approximately 7000 tonnes. Broadly speaking, it consists of a central *barrel* region with two *endcap* regions on either side of it. It is highly granular, and has a large longitudinal acceptance and almost complete azimuthal coverage. It consists of several sub-detectors that aim to detect (almost) all the particles produced in proton or ion collisions. The sub-detectors are arranged in concentric layers around the beampipe, centered on the collision point at Point 1.

Shown in Fig 3.5, the ATLAS detector is the largest collider-based particle physics detector ever built, and provided the data for the studies presented in this thesis.

### 3.2.1 The ATLAS coordinate system

The ATLAS coordinate system follows a right-handed cylindrical coordinate system, where the cylindrical axis is aligned with the beamline. The origin is at the ATLAS interaction point, with



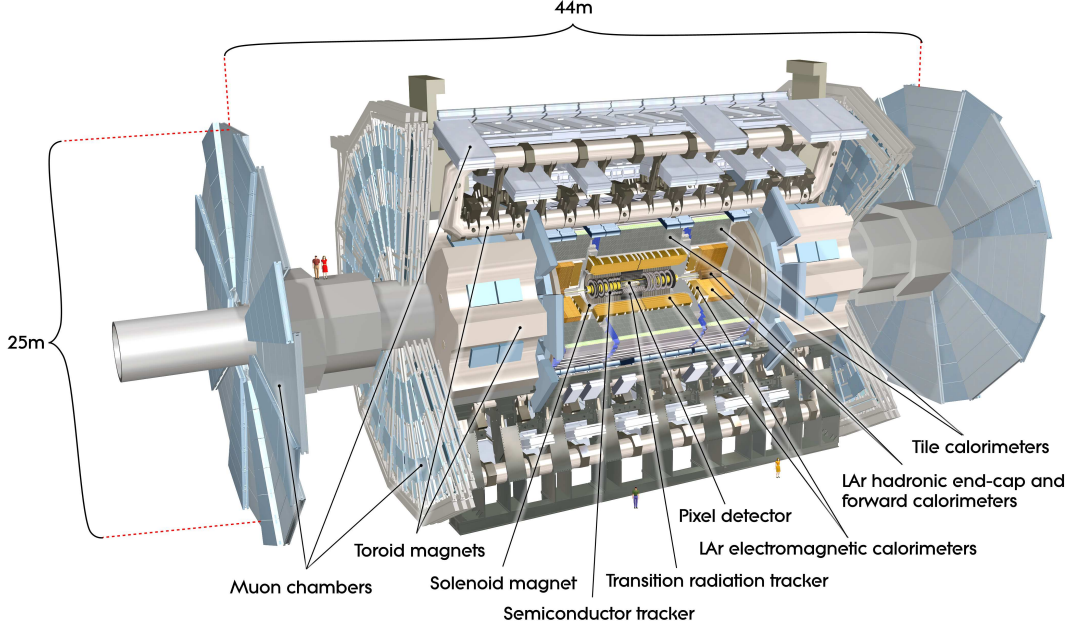


**Figure 3.5:** Rendition of the ATLAS detector [94]. A slice in the azimuthal angle is removed to show the different sub-detectors. Four people are shown for scale: two on the ground, and two on the forward shielding in between the muon wheels on the left side.

the  $z$ -axis pointing along the beamline towards Geneva airport, and the  $x$ -axis pointing towards the center of the LHC ring. The  $y$ -axis, orthogonal to the other two axes, is not orthogonal to the surface of the Earth, due to the LHC tunnel being slightly tilted with respect to the ground. The  $+z$  side of ATLAS is called the A side, while the other is called the C side.

Due to the detector geometry, the kinematics of particles are most conveniently described using cylindrical coordinates. For a particle with four-momentum  $p^\mu = (E, p_x, p_y, p_z)$  and mass  $p^\mu p_\mu = m^2$ , the *azimuthal angle*  $\phi$  is defined as

$$\phi = \arctan \frac{p_x}{p_y}, \quad (3.5)$$

and the *rapidity* or boost  $y$  is

$$y = \frac{1}{2} \ln \left( \frac{E + p_z}{E - p_z} \right). \quad (3.6)$$

Another commonly used quantity is the *pseudorapidity*  $\eta$ , defined by

$$\eta = -\ln \left( \tan \frac{\theta}{2} \right), \quad (3.7)$$

where  $\theta = \arccos(p_z/|\mathbf{p}|)$  is the longitudinal angle of the particle's three-momentum.

In cylindrical coordinates, the energy and momenta of particles are given in the transverse

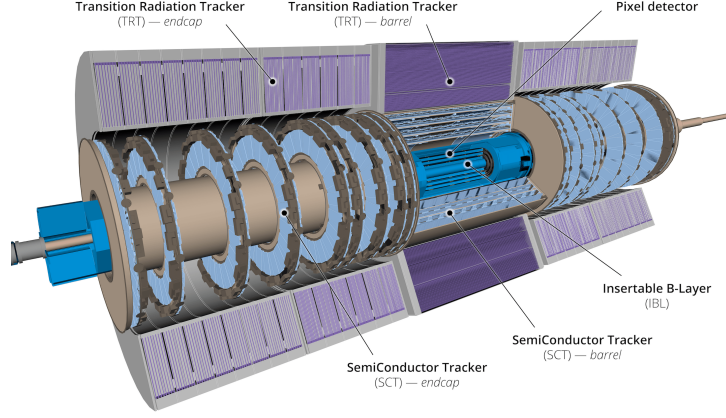


**Figure 3.6:** Illustration of the ATLAS Inner Detector [116].

plane using the *transverse momentum*  $p_T$  and *transverse energy*  $E_T$ , which are defined as

$$p_T = \sqrt{p_x^2 + p_y^2} \quad , \quad E_T = \sqrt{p_T^2 + m^2}. \quad (3.8)$$

With these definitions, a particle's four-momentum can be written as

$$p^\mu = (E_T \cosh \eta, p_T \sin \phi, p_T \cos \phi, E_T \sinh \eta). \quad (3.9)$$

The pseudorapidity and azimuthal angle can be interpreted as geometric quantities, describing the position of a particle in the transverse plane. It is useful to define the *angular separation*  $\Delta R$  between two particles with coordinates  $(\eta_1, \phi_1)$  and  $(\eta_2, \phi_2)$  as

$$\Delta R = \sqrt{\Delta\eta^2 + \Delta\phi^2} = \sqrt{(\eta_1 - \eta_2)^2 + (\phi_1 - \phi_2)^2}. \quad (3.10)$$

### 3.2.2 Inner Detector

The Inner Detector (ID), shown in Fig. 3.6, serves as the main tracker of the ATLAS experiment [117, 118]. Its purpose is to reconstruct the trajectories of charged particles, also called *tracks*, produced in proton or ion collisions. It is a cylindrically shaped detector, with a length of 7 m and an outer radius of 1.15 m, capable of providing tracking and momentum information for charged particles interacting with its active material up to  $|\eta| = 2.5$ . The sub-systems of the ID are described below in order of increasing radial distance from the beamline.

#### Pixel detector

The Pixel detector [119, 120] is the innermost tracking detector, consisting of four layers in the barrel region, and three discs in both endcap regions. The Insertable B-Layer (IBL) [121], installed during Long Shutdown 1, is situated in the barrel region at a radial distance of 33 mm. The remaining three layers sit at radial distances of 50.5 mm, 88.5 mm and 122.5 mm respectively. The three discs in the endcap regions are positioned at longitudinal distances of

$\pm 49.5$  mm,  $\pm 58.0$  mm and  $\pm 65.0$  mm. The active element of the Pixel detector is the eponymous silicon pixel detector, over 92 million of which are used in the Pixel detector. They have active areas in the range of  $50 \times 250$ – $600 \mu\text{m}^2$ , with the IBL containing the smallest so-called planar pixels. The IBL further includes 3D pixels [122], which differ from the planar pixels in the position of the electrodes. Overall, the spatial resolution of the pixel detector is  $10 \mu\text{m}$  in the transverse plane and  $115 \mu\text{m}$  in the longitudinal direction. Charged particles passing through the depleted region of the silicon detectors create electron-hole pairs, which drift towards the electrodes and create electrical signals. Four *hits* are expected from a charged particle passing through the Pixel detector. Being the closest detector to the beamline, the Pixel detector is required to be extremely resistant to radiation damage.

### SemiConductor Tracker

The SemiConductor Tracker (SCT) [123–125], in the same way as the Pixel detector, uses the ionization produced in silicon by traversing charged particles, to create electrical signals. Four concentric layers are situated in the barrel, between radial distances of 29.9 cm to 51.4 cm, while the discs in the endcaps are positioned at longitudinal distances of  $\pm 85.4$  cm to  $\pm 272.0$  cm. The active element of the SCT is a  $6 \text{ cm} \times 80 \mu\text{m}$  silicon strip. A total of 768 such strips constitute a sensor, four of which are used in one SCT module. The large length of the strips limits their spatial resolution in the longitudinal direction when compared to the Pixel detector, but allows them to cover a larger area. To improve the spatial resolution, the two layers of sensors in the modules are rotated by  $40 \mu\text{rad}$  with respect to each other. Overall, the SCT achieves a spatial resolution of  $17 \mu\text{m}$  in the transverse plane and  $580 \mu\text{m}$  in the longitudinal direction.

### Transition Radiation Tracker

The Transition Radiation Tracker (TRT) [126–128] is the outermost system of the ID, and consists of drift tubes called *straws* of 4 mm width, filled with a xenon-based gas mixture. In the barrel region, the straws are 144 cm in length and are parallel to the beamline, while they are 37 cm long and are arranged radially in wheels in the endcaps. The space between the straws is filled with polypropylene radiator foils. Over 300,000 straws are present in the TRT, which provides coverage up to  $|\eta| = 2$  and a spatial resolution of  $130 \mu\text{m}$  in the transverse plane. The straws themselves act as the cathode, with the anode being a  $30 \mu\text{m}$  gold-plated tungsten wire situated at the center of the straws. When charged particles traverse through the straws, they ionize the gas. The resulting ionization electrons drift towards the anode wire, creating an electrical signal. Due to a change in dielectric constants at the straw-foil boundary, incident particles are further accompanied by transition radiation. This produces additional ionization in the gas via the photoelectric effect, thereby contributing further to the signal. The rate of production of transition radiation is proportional to the Lorentz factor  $\gamma = E/m$  of the particles. This allows the use of the TRT for particle identification, e.g. to distinguish between

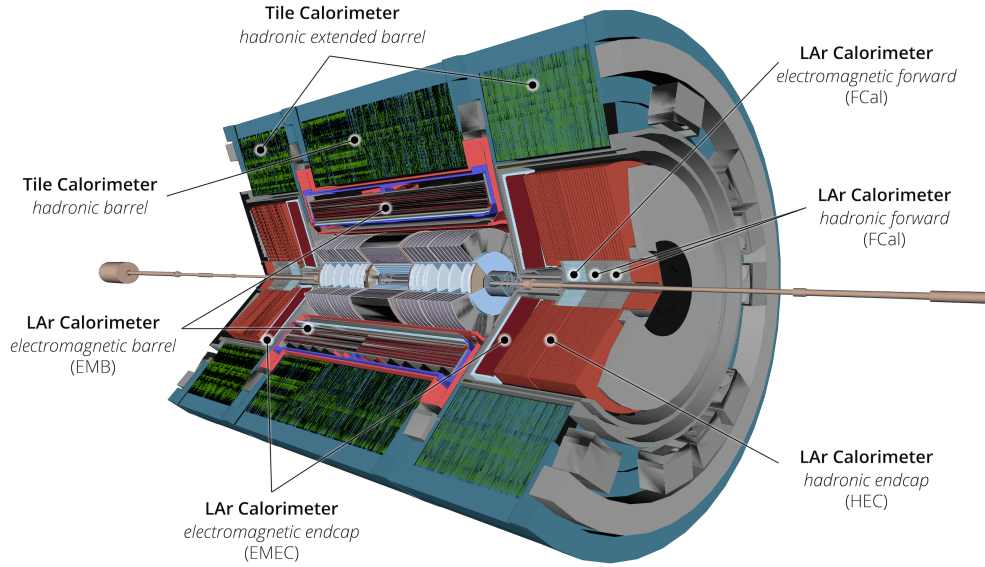


**Figure 3.7:** Illustration of the ATLAS calorimeter system [116].

pions and electrons. The TRT improves the quality of tracks reconstructed by the full ID in two ways: the spatial resolution is improved due to the high hit multiplicity, while the momentum resolution is improved by the large radial coverage.

### Beam Conditions Monitor

The Beam Conditions Monitor (BCM) [129] is designed to monitor the rate of beam-induced backgrounds inside the ATLAS detector, and to trigger a beam dump in case of unexpected conditions (e.g. the beam straying too far away from its nominal position) that may damage the detector. The BCM consists of two stations with four modules each, situated at a radial distance of 55 mm and a longitudinal distance of  $\pm 1.84$  m. This position, which corresponds to  $\eta = \pm 4.2$ , implies significantly higher radiation doses compared to the rest of the ID. Thus, the BCM uses diamond sensors, which together with their radiation hardness, also offer faster signal speed compared to silicon detectors. The signal generation process is similar to silicon detectors, i.e. charged particles traversing the BCM create electron-hole pairs, which are collected by the electrodes, resulting in electrical signals. Particles produced in collisions at the interaction point create signals in the two stations with a time difference that is a multiple of 25 ns, while particles produced away from the interaction point create time differences offset by 12.5 ns. The BCM's fast rise-time of around 1 ns allows it to distinguish between such signals. The timing resolution also lets the BCM provide bunch-by-bunch luminosity measurements.

### 3.2.3 Calorimeters

The ATLAS calorimeter system [130], shown in Fig. 3.7, measures the energies of particles produced in proton or ion collisions. It relies on the principle of *sampling* calorimetry, in which the detectors consist of interleaved *absorbers* and *active materials*. Particles passing

through the absorbers produce a shower of secondary particles; the electromagnetic component of the shower proceeds via pair-production and bremsstrahlung, while the hadronic component proceeds through inelastic nucleus-nucleus interactions. The shower particles then ionize the active material, which results in the creation of measurable signals. Two types of active material technologies are used in the ATLAS calorimeter system: Liquid Argon (LAr) [131] and scintillating tiles [132]. Overall, the calorimeters cover a pseudorapidity range of  $|\eta| < 4.9$ .

Broadly speaking, the ATLAS calorimeter system can be divided into two categories: the Electromagnetic Calorimeter (ECal) primarily measures the energies of electrons and photons, while the Hadronic Calorimeter (HCal) measures the energies of mesons and baryons. Additionally, the Forward Calorimeter (FCal) [133] contains modules for both electromagnetic and hadronic calorimetry.

### Electromagnetic Calorimeter

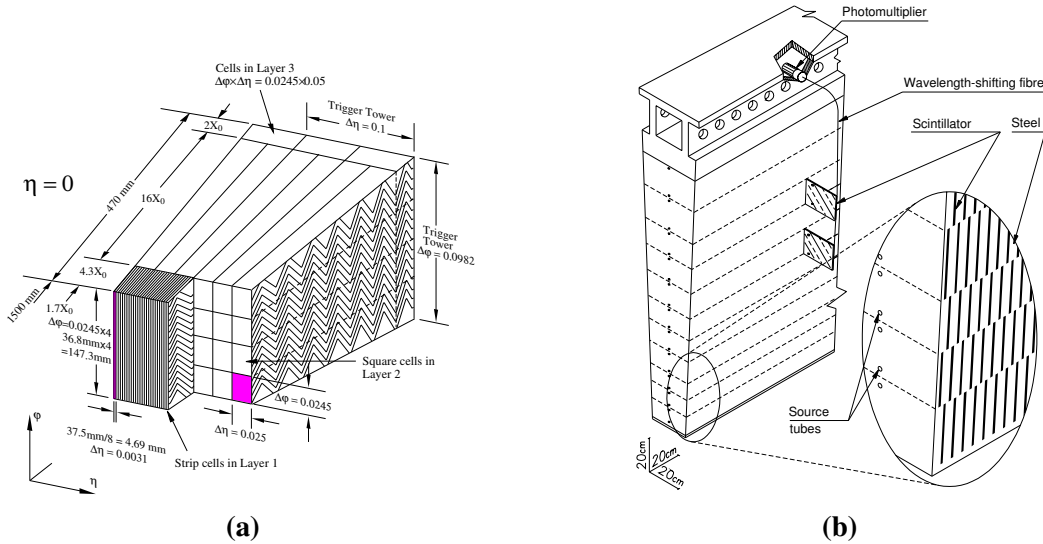


**Figure 3.8:** Illustrations of (a) a section of the barrel Electromagnetic Calorimeter, and (b) a section of the Tile Calorimeter. Figures taken from Ref. [94].

The ECal relies solely on LAr as the active material. The barrel region (EMB) covers  $|\eta| < 1.475$ , and consists of two identical half-barrels separated by a 4 mm *seam* at  $z = 0$ . The endcap region (EMEC) covers  $1.375 < |\eta| < 3.2$ , and consists of two co-axial wheels separated at  $|\eta| = 2.5$ . Sheets of lead arranged in an accordion-like geometry immersed in the liquid argon are used as absorbers in ECal. The thickness of the absorber sheets varies between 1.13 and 2.2 mm depending on the pseudorapidity. The ECal consists of three layers, increasing in radial distance from the beampipe, and decreasing in  $\eta - \phi$  segmentation (see Fig. 3.8a). In the central region ( $|\eta| < 1.8$ ) a *pre-sampler* is added, which is used to correct for the energy lost by particles before reaching the ECal. The pseudorapidity region of  $1.32 < |\eta| < 1.57$ , called the *crack* or *overlap* region, contains primarily support structures and services. It offers reduced particle detection capabilities, and is therefore not included in physics analyses.



### Hadronic Calorimeter

The HCal consists of three components: the barrel region covering  $|\eta| < 1.0$ , the extended barrel (or EB, often grouped together with the main barrel region) covering  $0.8 < |\eta| < 1.7$ , and the endcaps (HEC) covering  $1.5 < |\eta| < 3.2$ . The barrel region extends radially from 2.28 m to 4.25 m, and employs plastic scintillator tiles of 3 mm thickness as the active material, which are interleaved with steel absorbers. Hence, it is often referred to as the Tile Calorimeter (TileCal). The signals produced in the tiles are read out by wavelength shifting fibers into photomultiplier tubes (PMTs). The HEC instead uses LAr together with copper plates of thickness 25-50 mm, since LAr is better suited for the high radiation-dose environment of the HEC. It consists of 32 identical wedges with inner radii of 37.2–47.5 cm and an outer radius of 2.03 m. A schematic of a TileCal module is shown in Fig. 3.8b.

### Forward Calorimeter

The FCal increases the pseudorapidity coverage of the ATLAS calorimeter system, by instrumenting the  $3.1 < |\eta| < 4.9$  region. On both sides of the interaction point, it extends from  $z = 4.7 - 6.05$  m, and radially from around 7 – 45 cm. The FCal uses LAr as the active material, and consists of three layers, which are designed as metal matrices with regularly spaced longitudinal channels for the electrodes and LAr. The layer closest to the interaction point samples the electromagnetic shower using copper absorbers, while the remaining two layers sample the hadronic shower using tungsten absorbers. The distance traversed by particles crossing the active material is only an eighth of the 2 mm distance used in the ECal, in order to prevent ion build-up due to the low mobility of positive ions in LAr [133].

### Minimum Bias Trigger Scintillator

The Minimum Bias Trigger Scintillator (MBTS) [134] is an additional detector that is also part of the calorimeter system. It is situated on the front face of the LAr endcap cryostat at approximately  $\pm 3.6$  m from the interaction point, and covers the  $2.08 < |\eta| < 3.75$  region. The MBTS comprises 2 cm thick polystyrene scintillator counters, which are arranged in disks with eight-fold symmetry. Scintillation light from the counters is guided by wavelength shifting fibers into PMTs, which are then read out by the TileCal electronics. The MBTS provides triggering capabilities, particularly in low luminosity conditions, and for minimum bias events. A veto on MBTS hits can also be used to trigger on ultra-peripheral heavy ion collisions.

## 3.2.4 Muon System

The ATLAS Muon System (MS, also sometimes called the Muon Spectrometer) [135], shown in Fig. 3.9, is the outermost sub-detector, and is tasked with measuring the trajectories and momenta of muons produced in proton or ion collisions. In the barrel region, the MS components are arranged in three concentric layers at radial distances of around 5 m, 7.5 m and 10 m. A small gap around  $z = 0$  is present for accommodating the services to the ID, solenoid and

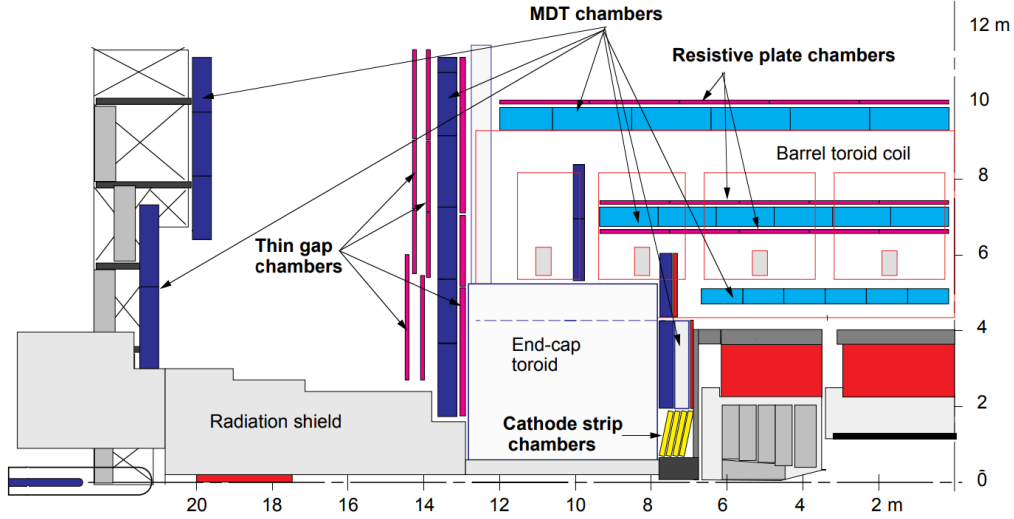


**Figure 3.9:** Illustration of the ATLAS Muon System [135]. The figure presents one quadrant of the transverse view.

calorimeters. In the endcap regions, three layers of detectors arranged in a wheel-like geometry are placed at longitudinal distances of  $\pm 7.4$  m,  $\pm 14$  m and  $\pm 21.5$  m respectively. All MS components employ gas-based detection technologies, and are either used for precision tracking, or for triggering on muons.

### Monitored Drift Tube

The Monitored Drift Tube (MDT) chambers are gas-filled drift tubes, i.e. the detection mechanism is similar to the TRT. They are used to precisely determine the trajectories of muons passing through the MS. Aluminum tubes of 30 mm diameter and various lengths (depending on the position of the MDT chambers) are filled with an Ar/CO<sub>2</sub> mixture, with a central tungsten-rhenium wire of 50  $\mu$ m thickness acting as the anode. The MDT chambers are located in the barrel region, providing a pseudorapidity coverage of  $|\eta| < 1.0$ , and in the endcap region covering  $1.0 < |\eta| < 2.7$  except for the innermost endcap layer, where the coverage extends only up to  $|\eta| = 2.0$ . Each MDT chamber consists of two so-called *multi-layers*, which combine three layers of drift tubes. In the innermost barrel layer of the MS, the MDT chambers use multi-layers with four layers of drift tubes, to improve the tracking performance.

### Cathode Strip Chambers

The Cathode Strip Chambers (CSCs), covering  $2.0 < |\eta| < 2.7$ , are used instead of MDTs in the innermost endcap layers of the MS to cope with the higher particle flux and background rates. The CSCs are multi-wire proportional chambers, with radially oriented gold-plated tungsten-rhenium wires of 30  $\mu$ m diameter acting as the anodes, and strip-shaped copper cathodes which are used for the read-out. An Ar/CO<sub>2</sub> mixture is used as the detection volume. The CSCs on both sides of the ATLAS detector are arranged in two wheels with eight chambers each. Each chamber consists of four CSC planes. The charges produced in the Ar/CO<sub>2</sub> gas

mixture by particles traversing the CSCs create induced charges on neighboring strips, which result in electrical signals. With strips oriented both parallel and orthogonal to the anode wires, the CSCs are capable of reconstructing the complete trajectories of particles.

### Resistive Plate Chambers

The Resistive Plate Chambers (RPCs), arranged in three concentric layers around the barrel region, provide the capability to trigger on muons within  $|\eta| < 1.5$ . Each layer is composed of *trigger stations*, which consist of two independent detection layers. The RPCs are gas ionization detectors, using a mixture of  $\text{C}_2\text{H}_2\text{F}_4/\text{Iso-C}_4\text{H}_{10}/\text{SF}_6$  in 2 mm wide gas gaps. Parallel plastic electrode plates of 2 mm thickness and metallic pickup strips are used for the readout of electrical signals. The pickup strips are arranged both parallel and orthogonal to the longitudinal direction, thereby allowing the RPCs to also measure both transverse coordinates. The RPCs operate in avalanche mode with a time resolution of around 1 ns. The first two RPC layers trigger on muons with  $p_T < 9$  GeV, while all three layers are used to trigger on muons with  $p_T > 9$  GeV due to the larger bending radius of high  $p_T$  muons.

### Thin Gap Chambers

The Thin Gap Chambers (TGCs) provide triggering capability in the  $1.05 < |\eta| < 2.4$  region. They are arranged in circular disks, in a doublet close to the first layer of endcap MDTs, and two doublets and one triplet around the second layer of endcap MDTs. The TGCs are multi-wire proportional chambers, and operate on the same principle as the CSCs, but with the characteristic that the wire-to-cathode distance of 1.4 mm is smaller than the wire-to-wire distance of 1.8 mm. The gas used in operation is a  $\text{CO}_2/\text{n-pentane}$  mixture. The TGCs operate in a quasi-saturated (i.e. proportional) mode, providing time resolutions of around 4 ns. Trigger signals from all TGCs are used in triggering high  $p_T$  muons, while the triplet may be omitted in triggering on low  $p_T$  muons.

## 3.2.5 Forward detectors

A number of smaller systems are situated in the *forward*, i.e. high pseudorapidity region, serving special purposes. Of relevance to this thesis are the LUCID and ZDC detectors, which are described below. The ATLAS Forward Proton (AFP) [136] and Absolute Luminosity for ATLAS (ALFA) [137] detectors are also part of the Run 2 forward detector configuration, but are not described further.

### LUCID

The LUMinosity Cherenkov Integrating Detector (LUCID, also denoted as LUCID-2) [138], shown in Fig. 3.10a, consists of set of 32 photomultiplier tubes, and serves as the primary luminosity detector for ATLAS. Sixteen PMTs are positioned on either side of the interaction point, at a longitudinal distance of around 17 m and a radial distance of around 125 mm from the beamline, corresponding to an  $|\eta|$  value of around 5.6. The PMTs use a 1.2 mm thick quartz



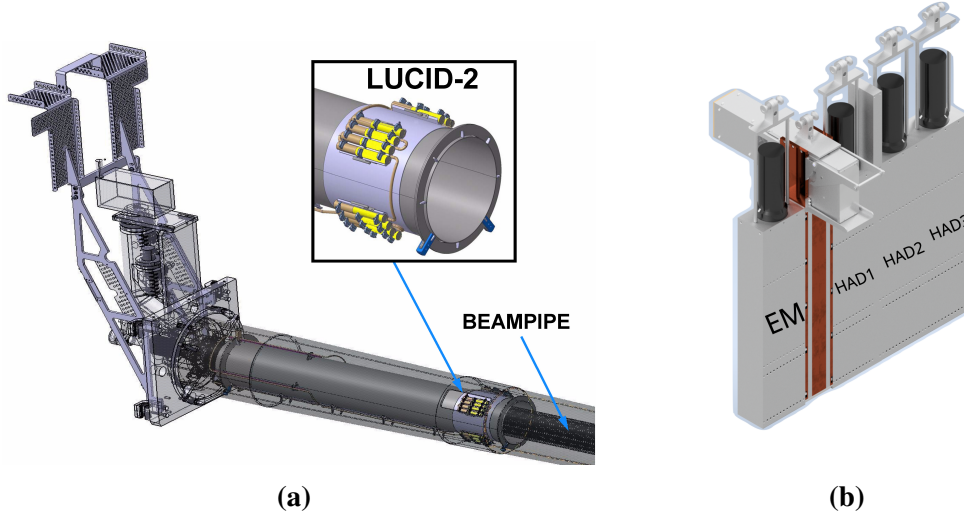


**Figure 3.10:** (a) Illustration of the LUCID detector in its Run 2 configuration [138, 139]. (b) Illustration of the ZDC detector in its Run 3 configuration. The Beam Rate of Neutrals (BRAN) system [140], visible in the figure as the component situated between the EM and HAD1 modules of the ZDC, was placed in front of the EM module in Run 2.

window as a Cherenkov medium. Particles traversing through the quartz window produce Cherenkov radiation, which is picked up by the PMTs and converted to electrical signals.

During Long Shutdown 1, significant upgrades were undertaken to improve the LUCID performance. As part of the upgrades, small amounts of radioactive  $^{207}\text{Bi}$  were deposited on the quartz windows. These deposits emit mono-energetic electrons, which are used to regularly calibrate the PMT voltages, thereby ensuring consistent pulse amplitudes over time. LUCID is capable of providing luminosity measurements for all 3564 bunch slots due to its dedicated fast electronics.

## ZDC

The Zero Degree Calorimeters (ZDCs) [141], shown in Fig. 3.10b, are sampling calorimeters, employing tungsten and steel as the absorbers and quartz rods as the active material. The ZDCs are located 140 m from the interaction point within the Target Absorber Neutral (TAN), which is also the point where the two separate beam pipes of the LHC merge into a single beam pipe leading into the interaction point. At this position, they cover a pseudorapidity region of  $|\eta| > 8.3$ . Both ZDC arms consist of four rectangular modules that are each read out by one PMT. The ZDCs are designed to detect neutral particles (e.g. photons, neutrons etc.) produced at high pseudorapidities in heavy ion collisions, since they are not bent away by the LHC magnets, and continue on a *zero degree* path after being produced.

The ZDCs are a crucial part of the ATLAS heavy ion program. In central heavy ion collisions, the amount of ZDC activity provides an important handle on the number of spectator neutrons. Vetoes on ZDC activity in one or both arms are used to select photonuclear and ultra-peripheral collisions, such as in this thesis.

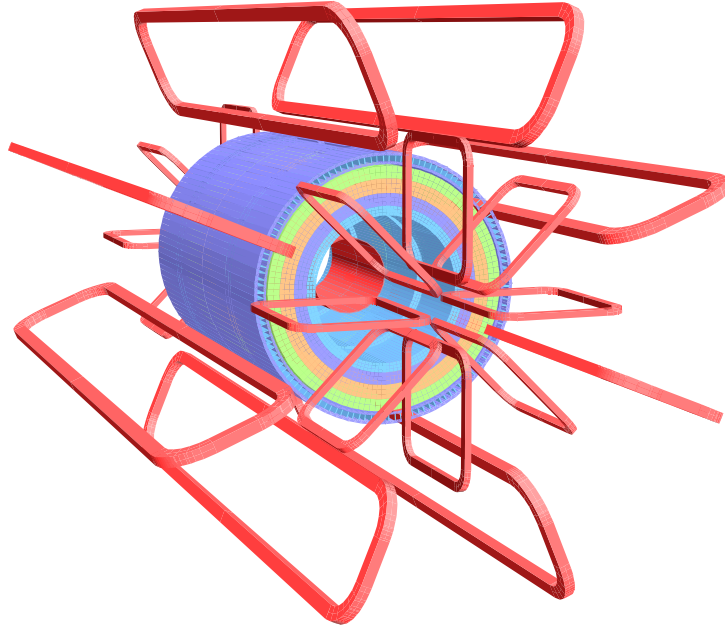


**Figure 3.11:** Illustration of the ATLAS magnet system [94]. The central solenoid, barrel toroid, and endcap toroid, are shown in red, in relation to a representation of the Tile Calorimeter.

### 3.2.6 Magnet system

The ID, calorimeter and MS systems are designed to measure the trajectories and energies of particles interacting with the ATLAS detector. However, if the trajectories do not *bend* in the transverse plane, it is not possible to determine their charge (rather, the sign of the charge) and momenta using these detectors alone. The ATLAS magnet system, shown in Fig. 3.11, provides the necessary magnetic field to bend the particle trajectories. It comprises four components: the central solenoid [142], the barrel toroid [143] and two endcap toroids [144].

The central solenoid is an aluminum stabilized Nb-Ti superconducting magnet, encompassing the Inner Detector. It provides an axial field of 2 T at the nominal operating current of 7.73 kA and at a temperature of 4.5 K. The solenoid is 5.8 m in length, with inner and outer radii of 2.46 m and 2.56 m respectively. The solenoid was designed to be as thin as possible, in order to minimize the material budget and energy lost by particles before reaching the calorimeter. The steel absorbers within the Hadronic Calorimeter act as the return yoke, thereby limiting stray magnetic fields from reaching the Muon System. By bending the trajectories of particles within the ID volume in the transverse plane, the solenoid facilitates charge and momentum measurements.

The barrel and endcap toroids use the same superconducting conductor as the solenoid, but with a different ratio of materials, and are situated outside the calorimeters amongst the MS components. Each toroid system consists of eight identical racetrack-shaped air-core toroids arranged symmetrically around the beamline. On average, the barrel and endcap toroids provide a magnetic field of approximately 0.5 T and 1.0 T respectively. Each of the barrel coils is

25.3 m long, with the inner and outer edges of the two straight sections parallel to the beamline at 4.87 m and 9.85 m respectively. The endcap coils are 4.3 m long in the longitudinal direction, with the inner and outer straight sections parallel to the beamline at 1.21 and 5.01 m.

The orientation of the toroid coils is such that muons passing through the toroids and the MS experience magnetic fields that are mostly orthogonal to their flight path, thereby bending their trajectories and allowing for charge and momenta measurements. Within  $|\eta| < 1.4$ , the bending is provided by the barrel toroids, for  $1.6 < |\eta| < 2.7$  the endcap toroids are responsible, and in the transition region of  $1.4 < |\eta| < 1.6$ , a combination of both are at play. The toroid systems are integrated into strong mechanical supports, to withstand both the several hundred-tonne masses of the toroids themselves, and the large magnetic forces exerted on the magnets during operation.

### 3.2.7 Trigger and Data Acquisition

Even though the LHC is capable of delivering collisions at a 40 MHz rate, the majority of events involve soft interactions at large rapidities, which are not relevant for the main ATLAS physics program. Moreover, it is not technologically feasible to permanently record the ATLAS detector's data at a 40 MHz rate. Thus, the ATLAS experiment uses a Trigger and Data Acquisition (TDAQ) system that filters collision events before storage, using (partial) data from the sub-detectors. The filtering, or *triggering*, decisions are based on the presence of *signatures*, e.g. the presence of high  $p_T$  leptons, jets, photons etc., that may arise from relevant high energy scattering processes. The ATLAS trigger system, shown in Fig. 3.12, consists of two parts: the Level-1 (L1) trigger [145] which reduces the event rate down to around 100 kHz, and the High Level Trigger (HLT) [146] which further reduces the event rate to around 1 kHz.

The L1 trigger is a hardware based trigger employing custom built electronics, and is designed to return a decision within  $2.5 \mu\text{s}$ . Signals from the calorimeters pass to the L1Calo system [147], which digitizes the analog signals and performs a fast reconstruction of electrons, photons and tau lepton candidates. Global properties of events, namely the (missing) total transverse energy, are also determined by the L1Calo system. Signals from the RPCs and TGCs enter the L1Muon system [148], where coincidence requirements between the various trigger stations (also including the TileCal), and deviations of the recorded hit pattern from that of a muon with infinite momentum, are used together to determine the multiplicity and approximate momenta of muons. The L1Topo system combines information from the L1Calo and L1Muon systems, to apply geometric or kinematic requirements on the L1 trigger objects.

The Central Trigger Processor (CTP) [149] forms the L1 decision using the L1 trigger objects, as well as with information from the MBTS, LUCID, ZDC and BPTX detectors. The decision can be based on the multiplicity of objects above a given threshold, topological requirements etc. While the L1 trigger decision is being formed, the detector data is stored in Front End (FE) buffers. During this time, the CTP applies *dead-time* so that read-out windows do not overlap (simple dead-time), and to prevent detector data buffers from overflowing (com-

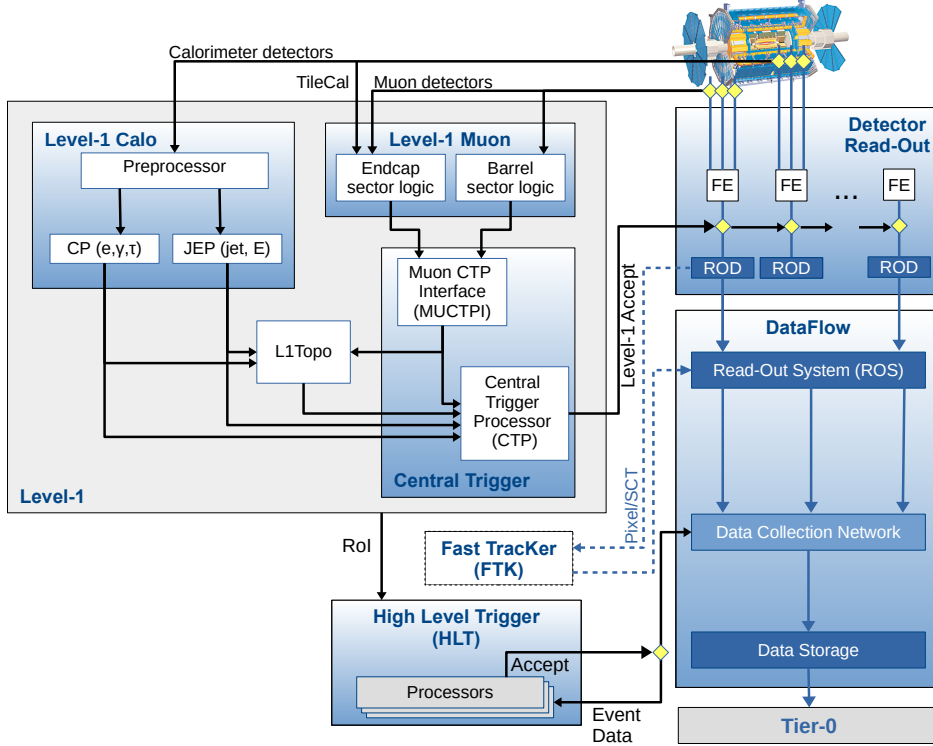


**Figure 3.12:** Illustration of the ATLAS Trigger and Data Acquisition system [150].

plex dead-time). The CTP is also capable of *pre-scaling* L1 triggers, which reduces the rate of L1 accepts for a given signature.

When an L1 accept is passed, so-called Regions of Interest (ROIs), i.e. regions of the detector with interesting activity as determined by the L1 trigger, are passed to the HLT. Additionally, the detector data stored in the FE buffers is also sent to the HLT. The HLT is a software based trigger, which is designed to return a decision within a few hundred milliseconds. It uses fast object reconstruction algorithms, followed by more CPU intensive ones, to form the trigger decision. The HLT is capable of forming decisions based on a variety of signatures, such as the multiplicity, kinematics, topological correlations etc. of trigger objects.

Individual trigger decision algorithms at L1 are called *items*, and are used as *seeds* for HLT algorithms, in order to form *chains* of trigger requirements. A collection of trigger chains active during operations is referred to as a *trigger menu*. The trigger menu during heavy ion data taking, for example, prioritizes the global properties of events, ultra-peripheral collisions, hard probes of the quark-gluon plasma, and minimum bias events [151]. The choice of active chains in the menu is designed to maximize the physics potential of the dataset, while at the same time respecting the TDAQ system limitations.

Once a HLT accept is passed, and if the HLT pre-scale allows it, the event data is permanently stored at the CERN data center and across the Worldwide LHC Computing Grid (WLCG) sites [152]. Events are written out to data *streams* which serve different purposes. For

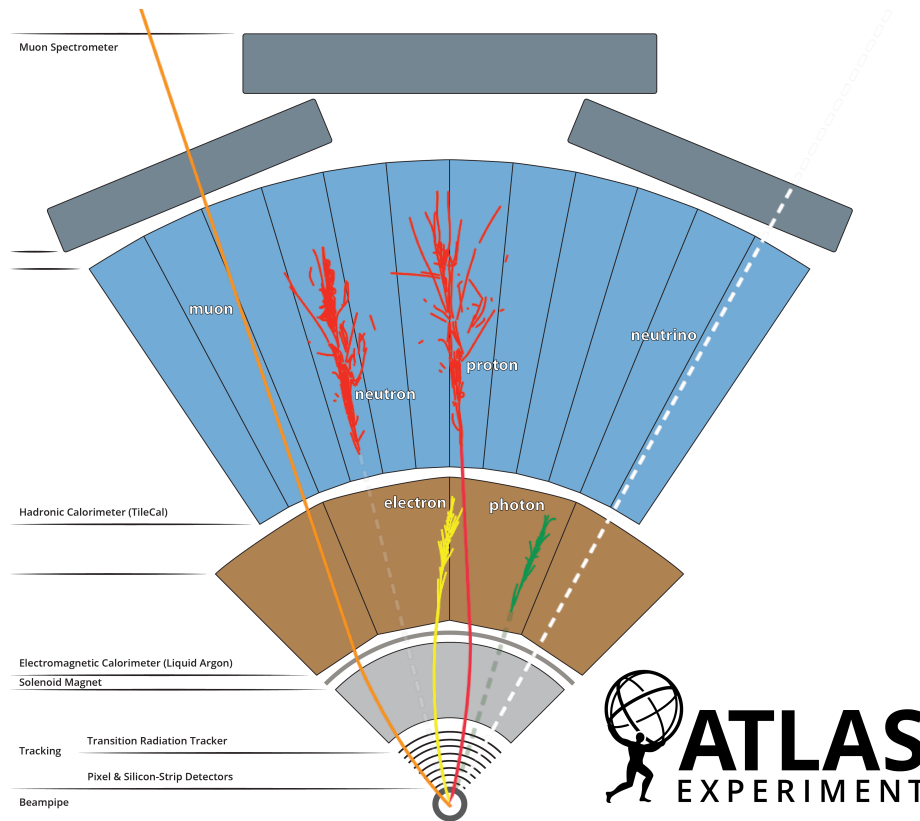


**Figure 3.13:** Illustration of the interactions of particles with the ATLAS detector [153].

example, the `Physics` stream contains data intended for physics measurements and searches, various `Calibration` streams contain partial event data (eg. ID-only, MS-only etc.) for calibration and monitoring, and so on. Initially, the `RAW` data is stored for every *luminosity block* (LB), which corresponds to a time period (usually 60 seconds long) where the data-taking conditions are assumed to be stable. The `RAW` data is later processed into AOD-based formats and flat ntuples for physics measurements.

### 3.3 Object reconstruction

After the particles produced in proton or ion collisions interact with the ATLAS detector (see Fig. 3.13), they leave behind electrical signals indicating their presence: electrons and photons interact with the ECal, while hadrons interact with the HCal (and to a lesser extent, the ECal); muons interact with all sub-detectors; all charged particles leave behind tracks in the Inner Detector. Neutrinos pass through the detector without any interaction. The purpose of *object reconstruction* is to use the raw data to build high-level objects that serve as proxies for the original particles, such that they can be used for physics measurements.

Reconstruction algorithms are designed to efficiently reconstruct *prompt* particles, i.e. those produced directly in proton or ion collisions. In contrast, *non-prompt* particles created from other sources are often treated as backgrounds. It is common to define *working points* (WPs) for the identification of reconstructed physics objects like electrons, muons etc., which relate to

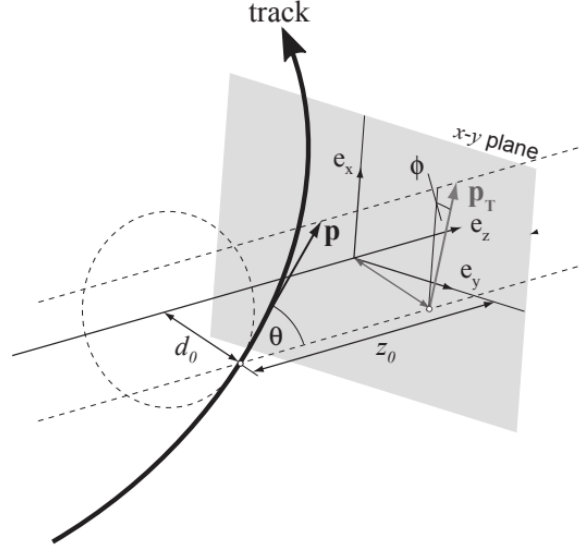


**Figure 3.14:** Schematics of the track parameters in the *perigee* representation, which defines them at the point of closest approach to a reference point. The longitudinal and transverse impact parameters,  $z_0$  and  $d_0$  respectively, give the distance of the perigee from the reference point, which may be the origin of the experiment coordinate system, or the centroid of all primary vertices. The track has momentum  $\mathbf{p}$  with transverse and longitudinal angles  $\phi$  and  $\theta$ . The associated transverse momentum is  $p_T$ . Figure taken from Ref. [154].

the purity of the objects. Reconstruction is performed either *online* during the triggering stage of the DAQ, or *offline* during further data processing. The various ATLAS offline reconstruction algorithms for the particles and objects relevant to this thesis are described below.

### 3.3.1 Tracks

When charged particles produced in proton or ion collisions cross the Inner Detector, they leave behind hits in the ID sub-detectors. Due to the axial magnetic field provided by the solenoid, the particles follow a helical trajectory through the ID. The hits can be used to reconstruct the trajectories of the particles, which are referred to as *tracks*. *Tracking* is the first step in offline event reconstruction procedure, since the tracks serve as inputs to the reconstruction of other objects.

Track finding is typically computationally intensive, particularly in high multiplicity events like central heavy ion collisions. The ATLAS tracking algorithm [155–157] is designed to be resource efficient, and to provide reliable results with minimal fake rates<sup>2</sup>. It also determines the parameters of the reconstructed tracks, as shown in Fig. 3.14. The ATLAS tracking algorithm is a multi-stage procedure as follows:

1. **Clusterization:** Charged particles crossing the Pixel and SCT detectors leave behind hits in the pixels and strips of these detectors respectively. The hits can be in adjacent sensors

<sup>2</sup>Fakes in this context refers to *fake tracks*, which are trajectories found by a tracking algorithm that are fictitious in nature. Fake tracks can arise due to combinatorics, detector noise, beam-induced backgrounds etc.



due to the incident angle of the particles, or due to charge sharing, cross-talk between readout channels etc. A Connected Component Analysis (CCA) [158] is used to form groups, or *clusters*, of adjacent pixels and strips in the same sensor using hits above a certain charge threshold.

2. **Space-point formation:** The clusters are then used to create *space-points*, which are three-dimensional coordinates indicating where the particles may have interacted with the detector's active material. A space-point is created from every cluster in the Pixel detector, while clusters in sensors from both sides of a SCT strip are paired to form space-points.
3. **Seeding:** Triplets of space-points on detector layers at different radial distances are combined to form *track seeds* that are consistent with a helical trajectory. The space-points need not be on contiguous layers. A loose set of selections is applied, such as on the  $\Delta R$  between space-points, to improve the seed finding. If possible, a fourth space-point is added to confirm the track hypothesis suggested by the seed.
4. **Track finding:** The track seeds are used to define *search roads*, which are a set of detector modules along a smooth trajectory defined by the track seed, where clusters may be expected. The implementation of search roads reduces the combinatorics, and consequently the compute resources required for tracking. A combinatorial Kalman filter [159] is then employed to extend the track seed by sequentially adding space-points along the search road. The algorithm seeks to add the best space-point on a given detector layer with a  $\chi^2$  fitting procedure, where the outcome of the fit is a track candidate with a smooth helical trajectory.
5. **Ambiguity solver:** While the combinatorial Kalman filter approach is fast, the resulting set of track candidates may contain fakes, or multiple candidates with overlapping space-points. These issues are addressed with an ambiguity solver, which uses a reward/penalty system to score track candidates based on a set of criteria. It favors tracks with more clusters, fewer holes<sup>3</sup>, and better track fits. The collection of track candidates refined by the ambiguity solver is then re-fit with a global  $\chi^2$  method to obtain high-precision estimates of the track parameters. Since the track candidates described in the steps so far only use Pixel and SCT hits, they are also referred to as Si (i.e. silicon) tracks.
6. **TRT extension:** For the last step, search roads are defined from the Si tracks into the TRT volume, and the Kalman filter is used once again. Hits in the TRT straws are included in the track candidates and the global  $\chi^2$  fit is re-performed. The TRT-extended tracks are rejected if the  $\chi^2$  worsens with respect to the Si-track, or if the degree of association between the track and the TRT hits is not high enough.

---

<sup>3</sup>A hole refers to a functioning detector module that is crossed by a track, but with no cluster being found. This definition properly accounts for disabled sensors and modules.

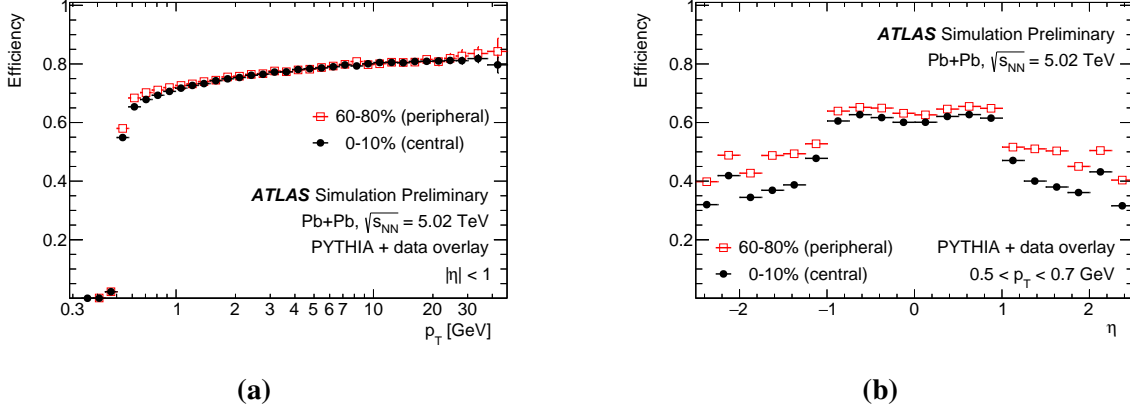


**Figure 3.15:** Tracking efficiency as a function of (a) track  $p_T$  and (b) track  $\eta$ , for different centrality classes [161]. The efficiency is determined with the data overlay method [162] for a heavy ion specific track working point.

The reconstruction algorithm described above assumes that tracks follow a smooth helical trajectory, which may not be satisfied in the presence of bremsstrahlung radiation. If a track seed does not result in a viable track candidate, the seed is checked for compatibility with a calorimeter ROI that may be associated with bremsstrahlung photons. If an ROI is found, the track fit is re-done including the ROI, and with looser quality requirements. Additionally, energy loss due to bremsstrahlung is included in the fit model. If the fit still fails, the pion mass hypothesis, which was used so far, is updated to the electron mass hypothesis. A subsequent fitting procedure using an optimized Gaussian-sum filter (GSF) [160] (a generalization of the Kalman filter), is used to better account for the non-linear behavior of bremsstrahlung radiation.

The steps above describe the so-called *inside-out* tracking procedure, as it starts with Pixel hits and ends with the TRT. An alternate tracking procedure called *outside-in* tracking instead starts from TRT, and uses detector hits not assigned to tracks during the inside-out tracking that was performed first. It is used to reconstruct the trajectories of secondary particles, i.e. those produced from photon conversion, decays of unstable particles etc. In the outside-in tracking procedure, TRT hits compatible with ROIs in the EM calorimeter are combined with short (i.e. two space-points only) SCT seeds, to form track candidates. These then go through similar track finding steps as for inside-out tracking, i.e. road search, Kalman filter, ambiguity solver, and  $\chi^2$  fitting. The track candidates are then extended back into the TRT to define the final track fits.

The tracking working points used by ATLAS optimize the performance metrics, i.e. a higher tracking efficiency and lower fake rate. The fake rate is generally higher for high multiplicity events (e.g. central heavy ion collisions) due to combinatorics. The tracking efficiency depends, among other things, on the kinematics of the tracks. Low  $p_T$  tracks have a smaller bending radius in the solenoid field compared to high  $p_T$  tracks, and may not reach the outer detector layers. They also have a higher probability of scattering with the detector material. Thus, the tracking efficiency increases with  $p_T$ . Further, the efficiency decreases at high pseu-



rapidity, due to the lower number of possible ID hits. Fig. 3.15 shows, as an example, the tracking efficiency in 2015 Pb+Pb data for a working point specific to heavy ion analyses. The working points relevant to this thesis are described in later chapters.

### 3.3.2 Vertices

Once the tracks in an event are reconstructed, they are used to form *vertices*, or points in space where tracks originate from. The *primary* vertex refers to a point along the beamline where particles were produced in proton or ion collision. Unstable particles with moderate lifetimes (such as  $B$  and  $D$  mesons) originating from the primary vertex traverse through parts of the detector before decaying, thus creating *secondary* vertices at the point of their decay within the detector volume. Secondary vertices are not relevant to this thesis, and are not discussed further.

The ATLAS primary vertex reconstruction algorithm consists of two steps: vertex finding and vertex fitting [163, 164]. The algorithm starts by defining seed positions for primary vertices, based on their position along the beamline<sup>4</sup>. Using a  $\chi^2$  minimization procedure, tracks close to the seed are used to fit the real position of the primary vertex. Each track used in the fit is assigned a weight, which quantifies the compatibility of the track with the vertex fit. Tracks which are incompatible with the vertex by more than seven standard deviations are removed from the vertex candidate, and are added back to the collection of unused tracks. The vertex reconstruction algorithm continues in this manner until no further primary vertices can be found, or until all tracks in the event have been assigned to primary vertices.

Since the (hadronic) pileup in Pb+Pb collisions in Run 2 was around  $\mathcal{O}(10^{-3})$  or less, the probability of more than one Pb+Pb collision per bunch crossing is at the  $10^{-7}$  level. Thus, during vertex reconstruction for Pb+Pb collisions it is assumed that there is only one primary vertex.

The collection of primary vertices reconstructed in a large number of events is used to reconstruct the *beam-spot*, or the *luminous region* of the colliding protons or ions. The beam-spot reconstruction uses only one primary vertex per event, which is the vertex with the largest  $\sum p_T^2$  of all associated tracks. Additionally, the primary vertices considered in the beam-spot determination are required to have at least five tracks. An unbinned maximum likelihood fit is performed, where the beam-spot is modeled by a three-dimensional Gaussian distribution with possible  $x$ - $y$  couplings and transverse tilts. The beam-spot can be reconstructed using events from around 10 minute intervals, or per luminosity-block such as during van der Meer scans. The longitudinal beam-spot size is related to the accelerator RF frequency, while the transverse size is related to the beam emittance.

---

<sup>4</sup>This refers to the so-called *sliding-window* approach for determining track seeds. Alternate approaches, such as defining vertex seeds based on their position with respect to the online beam-spot, have also been used by ATLAS in Runs 1 and 2.

### 3.3.3 Topoclusters

Particles interacting with the calorimeters (eg. electrons, photons, and hadrons) deposit their shower energies in clusters of calorimeter *cells*, which correspond to the smallest unit in  $\eta$ ,  $\phi$  and radial segmentation. Here, the radial segmentation is achieved due to the presence of multiple sampling layers. ATLAS employs a topological cell clustering algorithm [165], which reconstructs *topoclusters* from the calorimeter cell signals created by particles produced in proton or ion collisions. The topoclusters later serve as inputs to the reconstruction of higher-level objects like electrons and photons.

The basic quantity used in reconstructing topoclusters from calorimeter cell signals is the cell significance  $\varsigma_{\text{cell}}^{\text{EM}} = E_{\text{cell}}^{\text{EM}} / \sigma_{\text{noise,cell}}^{\text{EM}}$ , or the ratio of the energy deposited in the cell and the average (expected) noise<sup>5</sup>. The cell significance can also be negative, due to the bipolar shape of the LAr calorimeter signals. Topocluster reconstruction follows a growing-volume algorithm, which is seeded by cells, or *proto-clusters*, with  $|\varsigma_{\text{cell}}^{\text{EM}}| > 4$ . Neighboring calorimeter cells<sup>6</sup> with  $2 < |\varsigma_{\text{cell}}^{\text{EM}}| < 4$  are added to the proto-clusters. The proto-clusters are merged if the algorithm encounters neighboring cells with  $2 < |\varsigma_{\text{cell}}^{\text{EM}}| < 4$  associated to two proto-clusters. Merging is also performed if neighboring cells with  $|\varsigma_{\text{cell}}^{\text{EM}}| > 4$  other than the seed cell are found. The algorithm expands proto-clusters in all three spatial dimensions until a boundary condition of  $0 < |\varsigma_{\text{cell}}^{\text{EM}}| < 2$  is met.

The resulting proto-clusters then consist of a core of cells with highly significant energy deposits, surrounded by an envelope of less significant cells. They can, however, be too large for meaningful physics measurements, so they are further split. The splitting algorithm finds local maxima within the proto-cluster with  $E_{\text{cell}}^{\text{EM}} > 0.5$  GeV, which are required to have at least four neighboring cells that are already included in the proto-cluster. The local maxima are restricted to the outer layers of the ECal and the first layer of the FCal. In a later refinement step of the proto-cluster splitting algorithm, local maxima in the inner ECal layers, all HCal layers, and outer FCal layers, are permitted. The algorithm then assigns cells within the proto-cluster to at most two local maxima based on an energy and distance weighting procedure. Once the proto-clusters are split, they are called topoclusters, and are considered in the reconstruction of higher level objects.

### 3.3.4 Electrons and photons

The only difference between electrons and photons according to the ATLAS detector is the presence of tracks in the ID, associated with electrons (see Fig. 3.16) but not photons. Thus, the ECal alone is not capable of distinguishing between the two. In order to properly disentangle the two objects, information from the ID must therefore be included. The reconstruction of

---

<sup>5</sup>The energy and noise,  $E_{\text{cell}}^{\text{EM}}$  and  $\sigma_{\text{noise,cell}}^{\text{EM}}$ , are measured on the so-called electromagnetic (EM) scale, which correctly reconstructs the energies of showers generated by electrons and photons, but not hadrons.

<sup>6</sup>In this context, neighboring refers to adjacent cells in one sampling layers, or cells across adjacent sampling layers with partial geometric coverage.

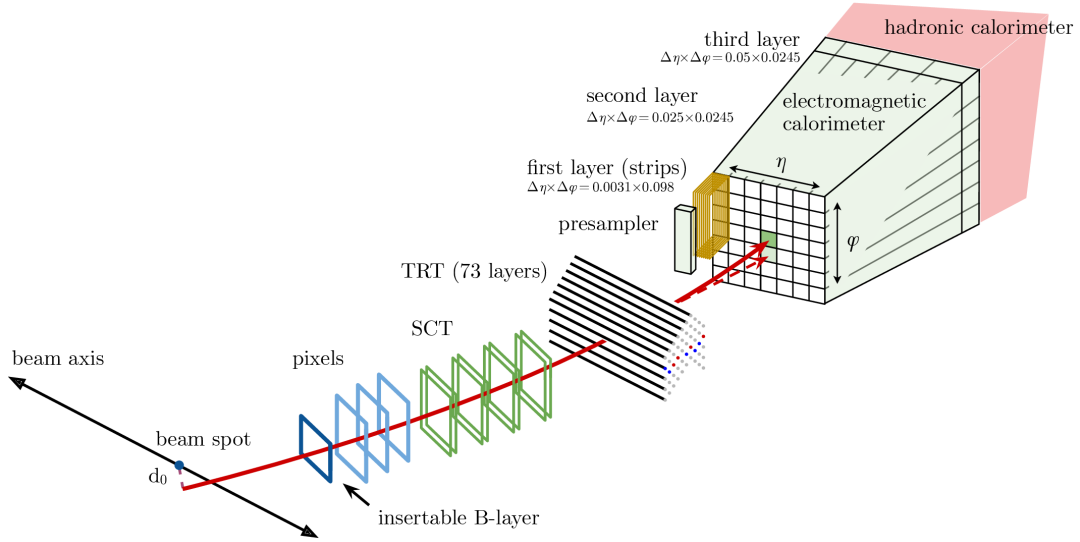


**Figure 3.16:** Illustration of the path of an electron through the ATLAS detector, shown as a solid red line. A bremsstrahlung photon is shown as a dashed red line. Figure taken from Ref. [166].

electrons and photons is further complicated by the fact that electrons can radiate additional photons via bremsstrahlung, while photons (either prompt or non-prompt) can convert into  $e^+e^-$  via pair production. The reconstruction of the two objects is therefore intertwined.

### Reconstruction

The ATLAS reconstruction algorithm for electrons and photons [166–168] begins with the selection of topoclusters with  $p_T > 400$  MeV. Even if topoclusters contain cells in both the ECal and HCal, only the fraction of topocluster energy contained in the ECal, or the electromagnetic fraction  $f_{EM}$ , is considered for electron and photon reconstruction. Following this, tracks in the event loosely matched to calorimeter ROIs are selected, where the matching is performed based on geometric proximity. If multiple tracks are matched to a topocluster, they are ranked based on their quality (tracks with Pixel hits are ranked higher than those with SCT hits but no Pixel hits), and based on the  $\Delta R$  to the cluster. The highest ranked track is then used to define the kinematics of the electron object.

Since converted photons leave behind two tracks (i.e. the  $e^+e^-$  pair), a search for the conversion vertex is performed. Two tracks with opposite charges are required to form a vertex consistent with a massless particle. The particle identification capabilities of the TRT are also used to improve the purity of conversion vertices, by requiring that the TRT determines a high probability of the associated tracks being electrons. Further, tracks with only TRT hits are also considered in the conversion vertex finding procedure. The conversion vertices are then matched to topoclusters, based on  $\Delta\eta$  and  $\Delta\phi$  requirements.

In the next stage of the reconstruction, the topoclusters in the event are grouped into *superclusters*. The process of supercluster formation involves finding candidate seeds from the

collection of  $E_T$ -ordered topoclusters. An electron supercluster seed is defined as a topocluster with  $E_T > 1$  GeV which has a matched track with at least four hits in the Pixel and SCT sub-detectors. A photon supercluster seed is defined as a topocluster with  $E_T > 1.5$  GeV, and with no additional requirements on matched tracks and conversion vertices. After the seeds are found, neighboring or *satellite* topoclusters are added to the supercluster seed. For both electrons and photons, topoclusters falling within a window of  $\Delta\eta \times \Delta\phi = 0.075 \times 0.125$  around the seed barycenter are classified as satellites. Additionally for electrons, topoclusters that share a best-matched track with the seed within  $\Delta\eta \times \Delta\phi = 0.125 \times 0.3$  are also counted as satellites. Satellites are added to photon supercluster seeds if the two tracks associated with a conversion vertex can be matched to the seed and the satellite.

After the superclusters are created, an initial energy and position calibration is applied to them. A matching procedure is then performed to the superclusters as a whole: tracks are matched to electron superclusters, while conversion vertices are matched to photon superclusters. Finally, the superclusters are used to create the electron and (converted and unconverted) photon object candidates, based on a series of requirements on the associated tracks, conversion vertices and clusters [168]. Since the creation of superclusters proceeds independently for electrons and photons, a given seed may be associated to both candidate objects. If the ambiguity cannot be resolved through the object definitions, both electron and photon objects are created, such that they can be separated at the analysis level.

### Calibration

The first step of the ATLAS electron and photon calibration procedure [169] involves the calibration of the supercluster energies, since they were originally determined on the EM scale. Using zero pileup Monte Carlo samples of single electrons and photons, a regression Boosted Decision Tree (BDT) corrects for smearing and energy loss. The calibration is then applied to both data and simulation. Following this, an *inter-calibration* is performed for the energy scales of different regions of the detector, such that the total reconstructed energy is accurate. The  $Z \rightarrow e^+e^-$  resonance is then used to calibrate the energy scale of electrons and photons in the data, and adjust the energy resolution in simulation. In order to validate the calibration procedure, the  $J/\psi \rightarrow e^+e^-$  resonance and radiative  $Z$  boson decays are compared between data and simulation.

### Identification

Before the reconstructed and calibrated electron objects are used in physics measurements, they are required to pass a set of selection criteria, in order to reject backgrounds, improve the object quality, and minimize systematic uncertainties. During Run 2, electrons were identified by ATLAS using a likelihood approach [166, 168], which uses the distributions of various shower shape and tracking variables to construct the likelihoods separately for signal (i.e. prompt) and background (i.e. non-prompt) electrons. A discriminant based on a ratio of the signal and

signal-plus-background likelihoods is then used to identify prompt electrons. Several working points are defined based on fixed thresholds on the discriminant. In increasing order of the threshold, these are the `VeryLoose`, `Loose`, `Medium` and `Tight` working points. The thresholds are optimized to ensure high identification efficiency across electron  $\eta$  and  $p_T$ , while rejecting background contamination. All WPs have fixed requirements on tracking criteria, i.e. the number of hits in the various ID sub-detectors. The analysis presented in this thesis makes use of the `VeryLoose` working point, which requires at least one Pixel hit, and no requirements on hits in the IBL.

The photons objects relevant to thesis are in a very low  $p_T$  range, where the common ATLAS photon identification algorithms do not apply. Instead, a neural network (NN) based photon identification was used, which was developed in the context of the ATLAS measurement of  $\gamma\gamma \rightarrow \gamma\gamma$  scattering in ultra-peripheral Pb+Pb collisions in Run 2 [170]. The NN was trained using photon shower shape variables. Signal  $\gamma\gamma \rightarrow \gamma\gamma$  events from Monte Carlo simulations were discriminated against fake photons obtained in the data. The NN was optimized to provide a 95% identification efficiency for photons with  $p_T > 2.5$  GeV and  $|\eta| < 2.37$ , excluding the crack region.

### Isolation

Prompt electrons and photons are typically well separated from other objects in the final state. However, processes like pileup, pair production, hadron decays, etc. result in non-prompt electrons and photons, which are associated with nearby activity. *Isolation requirements* therefore impose vetoes on neighboring activity, such that prompt and non-prompt objects can be separated. The analysis presented in this thesis uses extremely clean ultra-peripheral Pb+Pb events, where the final state objects have almost no activity surrounding them. As such, electron and photon isolation requirements are not required, and are not discussed further.

### 3.3.5 Muons

Muons, being approximately 206 times heavier than electrons, are minimum ionizing particles in the ATLAS detector. Muons interact with all sub-detectors: they produce tracks in the Inner Detector, leave (small) calorimeter signals, and produce tracks in the Muon Spectrometer. Thus, the reconstruction of muons requires a precise understanding of the complete detector.

### Reconstruction

The ATLAS muon reconstruction procedure [171, 172] is designed to reconstruct not only muons produced directly in proton or ion collisions, but also those produced via other interesting processes, such as through hadron decays. At the same time, it rejects muons associated with background processes, like cosmic radiation and beam-induced backgrounds.

The muon reconstruction procedure starts by reconstructing so-called *MS tracks* from hits in the Muon Spectrometer, as follows:

1. Hit patterns in the MDT and CSC modules are searched for to form *segments*, which correspond to hits aligned on a trajectory in the bending plane of the detector. The RPC and TGC hits provide an additional coordinate orthogonal to the bending plane. MS track candidates are then built by combining hits from segments in multiple layers.
2. Starting from the middle layer of the muon stations, a combinatorial search extends the track candidates inwards and outwards. A search seeded by segments in the inner and outer layer of the stations is also performed.
3. A global  $\chi^2$  fit of the track is performed, which takes into account the full magnetic field model, possible interactions with detector material, and misalignments of the stations. Hits that are outliers with respect to the fitted MS track are removed, and the fit is redone.
4. Since segments can be shared across multiple track candidates, an ambiguity resolver is used, which removes tracks that share many hits with high quality tracks.
5. The final collection of MS tracks is refit using the constraint that the trajectories are consistent with the interaction point. The trajectories are extrapolated back to the beamline, and the  $p_T$  of the MS tracks is expressed at the interaction point.

After the MS tracks are reconstructed, the reconstruction of the full muon object can proceed. Several definitions are available in the ATLAS muon reconstruction procedure, depending on the conditions and requirements of the muons. They are illustrated in Fig. 3.17 and are described below:

1. **Combined (CB)**: Tracks in the ID and MS, which are reconstructed independently, are combined using a global fit. An outside-in approach is taken, since the relatively large bending radius within the MS allows for better  $q/p$  resolution. A complementary inside-out approach is also used sometimes. During the global fit, additional MS hits may be added to the track to improve the quality of the fit. For  $|\eta| > 2.5$ , MS tracks are combined with short track segments only in the Pixel and SCT detectors, defining a subset of CB muons called Silicon Forward (SiF) muons. This definition allows for better use of the ID near the boundaries of its acceptance. Overall, CB muons have the highest purity across all identified muon working points (see below).
2. **Segment-tagged (ST)**: Tracks in the ID are combined with at least one reconstructed segment in the MDT or CSC chambers, rather than full MS tracks. This definition is used for muons with very low  $p_T$ , as they may not leave hits in all layers of the MS due to the smaller bending radius of the trajectory. It is also used when muons pass through regions of the MS with reduced acceptance, such as  $|\eta| < 0.1$  gap region. The parameters of the ID track are used to define the muon track's parameters.

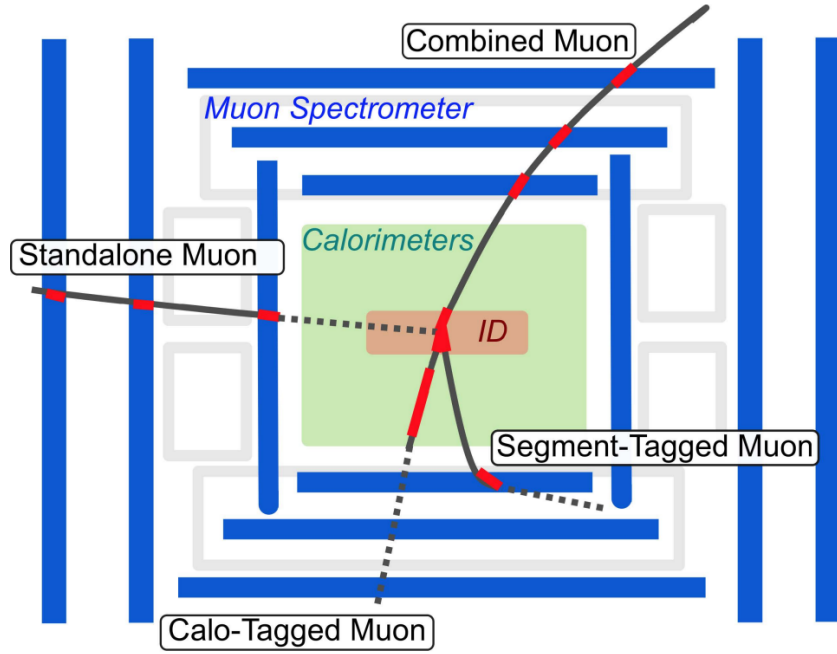


**Figure 3.17:** Illustration of the muon reconstruction algorithms available in ATLAS [173].

3. **Calorimeter-tagged (CT):** This type of muon reconstruction does not use MS tracks, but only ID tracks matched to a calorimeter signal that is consistent with a minimum ionizing particle. This definition is optimized for the  $|\eta| < 0.1$  gap region where the MS is only partially instrumented. It has the lowest purity out of all muon reconstruction algorithms. The track parameters are determined only from the ID track.
4. **Muon Spectrometer Extrapolated (ME) / Stand-alone (ST):** If a matching ID track is not found, the muon trajectory is defined using only the MS track. In the ME muon case, the muon trajectory is extrapolated back to the interaction point based on a loose compatibility requirement. The track parameters are defined at the beamline, taking into account the energy lost by the muon in the calorimeter. In the ST muon case, the trajectory is not extrapolated, and only the MS tracks are used. These types of muons are mainly used to extend the acceptance for muon reconstruction in the  $2.5 < |\eta| < 2.7$  region, which is not covered by the ID.

Since ID or MS tracks can be shared between different muon types, an overlap removal process is applied. When several muon types share an ID track, it is preferentially assigned first to CB muons, then to ST muons, and finally to CT muons. Overlaps with ME muons are resolved by identifying the better quality tracks, via an analysis of the track hit content and fit quality.

### Calibration

Reconstructed muons undergo a data-driven calibration procedure, so that their properties in data and simulation are consistent [171]. The scale (i.e. absolute value) and resolution (i.e.



spread) of the muon  $p_T$  for each WP is calibrated using well-known physics processes, namely the  $J/\psi \rightarrow \mu\mu$  and  $Z \rightarrow \mu\mu$  resonances. By comparing the mass peaks in data and simulation, calibration constants are derived, which correct for effects like detector misalignments, magnetic field inhomogeneities, energy loss due to interaction with the detector material, etc. The corrections are derived in  $\eta - \phi$  regions of the detector that are homogeneous in terms of detector technology and performance.

### Identification

Just like electrons and photons, muons also have to pass identification criteria to increase the purity, and to reduce background contamination [172]. In increasing order of background rejection, the `Loose`, `Medium` and `Tight` WPs are the most commonly used ones. They apply requirements on the number of ID and MS hits,  $q/p$  significance, track fit quality etc. The `HighPt` WP is designed to improve the momentum resolution for tracks with  $p_T > 100$  GeV, which generally suffer from reduced efficiencies as a consequence of the large bending radius.

The analysis presented in this thesis makes use of the `LowPt` working point, which is optimized for muons with small  $p_T$ . The WP is applied only to CB muons, primarily reconstructed using the inside-out approach as it has higher efficiency at lower  $p_T$ . At least one segment in the MDT or CSC layers is required for muons with  $|\eta| < 1.3$ , since the muons may not reach more than one MS layer. Muons with  $|\eta| > 1.3$  have sufficient momentum to reach more than two MS layers, so the requirement is increased to two precision chamber segments. Further requirements, such as vetoes on the presence of kinks in the tracks, are imposed to reject muons produced in hadron decays.

### Isolation

In the same manner as electrons and photons, prompt muons are typically well separated from other final state objects. However, processes like pileup, hadron decays, etc. produce non-prompt muons which can be reconstructed as one of the muon types discussed earlier. The analysis presented in this thesis uses extremely clean ultra-peripheral Pb+Pb events, where the final state objects have almost no activity surrounding them. As such, muon isolation requirements are not needed, and are not discussed further.

### 3.3.6 Other objects

The ATLAS detector is also capable of reconstructing other high-level objects that are commonly used in the analysis of proton or ion collisions. While these objects are not used in this thesis, they are nevertheless briefly discussed below.

#### Jets

Along with colorless particles like leptons and photons, colored particles, i.e. quarks and gluons, are also frequently found in the final states of proton or ion collisions. As they propagate away from the collision, they radiate additional colored particles: quarks can radiate gluons,



while gluons can either radiate more gluons (due to the self-interacting nature of QCD) or split into  $q\bar{q}$  pairs. This results in a cascade of QCD radiation, which produces colored particles with decreasing energies. It continues until the particles have energies around the QCD scale ( $\mathcal{O}(100)$  MeV), at which point *hadronization*, i.e. the formation of bound colorless hadrons occurs. Any unstable hadrons that are formed in this process subsequently decay. While the mechanism of hadronization is not known, several successful models have been employed in Monte Carlo event generators, which are tuned to experimental data [174, 175].

The full process of QCD showering and hadronization takes place within a few femtometers, so it cannot be resolved by the detector. Instead, a *jet* is observed, which is a collimated spray of energetic hadrons, leptons and photons, in the direction of the original parton. These particles leave behind tracks in the Inner Detector, and energy deposits in the calorimeters. Muons originating from the decays of hadrons within jets interact with the Muon System.

The experimental definition of a jet depends on the specific jet reconstruction technique. Jets reconstructed using only topoclusters are called *calorimeter jets* [165], while those reconstructed using both ID tracks and topoclusters are called *particle flow jets* [176]. For both types of jets, the most common approach used by ATLAS for clustering the low-level objects is the anti- $k_T$  algorithm [177], which results in the formation of cone-like regions with some radius  $R$  in the transverse plane that contains particles produced by the showering of the initial hard quark or gluon. In ATLAS, the standard jet definition uses  $R = 0.4$ ; large-radius jets with  $R = 1.0$  are also used in ATLAS analyses. Since jets are complex objects constructed with data from multiple sub-detectors, they go through a sophisticated calibration procedure before being used in analyses [178].

### Flavor tagging

The  $b$ -quarks produced in proton or ion collisions typically hadronize into  $B$ -mesons. Due to their relatively long lifetimes of around 1.5 ps, at LHC energies the  $B$ -mesons propagate a few millimeters into the detector before decaying further. Thus, a secondary vertex is found within the jet initiated by a  $b$ -quark. This signature can be used to distinguish between  $b$ -quark initiated jets, called  *$b$ -jets*, and jets initiated by gluons and lighter quarks. The process of *flavor tagging* refers to this discrimination process. Flavor tagging algorithms are required to have a high background rejection capability, while still maintaining a high efficiency. Several algorithms based on complex machine learning algorithms are used by ATLAS for this purpose [179].  *$b$ -jets* are an important aspect of many ATLAS analyses, as they can be used to identify top quarks decays,  $H \rightarrow b\bar{b}$  decays, potential decays of BSM particles etc.

### Hadronically decaying tau leptons

Tau leptons, as explained in Sec. 2.3, decay to leptons and hadrons, along with neutrinos. The leptonic decays are indistinguishable from electrons and muons produced in primary collisions,

but the visible component of the hadronic decays can be reconstructed and identified<sup>7</sup>. If the tau lepton is sufficiently boosted, the hadronic decay products can become collimated, thereby forming a jet. Hadronic tau jets are typically narrower than QCD-induced jets, since the decay products (mainly pions and kaons) are color neutral and do not produce QCD showers.

The ATLAS hadronic tau lepton reconstruction algorithm [180] starts with the reconstructed  $R = 0.4$  anti- $k_T$  jets in an event. The features of these jets, along with the features of their constituent tracks and topoclusters, are used as inputs to a Recurrent Neural Network (RNN) to distinguish between hadronically decaying tau leptons and QCD jets [181]. The ATLAS tools for tau lepton reconstruction and identification were designed for tau leptons with moderately high transverse momenta, i.e.  $p_T \gtrsim 25$  GeV. Since the tau leptons produced through the  $\gamma\gamma \rightarrow \tau^+\tau^-$  process in ultra-peripheral Pb+Pb collisions are softer than this threshold, the standard ATLAS tau lepton object has not been used in this thesis.

### Missing transverse momentum

The initial states of proton or ion collisions have zero transverse momentum, so the same must also hold true for the final states due to momentum conservation. If the vector sum of the transverse momenta of all reconstructed final state objects does not equal zero, it is assumed that some momentum was carried away by undetected particles. The missing transverse momentum, defined as

$$\mathbf{p}_T^{\text{miss}} = - \sum_{i \in \{\text{hard objects}\}} \mathbf{p}_T^i - \sum_{j \in \{\text{soft objects}\}} \mathbf{p}_T^j \quad (3.11)$$

therefore quantifies this lost momentum [182]. Here, the sum over hard objects includes electrons, photons, hadronically decaying tau leptons, muons, and jets; the sum over soft objects includes tracks not associated with other objects, or topoclusters not associated with other objects. Missing transverse momentum can be created by neutrinos, which are invisible to the ATLAS detector, or potential weakly interacting BSM particles. Experimental sources, such as detector inefficiencies and energy miscalibrations can also contribute to missing transverse momentum.

---

<sup>7</sup>The visible hadronic decay products are the neutral and charged hadrons, since they interact with the ATLAS detector. The neutrino, which does not interact with any sub-detector, is considered invisible.

# Chapter 4

## Luminosity measurement

This chapter is devoted to studies of the luminosity of the 2023 Pb+Pb dataset. The concept of luminosity, and how it is measured and calibrated by the ATLAS experiment are discussed in Sec. 4.1. Luminosity measurement in heavy ion collisions using Inner Detector tracks is introduced in Sec. 4.2. A preliminary calibration of the luminosity of the 2023 Pb+Pb dataset is presented in Sec. 4.3.

### 4.1 Introduction

#### 4.1.1 Concept of luminosity

As introduced in Sec. 3.1.1, luminosity is the proportionality constant between cross-sections and event rates. In principle, any reference scattering process can be used to measure luminosity through this proportionality. However, not all processes are suitable. For example, elastic scattering processes are not ideal since they deflect particles at very small angles relative to the beamline. Detecting such particles would require placing detectors in high radiation environments. In practice, collider experiments consider *inelastic collisions* as the reference process.

Suppose a luminosity detector, or *luminometer*, is able to detect the entire inelastic cross-section  $\sigma_{\text{inel}}$ . Then, the instantaneous luminosity of one colliding bunch can be written using the event rate  $dN/dt$  as

$$\mathcal{L}_{\text{inst}} = \frac{1}{\sigma_{\text{inel}}} \frac{dN}{dt} = \frac{\mu f_{\text{rev}}}{\sigma_{\text{inel}}}, \quad (4.1)$$

where  $f_{\text{rev}}$  is the revolution frequency of the bunches in the collider. Since bunches of protons or ions contain many particles, there is always the possibility of more (or less) than one interaction per bunch crossing. This is accounted for by the factor  $\mu$ , i.e. the *pileup*, which gives the number of particle collisions per bunch crossing.

A luminometer cannot detect every collision event as it is limited by geometric acceptance, detection efficiency, backgrounds etc. Thus, a luminometer only sees a fraction  $\epsilon$  of the total event rate, which corresponds to a *visible cross-section*  $\sigma_{\text{vis}} = \epsilon \sigma_{\text{inel}}$ . The instantaneous luminosity is then

$$\mathcal{L}_{\text{inst}} = \frac{\epsilon \mu f_{\text{rev}}}{\epsilon \sigma_{\text{inel}}} = \frac{\mu_{\text{vis}} f_{\text{rev}}}{\sigma_{\text{vis}}}, \quad (4.2)$$

where  $\mu_{\text{vis}}$  is the *visible pileup*, also called the *visible event rate*.

This equation defines luminosity in terms of luminometer data, but it can also be defined directly through the parameters of the colliding bunches. This is achieved by recognizing that the observed scattering process originates in the overlap area between two colliding bunches. In other words, the luminosity of one colliding bunch pair can also be expressed as

$$\begin{aligned} \mathcal{L}_{\text{inst}} &= K n_1 n_2 f_{\text{rev}} \Omega, \\ &= K n_1 n_2 f_{\text{rev}} \int dx dy dz dt \rho_1(x, y, z - t) \rho_2(x, y, z + t), \end{aligned} \quad (4.3)$$

where  $n_{1,2}$  are the intensities (i.e. number of protons or ions) in the two bunches,  $K$  is the Møller factor, and  $\Omega$  is the bunch overlap, which is defined as the spacetime integral of the normalized bunch densities  $\rho_{1,2}$ . In this equation, the time coordinate is placed alongside the longitudinal coordinate  $z$  so, that the bunches collide (i.e. achieve maximum overlap) at the interaction point situated at the origin at  $t = 0$ . The Møller factor is given by

$$K = \sqrt{(\mathbf{v}_1 - \mathbf{v}_2)^2 - (\mathbf{v}_1 \times \mathbf{v}_2)^2}, \quad (4.4)$$

where  $\mathbf{v}_{1,2}$  are the velocities of the bunches in the lab frame [183]. In the case of bunches colliding at the speed of light with no crossing angle between them,  $K = 2$ .

Suppose the bunch densities can be described by uncorrelated three-dimensional Gaussian distributions, i.e.<sup>1</sup>,

$$\rho_i(\mathbf{x}, t) = \frac{1}{(2\pi)^{3/2} \sigma_{i,x} \sigma_{i,y} \sigma_z} \exp\left(-\frac{x^2}{2\sigma_{i,x}^2} - \frac{y^2}{2\sigma_{i,y}^2} - \frac{(z \pm t)^2}{2\sigma_z^2}\right) \quad \text{with } i = 1, 2. \quad (4.5)$$

Since the longitudinal width is set by the radio-frequency acceleration system, it is assumed to be equal for the two bunches.

Using Eq. 4.3, the luminosity can be expressed as

$$\mathcal{L}_{\text{inst}} = \frac{n_1 n_2 f_{\text{rev}}}{2\pi \sqrt{\sigma_{1x}^2 + \sigma_{2x}^2} \sqrt{\sigma_{1y}^2 + \sigma_{2y}^2}} = \frac{n_1 n_2 f_{\text{rev}}}{2\pi \Sigma_x \Sigma_y}, \quad (4.6)$$

where  $\Sigma_{x,y}$  are called the *convolved beam widths* in the horizontal and vertical planes. The above is essentially a derivation of Eq. 3.3.

---

<sup>1</sup>Due to a combination of effects like synchrotron radiation, space charge, and intra-beam scattering, bunches of particles in a synchrotron are Gaussian-distributed, as a consequence of the central limit theorem. See Appendix A.II of Ref. [99].

### 4.1.2 Luminosity measurement in ATLAS

According to Eq. 4.2, the luminosity measured by a luminometer depends on the visible pileup  $\mu_{\text{vis}}$ . The data recorded by a luminometer is converted into  $\mu_{\text{vis}}$  using a *luminosity algorithm*. Broadly speaking, luminosity measurement algorithms can be categorized as follows [101]:

- **Event counting:** in these algorithms, the fraction of bunch crossings that contain collision events is counted, where collision events are defined by the number of registered detector hits (e.g. number of pixels, number of topoclusters etc.) within some predefined thresholds. Event counting algorithms work under the assumption that the observed number of collisions per bunch crossing is Poisson distributed, with a mean given by the  $\mu_{\text{vis}}$  of the algorithm. Suppose a luminometer detects hits in  $N_{\text{evt}}$  out of  $N_{\text{BC}}$  bunch crossings. The acceptance fraction  $f = N_{\text{evt}}/N_{\text{BC}}$  can be used as a proxy for  $P(\geq 1 \text{ collision})$ , giving

$$P(\geq 1 \text{ collision}) = \frac{N_{\text{evt}}}{N_{\text{BC}}} = 1 - e^{-\mu_{\text{vis}}}, \quad (4.7)$$

from which  $\mu_{\text{vis}}$  can be determined.

- **Hit counting:** here, the number of *hits* observed by a luminometer per bunch crossing (within some pre-defined thresholds) is counted. Suppose a luminometer, consisting of  $N_{\text{det}}$  identical detectors, registers hits in  $N_{\text{evt}}$  out of  $N_{\text{BC}}$  bunch crossings. Under the same Poisson assumption as in event counting, the relation

$$P(\geq 1 \text{ hit}) = \frac{N_{\text{evt}}}{N_{\text{BC}}N_{\text{det}}} = 1 - e^{-\mu_{\text{vis}}} \quad (4.8)$$

is obtained, from which  $\mu_{\text{vis}}$  can be determined.

- **Particle counting:** in these algorithms, the number of particles produced in bunch crossings is inferred using reconstructed quantities. In cases where the reconstructed objects act as true proxies of the produced particles (e.g. tracks, vertices, topoclusters etc.) the visible pileup is given by the first moment of the object multiplicity distribution, i.e.

$$\mu_{\text{vis}} = E[N_{\text{obj}}]. \quad (4.9)$$

The ATLAS sub-detectors used for luminosity measurement rely on all of the above techniques to compute  $\mu_{\text{vis}}$  from the low-level data. Described below are those algorithms which are used in heavy ion collisions to provide online and offline bunch-by-bunch luminosity measurements. Algorithms using calorimeter data are used for proton-proton collisions, but suffer from low statistics and instrumental noise during heavy ion data-taking, and are therefore not considered. Offline luminosity algorithms based on Inner Detector data (i.e. tracks) will be discussed in Sec. 4.2.

### LUCID algorithms

The LUMinosity Cherenkov Integrating Detector (LUCID, see Sec. 3.2.5) serves as the primary luminometer for the ATLAS experiment. Sixteen photomultiplier tubes (PMTs) are situated on either side of the ATLAS IP in eight azimuthally symmetric stations, such that each station houses two PMTs. Due to the radioactive  $^{207}\text{Bi}$  calibration source, the two PMTs in each station are called “Bi” and “Bi2”. The Bi and Bi2 PMTs are read out using separate electronics, ensuring redundancy during data-taking.

A hit in the LUCID PMTs is defined as a pulse with an amplitude above a given threshold. Generally speaking, hit counting algorithms based on the LUCID PMTs are not used in heavy ion collisions due to the low luminosity (i.e. low statistics) data-taking conditions. Event counting algorithms are used instead, particularly with combinations of multiple PMTs. The most important event counting algorithms based on the Bi PMTs are:

- LUCID BiEvtA : at least one of the Bi PMTs on the A side registers a hit.
- LUCID BiEvtC : same as LUCID BiEvtA, but with the C side Bi PMTs.
- LUCID BiEvtOR : at least one Bi PMT on either of the A or C sides registers a hit.
- LUCID BiEvtAND : at least one hit in both the A and C side Bi PMTs.

The detection efficiencies of these algorithms –  $\epsilon_A$ ,  $\epsilon_C$ ,  $\epsilon_{\text{OR}}$ , and  $\epsilon_{\text{AND}}$  – are related by the equation  $\epsilon_{\text{OR}} = \epsilon_A + \epsilon_C - \epsilon_{\text{AND}}$ . Due to this overlap with the other algorithms, the relation between the visible pileup and number of accepted events for the EvtAND algorithm is [184]

$$\frac{N_{\text{evt}}}{N_{\text{BC}}} = 1 - 2 \exp \left( -\frac{\mu_{\text{vis}}}{2} \left( 1 + \frac{\sigma_{\text{vis}}^{\text{OR}}}{\sigma_{\text{vis}}^{\text{AND}}} \right) \right) + \exp \left( -\mu_{\text{vis}} \frac{\sigma_{\text{vis}}^{\text{OR}}}{\sigma_{\text{vis}}^{\text{AND}}} \right), \quad (4.10)$$

which is obtained after assuming  $\epsilon_A = \epsilon_C$ . Here,  $\sigma_{\text{vis}}^{\text{OR}}$  and  $\sigma_{\text{vis}}^{\text{AND}}$  are the visible cross-sections of LUCID BiEvtOR and LUCID BiEvtAND. Due to the complexity of this equation, the  $\mu_{\text{vis}}$  of the EvtAND algorithm cannot be determined analytically. Instead, an iterative numerical procedure is used, which simultaneously extracts the  $\sigma_{\text{vis}}^{\text{AND}}$ , based on a known  $\sigma_{\text{vis}}^{\text{OR}}$  calibration.

Algorithms similar to the ones listed above using the Bi2 PMTs are also used during heavy ion data-taking. The algorithm names use “Bi2” instead of “Bi”. The  $\mu_{\text{vis}}$  determination strategies are identical to the Bi algorithms.

### ZDC algorithms

The Zero Degree Calorimeter (ZDC, see Sec. 3.2.5) is used for luminosity measurement only during heavy ion data-taking, since it is installed only for those periods. The two stations are located 140 m from the ATLAS IP on both sides.

A hit in the ZDCs is defined as an energy deposit above the threshold for one forward neutron, which in Run 3 Pb+Pb collisions corresponds to energies larger than 1 TeV. Using this, four event counting algorithms are defined: ZDC EvtA, ZDC EvtC, ZDC EvtOR and ZDC EvtAND. The nomenclature and  $\mu_{\text{vis}}$  determination follows that of the LUCID algorithms.

### BCM algorithms

The Beam Conditions Monitor (BCM, see Sec. 3.2.2) consists of two stations 1.84 m away from the ATLAS IP on both sides. Each station consists of four diamond sensor modules, arranged in a plus-shaped configuration that is aligned with the ATLAS coordinate system.

A hit in the BCM modules is defined by a signal amplitude crossing a given threshold. In principle, each of the BCM modules can be separately used for event counting algorithms. However, the single module algorithms suffer from large backgrounds, on account of the fact that the BCM serves as a beam-induced background monitor. Thus, combinations of modules are used instead. The BCM algorithms relevant to heavy ion data-taking are:

- BCM HEvtOR: hits in at least one horizontal module.
- BCM VEvtOR: hits in at least one vertical module.
- BCM TEvtOR: logical OR of the BCM HEvtOR and BCM VEvtOR algorithms.

### 4.1.3 Absolute calibration

The luminosity defined in Eq. 4.2 contains two variables, namely  $\mu_{\text{vis}}$  and  $\sigma_{\text{vis}}$ , both of which have to be known precisely. The strategies used by ATLAS to determine  $\mu_{\text{vis}}$  were introduced in the preceding subsection. The strategy used to determine visible cross-section  $\sigma_{\text{vis}}$ , which defines the *absolute scale* of a luminometer, is given below.

For well known reference processes like Drell-Yan scattering ( $pp \rightarrow Z \rightarrow \ell^+ \ell^-$ ,  $\ell = e, \mu$ ) where the uncertainty on the reference cross-section is around 3%, the detection efficiency  $\epsilon$  can be estimated using data-driven and Monte Carlo techniques [185]. Combining  $\epsilon$  with  $\sigma_{\text{inel}}$ , which is measured to 2-3% precision [186, 187],  $\sigma_{\text{vis}}$  can be determined. However, given the fact that the reference cross-section,  $\epsilon$  and  $\sigma_{\text{inel}}$  all have uncertainties, this approach to determining the absolute luminosity scale would incur large luminosity-related systematic uncertainties on physics measurements.

Thus, experiments at colliders rely on the *van der Meer* (vdM) method, also called *beam separation scans*, to determine  $\sigma_{\text{vis}}$  up to sub-percent precision for inelastic collisions. Originally developed by Simon van der Meer for un-bunched beams at the Intersecting Storage Rings at CERN [188], and later adapted to bunched beams by Carlo Rubbia [189], the vdM method is the primary luminosity calibration technique for the LHC experiments [187, 190–194]. The LHCb experiment also uses the *beam-gas imaging* method [194], where collisions between the bunches and residual gas in the LHCb interaction region are reconstructed. From

the distribution of the collision vertices, the beam overlap  $\Omega$ , and consequently the luminosity scale, are determined.

Suppose the two colliding beams are separated by  $\Delta x$  and  $\Delta y$  in the horizontal and vertical planes respectively. Eq. 4.3 can then be generalized to

$$\begin{aligned} \mathcal{L}_{\text{inst}}(\Delta x, \Delta y) = & K n_1 n_2 f_{\text{rev}} \int dx dy dz dt \rho_1 \left( x - \frac{\Delta x}{2}, y - \frac{\Delta y}{2}, z - t \right) \\ & \times \rho_2 \left( x + \frac{\Delta x}{2}, y + \frac{\Delta y}{2}, z + t \right). \end{aligned} \quad (4.11)$$

If the particle densities are assumed to *factorize* in all three coordinates, i.e. they take the form shown in Eq. 4.5, the luminosity can be written as

$$\mathcal{L}_{\text{inst}}(\Delta x, \Delta y) = \int dx dy n_1 n_2 f_{\text{rev}} \Omega_x(\Delta x) \Omega_y(\Delta y), \quad (4.12)$$

with

$$\begin{aligned} \Omega_x(\Delta x) &= \frac{1}{2\pi\sigma_{1x}\sigma_{2x}} \exp \left( -\frac{\left(x - \frac{\Delta x}{2}\right)^2}{2\sigma_{1x}^2} - \frac{\left(x + \frac{\Delta x}{2}\right)^2}{2\sigma_{2x}^2} \right), \\ \Omega_y(\Delta y) &= \frac{1}{2\pi\sigma_{1y}\sigma_{2y}} \exp \left( -\frac{\left(y - \frac{\Delta y}{2}\right)^2}{2\sigma_{1y}^2} - \frac{\left(y + \frac{\Delta y}{2}\right)^2}{2\sigma_{2y}^2} \right). \end{aligned} \quad (4.13)$$

After performing the integrals in Eq. 4.12, the luminosity becomes

$$\mathcal{L}_{\text{inst}}(\Delta x, \Delta y) = n_1 n_2 f_{\text{rev}} \frac{1}{\sqrt{2\pi}\Sigma_x} \frac{1}{\sqrt{2\pi}\Sigma_y} \exp \left( \frac{-\Delta x^2}{2\Sigma_x^2} \right) \exp \left( \frac{-\Delta y^2}{2\Sigma_y^2} \right). \quad (4.14)$$

Using this, the event rate observed by a luminometer, introduced in Eq. 4.2 for head-on collisions, can be allowed to depend on the beam separation, i.e.

$$\mu_{\text{vis}}(\Delta x, \Delta y) = \sigma_{\text{vis}} n_1 n_2 \frac{1}{\sqrt{2\pi}\Sigma_x} \frac{1}{\sqrt{2\pi}\Sigma_y} \exp \left( \frac{-\Delta x^2}{2\Sigma_x^2} \right) \exp \left( \frac{-\Delta y^2}{2\Sigma_y^2} \right). \quad (4.15)$$

If the beam positions are fixed at a given separation, the visible event rate will slowly reduce over time as the bunch intensities burn off due to collisions. Thus, for the analysis of vdM scans, the event rate is normalized by the bunch charge product  $n_1 n_2$ , to define the *specific visible event rate*

$$\bar{\mu}_{\text{vis}}(\Delta x, \Delta y) \equiv \frac{\mu_{\text{vis}}(\Delta x, \Delta y)}{n_1 n_2} = \frac{\sigma_{\text{vis}}}{2\pi\Sigma_x\Sigma_y} \exp \left( \frac{-\Delta x^2}{2\Sigma_x^2} \right) \exp \left( \frac{-\Delta y^2}{2\Sigma_y^2} \right), \quad (4.16)$$

which is in principle constant over time.

The idea of the van der Meer scan is to determine  $\Sigma_{x,y}$ , using the specific visible event rate



measured by a luminometer at a given set of beam separations. In a horizontal *on-axis* vdM scan, the beams are swept through *steps* in  $\Delta x$  with  $\Delta y = 0$ . In a vertical on-axis vdM scan, the beams are swept through  $\Delta y$  with  $\Delta x = 0$ . An example of a horizontal and vertical vdM scan pair is shown in Fig. 4.1. *Off-axis* scans are those where the separation in the non-scanning direction is set to a non-zero value.

These scans are typically referred to as *one-dimensional* scans, since the separation in the non-scanning plane is fixed. In contrast, in *two-dimensional* scans the separation in both planes can be varied. For example, in a *grid scan*,  $\bar{\mu}_{\text{vis}}$  is sampled in a grid of  $(\Delta x, \Delta y)$  points. *Diagonal* scans can also be performed, where  $\bar{\mu}_{\text{vis}}$  is recorded as the beams are separated in a coordinate system that is rotated with respect to the lab frame.

A pair of vdM scans, also referred to as *scan curves* (i.e.  $\bar{\mu}_{\text{vis}}$  vs. beam separation), can then be used to determine the convolved beam widths. Suppose a pair of orthogonal scans were performed parallel to the lab frame, such that the horizontal and vertical scans are maximized at  $x = x_0$  and  $y = y_0$  respectively. In an on-axis scan pair,  $(x_0, y_0)$  coincides with the origin under ideal conditions, and may deviate from the origin due to orbit drift. Then, the convolved beam widths can be determined using the equations

$$\begin{aligned}\Sigma_x &= \frac{1}{\sqrt{2\pi}} \frac{\int d\Delta x \bar{\mu}_{\text{vis}}(\Delta x, y_0)}{\bar{\mu}_{\text{vis}}(0, y_0)}, \\ \Sigma_y &= \frac{1}{\sqrt{2\pi}} \frac{\int d\Delta y \bar{\mu}_{\text{vis}}(x_0, \Delta y)}{\bar{\mu}_{\text{vis}}(x_0, 0)}.\end{aligned}\quad (4.17)$$

This can be used in Eq. 4.16 to obtain the  $\sigma_{\text{vis}}$  of the given luminometer,

$$\sigma_{\text{vis}} = 2\pi \Sigma_x \Sigma_y \frac{\bar{\mu}_{\text{vis}}(x_0, 0) \bar{\mu}_{\text{vis}}(0, y_0)}{\bar{\mu}_{\text{vis}}(x_0, y_0)}.\quad (4.18)$$

Since the horizontal and vertical scans are performed separately, the  $\bar{\mu}_{\text{vis}}(x_0, y_0)$  in the denominator is not measurable. Thus, the visible cross-section is determined using

$$\sigma_{\text{vis}} = 2\pi \Sigma_x \Sigma_y \frac{\bar{\mu}_{\text{vis}}(x_0, 0) \bar{\mu}_{\text{vis}}(0, y_0)}{\frac{1}{2} (\bar{\mu}_{\text{vis}}(x_0, 0) + \bar{\mu}_{\text{vis}}(0, y_0))}.\quad (4.19)$$

Once  $\sigma_{\text{vis}}$  is determined, it can be used in Eq. 4.2 to establish the absolute luminosity scale of a given luminometer, for a period of data taking that is close to the vdM scans. Typically, vdM scans at the LHC are performed once per colliding system per data-taking year.

In practice, the determination of  $\Sigma_{x,y}$  does not involve (numerically) computing the integrals in Eq. 4.17. Instead, the recorded scan curves are fit by Gaussian-like functions. In this thesis, Gaussians multiplied by  $N^{\text{th}}$  order polynomials, called GPN functions, have been investigated. The presence of the polynomials allows the fits to capture deformations in the scan curves with respect to simple Gaussians, due to effects that break the assumptions of the vdM formalism

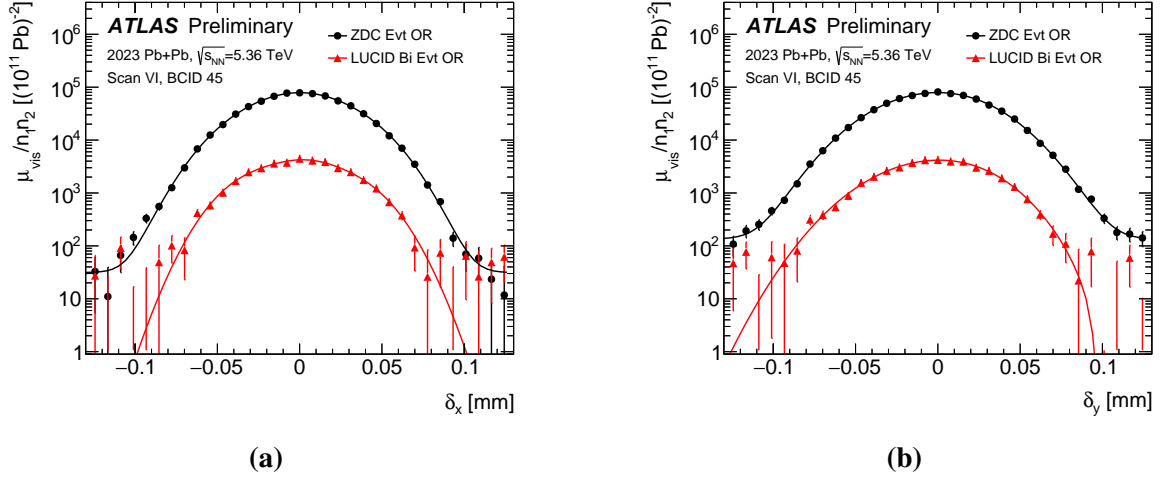


**Figure 4.1:** Specific visible event rate for one bunch measured using the ZDC EvtOR and LUCID BiEvtOR algorithms, versus beam separation during a (a) horizontal and (b) vertical vdM scan in Pb+Pb collisions [6]. Backgrounds arising due to noise, afterglow and beam-gas interactions are subtracted for LUCID, while only noise and afterglow backgrounds are subtracted for the ZDC. The error bars are statistical only. A GP4 fit is shown by the solid line.

(e.g. unexpected beam movement during the scans). These functions are defined as

$$\text{GPN}(\Delta x) = p_{0,x} \exp\left(-\frac{(\Delta x - \nu_x)^2}{2\sigma_x^2}\right) \left(1 + \sum_{k=2}^N \frac{c_k}{\Sigma'_x} \left(\frac{\Delta x - \nu_x}{\Sigma'_x}\right)^k\right), \quad (4.20)$$

for the horizontal scan as an example. Here,  $p_{0,x}$  is the peak specific visible event rate,  $\nu_x$  is the mean, and  $c_k$  are free polynomial coefficients. The convolved beam width  $\Sigma_x$  appears in

$$\Sigma'_x = \Sigma_x - \sum_{k \in \text{even}} (k-1)!! c_k, \quad (4.21)$$

where  $!!$  refers to the double factorial. The GPN function is defined in this manner so that the same quantity is obtained if  $\Sigma_x$  is treated as a fit parameter, or if Eq. 4.17 is used to obtain the convolved beam width. The free parameters of the GPN function are  $p_{0,x}$ ,  $\nu_x$ ,  $\Sigma_x$  and  $c_k$ .

Fits to vdM scan curves using GPN functions often yield good results (see Fig. 4.1). However, other Gaussian-like functions have also been considered in previous ATLAS vdM calibrations. For example, the Double Gaussian (DG) function, defined as

$$\text{DG}(\Delta x) = p_0 \frac{w}{\sqrt{2\pi}\sigma_{1,x}} \exp\left(-\frac{(\Delta x - \nu_{1,x})^2}{2\sigma_{1,x}^2}\right) + p_0 \frac{(1-w)}{\sqrt{2\pi}\sigma_{2,x}} \exp\left(-\frac{(\Delta x - \nu_{2,x})^2}{2\sigma_{2,x}^2}\right), \quad (4.22)$$

can also be used to fit vdM scan curves. Here,  $w \approx 1$  and  $\sigma_{1,x} < \sigma_{2,x}$  are usually enforced, so that the scan curve is given by the sum of a large amplitude narrow Gaussian, and a small amplitude wide Gaussian. The two means  $\nu_{1,x}$  and  $\nu_{2,x}$  can be forced to be identical.

## 4.2 Track-based luminosity measurement

The ATLAS luminosity algorithms introduced in Sec. 4.1.2 make use of special purpose sub-detectors, but it is also possible to measure luminosity with general purpose sub-detectors like the Inner Detector. Track-based luminosity measurement is a critical component of the ATLAS proton-proton luminosity measurement strategy [190], but was not studied in heavy ion collisions until the start of Run 3.

Unlike the LUCID, ZDC and BCM algorithms, track-based luminosity algorithms are offline algorithms, since the time required to reconstruct tracks exceeds the minimum latency for online algorithms. They cannot be used for luminosity measurement for every bunch crossing, due to the large data storage and compute resources that would be required. Thus, track-based luminosity algorithms make use of the unbiased trigger `HLT_lumipecb_L1RD0_FILLED` to reduce the recording rate. At Level-1, the `RD0_FILLED` item selects pseudo-random bunch crossings in which both beams have a filled bunch. At the HLT, `lumipecb` refers to a partial event building setup where only data from the Pixel and SCT sub-detectors are considered. No further selections are applied at the HLT.

### 4.2.1 Track selection

The reconstruction of tracks for luminosity measurement is similar to what is used for physics measurements, described earlier in Sec. 3.3.1, with the difference being that the Transition Radiation Tracker (TRT) is excluded from the reconstruction. In other words, only hits in the Pixel and SemiConductor Tracker (SCT) sub-detectors are used to reconstruct tracks.

Before the tracks can be used for luminosity measurement, they are required to pass a list of quality selections. The selections are applied on top of those considered by the `TightPrimary` working point (WP) [195], and are applied on the following variables:  $N_{\text{hits}}^{\text{Pix}}$  and  $N_{\text{hits}}^{\text{SCT}}$ , the number of hits in the Pixel and SCT sub-detectors, such that  $N_{\text{hits}}^{\text{Si}} = N_{\text{hits}}^{\text{Pix}} + N_{\text{hits}}^{\text{SCT}}$ ; the number of holes in the Pixel and SCT sub-detectors,  $N_{\text{holes}}^{\text{Pix}}$  and  $N_{\text{holes}}^{\text{SCT}}$ , such that  $N_{\text{holes}}^{\text{Si}} = N_{\text{holes}}^{\text{Pix}} + N_{\text{holes}}^{\text{SCT}}$ ; the number of hits in the first two layers of the Pixel sub-detector,  $N_{\text{hits}}^{\text{IBL}}$  and  $N_{\text{hits}}^{\text{B-Layer}}$ ; the number of Pixel and SCT modules shared between tracks,  $N_{\text{sh. mod.}}^{\text{Pix}}$  and  $N_{\text{sh. mod.}}^{\text{SCT}}$ , such that  $N_{\text{sh. mod.}}^{\text{Si}} = N_{\text{sh. mod.}}^{\text{Pix}} + N_{\text{sh. mod.}}^{\text{SCT}}/2$  (the number of shared SCT modules is halved due to the double-sided geometry of the SCT strips).

With this nomenclature, the specific selections are:

- $N_{\text{hits}}^{\text{Si}} \geq 9$  for  $|\eta| \leq 1.65$ , and  $N_{\text{hits}}^{\text{Si}} \geq 11$  for  $|\eta| > 1.65$ . Since there are four Pixel layers (including the IBL) and four SCT layers of double sided strips, a track that passes straight through all silicon layers is expected to produce twelve hits on average. This requirement therefore ensures that the tracks selected for luminosity measurement have a good probability of originating from the interaction point.
- $N_{\text{sh. mod.}}^{\text{Si}} \leq 1$ . This ensures that the reconstructed tracks in the event are well separated from each other.

- $N_{\text{hits}}^{\text{IBL}} + N_{\text{hits}}^{\text{B-Layer}} > 0$ , if hits are expected in the IBL or B-Layer. This assures that the tracks are of good quality, since the innermost Pixel layers offer good tracking performance due to their proximity to the interaction point.
- $N_{\text{holes}}^{\text{SCT}} \leq 2$  and  $N_{\text{holes}}^{\text{Pix}} = 0$ , which improves the quality of the tracks.

In order to study the impact of the selections described, a number of alternative WPs were defined. The following variables were investigated:  $N_{\text{holes}}^{\text{Pix}}$ ; the minimum transverse momentum  $p_{\text{T}}^{\text{min}}$ , and the significance of the transverse impact parameter,  $|d_0/\sigma_{d_0}|$ . The WPs considered in this study are shown in Tab. 4.1.

Working Point	$p_{\text{T}}^{\text{min}}$ (MeV)	$ d_0/\sigma_{d_0} $	$N_{\text{holes}}^{\text{Pix}}$
Tight500	500	–	= 0
Tight900	900	–	= 0
Tight500Lumi	500	< 7	= 0
Tight900Lumi	900	< 7	= 0
TightModFullEta500	500	–	≤ 1
TightModFullEta900	900	–	≤ 1
TightModFullEta500Lumi	500	< 7	≤ 1
TightModFullEta900Lumi	900	< 7	≤ 1

**Table 4.1:** Summary of track working points defined for the study of track-based luminosity measurement in Pb+Pb collisions.

### 4.2.2 Track-based luminosity algorithms

Two track-based luminosity algorithms have been investigated for Pb+Pb collisions. The first algorithm, called track counting (TC), is a type of particle counting algorithm. The visible pileup is defined as the first moment of the track multiplicity, i.e.

$$\mu_{\text{vis}}^{\text{TC}} = E[N_{\text{trk}}] = \frac{1}{N_{\text{evt}}} \sum_{i=1}^{N_{\text{evt}}} N_{\text{trk}}^i, \quad (4.23)$$

where the number of tracks per event,  $N_{\text{trk}}^i$ , is counted for a total of  $N_{\text{evt}}$  events. Each  $N_{\text{trk}}^i$  is treated as a random variable that is uncorrelated between events. Further, it is assumed that each event in the sum has the same underlying pileup.

In the  $N_{\text{evt}} \rightarrow \infty$  limit, the central limit theorem can be applied, which states the uncertainty of  $\mu_{\text{vis}}^{\text{TC}}$  can be expressed as

$$\Delta\mu_{\text{vis}}^{\text{TC}} = \sqrt{\frac{1}{N_{\text{evt}}} (E[(N_{\text{trk}})^2] - E[N_{\text{trk}}]^2)}, \quad (4.24)$$

$$= \sqrt{\frac{1}{N_{\text{evt}}} \left( \sum_{i=1}^{N_{\text{evt}}} (N_{\text{trk}}^i)^2 / N_{\text{evt}} - \left( \sum_{i=1}^{N_{\text{evt}}} N_{\text{trk}}^i / N_{\text{evt}} \right)^2 \right)}. \quad (4.25)$$

The TC algorithm has been used extensively in proton-proton luminosity studies, where the (assumed) linearity of  $\mu_{\text{vis}}^{\text{TC}}$  with the true pileup  $\mu$  has been utilized. It has been used to correct for the non-linearity of the LUCID hit counting algorithms at high  $\mu$ , and to check the time-stability of the luminosity calibration of other algorithms.

The second algorithm under consideration is track-based event counting (EC), which is a type of event counting algorithm, where events are accepted based on the presence of tracks. Suppose that out of  $N_{\text{evt}}$  recorded events, only a fraction  $f$  contain tracks passing a given selection. The number of accepted events is defined by  $N_{\text{pass}} = f \cdot N_{\text{evt}}$ . Using the methodology of event counting algorithms described in Sec. 4.1.2, the visible pileup is given by

$$\mu_{\text{vis}}^{\text{EC}} = -\log(1 - f). \quad (4.26)$$

The statistical uncertainty of  $\mu_{\text{vis}}^{\text{EC}}$  arises from the uncertainty of  $N_{\text{pass}}$ , which is assumed to be a binomial random variable. This gives

$$\Delta\mu_{\text{vis}}^{\text{EC}} = \sqrt{\frac{f}{N_{\text{evt}}(1 - f)}}. \quad (4.27)$$

The relative statistical uncertainty for event counting,  $\Delta\mu_{\text{vis}}^{\text{EC}}/\mu_{\text{vis}}^{\text{EC}}$ , diverges as  $f \rightarrow 0$  and  $f \rightarrow 1$ , so it is not beneficial to define an event counting condition that encounters this regime. In the low pileup conditions of heavy ion collisions at the LHC, it is beneficial to accept an event if it has at least one track passing a given selection, i.e.  $N_{\text{trk}}^i \geq 1$ .

### 4.2.3 Algorithm performance

Before the track-based luminosity algorithms described above can be used for measurement in Pb+Pb collisions, it is important to characterize the performance of the available WPs. In particular, the WP that provides the best (i.e. smallest) statistical uncertainty must be identified.

The performance of the algorithms was quantified in terms of the relative statistical uncertainty per luminosity block (LB), and was investigated in the 2023 Pb+Pb dataset in LHC Fill 9212, where the CMS experiment performed van der Meer scans. During this time, the ATLAS experiment recorded Pb+Pb collision events at around 25% of the maximum instantaneous luminosity, which was achieved through a partial separation of the beams. The trigger rate was approximately 67 kHz, which provided a large sample to investigate track-based luminosity measurement.

In Fig. 4.2a, the impact of the `Lumi` (i.e.  $|d_0/\sigma_{d_0}| < 7$ ) selection was investigated for the TC and EC algorithms. A negligible impact was observed in the relative statistical uncertainty of the TC algorithm, while the EC algorithm is unaffected. The impact of the `ModFullEta` (i.e.  $N_{\text{holes}}^{\text{Pix}} \leq 1$ ) selection was investigated in Fig. 4.2b. The relative statistical uncertainty of the EC algorithm is once again unaffected, while the TC algorithm was observed to have a slightly better precision without the `ModFullEta` requirement. This could be due to the

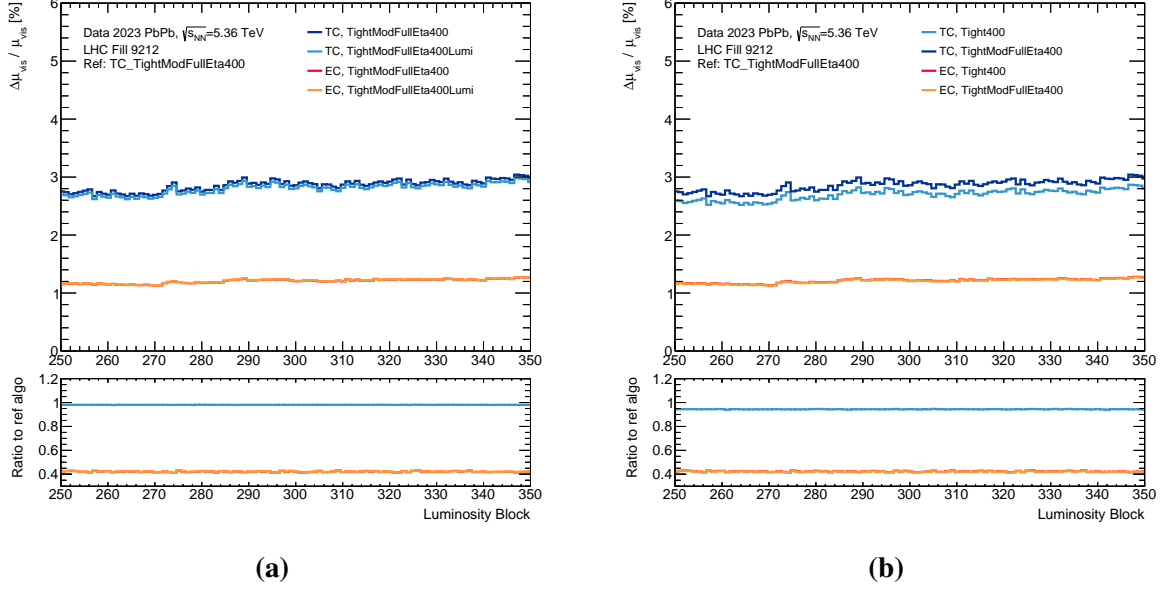


**Figure 4.2:** Relative statistical uncertainty of  $\mu_{\text{vis}}$  for various track counting and event counting algorithms, during 100 LBs in LHC Fill 9212. In Fig. (a), the Lumi selection is varied, and in fig. (b) the ModFullEta selection is varied. The lower panel shows a ratio of the relative statistical uncertainties to a reference algorithm, which is highlighted in the upper panel.

larger spread in the track multiplicity distribution when poor quality tracks are considered.

The impact of the different  $p_{\text{T}}^{\text{min}}$  selections under consideration, i.e. 400, 500 and 900 MeV, is shown in Fig. 4.3. The statistical precision of the EC algorithm is observed to improve with decreasing  $p_{\text{T}}^{\text{min}}$ . This is attributed to an increase in the acceptance fraction  $f$ , which decreases the relative statistical uncertainty, since  $f$  is  $\mathcal{O}(10^{-3})$  for Pb+Pb collisions. Interestingly, the statistical precision of the TC algorithm is found to improve with increasing  $p_{\text{T}}^{\text{min}}$ .

The  $p_{\text{T}}$ -dependence of the behavior of the TC algorithm can be explained as follows. In a measurement of the centrality-dependence of the  $dN_{\text{trk}}/dp_{\text{T}}$  spectrum in Pb+Pb collisions at  $\sqrt{s_{\text{NN}}} = 5.02$  TeV by the ALICE collaboration [196], the growth rate of  $dN_{\text{trk}}/dp_{\text{T}}$  as  $p_{\text{T}} \rightarrow 0$  was found to monotonically decrease when going from central collisions to peripheral collisions, particularly in the 0.5-2.0 GeV track  $p_{\text{T}}$  region. This indicates that when the  $p_{\text{T}}^{\text{min}}$  threshold is reduced, the increase in number of tracks is predominantly from central collisions. As a consequence, the spread of the track multiplicity distribution grows at a faster rate than the mean track multiplicity, resulting in a decrease of the performance of the TC algorithm.

From these studies, it was concluded that best performing TC algorithm was based on the TightModFullEta900Lumi working point, while the best performing EC algorithm was based on the TightModFullEta400 working point. Overall, the statistical precision of the EC algorithms is a factor of two better than the TC algorithms. Thus, the EC algorithm with the TightModFullEta400 working point was chosen as the preferred track-based luminosity algorithm.

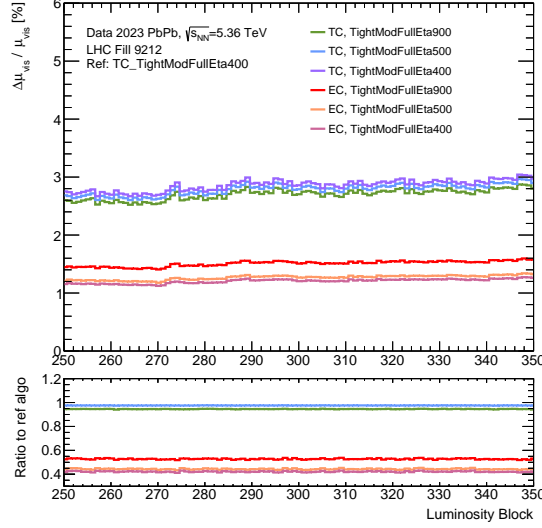


**Figure 4.3:** Same as in Fig. 4.2, but with varying  $p_T^{\min}$ .

### 4.3 Luminosity calibration of the 2023 Pb+Pb dataset

This section describes a preliminary calibration of the luminosity of the 2023 Pb+Pb dataset recorded by ATLAS, through an analysis of van der Meer scans. The primary luminosity algorithm under consideration is LUCID BiEvtOR, which has statistical uncertainties on the  $\mu_{\text{vis}}$  determined per luminosity-block of typically below 0.1%.

#### 4.3.1 Scan sequence

An overview of the 2023 Pb+Pb van der Meer scan program is shown in Fig. 4.4. Six on-axis scans and one two-dimensional grid scan were performed over three separate LHC fills. In Fill 9209, which had 374 bunches colliding in ATLAS, the on-axis Scans I, III, and IV were performed, along with a two-dimensional grid scan called Scan II; in Fill 9217 the on-axis Scan V was performed with 204 colliding bunches; in Fill 9218 the on-axis scans VI and VII were performed with 506 colliding bunches.

The parameters of the beams in these fills were identical to those during normal physics data taking. They had a minimum bunch spacing of 50 ns, a vertical half-crossing angle of  $170 \mu\text{rad}$  to reduce unwanted long-range collisions, and reached  $\beta^* = 50 \text{ cm}$  at the ATLAS interaction point. During the ATLAS vdM scans, the beams were partially separated at the other interaction points so as to minimize the loss in beam intensity due to collisions.

In order to achieve the required crossing angle and beam separations for Pb+Pb van der Meer scans, a *closed orbit bump* was activated at the ATLAS interaction point, which is a perturbation of the beam orbit at a localized point that does not affect the orbit in the rest of the ring. It can be achieved using four *corrector* or *steering* dipole magnets. For the purpose of vdM scans, four dipoles are required per beam and separation direction [101].



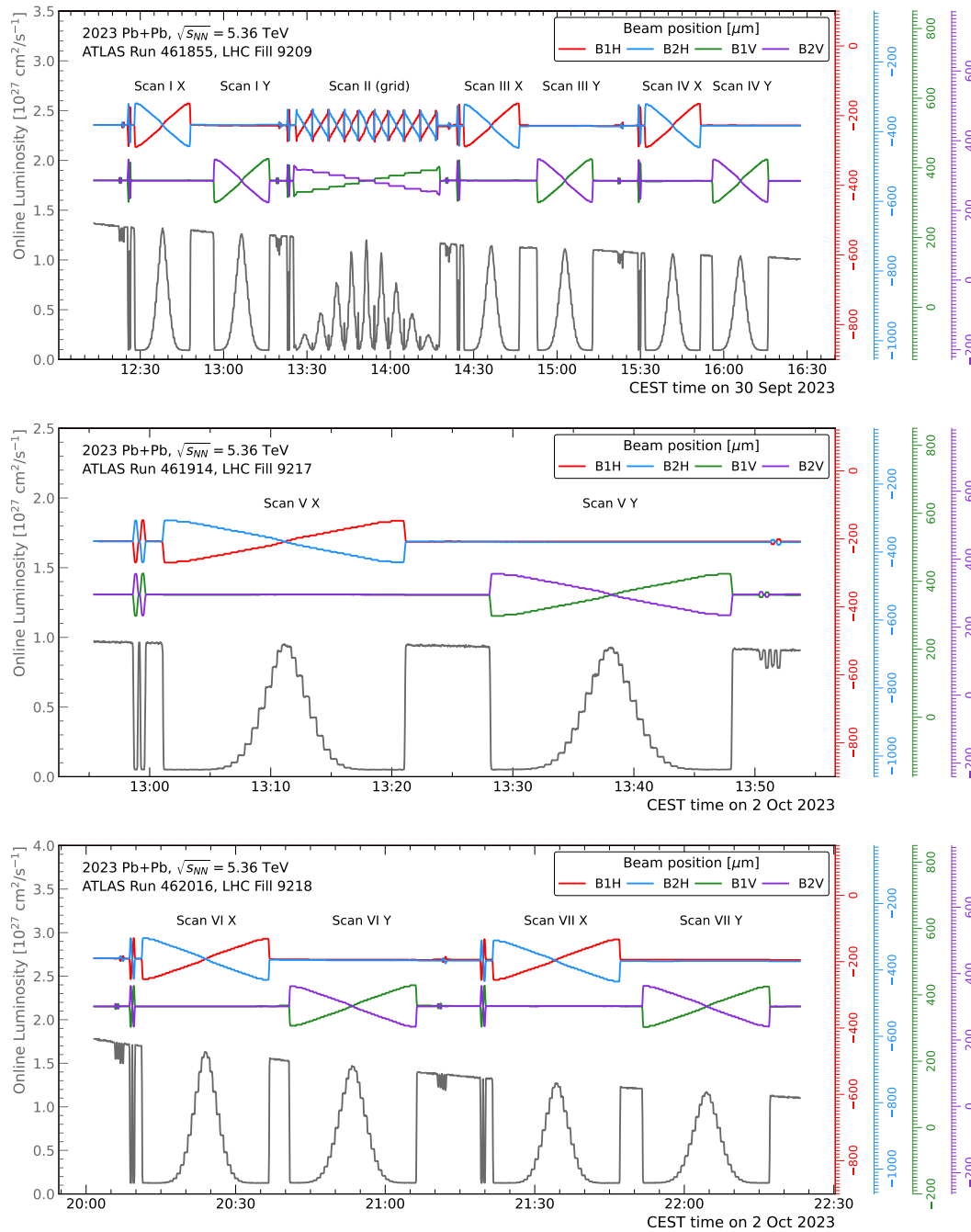


**Figure 4.4:** Sequence of the 2023 Pb+Pb van der Meer scans in LHC Fills 9209 (top), 9217 (middle) and 9218 (bottom). The online LUCID BiEvtOR luminosity is shown on the left side of the figures. The DOROS beam positions are shown on the right side of the figures, and in the legends, with “1” and “2” denoting the two beams, and “H” and “V” denoting the horizontal and vertical positions respectively.



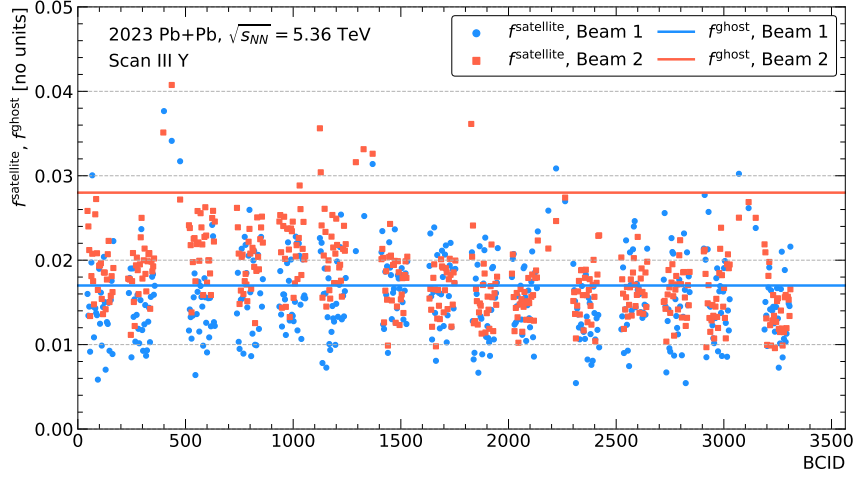


**Figure 4.5:** Ghost and satellite fractions at the peak of Scan III Y for all colliding BCIDs.

### 4.3.2 Bunch population measurement

The first step of the vdM calibration is to determine the bunch population product  $n_1 n_2$  for each colliding bunch. As mentioned in Sec. 3.1.3, the Fast Beam Current Transformer (FBCT), Direct Current Current Transformer (DCCT) and Beam Pickup Timing system (BPTX) systems are used to determine the bunch currents. The DCCT provides a measurement of the intensity of the full beam, while the FBCT and BPTX provide per-bunch readings.

All of these systems are sensitive to ghost and satellite charges, which must be subtracted from the bunch current measurements. During the 2023 Pb+Pb vdM scans, the ghost and satellite fractions were found by the Longitudinal Density Monitor (LDM) to be  $\mathcal{O}(1\%)$ . The measured ghost and satellite fractions for Scan III Y are shown, as an example, in Fig. 4.5.

For a given beam  $i$  and BCID (bunch crossing ID)  $j$ , the bunch population is given by

$$n_{ij} = \frac{N_{ij} N_i^{\text{DCCT}}}{Z_{\text{Pb}} \sum_j N_{ij}} \left(1 - f_i^{\text{ghost}}\right) \left(1 - f_{ij}^{\text{satellite}}\right), \quad (4.28)$$

where  $N_{ij}$  is the reading provided by the FBCT or BPTX,  $Z_{\text{Pb}} = 82$  converts the measured bunch currents into bunch populations,  $f_i^{\text{ghost}}$  is the fraction of ghost charge, and  $f_{ij}^{\text{satellite}}$  is the fraction of satellite charge at the given BCID. Since the DCCT measurement of the total beam intensity is believed to be more reliable than the sum of FBCT readings over all colliding bunches, the DCCT reading  $N_i^{\text{DCCT}}$  appears as an additional normalization to  $\sum_j N_{ij}$ .

The per-BCID bunch population measurements from the FBCT readings are treated as the nominal ones; the BPTX readings are used to define a systematic uncertainty. However, it was found that in Fill 9209, the  $\sigma_{\text{vis}}$  obtained through the BPTX and FBCT readings systematically differed by roughly 4% for around one quarter of all colliding bunches. In particular, the difference was found to be in almost every “fourth-in-sub-train” bunch, as shown in Fig. 4.6. For this reason, the BPTX readings are taken as the nominal ones in Scans I to IV.

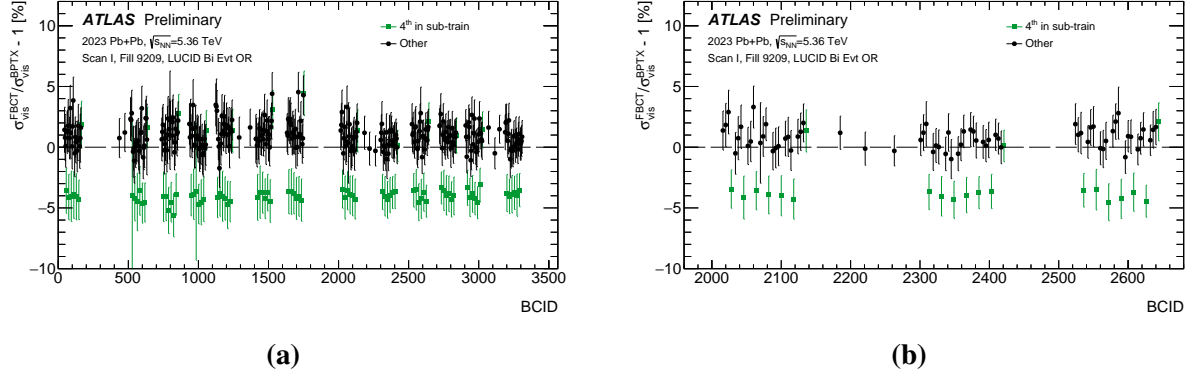


**Figure 4.6:** Difference in the  $\sigma_{vis}$  obtained using the FBCT and BPTX systems, for the LUCID BiEvtOR algorithm in Scan I [6]. The pattern of colliding bunches consisted of “trains” of 28 bunches, each consisting of seven “sub-trains” of four bunches separated by 50 ns. Ten bunches separated by at least 100 ns from other colliding bunches were also present. Fig. (a) shows all colliding bunches, while fig. (b) highlights a selection of three trains.

In the Run 2 luminosity calibrations, the uncertainty on the ghost and satellite fractions was determined by comparing the LDM results to those obtained by the LHCb experiment [194]. In the LHCb method, an inert gas like neon is injected into a vacuum chamber around the LHCb interaction point, such that the beam particles can collide with the gas nuclei. The resulting beam-gas vertices are easily identified, since they are longitudinally well separated from primary collision vertices. By comparing the rate of beam-gas vertices reconstructed in empty and unpaired BCIDs, the ghost and satellite fractions can be determined. At the time of preparing the preliminary 2023 Pb+Pb vdM calibration, the LHCb determination of the ghost and satellite charges was not available. Thus, a conservative uncertainty of 1.0% was set on the LDM determination of the ghost and satellite fractions, based on experience from proton-proton vdM calibrations in Run 3 [197].

The uncertainty on the bunch charge fraction was evaluated by comparing the bunch-averaged  $\sigma_{vis}$  values obtained using the FBCT and BPTX readings, the results of which are shown in Tab. 4.2. No corrections are applied, besides ghost and satellite corrections, and background subtraction. The largest absolute single-scan difference in the bunch-averaged  $\sigma_{vis}$  values is taken to be the uncertainty. In addition, an uncertainty of 0.28% on the calibration of the absolute DCCT scale was also considered in the total uncertainty on the bunch charge measurement [198].

Scan I	Scan III	Scan IV	Scan V	Scan VI	Scan VII
–	–	–	+0.12%	+0.19%	<b>+0.27%</b>

**Table 4.2:** Summary of bunch charge fraction comparison (FBCT vs BPTX) for all on-axis scans, for the LUCID BiEvtOR algorithm. The largest single-scan difference (Scan VII) is highlighted. Due to the issues with the FBCT measurements in Fill 9209, the comparison was not done for Scans I, III and IV.

### 4.3.3 Background subtraction

The data recorded by luminometers contains signals from colliding bunches, as well as other undesirable signals that are collectively called backgrounds. There are three sources of backgrounds to consider:

- **Noise:** purely instrumental noise that contributes to the observed event rate. In low-luminosity conditions, such as in heavy ion collisions, the LUCID bismuth calibration source introduces a large noise floor to all LUCID algorithms.
- **Beam-gas:** due to imperfect vacuum conditions in the beampipe around the interaction point, the bunches in the LHC may collide with residual gas particles, resulting in the production of additional signals.
- **Afterglow:** refers to luminometer signals that originate in preceding bunch crossings. In particular, the decays of long-lived particles and of radiologically activated detector material contributes to afterglow.

The noise background is assumed to be independent of bunch intensity, and is defined as the event rate in the BCID preceding a colliding BCID. This definition also includes the contribution from the (smaller) afterglow background. Since the two are inseparable, they are subtracted simultaneously.

The noise+afterglow background subtraction is applied for a colliding BCID  $N$  by a subtraction of the event rate in the  $(N - k)^{\text{th}}$  BCID, before normalizing by the bunch population product. Even though the noise+afterglow background is found to be independent of beam separation, in practice it is subtracted in a separation-dependent manner, i.e.

$$[\mu_{\text{vis}}(\Delta r)]_N \rightarrow [\mu_{\text{vis}}(\Delta r)]_N - [\mu_{\text{vis}}(\Delta r)]_{N-k}. \quad (4.29)$$

where  $\Delta r$  denotes  $\Delta x$  and  $\Delta y$  for the horizontal and vertical scans respectively. Here, the bracket notation indicates the BCID. For the 2023 Pb+Pb calibration,  $k = 1$  is taken for the nominal noise+afterglow background subtraction.

The method for subtracting the beam-gas background in proton-proton vdM calibrations involves a per-scan step subtraction of the determined beam-gas collision rate. This can introduce undesirable statistical fluctuations in the tails of the scan curves, especially in low luminosity conditions like heavy ion collisions. Thus, an alternate procedure was considered, which is specific to heavy ion vdM calibrations.

For a given beam  $i$  and unpaired bunch  $j$ , the quantity

$$[\bar{\mu}_{\text{vis}}(\Delta r)]_{ij} = \frac{[\mu_{\text{vis}}(\Delta r)]_j - [\mu_{\text{vis}}(\Delta r)]_{j-k}}{n_{ij}} \quad (4.30)$$

is calculated for every step in the vdM scans. Essentially, this is the specific visible event rate for the unpaired bunch  $j$ , with a  $(j - k)$  noise+afterglow subtraction applied. In the 2023 Pb+Pb vdM fills, some paired BCIDs were immediately followed by unpaired BCIDs. In order to avoid cross-contamination with the luminosity in the paired bunches,  $k = 2$  is chosen for the beam-gas rate determination.

Ideally, the rate of beam-gas collisions should be independent of beam separation. This is examined by fitting  $[\bar{\mu}_{\text{vis}}(\Delta r)]_{ij}$  with constant functions. If the constant function describes the data well, this results in a beam separation-averaged specific visible event rate  $\langle [\bar{\mu}_{\text{vis}}]_{ij} \rangle$  for all unpaired bunches in both beams.

The rate of beam-gas collisions should also be identical for all unpaired bunches. This is tested by fitting  $\langle [\bar{\mu}_{\text{vis}}]_{ij} \rangle$  versus BCID with a constant function for both beams. If the fits describe the data well, the fit results then define the beam-gas rate  $R_{1,2}$  for the two beams. Finally, the beam-gas background can be subtracted using a bunch population-weighted average of the two beam-gas rates, i.e. for a colliding BCID  $N$ ,

$$[\bar{\mu}_{\text{vis}}]_N \rightarrow [\bar{\mu}_{\text{vis}}]_N - \frac{n_{1N}R_1 + n_{2N}R_2}{n_{1N}n_{2N}}. \quad (4.31)$$

For the LUCID BiEvtOR algorithm, the noise+afterglow background is typically around 10% of the peak specific visible event rate. The beam-gas background is much smaller, typically less than 1% of the peak rate.

The systematic uncertainties on the two background sources are evaluated separately, reflecting the different subtraction methodologies. In both cases, the ghost and satellite fraction corrections were applied before the uncertainties were determined.

The uncertainty on the noise+afterglow subtraction was determined by comparing the nominal bunch-averaged  $\sigma_{\text{vis}}$ , which used the  $(N - 1)$  subtraction procedure, to the result obtained by using  $(N - 2)$  and  $(N - 3)$  background subtraction. The nominal beam-gas rates were used for the beam-gas subtraction, which is left enabled in this determination. Tab. 4.3 summarizes the obtained results for all six on-axis scans. As mentioned in Sec. 4.3.1, Scans VI and VII were performed in a physics fill with 50 ns bunch spacing, so the evaluation of the noise+afterglow subtraction systematic uncertainty cannot be performed in these scans. The largest absolute single-scan difference in the bunch-averaged  $\sigma_{\text{vis}}$  is taken to be the uncertainty.

Subtraction	Scan I	Scan III	Scan IV	Scan V	Scan VI	Scan VII
$N - 2$	-0.01%	-0.05%	-0.03%	+0.00%	-	-
$N - 3$	- <b>0.38%</b>	-0.38%	-0.22%	-0.23%	-	-

**Table 4.3:** Noise+afterglow background subtraction uncertainties for all on-axis scans, for the LUCID BiEvtOR algorithm. The largest single-scan difference (Scan I) is highlighted.

The uncertainty on the beam-gas subtraction is determined by comparing the nominal bunch-averaged  $\sigma_{\text{vis}}$  obtained using the GP 4 fit function, to the result obtained by disabling the

beam-gas subtraction and fitting the scan curves with a `GP4+const` fit function, i.e. including a separation-independent offset term. The noise+afterglow subtraction is enabled during this procedure. The largest absolute single-scan difference in the bunch-averaged  $\sigma_{\text{vis}}$  is taken to be the uncertainty. Tab. 4.4 summarizes the obtained results for all six on-axis scans.

Scan I	Scan III	Scan IV	Scan V	Scan VI	Scan VII
-0.29%	-0.51%	-0.39%	-0.32%	-0.38%	<b>-0.61%</b>

**Table 4.4:** Beam-gas background subtraction uncertainties for all on-axis scans, for the LUCID BiEvtOR algorithm. The largest single-scan difference (Scan VII) is highlighted.

#### 4.3.4 Bunch current offset correction

The visible event rate observed by a luminometer is proportional to the bunch population product  $n_1 n_2$ . Thus, the specific visible event rate, and in turn  $\sigma_{\text{vis}}$  as defined by Eq. 4.19, should be independent of  $n_1 n_2$ . However, small dependencies of unknown origin of  $\sigma_{\text{vis}}$  on  $n_1 n_2$  have been observed in Run 2 vdM calibrations [190]. This dependency could be attributed to potential non-linearities in the FBCT and BPTX readings, which are in general some function of the true bunch populations.

The exact form of the non-linearity is not known, but a simplistic model can be defined, which assumes that the FBCT readings are faithful around the average bunch population in the fill. Then, the bunch population for given beam  $i$  and bunch  $j$  can be modified into

$$n_{ij} \rightarrow n_{ij} + b_i (n_{ij} - \bar{n}_i), \quad (4.32)$$

where  $b_i$  are two offset parameters that create the non-linearity, and  $\bar{n}_i$  are the average bunch population. The average of the modified bunch populations is simply  $\bar{n}_i$ . Then, the corrected per-bunch visible cross-sections, denoted by  $[\sigma_{\text{vis}}^{\text{corr}}]_j$ , are obtained by minimizing

$$\chi^2 = \sum_j \frac{\left( [\sigma_{\text{vis}}^{\text{corr}}]_j \left( \frac{n_{1j} + b_1(n_{1j} - \bar{n}_1)}{n_{1j}} \right) \left( \frac{n_{2j} + b_2(n_{2j} - \bar{n}_2)}{n_{2j}} \right) - [\sigma_{\text{vis}}^{\text{uncorr}}]_j \right)^2}{\left( [\Delta\sigma_{\text{vis}}^{\text{uncorr}}]_j \right)^2}, \quad (4.33)$$

where the sum runs over all colliding bunches, and  $[\sigma_{\text{vis}}^{\text{uncorr}}]_j$  are the uncorrected visible cross-sections with uncertainties  $[\Delta\sigma_{\text{vis}}^{\text{uncorr}}]_j$ .

The bunch current offset correction was found to remove dependencies of  $\sigma_{\text{vis}}$  on  $n_1 n_2$  in the 2023 Pb+Pb vdM scans as expected. An example of the impact of the correction is shown in Fig. 4.7, where the ghost and satellite fraction corrections were applied, along with the background subtraction. The bunch current offset correction was also found to reduce the RMS of the per-bunch  $\sigma_{\text{vis}}$  values in all on-axis scans by around 0.1%.

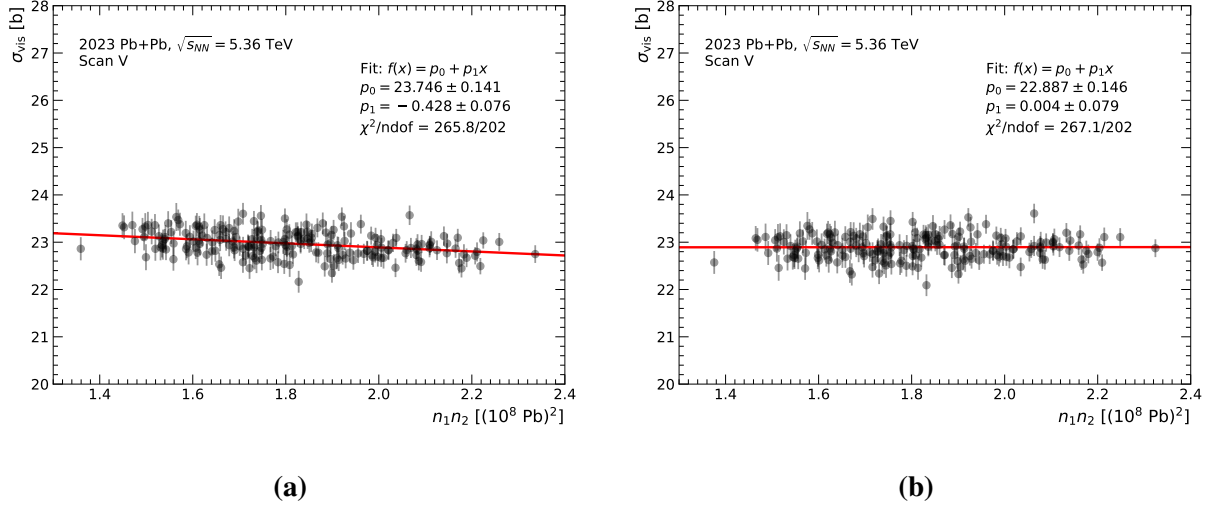


**Figure 4.7:**  $\sigma_{\text{vis}}$  determined in Scan V for the LUCID BiEvtOR algorithm, versus  $n_1 n_2$  determined using the FBCT readings, (a) before and (b) after the bunch current offset correction. Straight line fits show the impact of the correction.

### 4.3.5 Fit model

Ideally, the choice of fit function in the vdM calibration should not affect the extracted  $\sigma_{\text{vis}}$ . If a large deviation is observed between the results obtained from multiple fit functions, it should be treated as a systematic uncertainty. This is tested by comparing the bunch-averaged  $\sigma_{\text{vis}}$  obtained with GP0, GP2 and GP6 fit functions, to the nominal GP4 fit function. The largest absolute single-scan difference in the bunch-averaged  $\sigma_{\text{vis}}$  for the LUCID BiEvtOR algorithm across all fit functions was taken to be the uncertainty. Tab. 4.5 summarizes the obtained results for all six on-axis scans. The background subtraction, and ghost and satellite fraction corrections were applied before the fit model uncertainty was determined.

Fit model	Scan I	Scan III	Scan IV	Scan V	Scan VI	Scan VII
GP 0	+0.15%	+0.20%	+0.15%	-0.16%	+0.23%	+0.18%
GP 2	+0.44%	+0.61%	+0.63%	+0.47%	+0.56%	+0.60%
GP 6	+0.56%	+0.70%	+0.72%	+0.52%	-0.64%	<b>-0.82%</b>

**Table 4.5:** Fit model comparisons for all on-axis scans, with respect to the nominal GP 4 fit model, for the LUCID BiEvtOR algorithm. The largest single-scan difference (Scan VII, GP 6) is highlighted.

### 4.3.6 Specific luminosity

The peak specific visible event rate observed by a luminometer depends on the efficiency and acceptance of the detector and algorithm. However, every luminometer should, in principle, measure the same convolved beam widths. In particular, the *specific luminosity*, defined by

$$\mathcal{L}_{\text{sp}} = \frac{f_r}{2\pi \Sigma_x \Sigma_y}, \quad (4.34)$$

should be identical for every luminometer. Any deviations in  $\mathcal{L}_{\text{sp}}$  between algorithms is then treated as a systematic uncertainty. This was investigated by comparing the bunch-averaged  $\mathcal{L}_{\text{sp}}$  between LUCID BiEvtOR and all other algorithms described in Sec. 4.1.2. The nominal  $\mathcal{L}_{\text{sp}}$  for each algorithm was used in the comparison, which includes the background subtraction, and the ghost and satellite fraction corrections. The beam-gas rates were determined for each algorithm and scan separately.

Fig. 4.8 summarizes the results obtained in this comparison. The largest single-scan deviation in the specific luminosity is used to define the systematic uncertainty.

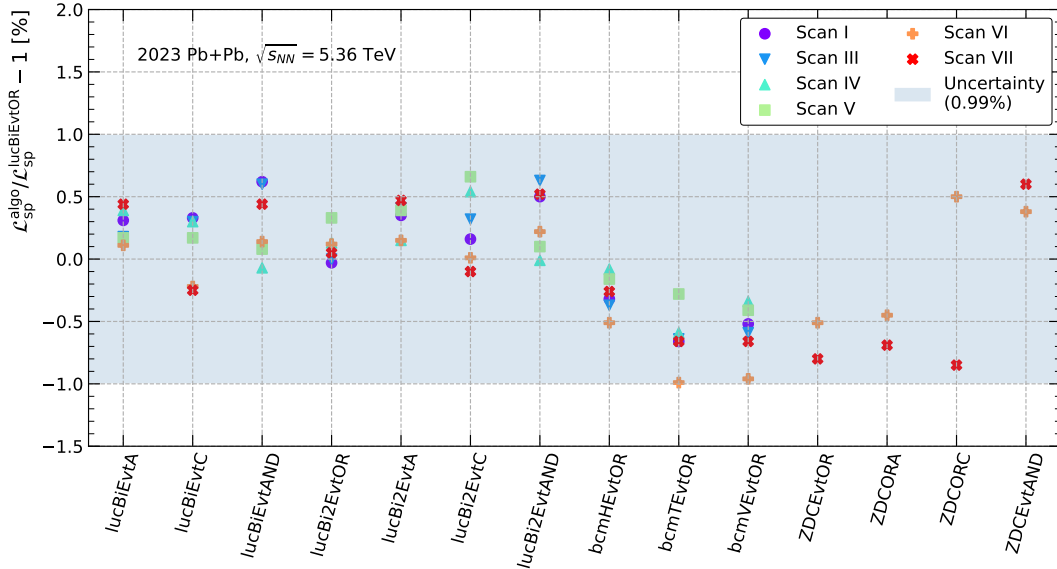


**Figure 4.8:** Summary of specific luminosity differences (in percent) between various algorithms and LUCID BiEvtOR, for all on-axis scans. The shaded region denotes the uncertainty on the specific luminosity.

### 4.3.7 Orbit drift correction

During vdM scans, it is critical that the beams are at the expected positions set by the corrector magnets. Environmental effects like temperature and pressure variations can affect the magnet performance, resulting in a change of the beam orbit. Ground movement and tidal effects can change the alignment of the accelerator components, causing additional orbit perturbations. Other machine-driven sources of orbit changes, like heating in the magnets, or misbehaving cryogenics, can also cause issues during vdM scans.

Collectively, these effects are referred to as *orbit drift*. If the beams drift in the direction of the scanning plane, the scan curves either widen or narrow, depending on if the time-dependence of the drift is positive or negative. If the beams drift in the direction of the non-scanning plane, a pair of orthogonal scans are effectively taken at an angle tilted with respect to the lab frame. Thus, both kinds of drifts affect the fits to the scan curves, and consequently the extracted visible cross-sections.

The beam positions during vdM scans are monitored using the DOROS and arc BPMs, as explained in Sec. 3.1.3. The DOROS BPMs are placed within the ATLAS orbit bump, so they can measure the beam displacements during the scans. The arc BPMs are placed outside the orbit bump, so their beam position readings are obtained by extrapolating to the ATLAS interaction point.

The effect of in-plane orbit drift is accounted for by a shift of the beam separation scale in the scan curves. For the horizontal scan, this takes the form

$$\Delta x_{\text{corr}}(t) = \Delta x_{\text{nominal}}(t) + \delta x_1(t) - \delta x_2(t), \quad (4.35)$$

where  $\Delta x_{\text{corr}}$  and  $\Delta x_{\text{nominal}}$  are the corrected and uncorrected beam separations respectively, and  $\delta x_{1,2}$  are the deviations of the measured beam positions with respect to their set positions, i.e.  $\delta x_{1,2} = 0$  when there is no orbit drift. This correction can be applied for every scan step, but for simplicity, it is applied based on a linear interpolation between the  $(\delta x_1 - \delta x_2)$  values immediately before and after a scan. A definition similar to Eq. 4.35 exists for the vertical scan, by replacing  $x$  with  $y$ .

Suppose the nominal vdM scan curves,  $\bar{\mu}_{\text{vis}}(\Delta x_{\text{nominal}})$  and  $\bar{\mu}_{\text{vis}}(\Delta y_{\text{nominal}})$ , are fit with functions  $f_x(\Delta x_{\text{nominal}})$  and  $f_y(\Delta y_{\text{nominal}})$  respectively, which are maximized at  $\nu_x$  and  $\nu_y$ . According to Eq. 4.19, the visible cross-section is

$$\sigma_{\text{vis}} = 2\pi \Sigma_x \Sigma_y \frac{f_x(\nu_x) f_y(\nu_y)}{\frac{1}{2}(f_x(\nu_x) + f_y(\nu_y))}. \quad (4.36)$$

where  $\Sigma_{x,y}$  are the widths of  $f_{x,y}$ . After applying the in-plane orbit drift correction, the scan curves are fit again, resulting in functions  $f'_x(\Delta x_{\text{corr}})$  and  $f'_y(\Delta y_{\text{corr}})$ . These “primed” functions have widths  $\Sigma'_{x,y}$  and are maximized at  $\nu'_{x,y}$ . The  $\Sigma'_{x,y}$  now represent the convolved beam widths corrected for in-plane orbit drift.

Since the horizontal and vertical scans in a vdM scan pair are not performed simultaneously, the denominator of Eq. 4.36 is underestimated in the presence of out-of-plane orbit drifts. Suppose the time at which the horizontal and vertical scans are at the midpoint scan steps are  $\hat{t}_x$  and  $\hat{t}_y$  respectively. The quantities

$$\begin{aligned} \Delta H &= (\delta x_1(\hat{t}_y) - \delta x_2(\hat{t}_y)) - (\delta x_1(\hat{t}_x) - \delta x_2(\hat{t}_x)), \\ \Delta V &= (\delta y_1(\hat{t}_x) - \delta y_2(\hat{t}_x)) - (\delta y_1(\hat{t}_y) - \delta y_2(\hat{t}_y)), \end{aligned} \quad (4.37)$$

are computed, which quantify the out-of-plane drift in between the peaks of the horizontal and vertical scans. The  $\sigma_{\text{vis}}$  equation, including a correction for out-of-plane orbit drifts, then becomes

$$\sigma_{\text{vis}} = 2\pi \Sigma'_x \Sigma'_y \frac{f_x(\nu_x) f_y(\nu_y)}{\frac{1}{2}(f_x(\Delta H) + f_y(\Delta V))}. \quad (4.38)$$



It should be noted that in this equation, the convolved beam widths are primed, while the  $f$ -functions are unprimed. This is done so that the cumulative effect of in-plane and out-of-plane orbit drift corrections can be realized. This prescription differs from orbit drift corrections in Run 2 ATLAS vdM calibrations, where the  $f$ -functions were also primed [190]. The choice of primed versus unprimed  $f$ -functions has negligible effects on proton-proton vdM calibrations, since the size of the orbit drift is typically much smaller than the convolved beam widths. However, it can have a sizeable effect in heavy ion vdM calibrations.

The orbit drift correction was found to impact the bunch-averaged  $\sigma_{\text{vis}}$  values by  $< 0.4\%$  in Scans I to V, and up to 0.5-0.7% in Scans VI and VII, as a consequence of large observed orbit drifts in Fill 9218.

The systematic uncertainty on the orbit drift correction was evaluated by using the arcBPMs instead of the DOROS BPMs. The largest absolute single-scan change in the bunch-averaged  $\sigma_{\text{vis}}$  for the LUCID BiEvtOR algorithm was taken to be the uncertainty. Tab. 4.6 summarizes the obtained results for all six on-axis scans. The background subtraction, and ghost and satellite fraction corrections were applied before the orbit drift uncertainty was determined.

Scan I	Scan III	Scan IV	Scan V	Scan VI	Scan VII
<b>+0.23%</b>	+0.17%	+0.02%	+0.14%	-0.13%	+0.03%

**Table 4.6:** Summary of orbit drift uncertainties (DOROS vs arcBPM) for all on-axis scans, for the LUCID BiEvtOR algorithm. The largest single-scan difference (Scan I) is highlighted.

### 4.3.8 Length scale calibration

Besides knowing the true positions of the beams during a vdM scan, it is also important to know if the length scale of the corrector magnets is precise. Here, the length scale is essentially the ratio of the real and requested beam separations. If this ratio differs from unity, the length scale is mis-calibrated, and consequently, the vdM scan curves are biased.

The length scale is determined using a special set of scans, shown for the 2023 Pb+Pb calibration in Fig. 4.9. Four length scale scans were performed, one in each direction of beam motion during vdM scans. In the B1X scan, the vertical beam positions are in the nominal position, while the beam 1 horizontal position is swept through nine scan points. At each step, a three-point mini-scan is performed by varying the beam 2 horizontal position. Similar mini-scans are performed for the other length scales, by replacing  $1 \leftrightarrow 2$  and  $X \leftrightarrow Y$  wherever appropriate.

While the corrector magnets may not be trusted, the reconstruction of the beamspot using ID tracks is extremely reliable. Thus, the position of the beamspot is used to calibrate the length scale. In each mini-scan, the specific luminosity versus beamspot position is fit with a Gaussian function. The fitted mean of the Gaussian is taken to be the true beam position at the given length scale scan step. Then, the true beam positions are calibrated to the set beam positions using a linear fit. For beams  $i = 1, 2$ , this results in four calibration constants defined

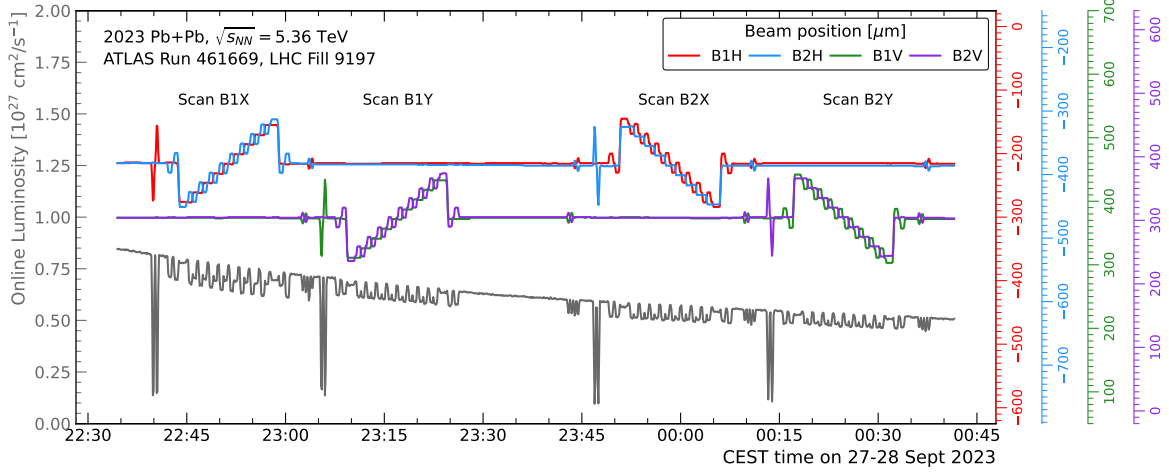


**Figure 4.9:** Sequence of the 2023 Pb+Pb length scale calibration scans in LHC Fill 9197. The online LUCID BiEvtOR luminosity is shown on the left side of the figures. The DOROS beam positions are shown on the right side of the figures, and in the legends, with “1” and “2” denoting the two beams, and “H” and “V” denoting the horizontal and vertical positions respectively.

by

$$x_{\text{true},i}(t) = M_1^{ix} x_{\text{set},i}(t) \quad , \quad y_{\text{true},i}(t) = M_1^{iy} y_{\text{set},i}(t) . \quad (4.39)$$

Using these calibration constants, the true beam separation in the horizontal and vertical planes are found to be

$$\Delta x_{\text{true}}(t) = \frac{M_1^{1x} + M_1^{2x}}{2} \Delta x_{\text{set}}(t) \quad , \quad \Delta y_{\text{true}}(t) = \frac{M_1^{1y} + M_1^{2y}}{2} \Delta y_{\text{set}}(t) . \quad (4.40)$$

This modification implies that at each step in a vdM scan, the beams are actually separated by  $\Delta x_{\text{true}}(t)$ ,  $\Delta y_{\text{true}}(t)$  rather than  $\Delta x_{\text{set}}(t)$ ,  $\Delta y_{\text{set}}(t)$ . By making this replacement in Eq. 4.17 without a change of variables, the  $\sigma_{\text{vis}}$  equation including the length scale calibration is given by

$$\sigma_{\text{vis}}^{\text{corr}} = \frac{M_1^{1x} + M_1^{2x}}{2} \frac{M_1^{1y} + M_1^{2y}}{2} \sigma_{\text{vis}}^{\text{uncorr}} = L_{xy} \sigma_{\text{vis}}^{\text{uncorr}} \quad (4.41)$$

where  $L_{xy}$  is called the *length scale product*.

In the 2023 Pb+Pb vdM scans, the linear length scale calibration (LSC) constants were found to be  $M_1^{1x} = 0.9930(10)$ ,  $M_1^{2x} = 0.9933(11)$ ,  $M_1^{1y} = 0.9930(10)$ , and  $M_1^{2y} = 0.9905(11)$ , from which  $L_{xy} = 0.9849(11)$  was obtained. The errors are the statistical uncertainties from the mini-scan and  $M_1$  fits.

Three sources of systematic uncertainties were considered for the length scale calibration. First, the statistical uncertainties of the  $M_1$  parameters were propagated through to the length scale product  $L_{xy}$ . This resulted in a 0.11% relative uncertainty. Then, the orbit drift correction to the LSC was varied, where the DOROS and arc BPM readings before and after the LSC

scans were used instead of the beamspot positions. The largest difference to the nominal  $L_{xy}$  was found to be 0.22%, which was used to define an uncertainty.

Finally, non-reproducibility and non-linearity effects were investigated, using fits where the LSC results were combined with the DOROS BPM readings in on-axis vdM scans, taking into account the beam-beam deflection seen by the DOROS BPMs (as they are positioned within the closed orbit bump). Alternate  $L_{xy}$  were derived, and the largest difference with respect to the nominal  $L_{xy}$  was found to be 0.36%, thereby defining a systematic uncertainty.

The total uncertainty on the 2023 Pb+Pb LSC was found to be 0.45%, which is the sum-in-quadrature of the relative uncertainties due to the three sources described above.

In addition to the aforementioned uncertainties, the uncertainty on the Inner Detector alignment also need to be considered, as it affects the precision of the reconstructed beamspot position. The ID length scale was studied in Monte Carlo simulations of minimum bias proton-proton collisions, by estimating the change in the reconstructed distance between two well separate beamspots after applying realistic variations of the ID geometry. A relative uncertainty of 0.12% was obtained [199], which is treated as an uncertainty on the length scale product, and consequently on  $\sigma_{\text{vis}}$ .

#### 4.3.9 Beam-beam effects

Since the colliding bunches travel at ultra-relativistic energies and are electrically charged, the electromagnetic fields emitted by them are highly non-linear. If the two bunches are not perfectly centered with respect to each other, the EM fields of one bunch (the *source* bunch) can affect the shape and trajectory of the other bunch (the *witness* bunch). These effects, collectively referred to as *beam-beam effects*, have a measurable impact on beam separation scans.

There are two beam-beam effects relevant to vdM scans [200]:

- **Orbit shift:** a collective deflection of the witness bunch due to the Lorentz force exerted on it by the source bunch. As a consequence, the true beam separation is different from the nominal beam separation.
- **Optical distortion:** a change in the *optics* of individual particles in the witness bunch, due to the electromagnetic field of the source bunch. Here, optics refers to the parameters of the betatron oscillations of the particles. Consequently, the transverse density of the bunches changes in a separation-dependent manner.

Beam-beam effects are quantified in terms of the *linear beam-beam parameter*  $\xi$ , which can be defined for both beams and both separation planes. For example, if beam 2 is the witness beam, the beam-beam parameter in the horizontal plane is given by [201]

$$\xi_{x,2} = \frac{n_1 r_0 Z_1 Z_2 \beta_{x,2}^*}{2\pi A_{\text{ion},2} \gamma_2 \sigma_{1,x} (\sigma_{1,x} + \sigma_{1,y})}. \quad (4.42)$$

Here,  $n_1$  is the bunch population of beam 1,  $r_0 = e^2/4\pi\epsilon_0 m_p c^2$  is the classical radius of the proton,  $Z_{1,2}$  are the atomic charge numbers of the particles in the two beams,  $\beta_{x,2}^*$  is the value of the horizontal betatron function for beam 2 at the interaction point,  $A_{\text{ion},2}$  is the atomic mass number of the particles in beam 2,  $\gamma_2$  is the Lorentz boost of beam 2, and  $\sigma_{1,x}$  and  $\sigma_{1,y}$  are the horizontal and vertical sizes of the bunches in beam 1. Similar definitions of the beam-beam parameter exist for the vertical plane, and for beam 1, by swapping  $1 \leftrightarrow 2$  and  $x \leftrightarrow y$  wherever appropriate.

Proton-proton vdM scans are typically performed with bunch intensities of around  $10^{11}$  protons per bunch and with  $\beta^* = 19.2$  m. At the Run 2 collision energy of  $\sqrt{s} = 13$  TeV, the beam-beam parameter is therefore in the  $\mathcal{O}(10^{-3})$  range. In the Run 2 proton-proton luminosity calibration, the orbit shift and optical distortion were found to affect the measured  $\sigma_{\text{vis}}$  with a percent-level magnitude and with opposite signs, such that the total correction due to beam-beam effects was around 0.5% [190].

The 2023 Pb+Pb vdM scans were taken with intensities of around  $10^8$  ions per bunch and with  $\beta^* = 0.5$  m. Using the per-nucleon Lorentz factor, the beam-beam parameter is found to be in the  $\mathcal{O}(10^{-4})$  range. Based on the magnitude of beam-beam effects in proton-proton vdM scans, the magnitude in Pb+Pb vdM scans can be safely assumed to be below 0.1%. Since the beam-beam correction is small with respect to other corrections and systematic uncertainties, it was not applied in the preliminary calibration. An uncertainty of 0.1% was therefore considered, to account for any residual effects due to the neglected correction.

#### 4.3.10 Emittance change

The visible cross-section defined by Eq. 4.19 implicitly assumes that the convolved beam widths and peak specific visible event rates are determined simultaneously. However, in an on-axis vdM scan pair, the horizontal and vertical scans are separated in time by around 30 minutes. In the presence of effects like intra-beam scattering and synchrotron radiation damping, the emittances of the colliding bunches (and consequently the convolved beam widths) can evolve over time [202]. Thus, the separation in time between a horizontal and vertical vdM scan can bias the  $\sigma_{\text{vis}}$  determination.

The effect of *emittance evolution* is accounted for by introducing time-dependence into  $\sigma_{\text{vis}}$ . Suppose the horizontal vdM scan is performed at some reference time  $t_1$ , which gives the horizontal convolved beam width  $\Sigma_x$  and peak specific visible event rate  $\bar{\mu}_{\text{vis}}^{\text{max},x}$ . Similarly, suppose the vertical vdM scan is performed at some reference time  $t_2$ , giving  $\Sigma_y$  and  $\bar{\mu}_{\text{vis}}^{\text{max},y}$ . The visible cross-section can be written in a time-dependent manner, using a simplified version of the  $\sigma_{\text{vis}}$  definition in Eq. 4.19, as

$$\sigma_{\text{vis}}(t_1, t_2) = 2\pi\Sigma_x(t_1)\Sigma_y(t_2)\frac{1}{2}(\bar{\mu}_{\text{vis}}^{\text{max},x}(t_1) + \bar{\mu}_{\text{vis}}^{\text{max},x}(t_2)). \quad (4.43)$$

The functional forms of the time-dependent quantities appearing in this equation are deter-

mined from a linear fit to the  $\Sigma_x$ ,  $\Sigma_y$ ,  $\bar{\mu}_{\text{vis}}^{\text{max},x}$  and  $\bar{\mu}_{\text{vis}}^{\text{max},y}$  values for a set of consecutive vdM scans in the same fill. In these fits, the reference timestamps are chosen as  $(t_1, t_2) = (\hat{t}_x, \hat{t}_y)$ , i.e. when the horizontal and vertical vdM scans are at their midpoints. The reference visible cross-section is then given by  $\sigma_{\text{vis}}(\hat{t}_x, \hat{t}_y)$ .

In general, Eq. 4.43 can be extrapolated to any common time  $t' = t_1 = t_2$  in order to correct for emittance evolution effects. A natural choice is the midpoint between the horizontal and vertical scans,  $t_{\text{mid}} = \frac{1}{2}(\hat{t}_x + \hat{t}_y)$ , which is then used to define the nominal correction for emittance evolution. In Run 2 proton-proton vdM calibrations, the extrapolation of all quantities in Eq. 4.43 to  $t' = \hat{t}_x$  and  $t' = \hat{t}_y$  was used to define a systematic uncertainty on the emittance evolution correction [190].

The emittance evolution correction factor  $c_\epsilon$  is defined as the fractional difference between the corrected and uncorrected visible cross-sections, i.e.

$$c_\epsilon = \frac{\sigma_{\text{vis}}(t_{\text{mid}}, t_{\text{mid}})}{\sigma_{\text{vis}}(\hat{t}_x, \hat{t}_y)} - 1. \quad (4.44)$$

In the 2023 Pb+Pb vdM calibration, the emittance evolution is estimated in Fill 9209 (between Scans I, III and IV) and in Fill 9218 (between Scans VI and VII). The results are shown in Fig. 4.10. The correction factors  $c_\epsilon$  were found to be on average  $< 0.1\%$  and  $< 0.5\%$  for Fills 9209 and 9218 respectively. Although they appear to be sizeable, it should be noted that the bunch-by-bunch linear evolution fits were performed with three and two data points respectively in the two fills, so the computed correction factors may not be representative of the true long-term emittance evolution. Additionally, the slopes of the  $\Sigma_{x,y}$  evolution were found to be consistent with zero given the statistical uncertainties, both on a bunch-by-bunch and bunch-averaged basis. This could be due to a genuine lack of emittance evolution, or simply a statistical effect.

Based on these observations, it was concluded that there is no statistically significant impact of emittance evolution on the 2023 Pb+Pb vdM calibration. The effect was not corrected for, and the largest bunch-averaged correction for a single scan (0.49% in Scan VII), was taken as a systematic uncertainty to cover any potential bias.

### 4.3.11 Non-factorization

One of the underlying assumptions of the vdM formalism is the fact that the observed event rate is factorizable in the horizontal and vertical beam separation, as indicated in Eq. 4.16. However, this need not always be true. The breakdown of the *factorizability* of  $\bar{\mu}_{\text{vis}}(\Delta x, \Delta y)$  is called *non-factorization*, and is a potential source of bias in the  $\sigma_{\text{vis}}$  determination using on-axis vdM scan pairs. Non-factorization can be present if the bunch densities themselves are non-factorizable, which can happen due to non-zero correlations in the covariance matrices of the bunch densities. Such correlations can arise due to imperfections and non-linearities in the beam dynamics, and due to electromagnetic interactions between particles in the bunches [203].

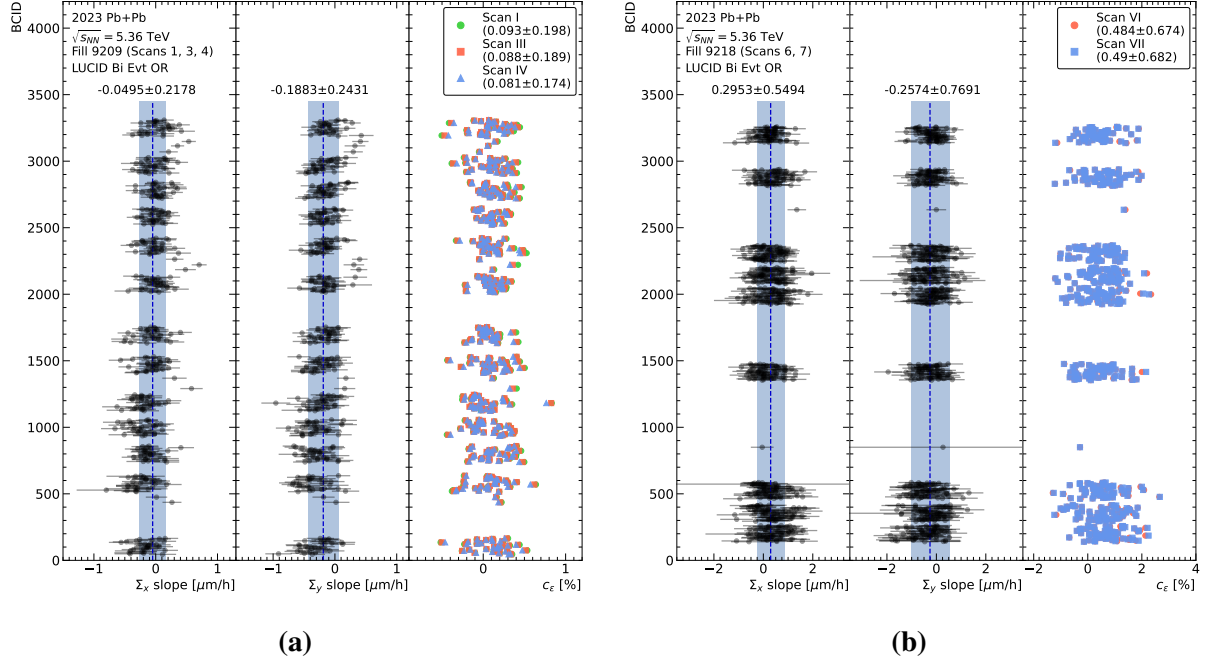


**Figure 4.10:** Results of the emittance change estimation for (a) Scans I, III and IV in Fill 9209 and (b) Scans VI and VII in Fill 9218. The left, center, and right panels show for each colliding bunch the  $\Sigma_x$  evolution slope,  $\Sigma_y$  evolution slope, and emittance change correction factor  $c_e$ . The numbers quoted in the figures are the mean and RMS of the relevant quantities. The error bars reflect the statistical uncertainties, and do not account for correlations.

Non-factorization can also be present if the bunch densities are non-Gaussian, such as in the case of double Gaussian distributions. Yet another (trivial) source of non-factorization is a non-zero crossing angle in both horizontal and vertical planes; this is fortunately never the case for proton and ion collisions at the ATLAS interaction point.

In the presence of non-factorization, Eq. 4.19 is no longer a valid definition of the visible cross-section. Instead, a generalized equation,

$$\sigma_{\text{vis}}^{2\text{D}} = \int d\Delta x d\Delta y \bar{\mu}_{\text{vis}}(\Delta x, \Delta y) \quad (4.45)$$

can be used, which is the two-dimensional integral of the specific visible event rate.

In order to determine  $\sigma_{\text{vis}}^{2\text{D}}$  it is necessary to record the specific visible event rate for a set of beam separations  $(\Delta x, \Delta y)$  that does not coincide with the ATLAS coordinate system in some manner. This can be achieved, for example, through a combination of an on-axis and off-axis scan pair, or using diagonal scans of the  $(\Delta x, \Delta y)$  plane. In the 2023 Pb+Pb vdM scan procedure, a two-dimensional scan was taken by sampling a uniform grid of  $(\Delta x, \Delta y)$  values, as shown in Fig. 4.11a.

The grid scan data was fit with a rotated two-dimensional version of the GP2 function, called the GP2XY function. It is defined as



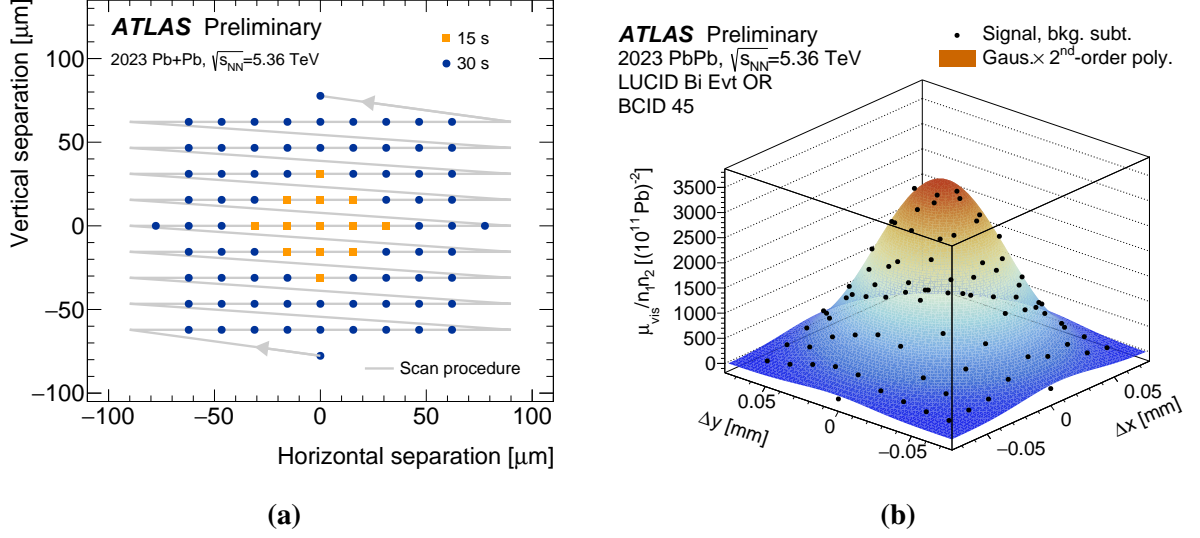


**Figure 4.11:** (a) Scanning sequence for the grid scan. Luminosity data were recorded for 15 s or 30 s per scan step at small (orange squares) or large (blue circles) beam separation respectively, to improve the statistical precision in the tails of the scan. (b) Specific visible event rate (subtracted by noise+afterglow and beam-gas backgrounds) in the grid scan using the LUCID BiEvtOR algorithm for one bunch. The error bars reflect only statistical uncertainties. The surface shape shows a fit with the GP2XY function. Figures taken from Ref. [6].

$$\begin{aligned} \text{GP2XY}(\Delta x, \Delta y) &= p_0 \exp \left( -\frac{1}{2} \frac{1}{1 - \rho^2} (\Delta x'^2 + \Delta y'^2 - 2\rho \Delta x' \Delta y') \right) \\ &\times (1 + c_{20} \Delta x'^2 + c_{02} \Delta y'^2 + c_{22} \Delta x'^2 \Delta y'^2) \end{aligned} \quad (4.46)$$

where

$$\Delta x' = \frac{\Delta x - \nu_x}{\sigma_x} \quad \text{and} \quad \Delta y' = \frac{\Delta y - \nu_y}{\sigma_y} \quad (4.47)$$

are used for brevity. The free parameters of the GP2XY function are  $\rho$ ,  $p_0$ ,  $\nu_{x,y}$ ,  $\sigma_{x,y}$ ,  $c_{02}$ ,  $c_{20}$  and  $c_{22}$ . After fitting the function to the grid scan,  $\sigma_{\text{vis}}^{2\text{D},j}$  is determined for each bunch  $j$  via numerical integration using Eq. 4.45. An example fit for one bunch is shown in Fig. 4.11b.

The GP2XY function was chosen to fit the grid scan data as it is one of the simplest non-factorizable two-dimensional functions that can be constructed. A non-zero  $\rho$  can introduce non-factorization in the ATLAS coordinate system, even if the  $c$ -parameters are set to zero. On the other hand, non-zero  $c$ -parameters can introduce non-factorization even if  $\rho = 0$ <sup>2</sup>. Extensions of the GP2XY function with additional higher order polynomial terms, as well as two-dimensional double Gaussian functions, were also investigated. However, these functions suffered from fit convergence issues due to limited statistics, so they were not pursued further.

<sup>2</sup>It should be noted that the GP2XY function is factorizable in the ATLAS coordinate system under the special condition of  $\rho = 0$  and  $c_{22} = c_{20} \times c_{02}$ . This condition is fortunately never satisfied in the 2023 Pb+Pb grid scan analysis, partly because the data supports  $\rho = -0.08$ .

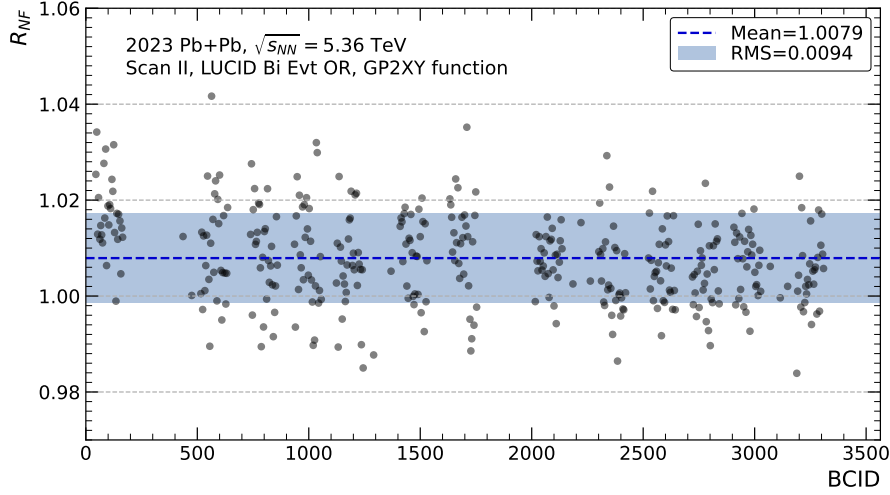


**Figure 4.12:** Non-factorization correction factor obtained using the GP2XY function, which is fit to the LUCID BiEvtOR data in Scan II. The mean and RMS of the per-bunch  $R_{\text{NF}}^j$  values are shown in the legend.

The fitted two-dimensional function can then be used to estimate the bias due to non-factorization. First, one-dimensional functions  $f_{x,y}$  are obtained by taking slices of the GP2XY function at the fitted means, i.e.

$$\begin{aligned} f_x(\Delta x) &= \text{GP2XY}(\Delta x, \nu_y), \\ f_y(\Delta y) &= \text{GP2XY}(\nu_x, \Delta y). \end{aligned} \quad (4.48)$$

These functions can be treated as the fit functions obtained from the analysis of a simulated on-axis vdM scan pair, and are used to determine the factorized visible cross-section  $\sigma_{\text{vis}}^{\text{fact}}$  according to Eq. 4.19. Then, the non-factorization correction factor  $R_{\text{NF}}^j$  is computed for each bunch  $j$ , which is defined as

$$R_{\text{NF}}^j = \frac{\sigma_{\text{vis}}^{\text{fact},j}}{\sigma_{\text{vis}}^{2\text{D},j}}. \quad (4.49)$$

The  $R_{\text{NF}}^j$  results obtained in the analysis of the grid scan are shown in Fig. 4.12. Although there is a large bunch-to-bunch spread, there is some indication of a statistically significant non-factorization bias at the level of around 0.8%. Due to the preliminary nature of this result, the statistical uncertainties on  $R_{\text{NF}}^j$ , which can be obtained through pseudo-experiments, were not estimated.

An alternate approach to the determination of  $R_{\text{NF}}^j$  is through the *luminous region evolution* (LRE) analysis, which combines beamspot and luminometer data during beam separation scans to determine the parameters (widths, correlations, tilts etc.) of the individual bunches. With these parameters, it is possible to map the beam overlap  $\Omega_j$  for each bunch as a function of  $\Delta x$  and  $\Delta y$ . Then, the non-factorization correction factor can be determined, which is defined as the ratio of factorized and non-factorized convolved beam widths, i.e.



$$R_{\text{NF}}^{\text{LRE},j} = \frac{\frac{1}{\sqrt{2\pi}} \int d\Delta x \Omega_j(\Delta x, 0) \frac{1}{\sqrt{2\pi}} \int d\Delta y \Omega_j(0, \Delta y)}{\frac{1}{2\pi} \int d\Delta x d\Delta y \Omega_j(\Delta x, \Delta y)}. \quad (4.50)$$

The difference between  $R_{\text{NF}}^j$  and  $R_{\text{NF}}^{\text{LRE},j}$  can be used to set a systematic uncertainty on the non-factorization correction. However, due to the preliminary nature of the 2023 Pb+Pb vdM calibration, the LRE analysis was not completed. Without a proper systematic uncertainty, the non-factorization correction was not applied. Thus, a conservative uncertainty of 1.5% was assigned to cover any potential bias due to the neglected correction. This uncertainty covers the mean+RMS of the  $R_{\text{NF}}^j$  shown in Fig. 4.12.

### 4.3.12 Reproducibility and consistency

After all the corrections have been applied, the visible cross-section for a scan  $k$ , denoted by  $\bar{\sigma}_{\text{vis}}^k$ , can be computed. It is defined as an error-weighted average over all bunches, i.e.

$$\bar{\sigma}_{\text{vis}}^k = \frac{1}{\sum_j \frac{1}{w_{j,k}^2}} \sum_j \left( \frac{[\bar{\sigma}_{\text{vis}}^k]_j}{w_{j,k}} \right)^2 \quad ; \quad w_{j,k} = [\Delta \bar{\sigma}_{\text{vis}}^k]_j. \quad (4.51)$$

In this equation, the sums run over all bunches in the scan, and  $[\bar{\sigma}_{\text{vis}}^k]_j$  is the visible cross-section for the given bunch  $j$ , with an uncertainty of  $[\Delta \bar{\sigma}_{\text{vis}}^k]_j$ . This uncertainty is statistical in nature, and arises from the errors of the scan curve fits. Eq. 4.51 is essentially the maximum likelihood estimator of the bunch-averaged  $\sigma_{\text{vis}}$ , assuming that all  $[\bar{\sigma}_{\text{vis}}^k]_j$  are Gaussian-distributed and have the same mean. The statistical uncertainty on  $\bar{\sigma}_{\text{vis}}^k$  is given by

$$\Delta \bar{\sigma}_{\text{vis}}^k = \sqrt{\sum_j \frac{1}{w_{j,k}^2}}. \quad (4.52)$$

In the 2023 Pb+Pb vdM calibration, the relative statistical uncertainty of the  $\bar{\sigma}_{\text{vis}}^k$  was around 0.05% for each scan. This is not included in the final uncertainty of the calibration, as it is negligible when compared to other systematic uncertainties.

The average visible cross-section over all scans, denoted by  $\bar{\sigma}_{\text{vis}}$ , is defined by a simple arithmetic mean, i.e.

$$\bar{\sigma}_{\text{vis}} = \frac{\sum_k \bar{\sigma}_{\text{vis}}^k}{N_{\text{scan}}}, \quad (4.53)$$

with the statistical uncertainty being

$$\Delta \bar{\sigma}_{\text{vis}} = \sqrt{\frac{\sum_k (\bar{\sigma}_{\text{vis}} - \bar{\sigma}_{\text{vis}}^k)^2}{N_{\text{scan}} - 1}}. \quad (4.54)$$

In principle, each vdM scan should result in the same visible cross-section. Thus,  $\Delta \bar{\sigma}_{\text{vis}}$  is used as a measure of the *scan-to-scan reproducibility*. In the 2023 Pb+Pb vdM calibration,

$\Delta\bar{\sigma}_{\text{vis}}/\bar{\sigma}_{\text{vis}} = 0.21\%$  was found, and was used to define a systematic uncertainty on the scan-to-scan (non)reproducibility.

Every bunch in a given scan should result in the same  $\sigma_{\text{vis}}$  within statistical uncertainties. More generally, the average statistical uncertainty should resemble the RMS of the per-bunch  $\sigma_{\text{vis}}$  values. This may not be satisfied if there are some other non-statistical effects that modify the RMS with respect to the expectation. In order to quantify this effect, the *bunch-by-bunch consistency*  $\delta\sigma_{\text{vis}}^k$  is computed for each scan  $k$ , which is defined as

$$\delta\sigma_{\text{vis}}^k = \sqrt{(\sigma_{\text{tot}}^k)^2 - (\sigma_{\text{avg}}^k)^2}, \quad (4.55)$$

where  $\sigma_{\text{avg}}^k$  is the average of per-bunch statistical errors  $[\Delta\bar{\sigma}_{\text{vis}}^k]_j$ , and  $\sigma_{\text{tot}}^k$  is the overall spread of the per-bunch visible cross-section values, which is taken as the width of a Gaussian fit to the  $[\bar{\sigma}_{\text{vis}}^k]_j$  distribution. The bunch-by-bunch consistency is shown for all on-axis scans in Tab. 4.7. The largest *inconsistency* for a single scan is used to define a systematic uncertainty.

Scan I	Scan III	Scan IV	Scan V	Scan VI	Scan VII
0.73%	+1.04%	0.89%	0.64%	0.37%	0.81%

**Table 4.7:** Bunch-by-bunch consistency for all on-axis scans, using the LUCID BiEvtOR algorithm. The largest single-scan difference (Scan III) is highlighted.

### 4.3.13 Long term stability

After the vdM calibration has been applied to a given collision dataset, it is important to estimate its stability over time. This can be achieved by checking ratios between the luminosities determined by different algorithms as a function of time, over the entire dataset. Any deviation can be used to define a systematic uncertainty on the *long term stability* of the luminosity calibration. In practice, the ratios are taken using integrated luminosities on a fill-by-fill basis in order to improve the statistical uncertainties, and to investigate fill-to-fill variations.

The long term stability results for the 2023 Pb+Pb dataset are shown in Fig. 4.13. The LUCID BiEvtOR luminosity is compared to luminometers from a diverse set of detector technologies. Preliminary data quality and cleaning selections were applied to remove luminosity blocks with data that are not usable for physics measurements. The luminosity ratios are normalized, or *anchored*, to LHC Fill 9223, which is a physics fill immediately after the vdM fills. This is done to equalize the luminosity scales of all algorithms (calibrated or otherwise).

The LUCID algorithms are found to be very stable with each other, as expected due to the correlated signals. The ZDC EvtOR algorithm is found to be remarkably stable with respect to LUCID BiEvtOR. Among the track-based algorithms that offer the best statistical precision, the EC algorithm has visibly better stability than the TC algorithm. The BCM VEvtOR algorithms is found to vary dramatically with respect to LUCID BiEvtOR, due to a known charge trapping effect in the diamond sensors that biases luminosity determination in short fills [204, 205].

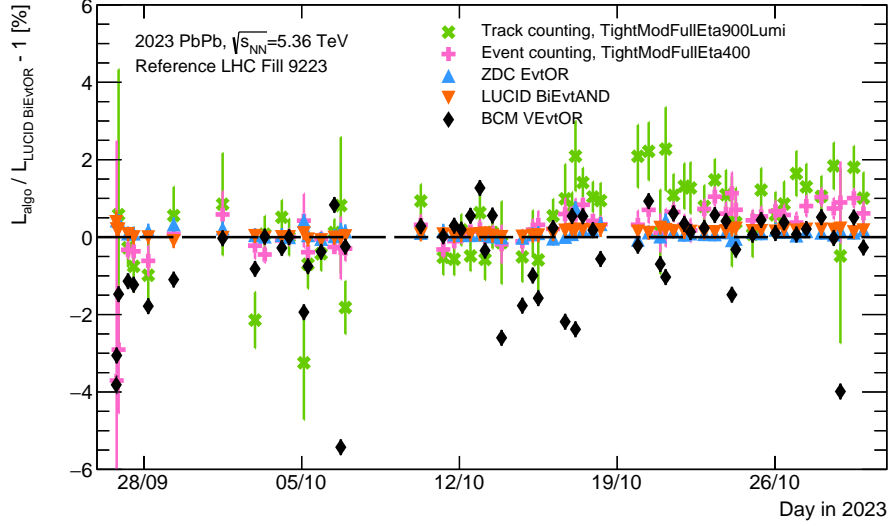


**Figure 4.13:** History of the fractional difference (in percent) between the fill-integrated luminosity determined with different algorithms and the LUCID BiEvtOR algorithm, in the 2023 Pb+Pb dataset. The error bars are statistical in nature.

As there are some observed deviations in the long term stability, a systematic uncertainty must be defined. This could be done using a coverage band or RMS of the fill-by-fill integrated luminosity ratios. These definitions, however, result in the systematic uncertainty being sensitive to statistical fluctuations, particularly in short fills during the first few days of Pb+Pb data taking. Moreover, they do not represent the stability of the luminosity calibration where it matters, i.e. the latter half of the data-taking period, where the bulk of the data resides.

Thus, the long term stability uncertainty is evaluated using a weighting method, which gives more importance to fills with a larger integrated luminosity. Each data point in Fig. 4.13 is weighted by the reference (LUCID BiEvtOR) integrated luminosity, and then projected onto the  $y$ -axis to build a histogram. The statistical uncertainties are neglected in this procedure. The histograms are shown in Fig. 4.14 along with their means and RMSs. Only the best performing algorithms from each detector are included in this comparison. The BCM algorithms are omitted due to the large fill-to-fill variations.

The means of the histograms were then used to accurately quantify the long term stability. The ZDC EvtOR and LUCID BiEvtAND show stabilities at the 0.1% level. The largest mean, 0.38% for track-based event counting, defined the long term stability uncertainty.

#### 4.3.14 Results of the preliminary 2023 Pb+Pb calibration

A summary of the corrections applied to the  $\sigma_{\text{vis}}$  of the LUCID BiEvtOR algorithm are presented in Tab. 4.8. The largest correction comes from the ghost and satellite fractions, which is unsurprising given that they were observed to be very large. After the applied corrections, the  $\sigma_{\text{vis}}$  is found to increase by 3-6%, and the scan-to-scan reproducibility is improved from around 1.85% to 0.21%. The corrected central value  $\bar{\sigma}_{\text{vis}}$  is 22.50 barns.

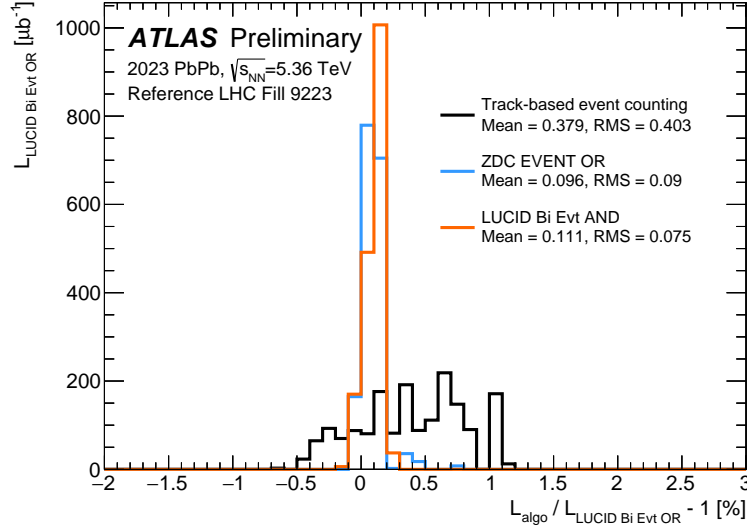


**Figure 4.14:** Histogram of the fractional difference (in percent) between the fill-integrated luminosity determined with different algorithms and the LUCID BiEvtOR algorithm, in the 2023 Pb+Pb dataset. Each entry in the histogram corresponds to one LHC fill, weighted by the integrated luminosity determined by the LUCID BiEvtOR algorithm. The fill-by-fill ratios for each algorithm are normalized to the integrated luminosity collected in LHC Fill 9223. The mean and RMS of each histogram is given in the legend. The `TightModFullEta400` selection was used for the track-based event counting algorithm. Figure taken from Ref. [6].

	Scan I	Scan III	Scan IV	Scan V	Scan VI	Scan VII
Uncorrected $\sigma_{\text{vis}}$ (barns)	21.22	21.18	20.89	21.84	21.73	21.78
Ghost & satellite fraction (%)	7.80	8.28	8.79	5.11	4.37	4.56
Bunch current offset (%)	0.04	0.01	-0.02	-0.28	-0.09	-0.19
Orbit drift (%)	-0.06	-0.19	0.35	-0.22	0.54	0.73
Length scale (%)	-1.51	-1.51	-1.51	-1.51	-1.51	-1.51
Corrected $\sigma_{\text{vis}}$ (barns)	22.52	22.54	22.45	22.50	22.44	22.55

**Table 4.8:** Summary of all corrections applied to the visible cross-section of the LUCID BiEvtOR algorithm. The corrections are cumulative and shown in percent.

A summary of the systematic uncertainties on the LUCID BiEvtOR  $\sigma_{\text{vis}}$  is shown in Tab. 4.9. The total uncertainty amounts to 2.71%. The largest individual component arises from non-factorization effects, which were left uncorrected in the preliminary result. Other large systematic uncertainties include the uncertainties on the ghost and satellite charge fractions, the bunch-by-bunch consistency, and the specific luminosity uncertainty. After applying the standard ATLAS data quality and cleaning selections [206], the usage of this preliminary luminosity calibration results in an integrated luminosity of  $1703.08 \pm 46.15 \mu\text{b}^{-1}$  for the 2023 Pb+Pb dataset.

The results of this preliminary calibration can be contextualized by comparing it to previous ATLAS calibrations. The uncertainty of the integrated luminosity of the Run 2 13 TeV p+p dataset was 0.83%, determined using the same methodology described in this chapter [190].

Source	Uncertainty (%)
Bunch charge fraction	0.27
Ghost & satellite fraction	1.00
DCCT uncertainty	0.28
Beam-gas subtraction	0.61
Noise+afterglow subtraction	0.38
Orbit drift	0.23
Length scale calibration	0.45
Absolute ID length scale	0.12
Beam-beam effects	0.10
Emittance change	0.49
Non-factorization	1.50
Specific luminosity	0.99
Fit model	0.82
Scan-to-scan reproducibility	0.21
Bunch-by-bunch consistency	1.04
Long term stability	0.38
Total	2.71

**Table 4.9:** Breakdown of (relative) systematic uncertainties for the preliminary 2023 Pb+Pb vdM calibration. The total uncertainty is a sum-in-quadrature of all individual sources.

Although the uncertainties for each data-taking year were larger than 1%, the uncertainty was reduced in the combination of the years. The uncertainty of the Run 2 5.02 TeV Pb+Pb dataset was 1.5%, determined using an alternate calibration approach that is manifestly two-dimensional. For the individual Pb+Pb data-taking years, the 2015 and 2018 uncertainties were 1.5% and 2.0% respectively.



# Chapter 5

## Measurement of $\gamma\gamma \rightarrow \tau^+\tau^-$ scattering cross-sections and constraints on tau lepton electromagnetic dipole moments

This chapter presents a measurement of differential fiducial cross-sections of  $\gamma\gamma \rightarrow \tau^+\tau^-$  scattering in ultra-peripheral Pb+Pb collisions (UPCs), and constraints on the electromagnetic dipole moments (EMDMs) of the tau lepton.

The general analysis strategy is outlined in Sec. 5.1. The data collection is described in Sec. 5.2, together with the trigger calibration. The Monte Carlo samples used in the analysis, and the relevant modeling aspects, are detailed in Sec. 5.3. The selection of objects and events is discussed in Sec. 5.4, while the background estimation is described in Sec. 5.5. The details of the unfolding procedure are discussed in Sec. 5.7. The systematic uncertainties considered in the cross-section measurement are detailed in Sec. 5.8. The measured differential fiducial cross-sections are presented in Sec. 5.9, which are then used to constrain the tau lepton EMDMs in Sec. 5.10.

### 5.1 Analysis strategy

As the tau lepton is an unstable particle, with a mean lifetime of around 0.29 ps in the rest frame [37], it decays before interacting with the ATLAS detector, even if boosted to GeV-scale energies. Thus, the presence of pairs of tau leptons in the final states of Pb+Pb collisions must be inferred from the presence of their decay products (see Fig. 2.5).

In principle, any final state containing the decay products of pairs of tau leptons could be used for this purpose. However, certain decays are preferred over others for experimental reasons. Fully hadronic final states suffer from large backgrounds due to photonuclear processes ( $\gamma\text{P} \rightarrow X$ , where P is the pomeron<sup>1</sup>) and meson production ( $\gamma\gamma, \gamma\text{P} \rightarrow M + X$ , where M is a meson like  $\rho^0, \omega, J/\psi$  etc., and X represents additional soft particles). Final states with

---

<sup>1</sup>The pomeron is a concept from Regge theory, which is often interpreted as a collective excitation of the QCD vacuum. It carries the same quantum numbers as the vacuum. See Ref. [207] for a pedagogical introduction.

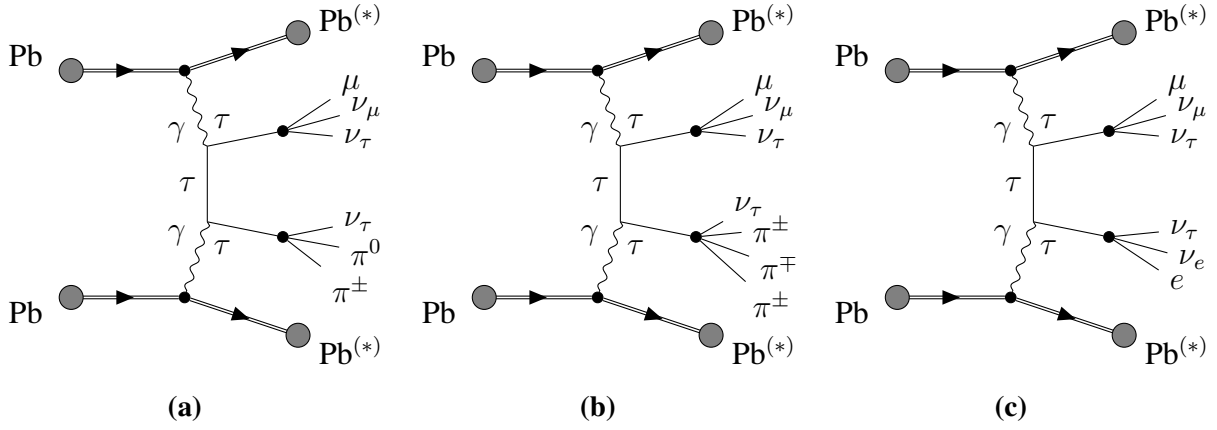


**Figure 5.1:** Schematic diagrams showing photon-induced tau lepton pair production in ultra-peripheral Pb+Pb collisions, with representative tau lepton decays in the (a)  $\mu 1T$ -SR, (b)  $\mu 3T$ -SR and (c)  $\mu e$ -SR regions. Effective vertices are denoted by black dots.

two same-flavor light leptons (i.e. electrons and muons) have very small branching ratios, and suffer from large backgrounds due to  $\gamma\gamma \rightarrow e^+e^-$ ,  $\mu^+\mu^-$  scattering. On the other hand, final states where one tau lepton decays leptonically, while the other decays hadronically, do not suffer from these backgrounds. At the same time, the hadronic backgrounds are brought under control due to the presence of one light lepton. These final states, dubbed  $\tau_\ell\tau_h$ , are therefore the focus of this analysis.

Collision events with  $\tau_\ell\tau_h$  final states can be triggered on by requiring the presence of at least one light lepton in the final state. Triggers targeting low  $p_T$  muons are used to identify  $\tau_\mu\tau_h$  events. Due to performance issues for low  $p_T$  electron triggers in Run 2 Pb+Pb data-taking, the  $\tau_e\tau_h$  final states are not considered.

The analysis defines three *signal regions* (SRs), i.e. areas in the final state phase space where  $\gamma\gamma \rightarrow \tau^+\tau^-$  events are enhanced, as follows:

- $\mu 1T$ -SR: one muon and one track, which targets the  $\tau^\pm \rightarrow \mu^\pm \nu_\tau \nu_\mu$  decay on the leptonic side, and the  $\tau^\pm \rightarrow \pi^\pm n \pi^0 \nu_\tau$  decays on the hadronic side.
- $\mu 3T$ -SR: one muon and three tracks, which targets the  $\tau^\pm \rightarrow \mu^\pm \nu_\tau \nu_\mu$  decay on the leptonic side, and the  $\tau^\pm \rightarrow \pi^\pm \pi^\mp \pi^\pm n \pi^0 \nu_\tau$  decays on the hadronic side.
- $\mu e$ -SR: one muon and one electron, targeting the  $\tau^\pm \tau^\mp \rightarrow \mu^\pm e^\mp 4\nu$  final state.

Examples of the types of  $\gamma\gamma \rightarrow \tau^+\tau^-$  final states that contribute to the signal regions are shown in Fig. 5.1.

The goals of the analysis are two-fold. The first goal is to measure the differential cross-section of  $\gamma\gamma \rightarrow \tau^+\tau^-$  scattering in the  $0n0n$  phase space, i.e. when no forward neutrons are emitted by the interacting Pb ions. The cross-sections are measured at the level of the tau decay products, in three *fiducial regions* (FRs), i.e. reference phase space regions. Seven



Region	Variable	Explanation
$\mu 1\text{T-FR}$	$p_{\text{T}}^{\mu}$	Muon $p_{\text{T}}$
	$p_{\text{T}}^{\text{trk}}$	Track $p_{\text{T}}$
	$p_{\text{T}}(\mu, \text{trk})$	Muon+track system $p_{\text{T}}$
	$m_{\text{inv}}(\mu, \text{trk})$	Muon+track system invariant mass
	$\eta(\mu, \text{trk})$	Muon+track system pseudorapidity
	$\Delta\eta(\mu, \text{trk})$	Pseudorapidity difference between muon & track
	$A_{\phi}(\mu, \text{trk})$	Acoplanarity between muon & track
$\mu 3\text{T-FR}$	$p_{\text{T}}^{\mu}$	Muon $p_{\text{T}}$
	$p_{\text{T}}^{\text{trks}}$	Tracks system $p_{\text{T}}$
	$p_{\text{T}}(\mu, \text{trks})$	Muon+tracks system $p_{\text{T}}$
	$m_{\text{inv}}(\mu, \text{trks})$	Muon+tracks system invariant mass
	$\eta(\mu, \text{trks})$	Muon+tracks system pseudorapidity
	$\Delta\eta(\mu, \text{trks})$	Pseudorapidity difference between muon & tracks system
	$A_{\phi}(\mu, \text{trks})$	Acoplanarity between muon & tracks system
$\mu e\text{-FR}$	$p_{\text{T}}^{\mu}$	Muon $p_{\text{T}}$
	$p_{\text{T}}^e$	Electron $p_{\text{T}}$
	$p_{\text{T}}(\mu, e)$	Muon+electron system $p_{\text{T}}$
	$m_{\text{inv}}(\mu, e)$	Muon+electron system invariant mass
	$\eta(\mu, e)$	Muon+electron system pseudorapidity
	$\Delta\eta(\mu, e)$	Pseudorapidity difference between muon & electron
	$A_{\phi}(\mu, e)$	Acoplanarity between muon & electron

**Table 5.1:** List of variables in each of the defined fiducial regions, for which the differential cross-section measurements are performed.

observables are measured in each fiducial region, in order to infer the  $\tau\tau$  kinematics through as many angles as possible. The measured variables are: the  $p_{\text{T}}$  of the muon, the  $p_{\text{T}}$  of the other object(s); the  $p_{\text{T}}$ , invariant mass and pseudorapidity of the system of all final state particles; the pseudorapidity difference and acoplanarity<sup>2</sup> between the muon and other object(s). The list of all measured variables, along with the nomenclature that is used for them, is shown in Tab. 5.1. In cases where systems of objects are considered, such as in  $p_{\text{T}}^{\text{trks}}$ , the kinematics are defined using the vector-sum of all constituent four-momenta.

The second goal of the analysis is to extract constraints on the tau lepton's EMDMs, by studying their impact on the measured  $\gamma\gamma \rightarrow \tau^+\tau^-$  scattering cross-sections. A statistical analysis using a Gaussian likelihood model is performed, which includes the statistical correlations between the bins of the measured cross-sections. The expected constraints on the tau lepton EMDMs obtained in this analysis are compared to the results of previous analyses, both by ATLAS and by other experiments.

<sup>2</sup>The acoplanarity between two objects with four momenta  $p_{a,b}$  is given by  $A_{\phi}(p_a, p_b) = 1 - \frac{|\Delta\phi(p_a, p_b)|}{\pi}$ , where  $\Delta\phi$  is defined within  $[0, \pi]$ .

## 5.2 Data collection

The analysis uses Pb+Pb collisions at  $\sqrt{s_{NN}} = 5.02$  TeV recorded by the ATLAS experiment in 2015 and 2018. The standard ATLAS data quality selections were applied [206], which remove data-taking periods with intolerable detector noise, non-functioning modules etc. that may compromise the integrity of the data, or bias physics measurements. The toroid magnet was not operational in the last days of 2018 data-taking, which affected the tracking and momentum reconstruction capabilities of the Muon Spectrometer. As the analysis relies on muons in the final state, the data affected by the toroid issues were removed from the dataset. The integrated luminosities of the 2015 and 2018 datasets are  $0.49 \text{ nb}^{-1}$  and  $1.44 \text{ nb}^{-1}$  respectively, which yields an integrated luminosity of  $1.93 \text{ nb}^{-1}$  for the Run 2 dataset. The average (hadronic) pileup was around  $\mu = 2 \times 10^{-3}$  for both datasets.

The triggers used for the analysis rely on the presence of at least one reconstructed muon in the final state, and vetoes on large event activity, as a signature of UPC processes. As they are unique triggers, compared to those commonly used in ATLAS physics measurements, they were not calibrated by the ATLAS trigger performance groups. Instead, the efficiencies and associated systematic uncertainties have been characterized using  $\gamma\gamma \rightarrow \mu^+\mu^-$  scattering in the context of UPC analyses.

The efficiencies of the various trigger selections have been evaluated using two techniques:

- **Bootstrapping:** the efficiency of a trigger  $A$  is defined as the fraction of events passing a reference trigger  $B$  that also pass the requirements of  $A$ , i.e.  $\epsilon = N_{A\&B}/N_B$ . The reference trigger is required to impose a looser version of the selections of the  $A$  trigger. This method is applied to trigger items that look at global event data.
- **Tag-and-probe:** this method is used for estimating the efficiencies of object-based trigger items. First, events are selected based on the presence of a well calibrated *tag* object. In these events, *probe* objects which correspond to the trigger signature of interest, are searched for. The efficiency of the trigger is then defined as the fraction of probes that fire the trigger under investigation, i.e.  $\epsilon = N_{\text{probe,triggered}}/N_{\text{probe,all}}$ .

### 5.2.1 Trigger in 2015

In 2015, the `HLT_mb_sptrk_vetombts2in_L1MU0_VTE50` trigger was used to select  $\gamma\gamma \rightarrow \tau^+\tau^-$  events. Going from the Level-1 seed to HLT selections, this item applied the following selections:

- VTE50: maximum  $E_T$  of 50 GeV in the entire calorimeter system (L1).
- MU0: presence of at least one Level-1 muon object reconstructed in the MS with no  $p_T$  selections being applied (L1).

- `vetombts2in`: maximum of one hit in the Minimum Bias Trigger Scintillators (MBTS) detectors on both A and C sides (HLT).
- `mb_sptrk`: at least one reconstructed HLT track with  $p_T > 0.2$  GeV (HLT).

The efficiency of the `VTE50` item was determined to be 100% in the ATLAS UPC  $\gamma\gamma \rightarrow e^+e^-$  analysis [208], using a `VTE200` seeded trigger as the reference. The efficiency of the `HLT_mb_sptrk` selection was assumed to be 100%, as it applies a very loose tracking requirement, and has often been used to measure the efficiency of other items. The efficiency of the `vetombts2in` selection was also taken to be 100%, based on a study in the ATLAS UPC  $\gamma\gamma \rightarrow \mu^+\mu^-$  analysis [209]. The fraction of events in unpaired BCIDs failing the MBTS selection was found to be negligible, implying that no inefficiency due to detector noise would transfer to paired BCIDs.

Thus, the total efficiency of the 2015 trigger is driven by the `MU0` item, whose efficiency was estimated using the tag-and-probe method in  $\gamma\gamma \rightarrow \mu^+\mu^-$  events. The events were required to have exactly two ID tracks matched to two muons of opposite charge passing the `LowPt WP` selection, with  $p_T > 4$  GeV,  $|\eta| < 2.4$ , and  $|d_0| < 0.3$  mm being imposed on the muons. The dimuon system was required to have  $p_T(\mu\mu) < 2$  GeV and  $A_\phi(\mu, \mu) < 0.01$ . The events were also required to pass the 2015 trigger selection, with no ZDC selections being applied.

In these events, tag muons were defined as those which passed the `Tight WP`, and were matched to a `MU0` region of interest (ROI) within  $\Delta R < 0.3$ . The other muon was then identified as the probe muon, whose efficiency was estimated by a  $\Delta R < 0.3$  matching to another `MU0` ROI. The efficiency was measured in bins of probe muon  $p_T$  and  $q \times \eta$ , where  $q$  is the muon charge. In the endcap region,  $1.05 < |q \times \eta| < 2.4$ , the efficiency was found to slowly increase with  $p_T$ , and saturate at values above 90% for  $p_T \gtrsim 10$  GeV. In the barrel region,  $0.1 < |q \times \eta| < 1.05$ , the maximum efficiency was around 80%, while in the gap region of  $|q \times \eta| < 0.1$  the maximum efficiency was 60%.

### 5.2.2 Trigger in 2018

In 2018, the `HLT_mu4_hi_upc_FgapAC3_L1MU4_VTE50` trigger was used to select  $\gamma\gamma \rightarrow \tau^+\tau^-$  events. Going from the Level-1 seed to HLT selections, this item applied the following selections:

- `VTE50`: maximum  $E_T$  of 50 GeV in the entire calorimeter system (L1).
- `MU4`: presence of at least one Level-1 muon object reconstructed in the MS with  $p_T > 4$  GeV (L1).
- `FgapAC3`: maximum of 3 GeV energy deposited on either side of the Forward Calorimeter, i.e.  $\sum E_T^{\text{FCal,A}} < 3$  GeV and  $\sum E_T^{\text{FCal,C}} < 3$  GeV (HLT).
- `mu4`: presence of at least one HLT muon object in the final state with  $p_T > 4$  GeV (HLT).

The efficiency of this trigger was estimated in the previous ATLAS  $\gamma\gamma \rightarrow \tau^+\tau^-$  analysis [3]. The efficiency of the VTE50 seed was determined to be 100%, based on the calorimeter energy distribution in  $\gamma\gamma \rightarrow \mu^+\mu^-$  events where the 2018 trigger selection was not applied. The efficiency of the FgapAC3 selection was determined to be 99.1% in the ATLAS  $\gamma\gamma \rightarrow e^+e^-$  analysis [208], using a trigger without the FgapAC3 selection, and estimating the fraction of  $\gamma\gamma \rightarrow e^+e^-$  events with FCal energy deposits less than 3 GeV. Thus, the total efficiency of the 2018 trigger is driven by the efficiencies of the MU4 and mu4 selections.

The efficiency of the MU4 selection was determined using the tag-and-probe method in  $\gamma\gamma \rightarrow \mu^+\mu^-$  events. The event selections applied were similar to those applied in the study of the 2015 trigger efficiency, with the exception of a  $|d_0/\sigma_{d_0}| < 3$  requirement instead of  $|d_0| < 0.3$  mm, and  $m_{\text{inv}}(\mu, \mu) > 10$  GeV instead of  $A_\phi(\mu, \mu) < 0.01$ . The behavior of the MU4 efficiency as a function of probe muon  $p_T$  and  $q \times \eta$  was observed to be similar to the 2015 MU0 efficiency, i.e. the maximum efficiency was found to be above 90%, around 80%, and 60% in the  $1.05 < |q \times \eta| < 2.4$ ,  $0.1 < |q \times \eta| < 1.05$  and  $0.1 < |q \times \eta|$  regions respectively.

The efficiency of the mu4 selection was also studied in the same selected  $\gamma\gamma \rightarrow \mu^+\mu^-$  events. Tag muons were defined as muons that pass the Tight WP selection and are matched to a MU4 ROI within  $\Delta R < 0.3$ , while the probe muons were only required to be MU4 matched. Then, the efficiency was defined as the fraction of probe muons matched within  $\Delta R < 0.01$  to the mu4 trigger. The efficiency was estimated only in bins of the probe muon  $p_T$ , and was found to saturate at around 98% for  $p_T > 10$  GeV.

## 5.3 Monte Carlo simulations and modeling

### 5.3.1 Samples

Several Monte Carlo samples of  $\gamma\gamma$  scattering processes in UPCs were produced for the analysis. The most relevant ones are samples of  $\gamma\gamma \rightarrow \ell^+\ell^-$  scattering, where  $\ell = e, \mu, \tau$ . In Ref. [3], additional background samples for  $\gamma\gamma \rightarrow q\bar{q}$  (where  $q$  is a quark) and non-diffractive photonuclear scattering were also created. As these backgrounds were found to be negligible in that analysis, they are not re-used here.

The STARlight event generator [79] was used to sample the  $\gamma\gamma \rightarrow \ell^+\ell^-$  cross-section (see Eq. 2.66 and Eq. 2.79) to produce the  $\gamma\gamma \rightarrow \ell^+\ell^-$  samples, which are inclusive in the forward neutron topologies. The Pythia8 generator [88] was used to simulate photon radiation from the leptons (before decay in case of the tau). The tau decay was performed by the Tauola [86] and Pythia8 generators, for the nominal and alternate  $\gamma\gamma \rightarrow \tau^+\tau^-$  samples, respectively. For the  $\gamma\gamma \rightarrow \tau^+\tau^-$  samples, the Photos generator [210] was used to simulate low  $p_T$  photon emission by the charged tau lepton decay products. An additional sample of  $\gamma\gamma \rightarrow \mu^+\mu^- + \gamma$  scattering was also prepared, in order to simulate hard photon radiation by the muons that cannot be reliably modeled by Pythia8. As STARlight does not support this final state, the sample was generated with the MadGraph5\_aMC@NLO generator [84],

using the photon flux of the proton. For all Monte Carlo samples, a sophisticated simulation of the interaction of the generated particles with the ATLAS detector was performed using the GEANT4 software [211].

Separate samples were produced for comparison to the 2015 and 2018 datasets, due to the different detector conditions in both years. Since the  $\gamma\gamma \rightarrow \ell^+\ell^-$  cross-section falls off as  $1/s^2$  (see Eq. 2.79), the samples were produced in slices of the dilepton invariant mass, to improve the statistical precision at high invariant masses. A particle-level filter requiring at least one charged particle with  $p_T > 3$  GeV and  $|\eta| < 2.6$  was considered in the generation of the  $\gamma\gamma \rightarrow \tau^+\tau^-$  sample. The filter was applied before the detector simulation, in order to increase the fraction of generated  $\gamma\gamma \rightarrow \tau^+\tau^-$  events with at least one muon with  $p_T > 4$  GeV, for which the expensive detector response was simulated.

The simulated events were weighted, so that the predictions of the Monte Carlo generators agree better with the data. The weights can be written as

$$w = \frac{\sigma_{\text{gen}} \epsilon_{\text{filt}} \mathcal{L}_{\text{int}}}{N_{\text{gen}}} w_{\text{theo}} w_{\text{det}}, \quad (5.1)$$

where  $\sigma_{\text{gen}}$  is the generated cross-section,  $\epsilon_{\text{filter}}$  is the efficiency of the charged particle filter ( $= 1$  if not applicable),  $\mathcal{L}_{\text{int}}$  is the integrated luminosity of the corresponding data sample,  $N_{\text{gen}}$  is the number of generated events,  $w_{\text{theo}}$  is the modeling weight associated with theoretical aspects, and  $w_{\text{det}}$  is the modeling weight associated with detector performance. Except for  $w_{\text{theo}}$  and  $w_{\text{det}}$ , all other quantities appearing in Eq. 5.1 are global weights.

A summary of the key parameters of the Monte Carlo samples generated for this analysis is shown in App. A.1.

### 5.3.2 Theoretical modeling

The theoretical modeling weight for the simulated events is given by a product of three terms,

$$w_{\text{theo}} = w_{\gamma\text{-flux}} \cdot w_{0n0n} \cdot w_{\text{MG5-SL}}, \quad (5.2)$$

where  $w_{\gamma\text{-flux}}$  is the photon flux reweighting factor,  $w_{0n0n}$  is the  $0n0n$  phase space reweighting factor, and  $w_{\text{MG5-SL}}$  is the MadGraph5\_aMC@NLO to STARlight reweighting factor, applicable only for the  $\gamma\gamma \rightarrow \mu^+\mu^- + \gamma$  Monte Carlo sample. These terms are determined using particle-level kinematics, and are described in more detail below.

#### Photon flux reweighting

It has been observed in previous ATLAS measurements of  $\gamma\gamma \rightarrow e^+e^-$  and  $\gamma\gamma \rightarrow \mu^+\mu^-$  scattering in UPCs, that the predictions of the SuperChic generator [77] agree better with the data, when compared to the STARlight generator. The two generators differ in the cross-section normalization by around 10-15%, which is due to the restriction in the impact parameter integration range imposed by STARlight, which essentially reduces the overall  $\gamma\gamma \rightarrow \ell^+\ell^-$

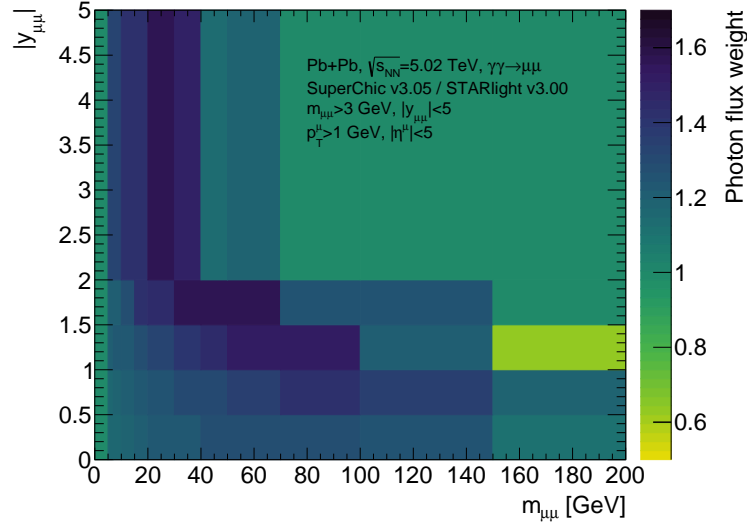


**Figure 5.2:** Photon flux weights, defined as the ratio between  $\gamma\gamma \rightarrow \mu^+\mu^-$  cross-sections predicted by SuperChic and STARlight.

cross-section prediction (see Sec. 2.3.1).

As this analysis relies on STARlight for the main Monte Carlo samples, it is necessary to reweight them in order to improve the data-Monte Carlo agreement. This reweighting is achieved by the factor  $w_{\gamma\text{-flux}}$ , which is defined as the ratio between  $\gamma\gamma \rightarrow \ell^+\ell^-$  cross-sections predicted by SuperChic and STARlight, i.e.  $w_{\gamma\text{-flux}} \sim \frac{\sigma^{\text{SuperChic}}}{\sigma^{\text{STARlight}}}$ . Since the  $\gamma\gamma \rightarrow \ell^+\ell^-$  cross-section only depends on the invariant mass and rapidity of the dilepton system when  $s \gg m_\ell^2$ ,  $w_{\gamma\text{-flux}}$  is derived using  $\gamma\gamma \rightarrow \mu^+\mu^-$  predictions, and applied universally for all dilepton samples. The ratio is determined differentially, in the following bins of dimuon mass and absolute rapidity:  $m_{\text{inv}}(\mu, \mu) \in [0, 5, 7, 10, 15, 20, 30, 40, 50, 70, 100, 150, 200]$  GeV and  $|y(\mu, \mu)| \in [0, 0.5, 1, 1.5, 2, 5]$ .

The photon flux reweighting factor is shown in Fig. 5.2. On average the factor is around 1.2, which is consistent with the previously observed data-STARlight deviations. The factor increases with  $m_{\text{inv}}(\mu, \mu)$  and  $|y(\mu, \mu)|$ , which is the region with smaller impact parameters, where the STARlight-SuperChic differences are expected to be larger.

### 0n0n phase space reweighting

The cross-section measurement presented in this analysis is performed in the 0n0n forward neutron phase space, i.e. when no forward neutrons are emitted by both interacting Pb ions. In the data, 0n0n events are selected by imposing cuts on the energy deposited in the two ZDC arms, i.e.  $E_{\text{ZDC}}^A < 1$  TeV and  $E_{\text{ZDC}}^C < 1$  TeV. At a per-nucleon collision energy of  $\sqrt{s_{\text{NN}}} = 5.02$  TeV, each nucleon in the Pb ions is expected to carry on average 2.76 TeV of energy. Thus, cutting on the ZDC energy distributions below 1 TeV safely isolates 0n0n events.

However, the STARlight dilepton samples are inclusive in the forward neutron topologies. In order to obtain predictions in the 0n0n phase space, the Monte Carlo samples are

weighted using  $w_{0n0n}$ . The weights are determined at particle-level with  $\gamma\gamma \rightarrow \mu^+\mu^-$  events, in bins of the particle-level dilepton mass and absolute rapidity.

The derivation of  $w_{0n0n}$  starts by computing the fraction of  $\gamma\gamma \rightarrow \mu^+\mu^-$  events in data with ZDC energies less than 1 TeV in both arms, called  $w_{0n0n}^{\text{reco}}$ . The fractions are derived differentially in the following bins:  $m_{\text{inv}}(\mu, \mu) \in [8, 10, 15, 20, 30, 40, 80]$  GeV and  $|y(\mu, \mu)| \in [0, 0.5, 1, 1.5, \infty]$ . These  $w_{0n0n}^{\text{reco}}$  are converted into particle-level fractions  $w_{0n0n}$  using

$$(w_{0n0n})_{i,j} = \sum_{k,l} (w_{0n0n}^{\text{reco}})_{k,l} \frac{(N^{\text{reco}})_{i,j}^{k,l}}{\sum_{p,q} (N^{\text{reco}})_{i,j}^{p,q}}. \quad (5.3)$$

Here,  $i$  and  $j$  are bin indices in the particle-level  $m_{\text{inv}}(\mu, \mu)$  and  $|y(\mu, \mu)|$  variables, and  $k$  and  $p$  are the bin indices in the  $m_{\text{inv}}(\mu, \mu)^{\text{reco}}$  variable;  $l$  and  $q$  are the bin indices in the reconstruction-level  $|y(\mu, \mu)|$ .  $(N^{\text{reco}})_{i,j}^{k,l}$  is the number of simulated reconstruction-level  $\gamma\gamma \rightarrow \mu^+\mu^-$  events in the  $(k, l)$  bin that also fall in the particle-level bin  $(i, j)$ . A similar definition applies for  $(N^{\text{reco}})_{i,j}^{p,q}$ . Essentially, this equation represents a pseudo-unfolding of  $w_{0n0n}^{\text{reco}}$  into the particle-level weights  $w_{0n0n}$ .

The average pileup of the Run 2 Pb+Pb dataset was around  $\mu = 2 \times 10^{-3}$ , so the contamination to the 0n0n fractions defined in Eq. 5.3 due to multiple Pb+Pb collisions is negligible. However, this number is actually the *hadronic* pileup  $\mu_{\text{had}}$ , as it is determined by the LUCID detector, which primarily detects minimum bias Pb+Pb collisions. It is related to the total inelastic hadronic cross-section of  $\sigma_{\text{had}} = 7.7$  b, as predicted by the Glauber model [212].

In contrast, the electromagnetic pileup due to single and mutual electromagnetic dissociation (EMD) is expected to be much larger. In these processes, the emission and absorption of quasi-real photons by the Pb ions leads to nuclear dissociation, where the neutral fragments are detected in the ZDCs, thus inducing pileup, which is not detected by LUCID.

Single EMD refers to dissociation of only one of the colliding ions, while mutual EMD refers to the situation where both colliding ions dissociate. An extrapolation of the ALICE measurement of  $\sigma_{\text{single EMD}}$  and  $\sigma_{\text{mutual EMD}}$  at  $\sqrt{s_{\text{NN}}} = 2.76$  TeV [213] up to  $\sqrt{s_{\text{NN}}} = 5.02$  TeV using the RELDIS model [214] yields

$$\begin{aligned} \sigma_{\text{single EMD}} &= 201 \pm 0.3(\text{stat.})_{-12.1}^{+14.2}(\text{syst}) \text{ b}, \\ \sigma_{\text{mutual EMD}} &= 6.0 \pm 0.1(\text{stat.}) \pm 0.4(\text{syst}) \text{ b}. \end{aligned} \quad (5.4)$$

As these cross-sections are comparable to  $\sigma_{\text{had}}$ , the derived 0n0n fractions suffer from contamination due to electromagnetic pileup. When comparing data to predictions that do not include a simulation of electromagnetic pileup, this must be corrected for.

The pileup due to single and mutual EMD cannot be determined using the ZDC data alone. However, the  $\mu_{\text{single EMD}}$  and  $\mu_{\text{mutual EMD}}$  values can be extrapolated from  $\mu_{\text{had}}$ , using the fact that the ratio of cross-section and pileup is proportional to the integrated luminosity, i.e.



$$\mu_{\text{single EMD}} = \mu_{\text{had}} \frac{\sigma_{\text{single EMD}}}{\sigma_{\text{had}}} \quad , \quad \mu_{\text{mutual EMD}} = \mu_{\text{had}} \frac{\sigma_{\text{mutual EMD}}}{\sigma_{\text{had}}} . \quad (5.5)$$

These pileup values are used to determine the probability of at least one single and mutual EMD collision, called  $p_{\text{single}}$  and  $p_{\text{mutual}}$ , using the relation  $p = 1 - e^{-\mu}$ , which arises from a Poisson assumption. The probabilities are determined by averaging over their per-luminosity block values (since  $\mu_{\text{had}}$  is determined per-LB), separately for both Pb+Pb data-taking years, resulting in

$$p_{\text{single}} = \begin{cases} 5.67 \times 10^{-2} & (2015) \\ 6.07 \times 10^{-2} & (2018) \end{cases} \quad , \quad p_{\text{mutual}} = \begin{cases} 1.74 \times 10^{-3} & (2015) \\ 1.88 \times 10^{-3} & (2018) \end{cases} . \quad (5.6)$$

The 0n0n fractions are finally corrected for electromagnetic pileup through

$$(w_{0n0n})_{i,j} \rightarrow \frac{(w_{0n0n})_{i,j}}{(1 - p_{\text{single}})(1 - p_{\text{mutual}})} . \quad (5.7)$$

The impact of the electromagnetic pileup correction increases the uncorrected 0n0n fractions by around 5%, which is primarily driven by the single EMD correction.

In practice, the  $w_{0n0n}$  are implemented in this analysis by fitting the histograms of 0n0n fractions with continuous functions of  $m_{\text{inv}}(\mu, \mu)$  for each  $|y(\mu, \mu)|$  bin. Two fit functions,

$$\begin{aligned} f_{\text{nominal}}(m_{\text{inv}}(\mu, \mu)) &= \exp(p_0 + p_1 m_{\text{inv}}(\mu, \mu)) , \\ f_{\text{alternate}}(m_{\text{inv}}(\mu, \mu)) &= p_0 + \exp(p_1 + p_2 m_{\text{inv}}(\mu, \mu)) , \end{aligned} \quad (5.8)$$

are used to determine a nominal and alternate version of the  $w_{0n0n}$ , where the alternate results are used to define a systematic uncertainty on the modeling of the 0n0n weights. These functions are chosen for the fits, as it is expected that the 0n0n fractions smoothly fall off with  $m_{\text{inv}}(\mu, \mu)$ , and asymptotically approach zero at very large invariant masses.

The 0n0n fractions after the EM pileup corrections, and the resulting fits, are shown in Fig. 5.3. Both fit functions describe the data reasonably well.

### MadGraph5\_aMC@NLO to STARlight reweighting

The weight  $w_{\text{MG5-SL}}$  is only relevant for the  $\gamma\gamma \rightarrow \mu^+\mu^- + \gamma$  sample, as it converts the photon flux of the proton (used in the generation) into that of the Pb ion. It is defined as the ratio of particle-level cross-sections of  $\gamma\gamma \rightarrow \mu^+\mu^-$  scattering in Pb+Pb and proton-proton collisions simulated using STARlight and MadGraph5\_aMC@NLO respectively. The weight is differential in the particle-level  $m_{\text{inv}}(\mu, \mu)$  and  $|y(\mu, \mu)|$ , and also accounts for the overlap between the STARlight  $\gamma\gamma \rightarrow \mu^+\mu^-$  and MadGraph5\_aMC@NLO  $\gamma\gamma \rightarrow \mu^+\mu^- + \gamma$  samples, by removing the  $\gamma\gamma \rightarrow \mu^+\mu^- + \gamma$  events from STARlight events showered by Pythia8, which have photons with  $p_T < 2$  GeV.



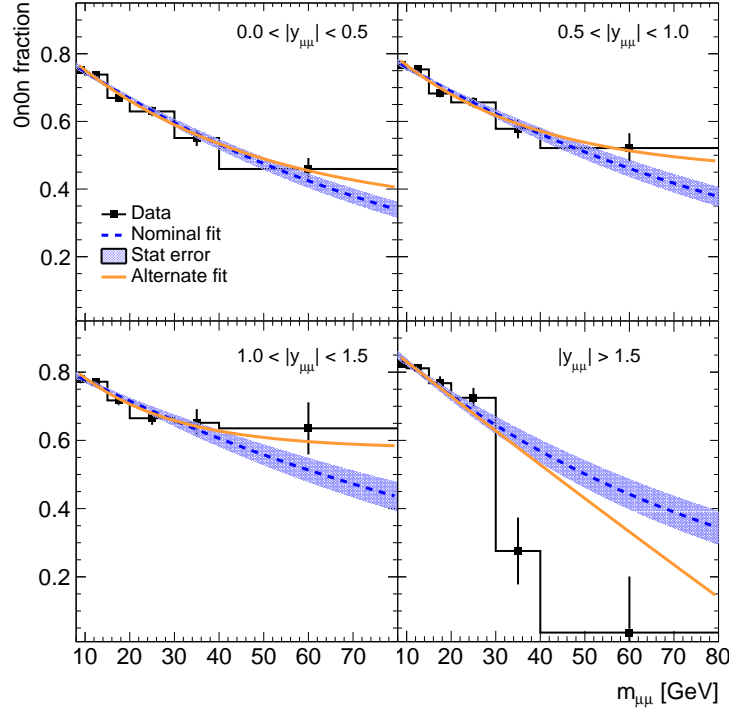


**Figure 5.3:** Derived 0n0n weights in the four  $|y(\mu, \mu)|$  bins. The data (black squares) corresponds to the fraction of  $\gamma\gamma \rightarrow \mu^+\mu^-$  events with  $E_{\text{ZDC}}^{\text{A,C}} < 1$  TeV, and is corrected for electromagnetic pileup. The shaded band corresponds to the  $1\sigma$  statistical uncertainty of the nominal fit function (blue dashed line). The alternate fit is shown in orange.

### 5.3.3 Detector performance modeling

The detector performance modeling weights,  $w_{\text{det}}$ , reconcile any differences between the data and Monte Carlo simulations, that are associated with the imperfect simulation of the detector performance. The weight for an event  $i$  is given by the product of the following factors:

- $w_{\text{L1 trig SF}}$ : The efficiencies of the L1 triggers in both data-taking years were measured separately in data and Monte Carlo, according to the methods outlined in Sec. 5.2. Observed differences are captured in the ratio  $w_{\text{L1 trig SF}} = \frac{\epsilon_{\text{L1 trig, data}}}{\epsilon_{\text{L1 trig, MC}}}$ , which are then consistently applied to simulated events, so that the performance of the L1 triggers in simulation matches that of the data.
- $w_{\text{HLT trig SF}}$ : The same as  $w_{\text{L1 trig SF}}$ , but for the HLT triggers in both data-taking years.
- $w_{\text{FgapAC3 SF}}$ : The efficiency of the FgapAC3 selection was found to be 99.1% in data and 100% in simulation. Thus, a global scale factor,  $w_{\text{FgapAC3 SF}} = 0.991$ , is used to account for this difference in the 2018 Monte Carlo samples.
- $w_{\text{topocluster}}$ : The number of unmatched topoclusters in  $\gamma\gamma \rightarrow \mu^+\mu^-$  events is found to be larger in Monte Carlo simulations than in data by 2.5%. Thus, a global scale factor of  $w_{\text{topocluster}} = 0.975$  is introduced to address this mis-modeling.

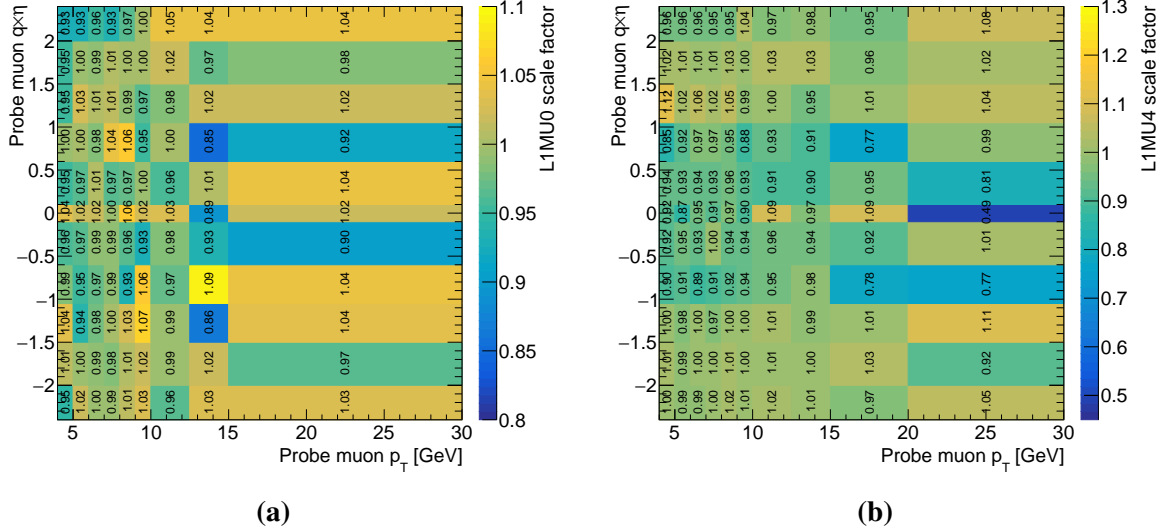


**Figure 5.4:** L1 trigger scale factors for (a) MU0 in 2015 data and (b) MU4 in 2018 data, as a function of the probe muon  $p_T$  and  $q \times \eta$ .

- $w_{\text{electron reco+id SF}}$ : Differences in the total reconstruction+identification efficiency of electrons at the level of 5% are observed between data and Monte Carlo, for electrons with  $p_T > 4$  GeV (see Sec. 5.4.3). These differences are captured in the scale factors  $w_{\text{electron reco+id SF}} = \frac{\epsilon_{\text{electron reco+id, data}}}{\epsilon_{\text{electron reco+id, MC}}}$ , and are applied as a function of electron  $p_T$ .
- $w_{\text{muon reco+id SF}}$ : Differences in the total reconstruction+identification efficiency of muons at the level of 2% are observed between the data and Monte Carlo, for muons with  $p_T > 4$  GeV (see Sec. 5.4.5). These differences are captured in the scale factors  $w_{\text{muon reco+id SF}} = \frac{\epsilon_{\text{muon reco+id, data}}}{\epsilon_{\text{muon reco+id, MC}}}$ , and are applied as a function of muon  $p_T$ .

Among the detector performance modeling weights, the L1 trigger scale factors have the largest impact on the Monte Carlo simulations. They are shown in Fig. 5.4.

### 5.3.4 Spin correlation effects

Since the decay of the tau lepton proceeds via the chiral weak interaction, it is important to properly model the effect of spin correlations in the tau production and decay (see Sec. 2.3.4). The Monte Carlo samples of  $\gamma\gamma \rightarrow \tau^+\tau^-$  scattering described in Sec. 5.3.1 somewhat mis-model the spin correlation effects, as the `Pythia8` and `Tauola` versions used in those samples included the  $\gamma^* \rightarrow \tau^+\tau^-$  spin correlations. It is not expected that the modeling of spin correlation effects significantly impacts the measurement of the  $\gamma\gamma \rightarrow \tau^+\tau^-$  fiducial cross-sections performed in this analysis. The effect, if treated as a modeling uncertainty, largely vanishes in the unfolding procedure. However, spin correlation effects can be relevant in the interpretation of the measured cross-sections, particularly in the extraction of constraints on the tau lepton's EMDMs, which are quantities inherently related to spin.

In order to investigate the impact of full spin correlations in this analysis, a Monte Carlo

study was performed using a sample of 45 million events generated with the following setup. The `gammaUPC` generator [78] was used to simulate the photon flux from Pb ions, using the Woods-Saxon charge distribution. The `MadGraph5_aMC@NLO` generator was used to simulate the  $\gamma\gamma \rightarrow \tau^+\tau^-$  hard scattering, and the taus were decayed using `Tauola`. The `TauSpinner` [89] generator was then used to compute the spin weights  $w_{\text{spin}}$  on an event-by-event basis. Unlike in the ATLAS samples, `Pythia8` was not used to simulate photon radiation before the tau decay. The current version of `TauSpinner` does not recognize final states of tau decays that are not hard-coded into `Tauola`, so allowing for additional photon radiation beyond what `Tauola` already simulates would result in a large fraction of generated events not being considered in the study of spin correlation effects. A charged particle-level filter identical to the one used in the ATLAS sample was included in the post-processing.

Following the event generation, the fiducial objects were constructed, and the fiducial selections were applied (see Sec. 5.7.1). The raw yield of events in the  $\mu 1\text{T-FR}$ ,  $\mu 3\text{T-FR}$  and  $\mu e\text{-FR}$  regions was approximately 137.0k, 36.7k and 13.6k, respectively, which is about four times larger than the raw yield of events in the ATLAS samples for either of the two data-taking years. The particle-level differential cross-sections for the observables listed in Tab. 5.1 were constructed, using the same binning as in Sec. 5.7.2. In the weighting, only the theoretical modeling weights given in Eq. 5.2 were included. Two versions of the cross-sections, called the *polarized* cross-sections  $\frac{d\sigma^{\text{pol}}}{dx}$  and the *un-polarized* cross-sections  $\frac{d\sigma^{\text{unpol}}}{dx}$  were created by including and excluding the  $w_{\text{spin}}$  in the event weights.

The ratio of the polarized and un-polarized cross-sections for each kinematic observable was taken as a measure of the spin correlation effects. This follows from Eq. 2.82, which implies the relation

$$\left(\frac{d\sigma^{\text{pol}}}{dx}\right) \bigg/ \left(\frac{d\sigma^{\text{unpol}}}{dx}\right) \equiv w_{\text{spin}}. \quad (5.9)$$

By construction, the average spin weight for a given process, denoted by  $\langle w_{\text{spin}} \rangle$ , should be unity. However, this is only true for inclusive processes, i.e. when no phase space cuts are applied. In the presence of cuts, such as the fiducial selections applied in this study,  $\langle w_{\text{spin}} \rangle$  can differ from unity. Thus, the ratio of polarized to un-polarized cross-sections is normalized by the  $\langle w_{\text{spin}} \rangle$  of the given fiducial region, in order to restore the average.

The results of the study are shown in Fig. 5.5 for all kinematic observables in each of the fiducial regions. In the  $\mu e\text{-FR}$  region, the presence of one light lepton and two (undetected) neutrinos per tau decay, dilutes the available spin information in the fiducial cross-sections, resulting in the ratio of polarized and un-polarized cross-sections being close to unity (within statistical uncertainties). In the  $\mu 3\text{T-FR}$  region, the presence of intermediate resonances in the hadronic decay chains (such as  $\tau^- \rightarrow \nu_\tau a_1^- \rightarrow \nu_\tau \rho^0 \pi^- \rightarrow \nu_\tau \pi^+ \pi^- \pi^-$  [215]) and the undetected neutral pions also weakens the impact of spin correlations.

In contrast, distributions in the  $\mu 1\text{T-FR}$  region exhibit strong sensitivity to spin correlation

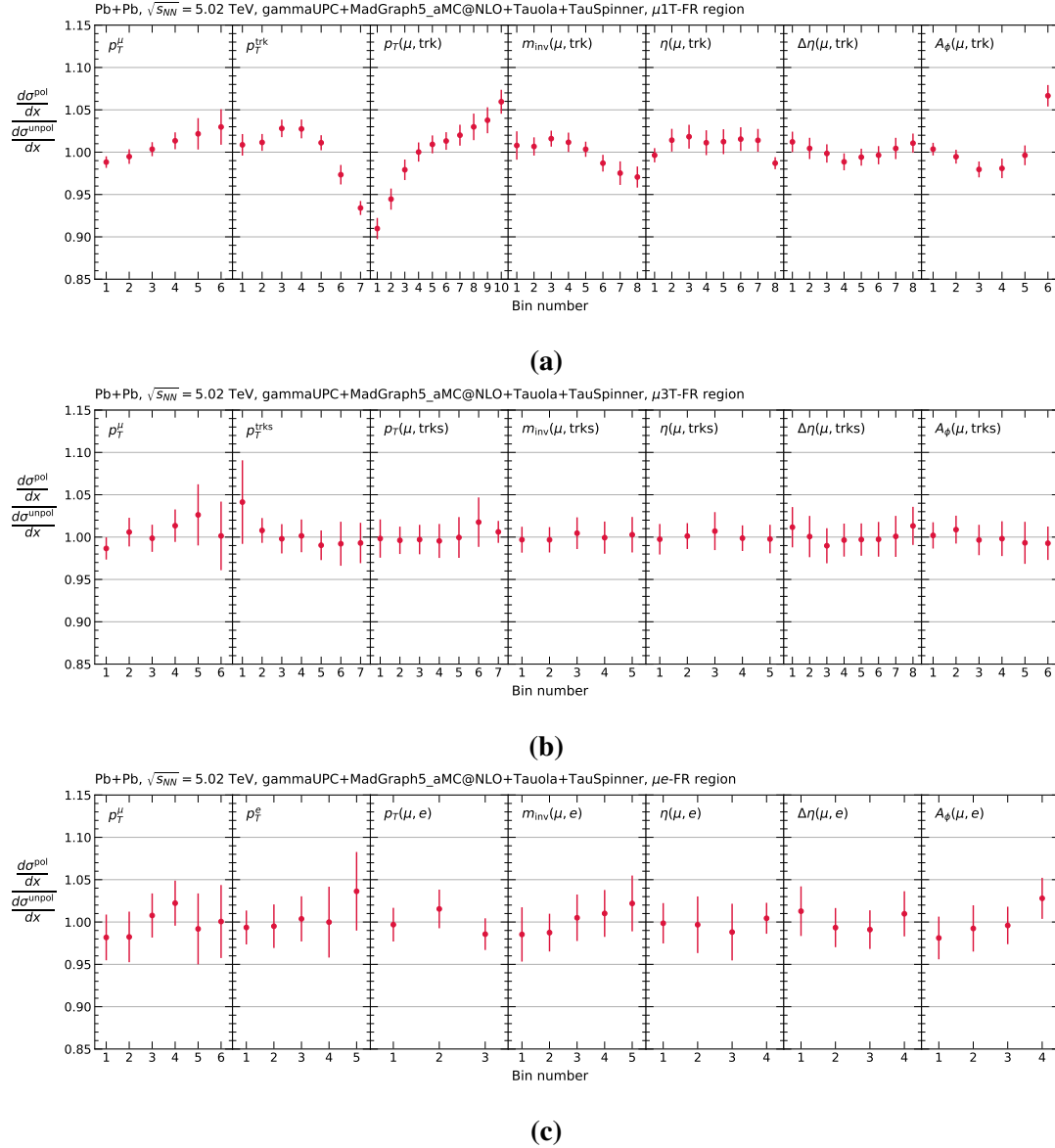


**Figure 5.5:** Ratio of polarized and un-polarized particle-level cross-sections, for all bins of the kinematic observables of interest in the (a)  $\mu 1T$ -FR, (b)  $\mu 3T$ -FR and (c)  $\mu e$ -FR regions. Error bars correspond to the statistical uncertainties.

effects. In particular, the  $p_T^{\text{trk}}$ ,  $p_T(\mu, \text{trk})$  and  $A_\phi(\mu, \text{trk})$  variables show deviations of up to 5-10% in the tails. This can be understood as follows. The  $\mu 1T$ -FR selection primarily contains the  $\tau^- \rightarrow \nu_\tau \pi^-$  and  $\tau^- \rightarrow \nu_\tau \rho^- \rightarrow \nu_\tau \pi^- \pi^0$  decays on the hadronic side of the  $\tau\tau$  decay, since they have the largest branching ratios (see Fig. 2.5a). For the single pion decay, the polarimetric vector is simply given by the direction of flight of the charged pion [216]. Thus, observables that are related to the transverse direction of the charged hadrons, like  $p_T^{\text{trk}}$ ,  $p_T(\mu, \text{trk})$  and  $A_\phi(\mu, \text{trk})$ , are more sensitive to spin correlation effects, compared to observables related to the pseudo-rapidity and “energy” (i.e.  $p_T$  and invariant mass) of the involved objects.

Based on these observations, the effect of spin correlations in the study of the  $\gamma\gamma \rightarrow \tau^+\tau^-$  process is only considered for the  $\mu 1T$ -FR region. Due to the presence of photon radiation

before the tau decays in the ATLAS samples of  $\gamma\gamma \rightarrow \tau^+\tau^-$  scattering, the results of the spin correlation study cannot be included on an event-by-event basis. Instead, they are included as a bin-by-bin correction factor, when the various available Monte Carlo predictions are compared to the measured cross-sections in data.

## 5.4 Object and event selections

### 5.4.1 Tracks and vertices

Tracks are reconstructed using the procedure described in Sec. 3.3.1, and are selected for the analysis using the LoosePrimary working point (WP), with additional kinematic requirements of  $p_T > 0.1$  GeV,  $|\eta| < 2.5$  and  $|d_0| < 1.5$ . Following the notation of track variables introduced in Sec. 4.2.1, the LoosePrimary WP applies the following selections [195]:  $N_{\text{hits}}^{\text{Si}} \geq 7$  if  $N_{\text{sh. mod.}}^{\text{Si}} = 0$ ,  $N_{\text{hits}}^{\text{Si}} \geq 10$  if  $N_{\text{sh. mod.}}^{\text{Si}} = 1$ ,  $N_{\text{holes}}^{\text{Si}} < 2$ , and  $N_{\text{holes}}^{\text{Pix}} < 1$ . The tracking efficiency was studied in Monte Carlo simulations using charged pions produced in  $\gamma\gamma \rightarrow \tau^+\tau^-$  events. It was defined as the fraction of truth pions that are reconstructed and identified as LoosePrimary tracks, and was estimated as a function of the truth pion  $p_T$ . The efficiency was observed to follow a sigmoid-like curve, being around 10% at  $p_T = 0.1$  GeV, around 85% at  $p_T = 0.6$  GeV, and eventually saturating at 90% for  $p_T \geq 2$  GeV.

As this analysis uses Pb+Pb collision datasets with  $\mathcal{O}(10^{-3})$  pileup, and targets final states with very low charged particle multiplicities, it is reasonable to not impose the presence of at least one reconstructed primary vertex in the selected events. Nevertheless, requirements on the transverse impact parameters ( $d_0$ 's) of track-based objects like electrons and muons are imposed to suppress tracks that do not originate from Pb+Pb collisions. The difference between the longitudinal impact parameters ( $z_0$ 's) of the selected muons and other object(s) – namely the track, tracks, and electron, in the  $\mu 1\text{T-SR}$ ,  $\mu 3\text{T-SR}$  and  $\mu e\text{-SR}$  regions respectively – was also investigated. The difference was found to be consistent with zero up to the  $z_0$  reconstruction resolution, indicating that all final state particles originate from a single Pb+Pb collision vertex at the interaction point.

### 5.4.2 Topoclusters

Topoclusters are reconstructed from the calorimeter energy deposits as outlined in Sec. 3.3.3. They are required to have  $|\eta| < 4.9$ , with  $p_T > 1$  GeV for  $|\eta| < 2.5$  and  $p_T > 0.1$  GeV for  $2.5 < |\eta| < 4.9$ .

As this analysis focuses on very low  $p_T$  objects, topoclusters and the objects reconstructed from them (i.e. electrons and photons) are susceptible to low  $p_T$  calorimeter noise. Typically, noisy calorimeter cells are masked during a quality assessment procedure immediately following data-taking. However, the standard procedure focuses on topoclusters with  $p_T > 10$  GeV, which exceeds the typical energy scale of the objects in this analysis.

Thus, a dedicated noise cleaning procedure was considered. The contribution of electronic

noise to the topocluster formation was suppressed by an  $\eta$ -dependent cell significance cut, as outlined in Ref. [217]. Signals from large-scale coherent noise, called *noise bursts*, are known to occur in the LAr calorimeters, possibly due to issues related to the high voltage supply [218]. Regions of the calorimeter layers containing topoclusters formed due to noise bursts, called *hotspots*, were identified by selecting events simultaneously passing  $\gamma\gamma \rightarrow e^+e^-$ ,  $\gamma\gamma \rightarrow \mu^+\mu^-$  and cosmic<sup>3</sup> selections. Only those topoclusters that passed the cell significance cuts and were not matched to the selected leptons were considered for the hotspot finding procedure. In the 2018 data, one hotspot of width  $\Delta\eta \times \Delta\phi = 0.2 \times 0.2$  around  $(\eta, \phi) = (-2.3, 0.1)$  was found in the first HEC layer, along with other smaller ( $< 0.1$  width in both  $\eta$  and  $\phi$ ) hotspots in the second HEC layer and first FCal layer. The topoclusters contained in these hotspot regions were then excluded from the analysis.

The topocluster reconstruction efficiency was studied using the tag-and-probe method in  $\gamma\gamma \rightarrow e^+e^- + \gamma$  events, with exactly one identified electron and two tracks. One track is required to pass the `TightPrimary` working point [195] with no matching requirements to the electrons; the second track is matched to an electron, with no quality conditions being imposed. The identified electron is treated as the tag object. If the unidentified electron were to emit a bremsstrahlung photon, a  $p_T$  imbalance between the identified electron, called  $e$ , and unmatched track, called “trk”, would be observed. Thus, the  $p_T$  of the (assumed) bremsstrahlung photon, given by  $p_T^\gamma \approx E_T^e - p_T^{\text{trk}}$ , serves as the probe object. The topocluster reconstruction efficiency is then given by the fraction of all selected events that have a topocluster matched within  $\Delta R = 0.3$  to the probe. The efficiency was found to be around 97% in both data and Monte Carlo, with negligible dependence on  $p_T^\gamma$  and  $\eta^{\text{trk}}$ .

In the selected  $\gamma\gamma \rightarrow e^+e^- + \gamma$  events, the  $p_T$  of the identified electron and the cluster+track system should be similar, due to the transverse momentum of the initial state being almost zero. The  $(p_T^e - p_T^{\text{clus+trk}})$  balance was therefore used to characterize the topocluster energy response in both data and Monte Carlo. Small differences in the mean topocluster energy response in data and Monte Carlo were observed, at the level of  $\mathcal{O}(0.01)$  GeV for  $p_T^{\text{clus}} \in [2, 4]$  GeV and  $\mathcal{O}(0.1)$  GeV for  $p_T^{\text{clus}} < 2$  GeV and  $p_T^{\text{clus}} > 4$  GeV. These differences are treated as a systematic uncertainty (see Sec. 5.8).

### 5.4.3 Electrons

The reconstruction of electrons follows the procedure described in Sec. 3.3.4. The electrons are required to have  $p_T > 4$  GeV,  $|d_0| < 0.5$  mm and  $|\eta| < 2.47$ , excluding the crack region of  $1.37 < |\eta| < 1.52$ .

The electron reconstruction and identification efficiency was studied in  $\gamma\gamma \rightarrow e^+e^-$  events in the ATLAS measurement of  $\gamma\gamma \rightarrow \gamma\gamma$  scattering using Run 2 Pb+Pb collisions [170]. Can-

---

<sup>3</sup>This selection used a dedicated trigger targeting low detector activity ( $E_T < 3$  GeV in both sides of the FCal, less than 15 pixel hits, total calorimeter energy between 4 and 200 GeV) in empty BCIDs. It was used in Ref. [170] to study low  $p_T$  backgrounds due to cosmic radiation.

didate events were selected using a trigger targeting the presence of topoclusters, and minimal activity in the Pixel detector and calorimeters. The efficiency was measured using the tag-and-probe method, where the tag object was an electron passing the `Tight` selection, and the probe objects were pixel-tracks<sup>4</sup>. Topoclusters were not chosen as the probe object due to the low topocluster reconstruction efficiency as a function of pseudorapidity (around 40% on average), which was determined by comparison to particle-level electrons. Dielectron events were then selected based on the presence of oppositely charged tag+probe pairs with invariant mass greater than 5 GeV, and acoplanarities of less than 0.1.

The electron reconstruction efficiency  $\epsilon_{\text{reco}}$  was then defined as the fraction of pixel-tracks that were reconstructed as good-quality electrons, and was determined as a function of the tag electron  $p_T$ . The efficiency was around 30% at  $p_T = 3$  GeV, and was found to rise slowly until a plateau of 95% was reached around  $p_T = 15$  GeV. The electron identification efficiency  $\epsilon_{\text{id}}$  was defined as the fraction of probes identified as good-quality electrons that were also reconstructed as electrons passing the `Loose` selection, and was determined as a function of the tag electron  $p_T$ . The identification efficiency was found to be approximately flat at around 90%, increasing only by a few percent with the tag electron  $p_T$ . The total electron reconstruction+identification efficiency is given by the product  $\epsilon_{\text{reco}} \times \epsilon_{\text{id}}$ . Its shape as a function of the tag electron  $p_T$  follows that of  $\epsilon_{\text{reco}}$  scaled down by approximately 90%.

#### 5.4.4 Photons

The reconstruction of photons follows the procedure described in Sec. 3.3.4. The reconstructed photons are required to have  $E_T > 1.5$  GeV and  $|\eta| < 2.37$ , excluding the crack region of  $1.37 < |\eta| < 1.52$ .

A neural network-based algorithm, developed in Ref. [170], was used to identify photons originating from genuine hard scattering processes (i.e. *signal* photons), and reject photons originating from other sources like calorimeter noise and cosmic muons (i.e. *background* photons). The neural network was based on the `Keras` framework [220], and used variables related to the shape of the photon showers within the electromagnetic calorimeters to perform the signal-background discrimination. At a reference signal efficiency of 95%, the background rejection efficiency was 97% for photons with  $|\eta| < 1.37$ , and 87-90% for  $|\eta| > 1.52$ . The efficiency in data and Monte Carlo as a function of photon  $p_T$  and  $\eta$  were found to agree within 5%. As this analysis only uses the reconstructed photons to reject  $\gamma\gamma \rightarrow \mu^+\mu^- + \gamma$  backgrounds, these differences were not included in the Monte Carlo modeling. Further, no additional studies of the photon object performance were performed.

---

<sup>4</sup>Pixel-tracks are charged particle trajectories reconstructed using only the IBL and Pixel detectors, as opposed to the full Inner Detector. They have a very high (almost 100%) reconstruction efficiency in low density environments, and are less susceptible to ID material budget uncertainties than full ID tracks [219].



### 5.4.5 Muons

The reconstruction of muons using hits in the Inner Detector and Muon Spectrometer follows the procedure described in Sec. 3.3.5. Muons are required to have  $p_T > 4$  GeV,  $|\eta| < 2.4$ ,  $|d_0| < 0.3$  mm (measured with respect to the beamline), and must pass the `LowPt` working point selection. The total reconstruction efficiency of the `LowPt` WP is factorized as

$$\epsilon(\text{LowPt}) = \epsilon(\text{LowPt}|\text{ID}) \epsilon(\text{ID}|\text{MS}), \quad (5.10)$$

where  $\epsilon(\text{ID}|\text{MS})$  is the efficiency of a reconstructed MS track having a matched ID track, and  $\epsilon(\text{LowPt}|\text{ID})$  the efficiency of an ID track being identified as a `LowPt` muon.

Both components of the total efficiency were characterized using the tag-and-probe method in  $\gamma\gamma \rightarrow \mu^+\mu^-$  events, which were selected by requiring the presence of at most two opposite-charge ID tracks, and at least one muon passing any quality selection. The tag objects were defined as identified `LowPt` muons with  $p_T > 4$  GeV and  $|\eta| < 2.4$ . For evaluating the ID efficiency, the probe objects were taken to be MS tracks extrapolated back to the ID.  $\epsilon(\text{ID}|\text{MS})$  was then defined as the fraction of probes with a matched ID track within  $\Delta R < 0.1$ . For evaluating the MS efficiency, probes were defined as ID tracks passing the `Loose` muon selection.  $\epsilon(\text{LowPt}|\text{ID})$  was then taken to be the fraction of probes that were matched to identified `LowPt` muons within  $\Delta R < 0.01$ .

The muon reconstruction efficiencies were measured as a function of the probe  $p_T$  and  $q \times \eta$ . In both data and Monte Carlo, and for both data-taking years,  $\epsilon(\text{ID}|\text{MS})$  is approximately 99% at  $p_T^{\text{MS-trk}} = 4$  GeV and nearly 100% for higher  $p_T$ , while it is flat at around 99% with  $q \times \eta$ . Further,  $\epsilon(\text{LowPt}|\text{ID})$  is 90% at  $p_T^{\text{ID}} = 4$  GeV and flat at around 94% for higher  $p_T$  values; it is measured to be around 95% as a function of the probe  $q \times \eta$ , except for dips up to 85% for  $|q \times \eta| < 0.1$  and up to 90% for  $1 < |q \times \eta| < 1.5$ . These low efficiency regions correspond to regions of the MS coverage with limited coverage.

### 5.4.6 Event selections

The reconstruction-level selection of events in the three  $\gamma\gamma \rightarrow \tau^+\tau^-$  signal regions was developed in Ref. [3], and is the same for this analysis. Events are required to pass the low  $p_T$  muon triggers described in Sec. 5.2. Data events are required to have energy deposits below 1 TeV on both (i.e. A and C) sides of the ZDCs in order to select 0n0n events. In the Monte Carlo samples, this selection is replaced by the 0n0n reweighting. Then, region-specific selections are applied, which are detailed in Tab. 5.2.

These selections target exclusive final states with exactly one muon and either one track, three tracks, or one electron. The tracks are required to be separated from the electrons and muons by  $\Delta R > 0.1$ , in order to remove events with overlapping objects. Events in the  $\mu 1\text{T-SR}$  and  $\mu 3\text{T-SR}$  regions are required to have zero unmatched topoclusters, to limit the contamination from soft backgrounds. The sum of charges of the final state objects should



	$\mu 1\text{T-SR}$	$\mu 3\text{T-SR}$	$\mu e\text{-SR}$
Pass trigger	True	True	True
$E_{\text{ZDC}}^{\text{A}}$	$< 1 \text{ TeV}$	$< 1 \text{ TeV}$	$< 1 \text{ TeV}$
$E_{\text{ZDC}}^{\text{C}}$	$< 1 \text{ TeV}$	$< 1 \text{ TeV}$	$< 1 \text{ TeV}$
$N_{\mu}$	$= 1$	$= 1$	$= 1$
$N_e$	$= 0$	$= 0$	$= 1$
$N_{\text{trk}} (\Delta R > 0.1 \text{ from } \mu)$	$= 1$	$= 3$	$= 0$
$N_{\text{trk}} (\Delta R > 0.1 \text{ from } e)$	$-$	$-$	$= 0$
$N_{\text{topocluster}}^{\text{unmatched}}$	$= 0$	$= 0$	$-$
Sum of charges	$= 0$	$= 0$	$= 0$
$p_{\text{T}} (\mu, \text{trk})$	$> 1 \text{ GeV}$	$-$	$-$
$p_{\text{T}} (\mu, \text{trk}, \gamma)$	$> 1 \text{ GeV}$	$-$	$-$
$p_{\text{T}} (\mu, \text{trk}, \text{topocluster})$	$> 1 \text{ GeV}$	$-$	$-$
$m_{\text{inv}} (\text{trks})$	$-$	$< 1.7 \text{ GeV}$	$-$
$A_{\phi} (\mu, \text{trk(s)})$	$< 0.4$	$< 0.2$	$-$

**Table 5.2:** Selections applied for all three  $\gamma\gamma \rightarrow \tau^+\tau^-$  signal regions.  $E_{\text{ZDC}}^{\text{A,C}}$  are the reconstructed ZDC energies on the A and C side.  $N_{\mu,e,\text{trk}}$  are the number of reconstructed muons, electrons, and tracks. The tracks are required to be separated by  $\Delta R > 0.1$  from the light leptons.  $N_{\text{topocluster}}^{\text{unmatched}}$  is the number of unmatched topoclusters.  $m_{\text{inv}} (\text{trks})$  is the invariant mass of the three-track system. The nomenclature of the remaining selections has been introduced elsewhere in this chapter.

be zero, so that the oppositely charged tau leptons from  $\gamma\gamma \rightarrow \tau^+\tau^-$  scattering are selected. In the  $\mu 1\text{T-SR}$  region, the  $p_{\text{T}} (\mu, \text{trk}) > 1 \text{ GeV}$  requirement reduces the contamination from  $\gamma\gamma \rightarrow \mu^+\mu^-$  scattering, which is peaked towards lower values of  $p_{\text{T}} (\mu, \text{trk})$ . Additionally, the  $p_{\text{T}} (\mu, \text{trk}, \gamma) > 1 \text{ GeV}$  and  $p_{\text{T}} (\mu, \text{trk}, \text{topocluster}) > 1 \text{ GeV}$  conditions suppress the  $\gamma\gamma \rightarrow \mu^+\mu^- + \gamma$  background, by limiting the  $p_{\text{T}}$  of the muon+track+photon/topocluster systems, if a photon or topocluster within  $\Delta R < 1$  of the muon is reconstructed in the event. In the  $\mu 3\text{T-SR}$  region, the  $m_{\text{inv}} (\text{trks}) < 1.7 \text{ GeV}$  cut ensures that the three tracks originate from a tau decay. The cuts on the acoplanarity of the muon+track(s) systems in the  $\mu 1\text{T-SR}$  and  $\mu 3\text{T-SR}$  regions reduce the backgrounds from photonuclear processes, by requiring that the muon and track(s) be roughly back-to-back in the transverse plane.

## 5.5 Background estimation

Scattering processes besides  $\gamma\gamma \rightarrow \tau^+\tau^-$ , which also contribute to the total number of events observed in the signal regions, are collectively called *background* processes. The two largest background contributions are due to exclusive muon pair production and diffractive photonuclear scattering. The background contribution due to other processes like  $\gamma\gamma \rightarrow e^+e^-$ ,  $\gamma\gamma \rightarrow q\bar{q}$ , and non-diffractive photonuclear processes were found to be negligible in Ref. [3], and are therefore not considered further. As an advancement of the background estimation studies performed in Ref. [3], this analysis also investigated the contribution of simultaneous UPC scattering.

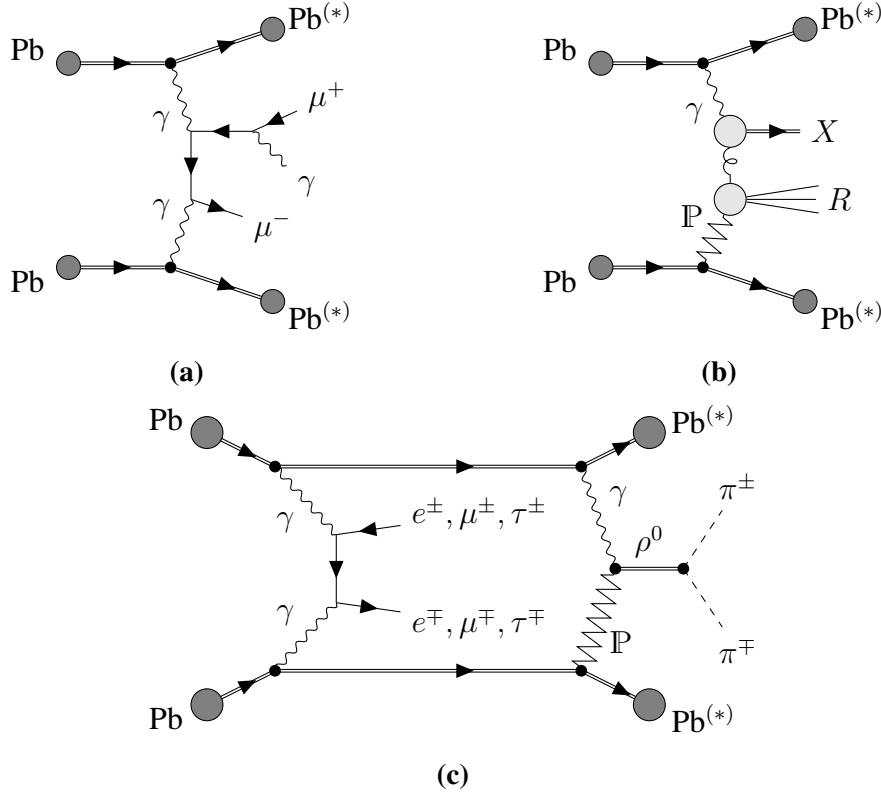


**Figure 5.6:** Schematic diagrams of scattering processes in ultra-peripheral Pb+Pb collisions that constitute the backgrounds in this analysis: (a)  $\gamma\gamma \rightarrow \mu^+\mu^- (+\gamma)$  scattering, (b) diffractive photonuclear particle production, and (c) simultaneous  $\gamma\gamma \rightarrow \ell^+\ell^-$  (where  $\ell = e, \mu, \tau$ ) and  $\gamma P \rightarrow \rho^0 \rightarrow \pi^+\pi^-$  scattering. Effective vertices are denoted by black dots and light-gray filled circles.

### 5.5.1 Exclusive muon pair production

Exclusive muon pair production, shown in Fig. 5.6a, is the largest individual background source in this analysis. If one of the muons from  $\gamma\gamma \rightarrow \mu^+\mu^-$  scattering is not fully reconstructed as a muon, but simply as an ID track, it can contribute to the  $\mu 1\text{T-SR}$  region. The process can contribute to the  $\mu 3\text{T-SR}$  region if additional tracks are reconstructed from the conversion of bremsstrahlung photons into  $e^+e^-$  pairs. If one of the converted electrons is fully reconstructed, the process can also contribute to the  $\mu e\text{-SR}$  region. Such extra tracks and electrons can also arise from the interaction of the muons with the detector material.

The contribution of  $\gamma\gamma \rightarrow \mu^+\mu^-$  scattering to the total background is modeled with Monte Carlo simulations, using the samples described in Sec. 5.3.1. The quality of the simulations is checked in a dedicated two-muon *control region*, called  $2\mu\text{-CR}$ . Events in this control region are required to pass the muon trigger selection (see Sec. 5.2), have  $E_{\text{ZDC}}^{\text{A,C}} < 1$  TeV, exactly two oppositely charged muons with  $p_{\text{T}} > 4$  GeV and with an invariant mass larger than 11 GeV (to suppress the contribution of  $\gamma P \rightarrow \Upsilon \rightarrow \mu\mu$ ), and no tracks that are separated by  $\Delta R > 0.1$  from the muons. The weights defined in Eq. 5.1 are considered in the modeling of the  $\gamma\gamma \rightarrow \mu^+\mu^-$  Monte Carlo sample. The contribution of  $\gamma\gamma \rightarrow \tau^+\tau^- \rightarrow \mu\mu 4\nu$  scattering to the

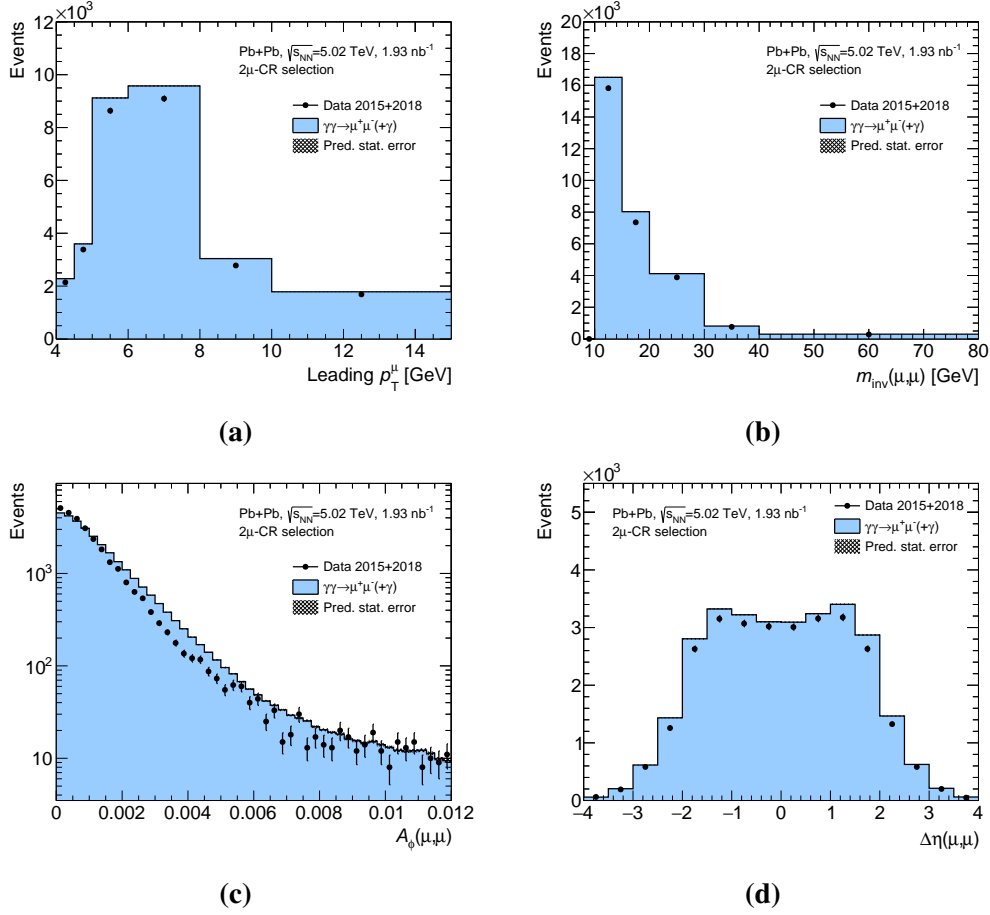


**Figure 5.7:** Kinematic distributions in the  $2\mu$ -CR region: (a) leading muon  $p_T$ , (b)  $m_{\text{inv}}(\mu, \mu)$  i.e. dimuon invariant mass, (c)  $A_\phi(\mu, \mu)$  i.e. dimuon acoplanarity, and (d)  $\Delta\eta(\mu, \mu)$  i.e. pseudorapidity difference between the two muons.

$2\mu$ -CR region, determined using simulations, is at the level of 0.1%, and is therefore considered negligible.

Kinematic distributions of the two muons in the  $2\mu$ -CR region are shown in Fig. 5.7. Overall, the Monte Carlo sample is able to describe the data reasonably well. The Monte Carlo sample is about 5% above the data and is slightly mis-modeled in the  $A_\phi(\mu, \mu)$  variable (see Fig. 5.7c). However, since the fraction of background events relative to the total data yield in the three  $\gamma\gamma \rightarrow \tau^+\tau^-$  signal region is only 5-15% (see Tab. 5.3), the observed mis-modeling of  $\gamma\gamma \rightarrow \mu^+\mu^-$  scattering in the  $2\mu$ -CR region is considered acceptable.

### 5.5.2 Diffractive photonuclear processes

Diffractive photonuclear scattering processes also contribute to the total background in the  $\gamma\gamma \rightarrow \tau^+\tau^-$  signal regions. The term “diffractive” in this context is borrowed from wave optics, where diffraction fringes are formed when the wavelength of a probe is larger than the size of a target. In UPCs, the probes are typically low energy photons and pomerons, which are emitted by the colliding ions. The exchanged particles can interact with the ions *directly*,

or through *resolved* processes, where the particle fluctuates into a virtual hadronic state before the hard scattering. In the case of resolved processes, the presence of the virtual hadronic state can result in soft hadronic particles being produced in the forward direction, filling the rapidity gap on one side of the detector [221]. An example of such a process is shown in Fig. 5.6b, where a direct photon and a resolved pomeron create a central system  $X$ , with  $R$  being the soft *remnants* of the resolved pomeron.

The contribution of diffractive photonuclear processes to the signal regions is estimated using a data-driven approach, exploiting the signature of a central system with additional soft particles being present in the final state. Two control regions are defined with respect to the  $\mu$ 1T-SR and  $\mu$ 3T-SR regions, called  $\mu$ 2T-CR and  $\mu$ 4T-CR respectively, by loosening the signal region definitions to allow for more event activity. They are defined by relaxing the  $N_{\text{topocluster}}^{\text{unmatched}} = 0$  requirement to  $N_{\text{topocluster}}^{\text{unmatched}} \leq 8$ , by removing the  $E_{\text{ZDC}}^{\text{A,C}} < 1$  TeV cuts, and by allowing for one more track (not within  $\Delta R < 0.1$  of the muon) with  $p_T < 0.5$  GeV. To reduce the contribution of  $\gamma\gamma \rightarrow \tau^+\tau^-$  events in the  $\mu$ 2T-CR region, the invariant mass of the two tracks is required to be larger than 1 GeV, and the acoplanarity between the muon and the leading track must be less than 0.2. In the  $\mu$ 4T-CR region, the sum of charges requirement is dropped. No control region is defined for the  $\mu e$ -SR region, as the contribution of photonuclear backgrounds is negligible due to the high signal purity.

The distributions of the kinematic observables in the control regions are used to define templates for the photonuclear backgrounds. The templates are normalized to the total number of data events in the  $4 \leq N_{\text{topocluster}}^{\text{unmatched}} \leq 8$  region, where the contribution of  $\gamma\gamma \rightarrow \mu^+\mu^-$  and  $\gamma\gamma \rightarrow \tau^+\tau^-$  scattering events is found to be zero using simulation. Examples of the data distributions in the  $4 \leq N_{\text{topocluster}}^{\text{unmatched}} \leq 8$  region in the  $\mu$ 2T-CR and  $\mu$ 4T-CR regions are shown in Fig. 5.8, together with the normalized photonuclear background templates. The shape of the templates after normalization agrees with the data reasonably well.

### 5.5.3 Multiple UPC scattering

Due to the strong flux of electromagnetic fields surrounding heavy ions at ultra-relativistic energies, there is the possibility of multiple photon-induced scattering processes to occur between the same pair of colliding ions (see Fig. 5.6c). Recently, the ATLAS collaboration measured, for the first time, the rate of coincident  $\gamma\gamma \rightarrow \mu^+\mu^-$  and  $\gamma\mathbb{P} \rightarrow \rho^0 \rightarrow \pi^\pm\pi^\mp$  scattering using Run 2 and Run 3 Pb+Pb collisions [222]. The analysis identified events with two oppositely charged muons, and a pair of low- $p_T$  tracks with an invariant mass close to  $m_{\rho^0} = 0.77$  GeV [37]. The rate of such events relative to exclusive  $\gamma\gamma \rightarrow \mu^+\mu^-$  events was found to be around one percent depending on the ZDC selection. In particular, the observed fraction for the 0n0n selection was around 0.2%-0.4% depending on  $m_{\text{inv}}(\mu, \mu)$ .

Simultaneous UPC processes alongside  $\gamma\gamma \rightarrow \tau^+\tau^-$  production can potentially spoil the exclusivity of the signal regions defined in this analysis. In addition, the observation of simultaneous  $\gamma\gamma \rightarrow \mu^+\mu^-$  and  $\gamma\mathbb{P} \rightarrow \rho^0 \rightarrow \pi^\pm\pi^\mp$  scattering may merit a correction to the

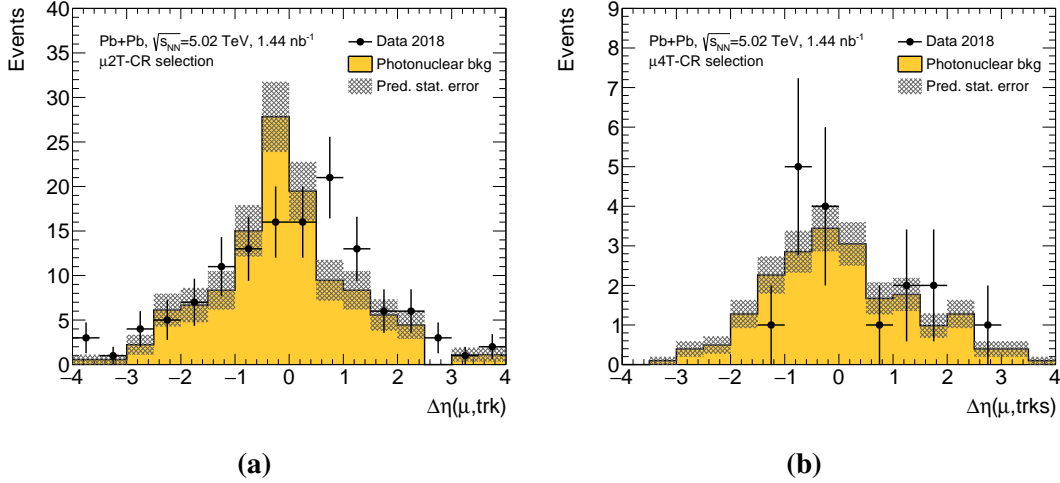


**Figure 5.8:** Photonuclear background estimate in 2018 data, after requiring  $4 \leq N_{\text{topocluster}}^{\text{unmatched}} \leq 8$ , for the (a)  $\Delta\eta(\mu, \text{trk})$  observable in the  $\mu 2\text{T-CR}$  region, and (b)  $\Delta\eta(\mu, \text{trks})$  observable in the  $\mu 4\text{T-CR}$  region. The shaded region corresponds to the statistical uncertainty of the background estimate.

$\gamma\gamma \rightarrow \mu^+\mu^-$  background modeling. Based on the results of Ref. [222], these corrections are expected to be small, but it is nevertheless relevant to study them in this analysis.

Through Monte Carlo simulation alone, it is not easily possible to determine if simultaneous  $\rho^0$  production accompanies  $\gamma\gamma \rightarrow \mu^+\mu^-$  or  $\gamma\gamma \rightarrow \tau^+\tau^-$  scattering. Thus, a more general data-driven study was performed to probe the impact on this analysis. The strategy was to relax the track vetoes in the signal region definitions to allow for additional soft tracks, which are assumed to be pions, and to search for track pairs consistent with a  $\rho^0$  signature, i.e.  $\Delta\phi \approx \pi$  and  $m_{\text{inv}} \approx 0.77$  GeV. Allowing for arbitrarily many tracks would lead to additional contamination from photonuclear processes, so the  $\mu 1\text{T-SR}$  and  $\mu 3\text{T-SR}$  regions were extended by up to two additional tracks. The corresponding control regions are called  $\mu 1\text{T}+n\text{T-CR}$  and  $\mu 3\text{T}+n\text{T-CR}$ , with  $n = 1, 2$ . The  $\mu e\text{-SR}$  region was not investigated due to the limited statistics.

The signature of coincident  $\gamma\text{P} \rightarrow \rho^0 \rightarrow \pi^\pm\pi^\mp$  scattering was searched for in the control regions using only the 2018 data<sup>5</sup>. Only two candidates for simultaneous  $\rho^0$  mesons were found: one in the  $\mu 1\text{T}+1\text{T-CR}$  region combining the leading and sub-leading tracks, and one in the  $\mu 3\text{T}+1\text{T-CR}$  combining the sub-leading and sub-sub-leading tracks. The corresponding  $\Delta\phi - m_{\text{inv}}$  correlations are shown in Fig. 5.9. Several other  $\rho^0$  candidates with nearby (i.e.  $\Delta\phi \sim 0$ ) pions are also observed in the correlation plots. These are assumed to originate in the decay chain of the tau lepton to three pions, e.g. in the  $\tau^- \rightarrow \nu_\tau a_1^- \rightarrow \nu_\tau \rho^0 \pi^- \rightarrow \nu_\tau \pi^+ \pi^- \pi^-$  decay.

Based on the above observations, it was concluded that the background contribution of simultaneous UPC scattering to the signal regions in this analysis is negligible. It was therefore not considered in the subsequent studies.

<sup>5</sup>Including the 2015 data (25% of the total Run 2 dataset) does not change the conclusions of the study.

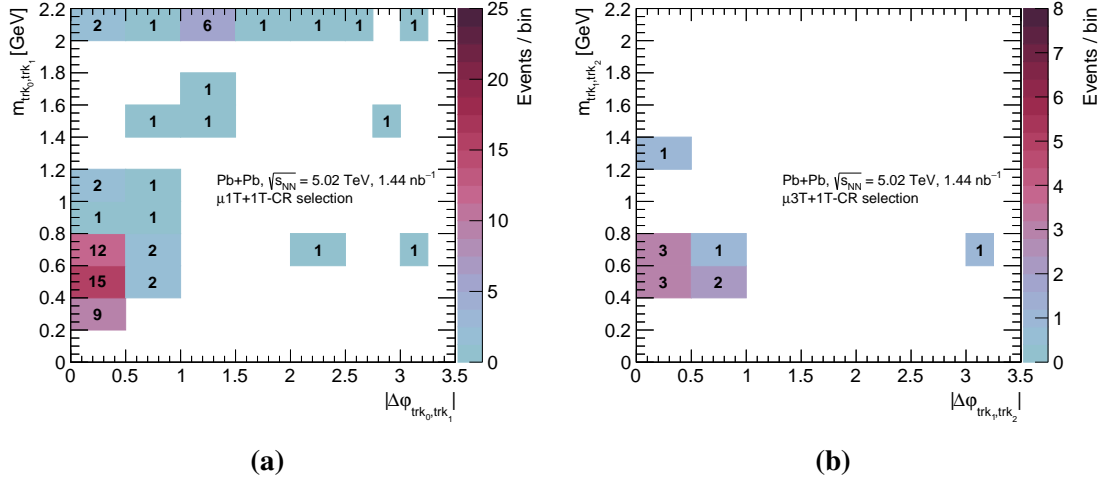


**Figure 5.9:**  $\Delta\phi$  and invariant mass correlation between (a) the leading ( $trk_0$ ) and sub-leading ( $trk_1$ ) tracks in the  $\mu 1T+1T$ -CR region, and (b) sub-leading ( $trk_1$ ) and sub-sub-leading ( $trk_2$ ) tracks in the  $\mu 3T+1T$ -CR region.

It should be noted that a recent update to *SuperChic* included, for the first time, an approach to modeling simultaneous  $\gamma\gamma \rightarrow \mu^+\mu^-$  and  $\gamma P \rightarrow \rho^0 \rightarrow \pi^\pm\pi^\mp$  scattering, albeit with a normalization of the  $\rho^0$  photo-production cross-section in UPCs to an ALICE measurement of the same [223]. This update, which successfully explains the results of [222], was not available the time of writing this thesis. Regardless, the impact of simultaneous UPC processes on this analysis is negligible, so the studies do not have to be revisited with updated Monte Carlo generators.

## 5.6 Reconstruction-level distributions

The distributions of the kinematic observables defined in Tab. 5.1 are shown at reconstruction-level in Figs. 5.10 to 5.12 for the  $\mu 1T$ -SR,  $\mu 3T$ -SR and  $\mu e$ -SR regions respectively. The combined signal and background predictions are found to model the data reasonably well across all of the observables. The number of signal, background and data events entering these histograms is given in Tab. 5.3.

	$\mu 1T$ -SR	$\mu 3T$ -SR	$\mu e$ -SR
Signal $\gamma\gamma \rightarrow \tau^+\tau^-$ ( $S$ )	633.4	115.9	43.4
$\gamma\gamma \rightarrow \mu^+\mu^-$	100.0	10.1	4.4
Photonuclear background	15.6	3.2	–
Total background ( $B$ )	115.6	13.3	4.4
$S + B$	749.0	129.2	47.8
Data	723	124	53

**Table 5.3:** Yields of signal, background and data events in the three  $\gamma\gamma \rightarrow \tau^+\tau^-$  signal regions.

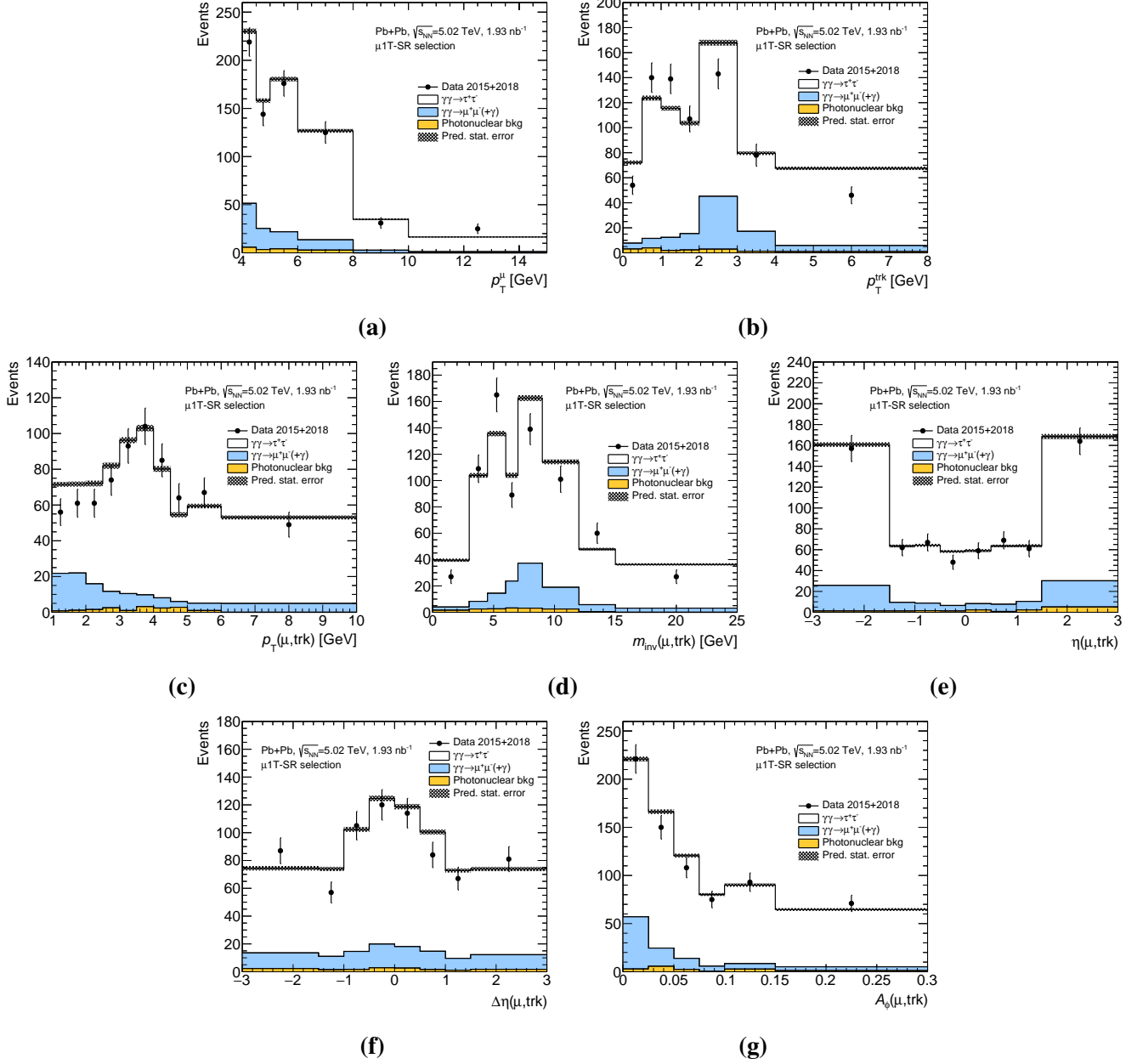


**Figure 5.10:** Reconstruction-level distributions of the kinematic observables in the  $\mu 1T$ -SR region: (a)  $p_T^\mu$ , (b)  $p_T^{\text{trk}}$ , (c)  $p_T(\mu, \text{trk})$ , (d)  $m_{\text{inv}}(\mu, \text{trk})$ , (e)  $\eta(\mu, \text{trk})$ , (f)  $\Delta\eta(\mu, \text{trk})$ , and (g)  $A_\phi(\mu, \text{trk})$ . Data points are shown in black markers, while Monte Carlo predictions are shown as filled histograms. The shaded band represents only the statistical uncertainty of the predictions.

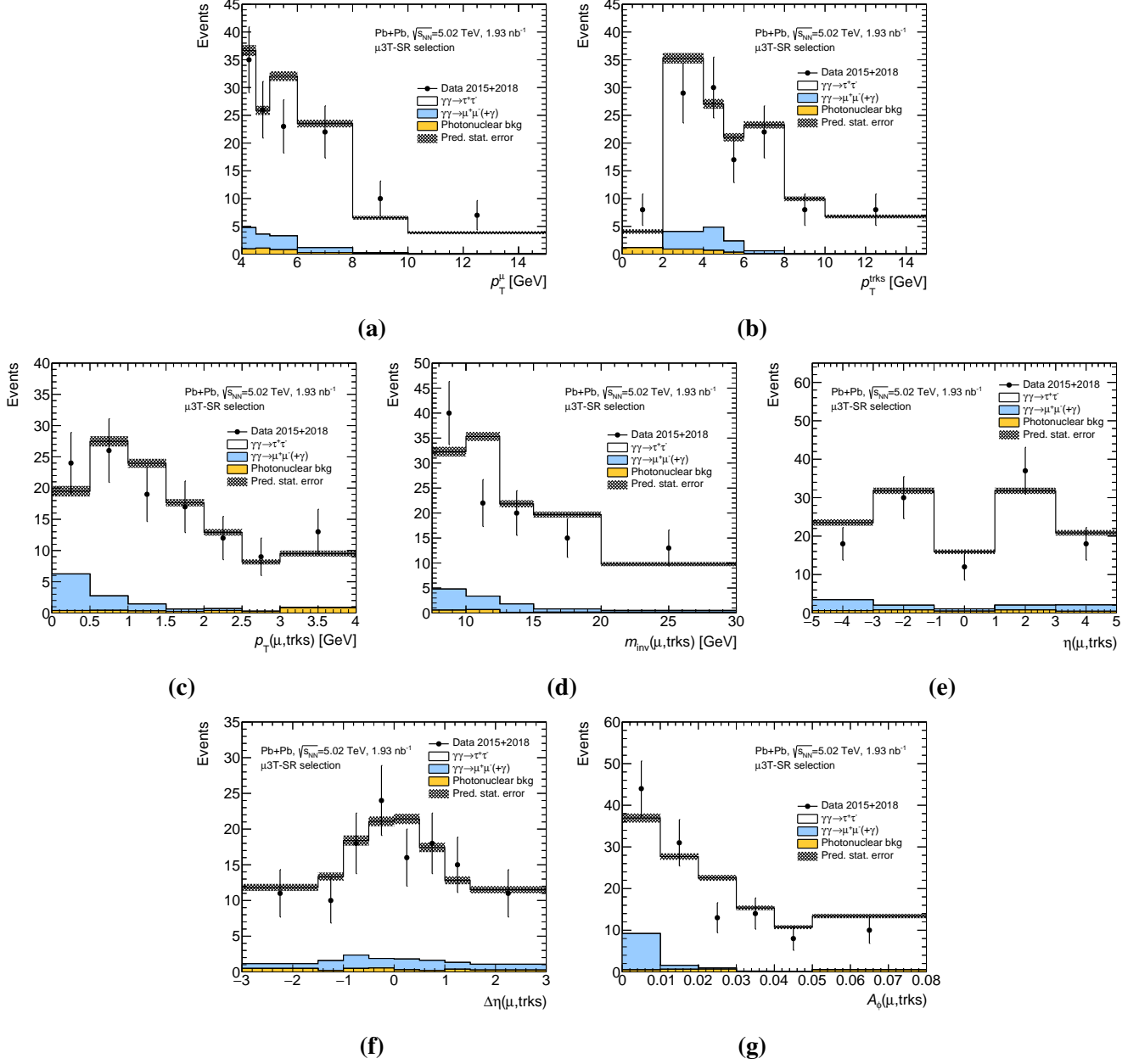


**Figure 5.11:** Reconstruction-level distributions of the kinematic observables in the  $\mu 3T$ -SR region: (a)  $p_T^\mu$ , (b)  $p_T^{\text{trks}}$ , (c)  $p_T(\mu, \text{trks})$ , (d)  $m_{\text{inv}}(\mu, \text{trks})$ , (e)  $\eta(\mu, \text{trks})$ , (f)  $\Delta\eta(\mu, \text{trks})$ , and (g)  $A_\phi(\mu, \text{trks})$ . Data points are shown in black markers, while Monte Carlo predictions are shown as filled histograms. The shaded band represents only the statistical uncertainty of the predictions.



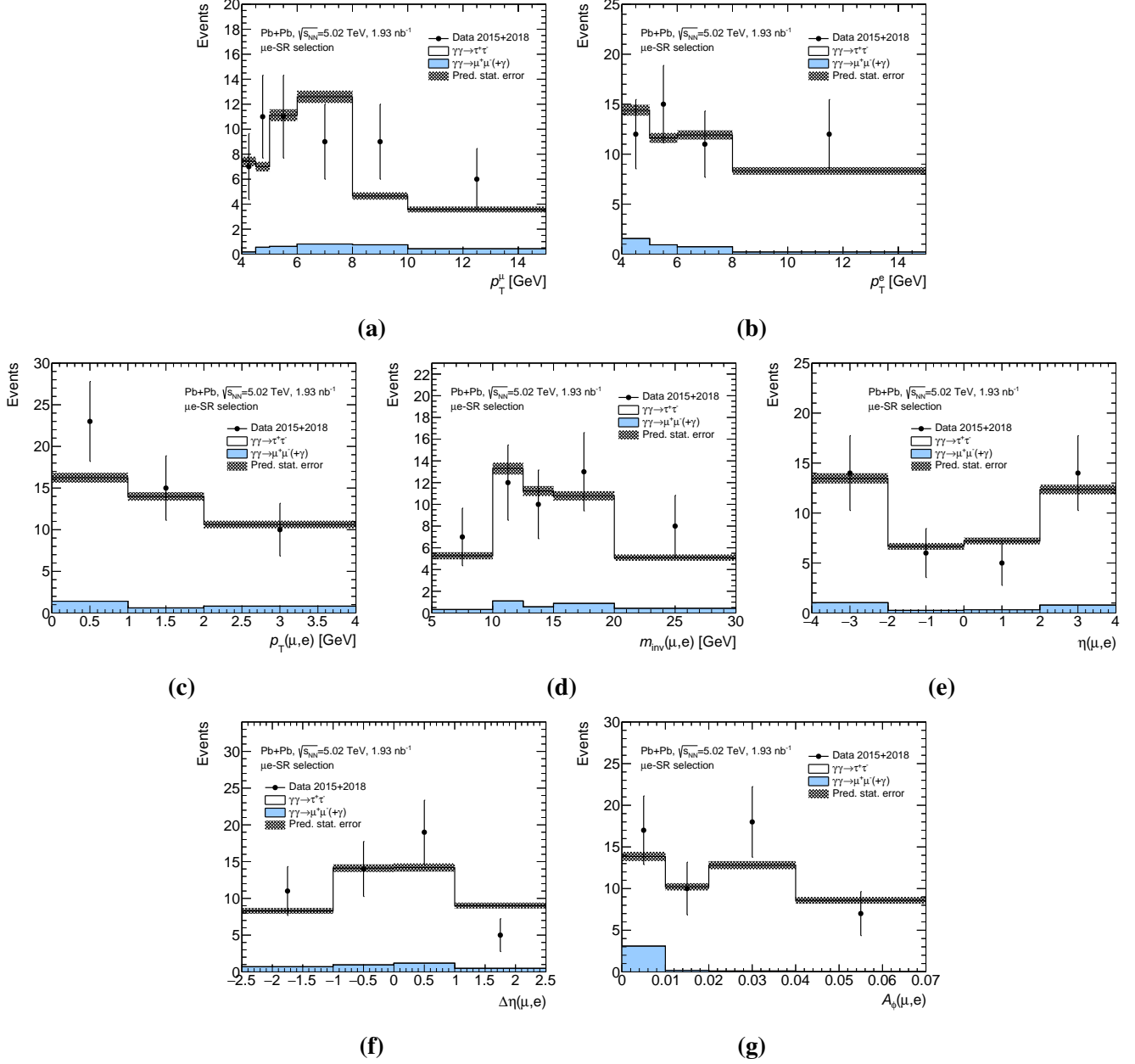


**Figure 5.12:** Reconstruction-level distributions of the kinematic observables in the  $\mu e$ -SR region: (a)  $p_T^\mu$ , (b)  $p_T^e$ , (c)  $p_T(\mu, e)$ , (d)  $m_{\text{inv}}(\mu, e)$ , (e)  $\eta(\mu, e)$ , (f)  $\Delta\eta(\mu, e)$ , and (g)  $A_\phi(\mu, e)$ . Data points are shown in black markers, while Monte Carlo predictions are shown as filled histograms. The shaded band represents only the statistical uncertainty of the predictions.

## 5.7 Unfolding

There are two ways in which the collision data recorded by an experiment can be compared to the predictions of different theoretical models. First, the predictions can be convoluted, or *folded*, with a simulation of the detector, so that they can be compared to the data. However, physics interpretations at high precision (both theoretically and experimentally) warrant a complete and realistic detector simulation. This requires require a large amount of computing resources, as well as detailed detector descriptions, that are often not available outside large experimental collaborations.

The second approach to data-theory comparisons is the inverse process of *unfolding* [224]. Here, the data recorded by the experiment is corrected for detector effects, which cause the smearing and migration of the measured quantities. The unfolding procedure results in distributions of particle kinematics that can then be directly compared to various theoretical predictions, and to the results obtained by other experiments, without the need of an accurate detector simulation. Detector effects are inherently probabilistic, due to the quantum nature of the physics behind particle-detector interactions. Thus, unfolding can only yield an *estimate* of the *true* particle spectra before interaction with the detector.

Traditionally, unfolding is performed using *binned* techniques, where histograms of kinematic observables are corrected for detector effects. These methods transform histograms of the kinematics of reconstruction-level objects, into histograms of the kinematics of fiducial objects. In this thesis, fiducial objects are interchangeably referred to as *particle-level* and *truth-level* objects. Recently, machine learning approaches to unfolding have started to gain traction, (see Ref. [225]). These techniques can perform *unbinned* unfolding, i.e. on an event-by-event basis, without having to define histograms. They can also be used to unfold complete events, rather than individual kinematic distributions. One such method called OmniFold [226] has been used recently by the ATLAS collaboration to simultaneously measure the differential cross-sections of 24 kinematic observables related to  $Z$ +jets production in Run 2 proton-proton collisions [227]. The core concept of the OmniFold technique is the event-by-event reweighting of kinematic spectra, which is achieved using neural networks set up for classification problems. Naturally, this requires large training samples of both data and Monte Carlo simulations. As this analysis uses less than 1,000 data events in all three signal regions combined, the OmniFold technique was found to be impractical. Thus, this analysis only relies on binned unfolding methods.

### 5.7.1 Fiducial object and region definitions

The kinematics of the reconstruction-level objects described in Sec. 5.4 are unfolded into the kinematics of the following fiducial objects:

- **Muons:** truth muons with  $p_T > 4 \text{ GeV}$  and  $|\eta| < 2.5$ .
- **Electrons:** truth electrons with  $p_T > 4 \text{ GeV}$  and  $|\eta| < 2.5$ .

- **Tracks:** truth stable charged hadrons with  $p_T > 0.1$  GeV and  $|\eta| < 2.5$ . Here, stable hadrons refers to pions and kaons. Truth muons and electrons with  $0.1 < p_T < 4$  GeV are also counted as tracks. The tracks are required to be separated from the muons and electrons by  $\Delta R > 0.1$ .

The muons and electrons in this analysis are not “dressed”, which is a procedure where the four-momenta of radiated photons within  $\Delta R < 0.1$  of the leptons are added back to the four-momenta of the leptons. Doing so would cause the results of this analysis to be dependent on the modeling of photon radiation at low  $p_T$ , which is expected to be small.

The fiducial region definitions are similar to the signal region definitions shown in Tab. 5.2. The selections are applied using the fiducial objects, rather than the reconstruction-level objects. The trigger, ZDC and topocluster selections are not applied as these are reconstruction-level selections. The selections on the  $p_T$  of the muon+track+photon/topocluster systems are also neglected, as these cuts are primarily used to reduce the  $\gamma\gamma \rightarrow \mu^+\mu^- + \gamma$  background contamination. A summary of the definitions of the three fiducial regions, called  $\mu 1\text{T-FR}$ ,  $\mu 3\text{T-FR}$  and  $\mu e\text{-FR}$ , is given in Tab. 5.4.

Variable	$\mu 1\text{T-FR}$	$\mu 3\text{T-FR}$	$\mu e\text{-FR}$
$N_\mu$	= 1	= 1	= 1
$N_e$	= 0	= 0	= 1
$N_{\text{trk}} (\Delta R > 0.1 \text{ from } \mu)$	= 1	= 3	= 0
$N_{\text{trk}} (\Delta R > 0.1 \text{ from } e)$	–	–	= 0
Sum of charges	= 0	= 0	= 0
$p_T (\mu, \text{trk})$	> 1 GeV	–	–
$m_{\text{inv}} (\text{trks})$	–	< 1.7 GeV	–
$A_\phi (\mu, \text{trk} (s))$	< 0.4	< 0.2	–

**Table 5.4:** Summary of selections applied for all three  $\gamma\gamma \rightarrow \tau^+\tau^-$  fiducial regions.

### 5.7.2 Binning and weights

The choice of bin edges in the unfolding of each of the kinematic distributions, which was taken to be identical at reconstruction- and truth-level, was determined as follows. At least ten  $\gamma\gamma \rightarrow \tau^+\tau^-$  events per reconstruction-level bin were required, which permits the modeling of the unfolded bin contents as Gaussian random variables in the extraction of the tau lepton EMDMs. The bin edges were chosen so that in a given distribution, the unfolded bins would have similar statistical uncertainties. The bin edges used in this analysis are presented in Tab. 5.5.

The weights applied when filling the truth-level histograms are

$$w = \frac{\sigma_{\text{gen}} \epsilon_{\text{filt}} \mathcal{L}_{\text{int}}}{N_{\text{gen}}} w_{\text{theo}}, \quad (5.11)$$

which is the same as Eq. 5.1 except for the detector performance modeling weights not being included. The relevant terms have been described in Sec. 5.3.

Region	Variable	Binning
$\mu 1T\text{-FR}$	$p_T^\mu$	[4, 4.5, 5, 6, 8, 10, 15]
	$p_T^{\text{trk}}$	[0, 0.5, 1, 1.5, 2, 3, 4, 8]
	$p_T(\mu, \text{trk})$	[1, 1.5, 2, 2.5, 3, 3.5, 4, 4.5, 5, 6, 10]
	$m_{\text{inv}}(\mu, \text{trk})$	[0, 3, 4.5, 6, 7, 9, 12, 15, 25]
	$\eta(\mu, \text{trk})$	[-3, -1.5, -1, -0.5, 0, 0.5, 1, 1.5, 3]
	$\Delta\eta(\mu, \text{trk})$	[-3, -1.5, -1, -0.5, 0, 0.5, 1, 1.5, 3]
	$A_\phi(\mu, \text{trk})$	[0, 0.025, 0.05, 0.075, 0.1, 0.15, 0.3]
$\mu 3T\text{-FR}$	$p_T^\mu$	[4, 4.5, 5, 6, 8, 10, 15]
	$p_T^{\text{trks}}$	[0, 2, 4, 5, 6, 8, 10, 15]
	$p_T(\mu, \text{trks})$	[0, 0.5, 1, 1.5, 2, 2.5, 3, 4]
	$m_{\text{inv}}(\mu, \text{trks})$	[7.5, 10, 12.5, 15, 20, 30]
	$\eta(\mu, \text{trks})$	[-5, -3, -1, 1, 3, 5]
	$\Delta\eta(\mu, \text{trks})$	[-3, -1.5, -1, -0.5, 0, 0.5, 1, 1.5, 3]
	$A_\phi(\mu, \text{trks})$	[0, 0.01, 0.02, 0.03, 0.04, 0.05, 0.08]
$\mu e\text{-FR}$	$p_T^\mu$	[4, 4.5, 5, 6, 8, 10, 15]
	$p_T^e$	[4, 5, 6, 8, 15]
	$p_T(\mu, e)$	[0, 1, 2, 4]
	$m_{\text{inv}}(\mu, e)$	[5, 10, 12.5, 15, 20, 30]
	$\eta(\mu, e)$	[-4, -2, 0, 2, 4]
	$\Delta\eta(\mu, e)$	[-2.5, -1, 0, 1, 2.5]
	$A_\phi(\mu, e)$	[0, 0.01, 0.02, 0.04, 0.07]

**Table 5.5:** Bin edges for each of the unfolded variables.

### 5.7.3 Unfolding methods

Several binned unfolding methods are described below. This analysis uses Iterative Bayesian Unfolding implemented in `RooUnfold` [228] as the primary unfolding method. The other methods have been used for cross-checks at various steps in the analysis.

#### Bin-by-bin unfolding

In this method,  $U_k$ , i.e. the contents of the  $k^{\text{th}}$  bin of the unfolded histogram, is given by

$$U_k = (D_k - B_k) \frac{T_k}{R_k}, \quad (5.12)$$

where  $D_k$ ,  $B_k$ ,  $T_k$  and  $R_k$  are the content of the  $k^{\text{th}}$  bin of the Data, Background, signal Truth, and signal Reconstructed histograms respectively.

Bin-by-bin unfolding is the simplest unfolding method, and while it is easy to implement, it does not account for migration between reconstructed and truth bins. Thus, this method is only used for cross-checks (both technical and conceptual), and not for performing real measurements of differential cross-sections.

### Matrix inversion

Here, the effect of the detector response is modeled as a matrix  $M$ , called the *migration matrix*. In vector notation, it connects the reconstructed histogram  $R$  and truth histogram  $T$  via the equation

$$R = M \cdot T. \quad (5.13)$$

The unfolded histogram  $U$  is obtained by applying  $M^{-1}$  to the data histogram  $D$  after subtracting the background histogram  $B$ , i.e.

$$U = M^{-1} (D - B). \quad (5.14)$$

As the matrix inversion method can account for bin migrations, it is an improvement over bin-by-bin unfolding. However, in the case of large smearing (i.e. large off-diagonal elements in the migration matrix),  $M^{-1}$  can exhibit large entry-to-entry fluctuations, which can manifest as large bin-to-bin fluctuations in  $U$ . Moreover, applying this method requires  $M$  to be invertible, which may not be guaranteed. Thus, the matrix inversion method is not used as the nominal unfolding method, but only for technical cross-checks.

The concept of the migration matrix can be used to define the following quantities:

- **Response matrix:** same as the migration matrix, but the entries are weighted by the reconstruction-level weights while filling the matrix. The migration matrix has entries that are numerically  $\mathcal{O}(1)$  (at least along the main diagonal), while the response matrix entries are numerically large, with units of reconstructed-events-per-bin.
- **Acceptance:** fraction of reconstructed events that also pass the truth-level selections. It is computed as a ratio between the response matrix projected onto the reconstruction axis, and the reconstructed histogram.
- **Efficiency:** fraction of truth events that also pass the reconstruction-level selections. It is computed as a ratio between the response matrix projected onto the truth axis, and the truth histogram.

### Singular value decomposition

The singular value decomposition (SVD) method [229] attempts to address the inversion-related issues in the matrix inversion method. It formulates the problem of unfolding as a least-squares minimization problem of the form

$$(M\mathbf{x} - \mathbf{d})^T B^{-1} (M\mathbf{x} - \mathbf{d}) + \tau (C\mathbf{x})^T (C\mathbf{x}) = \min. \quad (5.15)$$

Here,  $\mathbf{x}$  is the unfolded histogram,  $\mathbf{d}$  is the background-subtracted data histogram,  $B$  is the

covariance matrix of  $\mathbf{x}$ ,  $C$  is the discrete curvature matrix<sup>6</sup>, and  $\tau$  is a regularization parameter. In the original formulation,  $\tau$  is typically chosen as the second or third largest singular value of the migration matrix, hence the name of the method.

While the issue of problematic inverse migration matrices is avoided in the SVD method, it can result in large statistical bin-to-bin correlations in the unfolded distribution if the minimization routine finds an unfavorable solution. Thus, the SVD method was also only used for cross-checks in this work.

### Iterative Bayesian unfolding

The iterative Bayesian unfolding (IBU) method, originally proposed by D’Agostini [230, 231], reformulates the matrix inversion method into a problem of probabilities, by identifying the truth histogram  $\mathbf{T}$  and reconstructed histogram  $\mathbf{R}$  as being a *cause* and *effect* pair,  $\mathbf{C}$  and  $\mathbf{E}$ , in accordance with Bayesian principles. Then, Eq. 5.13 and Eq. 5.14 can be written using conditional probabilities as

$$\begin{aligned} \mathbf{R} = \mathbf{M} \cdot \mathbf{T} &\longrightarrow R_i = \sum_j P(E_i|C_j) T_j, \\ \mathbf{U} = \mathbf{M}^{-1} (\mathbf{D} - \mathbf{B}) &\longrightarrow U_i = \sum_j P(C_i|E_j) (D_j - B_j), \end{aligned} \quad (5.16)$$

The unknown quantities  $P(C_i|E_j)$  are determined using

$$P(C_i|E_j) = \frac{P(E_j|C_i) \Pr(C_i)}{\sum_k P(E_j|C_k) \Pr(C_k)}, \quad (5.17)$$

where the  $P(E_i|C_j)$ , i.e. the entries of the migration matrix, are known from simulation, and  $\Pr(C_i)$  is the Bayesian prior for the cause  $C_i$ .

The algorithm behind the IBU method proceeds as follows:

1. The first iteration of the inverse migration matrix,  $P_0(C_i|E_j)$ , is calculated using Eq. 5.17, where the self-normalized truth histogram is typically chosen to be the initial prior.
2. The first iteration of the unfolded histogram is computed using

$$U_{i,1} = \frac{1}{\epsilon_i} \sum_j f_j P_0(C_i|E_j) (D_j - B_j), \quad (5.18)$$

where  $\epsilon_i$  and  $f_j$  are the efficiency and acceptance factors, that account for possible flow of events from outside the pre-defined fiducial and signal regions.

---

<sup>6</sup>The discrete curvature matrix encodes the *curvature* of a histogram, constructed in a way following the first principles definition of the second derivative  $f''(\mathbf{x})$ . Effectively, it allows the minimization routine to penalize large bin-by-bin fluctuations in the unfolded histogram, i.e. the unfolding favors smooth distributions. Further details can be found in Section 6 of Ref. [229].

3. The  $U_{i,1}$  histogram is self-normalized, and is taken as the prior for the next iteration of computing the inverse migration matrix  $P_1(C_i|E_j)$  and unfolded histogram  $U_{i,2}$ .
4. The above three steps are repeated for a given number of iterations. The optimal choice of the number of iterations is analysis dependent. The approach taken in this analysis is described in Sec. 5.7.6.

### 5.7.4 Unfolding inputs

Regardless of the unfolding method, there are generally five sets of input histograms that are required for the unfolding procedure: data, background, reconstructed signal, truth signal, and the response matrix. The data and background histograms were shown in Figs. 5.10 to 5.12. The reconstructed and truth signal histograms, and the response matrices, for the  $p_T^\mu$  observable in all three fiducial regions are shown in Fig. 5.13. The corresponding inputs for the other kinematic observables are shown in App. A.2. In addition, App A.2 also shows the acceptance and efficiency factors for all kinematic observables of interest. Generally, the reconstructed signal histograms are below the truth signal histograms by a factor of around two, indicating that the efficiency factor is around 50%. The response matrices are found to be largely diagonal, showing that the detector effects do not dramatically distort the shapes of kinematic observables.

### 5.7.5 Monte Carlo closure test

Before the kinematic observables in data are unfolded, it is important to check if the unfolding procedure has been set up correctly. This is done using the *Monte Carlo closure test*, where the reconstructed signal distribution is unfolded using the inputs set up for unfolding the data, and compared to the truth signal distribution. By construction, the unfolded histogram produced in the test should be identical to the truth histogram. Any observed deviation hints at the unfolding procedure not being set up correctly.

The Monte Carlo closure test was performed for every kinematic observable of interest. For the purpose of technical cross-checks, all of the unfolding methods described in Sec. 5.7.3 were investigated. For the IBU method, only one iteration was used. For the SVD method, the second singular value was used for the regularization parameter  $\tau$ .

The results of the closure test are shown in Fig. 5.14 for the  $p_T^\mu$  observable in all three fiducial regions. For each of the unfolding methods, the unfolded reconstructed signal distribution is identical to the truth signal distribution, as indicated by the ratios in the lower panels being at unity. This implies that the procedure has been set up correctly. Perfect closure is also observed for the other kinematic observables, which are shown in App. A.3

### 5.7.6 Number of iterations

The number of iterations ( $N_{\text{iter}}$ ) is the regularization parameter of the Iterative Bayesian Unfolding method. Thus, it needs to be chosen appropriately. In this analysis, the optimal  $N_{\text{iter}}$



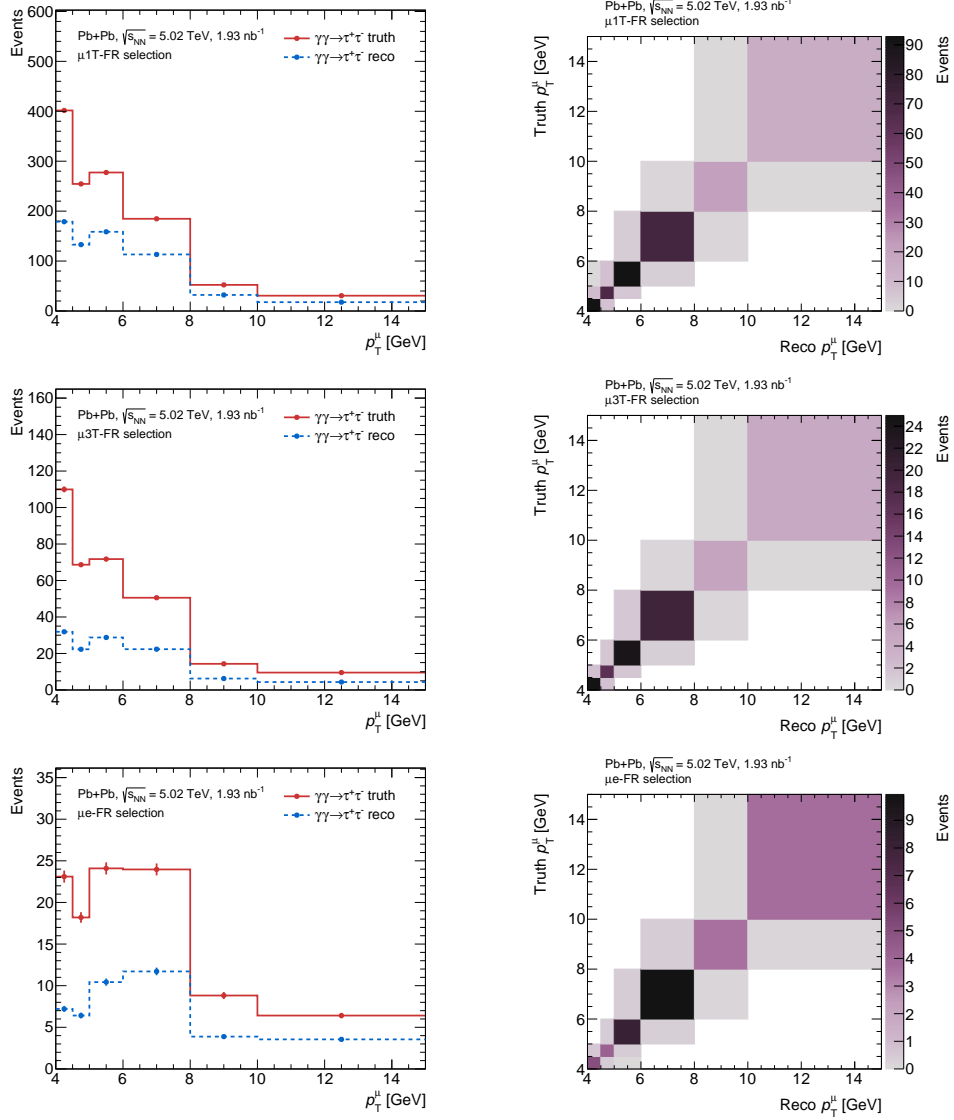


**Figure 5.13:** Reconstruction-level and truth-level distributions (left column) and migration matrices (right column) for the  $p_T^\mu$  observable in the  $\mu 1T$ -FR,  $\mu 3T$ -FR and  $\mu E$ -FR regions (top, middle, and bottom rows respectively).

was determined for each unfolded observable by scanning over  $N_{\text{iter}} = 1, 2, \dots, 10$  and noting the following at each step in the scan:

1. The relative statistical uncertainty per unfolded bin (as reported by RooUnfold). The optimal number of iterations is one where going from  $N_{\text{iter}} \rightarrow N_{\text{iter}} + 1$  does not significantly increase the relative statistical uncertainty. Additionally, it should not become smaller than the relative statistical uncertainty per bin of the truth distribution.
2. Two types of uncorrelated  $\chi^2$ 's between the unfolded distribution  $U$  and truth distributions  $T$ , defined as

$$\chi_{\text{unf}}^2 = \sum_{i=1}^{N_{\text{bins}}} \left( \frac{U_i - T_i}{\sigma_i^{\text{unf}}} \right)^2, \quad \chi_{\text{truth}}^2 = \sum_{i=1}^{N_{\text{bins}}} \left( \frac{U_i - T_i}{\sigma_i^{\text{truth}}} \right)^2, \quad (5.19)$$

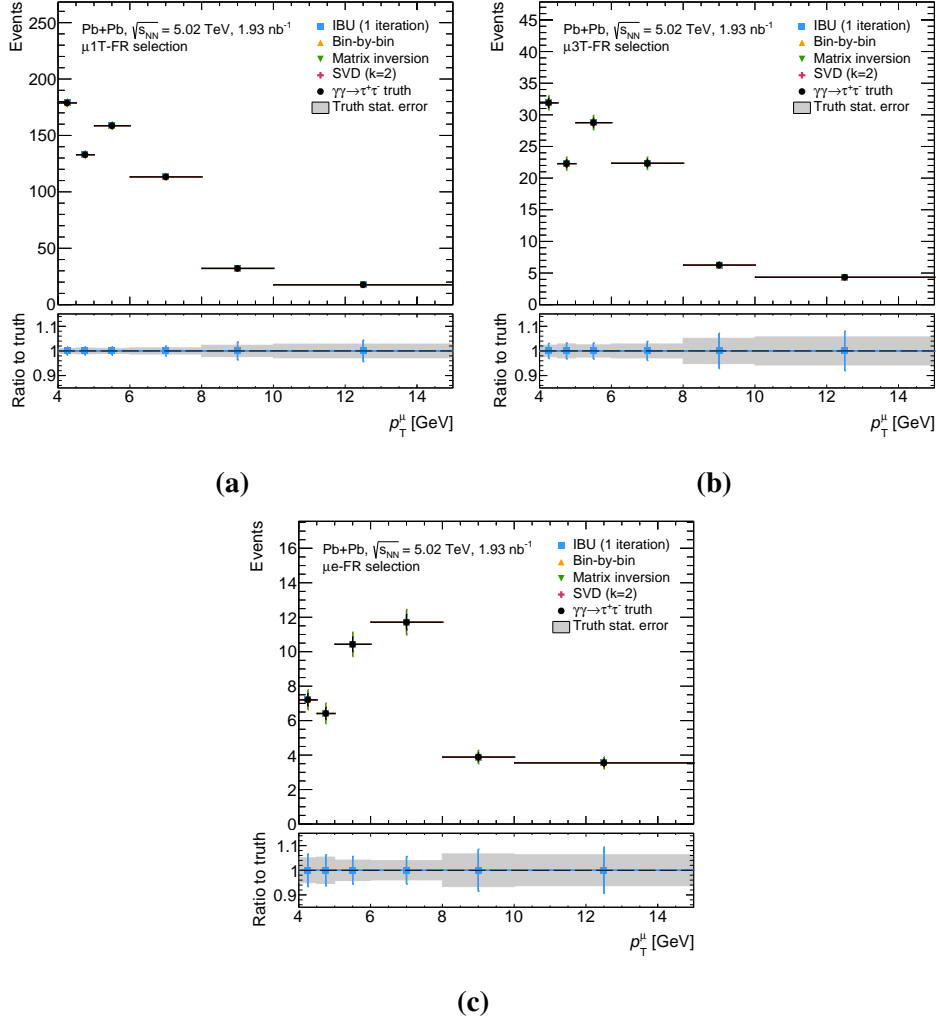


**Figure 5.14:** Results of the Monte Carlo closure test for the  $p_T^\mu$  observable in the (a)  $\mu 1T$ -FR region, (b)  $\mu 3T$ -FR and (c)  $\mu e$ -FR regions. Several unfolding methods are shown. For the IBU method, only one iteration is used. For the SVD method, the second singular value is used for  $\tau$ . Ratios of the unfolded distributions to the signal truth are shown in the lower panels. The shaded band shows the statistical uncertainty of the  $\gamma\gamma \rightarrow \tau^+\tau^-$  truth sample.

where  $\sigma_i^{\text{unf}}$  and  $\sigma_i^{\text{truth}}$  are the statistical errors of the unfolded distribution (as reported by `RoofUnfold`), and the truth distribution, respectively. The optimal number of iterations is one where going from  $N_{\text{iter}} \rightarrow N_{\text{iter}} + 1$  does not significantly change  $\chi_{\text{truth}}^2$ , even if  $\chi_{\text{unf}}^2$  is still evolving with increasing number of iterations. This implies that the numerator of both  $\chi^2$ 's (the sum of squared differences between the unfolded and truth distributions) has stabilized, but the  $\sigma_i^{\text{unf}}$  is needlessly increasing with  $N_{\text{iter}}$ , due to the iterative reuse of the unfolding prior.

The results of the  $N_{\text{iter}}$  scans for all kinematic observables of interest are shown in App. A.4; a summary of the optimal number of iterations is given in Table 5.6. The study was performed using the combined 2015+2018 data, in order to limit potential statistical issues. Typically, two iterations are sufficient to meet the constraints described above. Only four out of 21 observables

Variable	$N_{\text{iter}}$	Variable	$N_{\text{iter}}$	Variable	$N_{\text{iter}}$
$p_T^\mu$	3	$p_T^\mu$	2	$p_T^\mu$	3
$p_T^{\text{trk}}$	2	$p_T^{\text{trks}}$	2	$p_T^e$	3
$p_T(\mu, \text{trk})$	2	$p_T(\mu, \text{trks})$	2	$p_T(\mu, e)$	4
$m_{\text{inv}}(\mu, \text{trk})$	3	$m_{\text{inv}}(\mu, \text{trks})$	3	$m_{\text{inv}}(\mu, e)$	2
$\eta(\mu, \text{trk})$	2	$\eta(\mu, \text{trks})$	2	$\eta(\mu, e)$	2
$\Delta\eta(\mu, \text{trk})$	2	$\Delta\eta(\mu, \text{trks})$	2	$\Delta\eta(\mu, e)$	1
$A_\phi(\mu, \text{trk})$	2	$A_\phi(\mu, \text{trks})$	2	$A_\phi(\mu, e)$	2
(a)		(b)		(c)	

**Table 5.6:** Number of iterations used for the Iterative Bayesian Unfolding method, for the kinematic observables in the (a)  $\mu 1\text{T-FR}$ , (b)  $\mu 3\text{T-FR}$ , and (c)  $\mu e\text{-FR}$  regions.

require three iterations, while one observable ( $p_T(\mu, e)$ ) requires four iterations. The  $\Delta\eta(\mu, e)$  observable only requires one iteration, likely due to it having an almost perfectly diagonal response matrix (see Fig. A.6e).

### 5.7.7 Statistical uncertainties and correlations

As this analysis is limited by data statistics, it is crucial to determine the statistical uncertainty on the unfolded distributions appropriately. To propagate the statistical uncertainties of the data through the unfolding procedure, a numerical technique called *bootstrapping* [232, 233] was employed. The bootstrap procedure is commonly used to determine the statistical properties of discrete and finite datasets. It makes use of *replicas* of the original dataset, which are created through random sampling with replacement.

In this analysis, 10,000 bootstrap replicas of the data histograms were created using a Poisson reweighting approach. Here, events are filled into a copy of the data histogram with a weight sampled from a Poisson distribution with a mean of unity, rather than the nominal weights of unity for every event. In the large  $N$  limit, this is equivalent to random sampling with replacement. While creating the bootstrap replicas, the seed used in the random sampling is fixed to the recorded event number for every event, which ensures reproducibility.

The unfolding is repeated for each of the data histogram replicas, keeping the other inputs the same. Given  $N_{\text{repl}}$  replicas, the statistical covariance between two bins  $i$  and  $j$  in the unfolded distributions is given by

$$\text{Cov}_{ij} = \frac{1}{N_{\text{repl}}} \sum_{k=1}^{N_{\text{repl}}} (b_{ik} - \bar{b}_i) (b_{jk} - \bar{b}_j), \quad (5.20)$$

where  $b_{ik}$  and  $b_{jk}$  are the content of bins  $i$  and  $j$  in the  $k^{\text{th}}$  bootstrap replica, and  $\bar{b}_i$  and  $\bar{b}_j$  are the average bin content of bins  $i$  and  $j$  over all bootstrap replicas. The statistical uncertainty on the bin  $i$  is given by

$$\sigma_i^{\text{stat}} = \sqrt{\text{Cov}_{ii}}. \quad (5.21)$$

The statistical correlation between two unfolded bins  $i$  and  $j$  is defined as

$$\text{Corr}_{ij} = \frac{\text{Cov}_{ij}}{\sqrt{\text{Cov}_{ii}\text{Cov}_{jj}}}. \quad (5.22)$$

The above definitions do not impose that the bins  $i$  and  $j$  be from the same unfolded distribution. Bootstrapping can therefore be used to determine the statistical covariance and correlation between bins of *different* unfolded variables. This fact enables the proper statistical combination of multiple unfolded distributions when they are used to measure physical parameters of interest. In this analysis, bins across different fiducial regions are uncorrelated by design.

The statistical covariance and correlation matrices for all unfolded bins in the three fiducial regions are shown in Fig. 5.15. Solid black lines denote the boundaries between bins of different kinematic observables. Generally, the correlation between bins of the same variable is close to zero, except for a small anti-correlation ( $\approx -0.1$ ) between neighboring bins along the main diagonals. Strong correlations between bins of different variables can also be seen, following the physical expectations. Some examples are:

- The  $p_T(\mu, \text{trk})$  and  $m_{\text{inv}}(\mu, \text{trk})$  variables in the  $\mu 1\text{T-FR}$  region are anti-correlated due to the relation  $m^2 = E^2 - p_T^2 - p_z^2$ . The same holds true, albeit to a weaker extent, for the analogous system  $p_T$  and mass variables in the  $\mu 3\text{T-FR}$  and  $\mu e\text{-FR}$  regions.
- In the  $\mu 1\text{T-FR}$  region, the  $p_T^\mu$  and  $p_T^{\text{trk}}$  variables are correlated and anti-correlated with  $p_T(\mu, \text{trk})$  respectively. This may be due to the imbalance in minimum  $p_T$  in the object definitions of the muon and track, biasing  $p_T(\mu, \text{trk})$  towards the muon. A similar (but weaker) observation holds for the  $\mu 3\text{T-FR}$  region, but not for the  $\mu e\text{-FR}$  region, where the  $p_T(\mu, e)$  variable is correlated with both  $p_T^\mu$  and  $p_T^e$ . Since both electrons and muons are defined with the same minimum  $p_T$  threshold, the  $\mu e\text{-FR}$  selection may be biased towards the  $\gamma\gamma \rightarrow \tau^+\tau^-$  phase space regions where the muon and the electron are more likely to be back-to-back in the transverse plane ( $|y(\tau, \tau)| \approx 0$ , i.e.  $E_{\tau^+} \approx E_{\tau^-}$ ). As a consequence, the  $p_T(\mu, e)$  variable is (approximately) equal to the sum-in-quadrature of  $p_T^\mu$  and  $p_T^e$ .
- In all fiducial regions, the  $m_{\text{inv}}$  variable is correlated with the  $p_T$  of both the muon and the other object(s). Since the initial state photons in  $\gamma\gamma \rightarrow \tau^+\tau^-$  scattering have almost zero  $p_T$ , the  $p_T$  of the taus (and consequently their decay products) is limited by  $m_{\text{inv}}(\tau, \tau)$ . Thus, selecting events with a larger  $m_{\text{inv}}$  (which is a proxy for  $m_{\text{inv}}(\tau, \tau)$ ) automatically selects events where the tau decay products have higher  $p_T$  values.

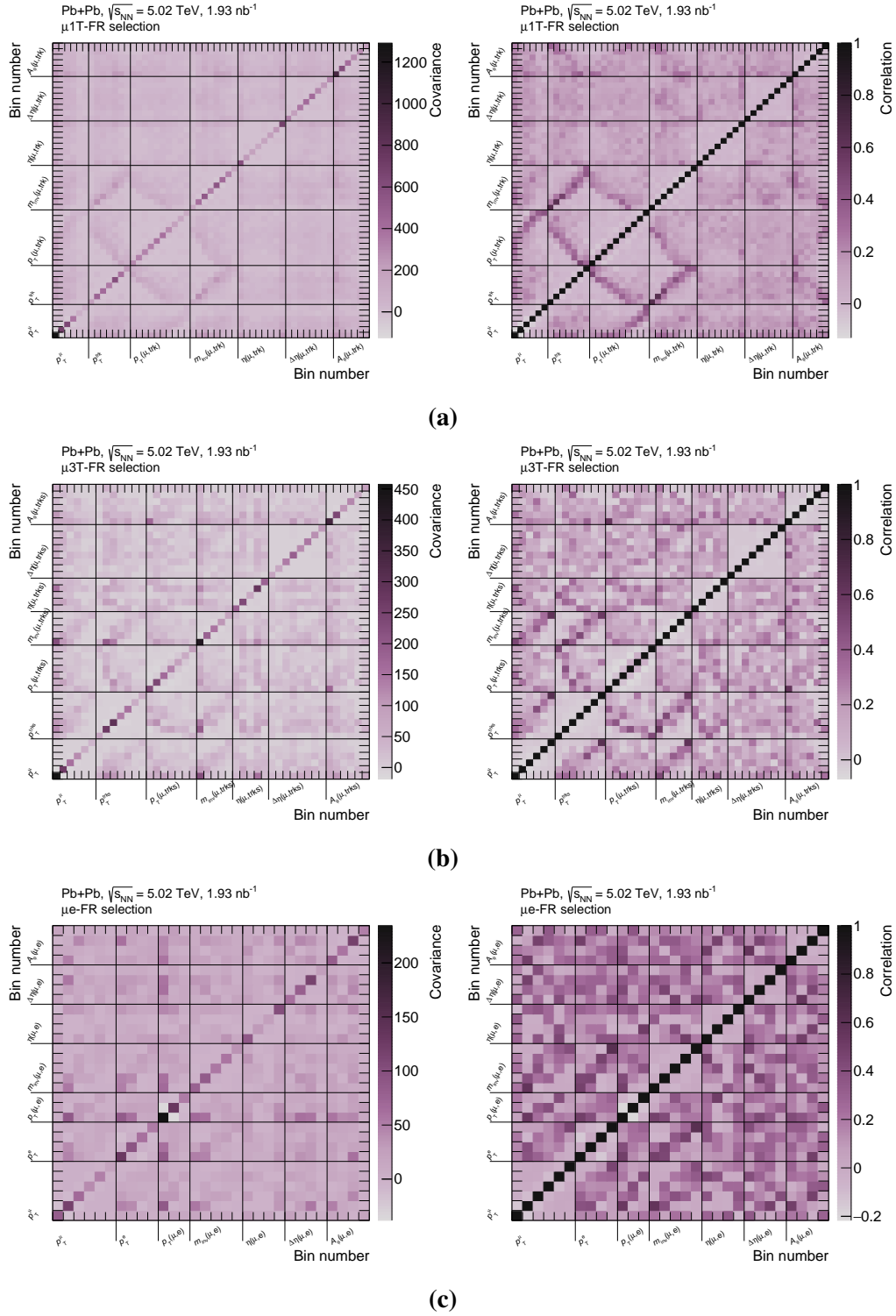


**Figure 5.15:** Statistical covariance (left) and statistical correlation (right) for all measured bins in the (a)  $\mu 1T$ -FR, (b)  $\mu 3T$ -FR and (c)  $\mu e$ -FR regions. The solid black lines denote the boundaries between the bins of separate kinematic observables, which are also labelled in the figures. The ordering of bins in each observable is given in Tab. 5.5.

## 5.8 Systematic uncertainties

### 5.8.1 Object calibration and performance

#### Tracks

The systematic uncertainty of the track reconstruction efficiency was determined by re-deriving the efficiency (as outlined in Sec. 5.4.1) with alternate detector geometries in the Monte Carlo simulation. The following variations were considered: +5% to the overall Inner Detector material; +10% to the IBL material; +25% to the Patch Panel Zero (PP0) [94] material. Further, an alternate list of particle-detector interaction processes included in the GEANT4 detector simulation, was also considered. The systematic uncertainties were evaluated as a function of the  $p_T$  and  $\eta$  of particle-level pions, muons and electrons. For tracks with very low  $p_T$  (0.1-0.2 GeV) the efficiency variations are at the level of 5-10%. At higher  $p_T$ , the variations are around 1-2% or lower. Generally, the variations are larger for  $|\eta| > 1.5$ , due to the limited tracking performance at high pseudorapidity. The tracking efficiency systematics are propagated through the analysis by randomly removing tracks in the nominal Monte Carlo samples, within a fraction commensurate with the systematic uncertainty determined for the given track  $p_T$  and  $\eta$  bin.

#### Topoclusters, electrons and photons

In the determination of the topocluster reconstruction efficiency (see Sec. 5.4.2), small differences of around 1% were observed between the efficiency in data and Monte Carlo. A conservative 2% systematic uncertainty was therefore assigned to the modeling of the topocluster reconstruction efficiency. Similar to the tracking systematics, this uncertainty was applied by randomly removing 2% of reconstructed topoclusters in the Monte Carlo samples. The difference in the mean topocluster energy response between data and Monte Carlo, described in Sec. 5.4.2, was applied as a calibration factor to the Monte Carlo samples to improve the modeling. The difference in the predictions between the uncorrected and corrected samples was taken as the systematic uncertainty on the topocluster energy response.

Before reconstructed electrons and photons are included in the analysis, a calibration of their energy scale and resolution is applied (see Sec. 3.3.4). The calibration is based on the standard ATLAS procedure for calibration of low luminosity (and zero pileup) collision data. In principle, this calibration has over 70 individual sources of systematic uncertainties associated with it. However, as this analysis relies primarily on events with muons, a simplified uncertainty scheme is considered, which provides a combined uncertainty for the energy response, and energy resolution, of electrons and photons. The effect of these uncertainties is included in the analysis by varying the reconstructed energy of the simulated objects. The impact is at the level of 1% for kinematic observables in the  $\mu e$ -SR. Small impacts at the level of 0.1% are observed in the  $\mu 1T$ -SR region, due to photons and topoclusters being included in the event selection (see Tab. 5.2), while the  $\mu 3T$ -SR is unaffected.

The uncertainties associated with the electron reconstruction+identification scale factors,

described in Sec. 5.4.3, are also considered in the analysis. The statistical uncertainty of the scale factors is included as a systematic uncertainty, while an additional uncertainty is determined by quantifying the change in the scale factors due to variations in the selection of  $\gamma\gamma \rightarrow e^+e^-$  events. These uncertainties are at the level of 5-10% as a function of electron  $p_T$  and  $\eta$ , and are only relevant for the  $\mu e$ -SR region.

The efficiency of the photon reconstruction+identification in data and Monte Carlo simulations were found to differ by at most 5% as a function of photon  $p_T$  (see Sec. 5.4.4). Thus, a systematic uncertainty of 5% is considered due to the photon performance, which is applied to all Monte Carlo samples by randomly removing 5% of the simulated photons. This uncertainty has a negligible impact ( $< 0.1\%$ ) in the  $\mu 1T$ -SR, due to photons being included in the event selection, while the  $\mu 3T$ -SR and  $\mu e$ -SR regions are unaffected.

## Muons

Before reconstructed muons are included in the analysis, a calibration of their momentum scale and resolution is applied (see Sec. 3.3.5). The calibration is based on the standard ATLAS procedure. Five sources of systematic uncertainties are considered, by applying  $\pm 1\sigma$  variations to the following aspects of the muon calibration: associated ID track resolution; associated MS track resolution; momentum scale; charge-dependence of the momentum scale, based on the combination of all corrections applied in the calibration; charge-dependence of the momentum scale, based on the residual charge-dependent bias after corrections. Each source affects the measured kinematic observables by at most 1%.

The uncertainties associated with the muon reconstruction+identification scale factors, described in Sec. 5.4.5, are also included in the analysis by considering plain variations of the scale factors. The statistical uncertainty of the scale factors is included as a systematic uncertainty, while an additional uncertainty is determined by quantifying the change in the scale factors due to variations in the selection of  $\gamma\gamma \rightarrow \mu^+\mu^-$  events. These uncertainties are at the level of 1% for muons with  $p_T$  between 4 and 15 GeV, and are in the 2-5% range for muons with  $p_T > 15$  GeV.

### 5.8.2 Trigger

The systematic uncertainty of the MU0 trigger efficiency was determined by applying alternate event selections and tag muon definitions, and re-evaluating the efficiency. In particular, the following variations were studied: probe muon  $|d_0| < 1.1$  mm instead of  $|d_0| < 0.3$  mm;  $1 \leq N_{\text{track}} \leq 3$  instead of  $N_{\text{track}} = 2$ ; tag muon passes Medium WP selection instead of Tight selection. The uncertainty was defined as the largest difference in the trigger efficiency due to these variations. The uncertainties were estimated to be in the  $\mathcal{O}(1\%)$  range, except for the gap region where it was found to be in the 5%-25% range depending on the muon  $p_T$ .

The systematic uncertainty of the MU4 trigger efficiency was estimated in a similar manner as the 2015 trigger. The same variations as for the 2015 trigger were considered, along with



an additional variation where the ZDC 0n0n requirement was imposed in the  $\gamma\gamma \rightarrow \mu^+\mu^-$  selection. The systematic uncertainty of the MU4 efficiency was found to be in the 2%-5% range at low  $p_T$  and  $|q \times \eta|$ , and in the 5%-20% range at high  $p_T$  and  $|q \times \eta|$ .

Similar variations of the event selections and object definitions as for the MU4 efficiency were used to determine the systematic uncertainty of the mu4 efficiency. An additional variation of the HLT matching condition was also considered, where the requirement was varied to  $\Delta R = 0.008$  and  $\Delta R = 0.012$ . The systematic uncertainties were found to be below 1%, indicating that the mu4 selection was performant and robust.

In addition to the uncertainties described above, the statistical uncertainties of the L1 and HLT trigger efficiencies are also considered as systematic uncertainties in the analysis. They arise due to the limited  $\gamma\gamma \rightarrow \mu^+\mu^-$  statistics.

The effects of the trigger-related systematic uncertainties described above are included in the analysis by considering the variations in the corresponding trigger scale factors, i.e.  $\epsilon_{\text{data}}/\epsilon_{\text{MC}}$ , which are applied in the same bins of muon  $p_T$  and  $|q \times \eta|$  as the original determination of the trigger efficiencies.

### 5.8.3 Monte Carlo modeling

#### Photon flux

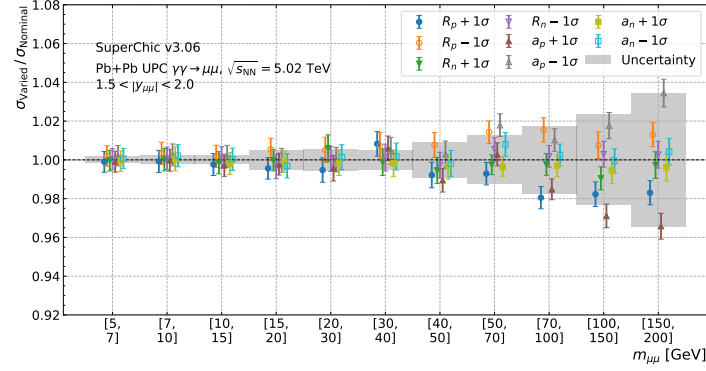
In Ref. [3], the uncertainty on the modeling of the photon flux (or rather the two-photon luminosity) was defined as the full difference between the STARlight and SuperChic Monte Carlo predictions. This was done by enabling and disabling the  $w_{\gamma\text{-flux}}$  weights, which led to an uncertainty of 15-20% on the normalization of the Monte Carlo predictions. Despite being rather large, the size of the uncertainty was constrained by around a factor of 5 in the extraction of the tau lepton's AMDM, by including a  $\gamma\gamma \rightarrow \mu^+\mu^-$  control region, which is affected by the photon flux uncertainty in the same way as the signal regions. Further, the associated nuisance parameter was pulled by around 0.25 units, indicating that the data favors a photon flux model between the STARlight and SuperChic predictions. Since a pulled nuisance parameter does not correspond to a physical model of nature, the result of the fit cannot truly be used to constrain the photon flux. More generally, constraints on theoretical modeling parameters should not be extracted at the same time as BSM parameters. For these reasons, the treatment of the photon flux uncertainty was revisited in this analysis.

As mentioned in Sec. 2.3.1, the SuperChic generator uses the Woods-Saxon distribution for the nuclear charge density (see Eq. 2.70). More precisely, it uses a weighted sum of Woods-Saxon distributions for the proton and neutron densities, to define the *nucleon* density<sup>7</sup>

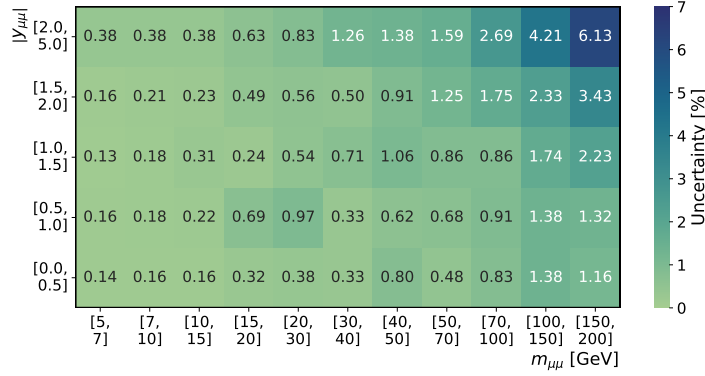
$$\rho_n(r) = \frac{Z}{A} \frac{1}{1 + \exp\left(\frac{r-R_p}{a_p}\right)} + \frac{A-Z}{A} \frac{1}{1 + \exp\left(\frac{r-R_n}{a_n}\right)}, \quad (5.23)$$

<sup>7</sup> $\rho_n(r)$  is not normalized to unity in the form presented above.





(a)



(b)

**Figure 5.16:** (a) Change in  $\gamma\gamma \rightarrow \mu^+\mu^-$  cross-section due to variations of the Woods-Saxon parameters of the Pb ion nucleon density, as a function of  $m_{\text{inv}}(\mu, \mu)$  for  $1.5 < |y(\mu, \mu)| < 2.0$ . (b) Map of the determined photon flux uncertainty for all  $m_{\text{inv}}(\mu, \mu)$  and  $|y(\mu, \mu)|$  bins.

where  $Z = 82$  and  $A = 208$  for Pb, and  $R_p = 6.68 \pm 0.02$  fm,  $R_n = 6.69 \pm 0.03$  fm,  $a_p = 0.447 \pm 0.01$  fm, and  $a_n = 0.560 \pm 0.03$  fm [212, 234, 235]. The proton density sources the photon flux, while both the proton and neutron densities contribute to the nuclear opacity.

The experimental errors of  $R_{p,n}, a_{p,n}$  are used to define a systematic uncertainty on the modeling of the photon flux. It is computed as the maximum deviation in the  $\gamma\gamma \rightarrow \mu^+\mu^-$  cross-section (inclusive in forward neutron topologies) predicted by SuperChic, due to the variations in  $R_{p,n}, a_{p,n}$  quoted above. The uncertainty is symmetrized in the largest (absolute) up- and down-deviations, and is computed in bins of  $m_{\text{inv}}(\mu, \mu)$  and  $|y(\mu, \mu)|$  using the same binning as the original  $w_{\gamma\text{-flux}}$  definition. Since the photon flux depends only on the invariant mass and rapidity of the centrally produced system (when  $s \gg m_X^2$ ), the uncertainty computed using  $\gamma\gamma \rightarrow \mu^+\mu^-$  events is also valid for  $\gamma\gamma \rightarrow \tau^+\tau^-$  events.

The  $\gamma\gamma \rightarrow \mu^+\mu^-$  cross-section deviations for the  $1.5 < |y(\mu, \mu)| < 2.0$  bin are shown in Fig. 5.16a as an example. The proton parameters have a larger impact on the  $\gamma\gamma \rightarrow \mu^+\mu^-$  cross-section than the neutron parameters, as the former are responsible for the photon flux and survival factor (through the nuclear opacity), while the latter affect the survival factor alone. The cross-section decreases for  $+1\sigma$  variations of all parameters, while it increases for all  $-1\sigma$

variations. This is likely due to the change in the extent of the nucleus affecting the available impact parameter range for  $\gamma\gamma$  processes. In particular, a larger nucleus ( $+1\sigma$ ) decreases the available impact parameter range, resulting in a smaller cross-section, and vice versa.

A map of the symmetrized uncertainty on the photon flux for all  $m_{\text{inv}}(\mu, \mu)$  and  $|y(\mu, \mu)|$  bins is shown in Fig. 5.16b. The uncertainty grows with both  $m_{\text{inv}}(\mu, \mu)$  and  $|y(\mu, \mu)|$ , also due to the impact parameter dependence of the cross-section: a large  $m_{\text{inv}}(\mu, \mu)$  or  $|y(\mu, \mu)|$  is more likely to occur at small impact parameters, where variations in the nuclear density have larger effects. The uncertainty is of the order of 0.5% in bins with the largest number of observed  $\gamma\gamma \rightarrow \tau^+\tau^-$  events (i.e.  $m_{\text{inv}}(\mu, \mu) \lesssim 50$  GeV and  $|y(\mu, \mu)| \lesssim 2.0$ ).

As mentioned already, the variations of the Woods-Saxon parameters also affect the survival factor, as it depends on the nuclear opacity (see Sec. 2.3.2). Thus, the  $\gamma\gamma \rightarrow \mu^+\mu^-$  cross-section ratios also contain experimentally-motivated sources of uncertainties on the survival factor. However, this does not address the question of the choice of survival factor model itself. In Ref. [236], it was found that instead of using Eq. 2.75, defining  $P_{\text{surv}}(\mathbf{b}) = \Theta(b - 2R_{\text{Pb}})$  leads to the fiducial cross-section of  $\gamma\gamma \rightarrow \mu^+\mu^-$  scattering in Pb+Pb collisions at  $\sqrt{s_{\text{NN}}} = 5.02$  TeV increasing by about 6.4%. Taking this difference as a theoretical uncertainty on the survival factor model is not well motivated, as the alternate model neglects the finite range of the strong interaction, and does not account for the non-zero nuclear density for  $b > R_{\text{Pb}}$ . Since it was noted in Ref. [236] that this replacement of the survival factor is rather unphysical, only a fraction of the quoted difference is considered as an uncertainty in this analysis. Thus, at both reconstruction- and truth-level, a flat 2.5% uncertainty is assigned on the theoretical modeling of the survival factor<sup>8</sup>.

### 0n0n weights

The statistical uncertainty of the 0n0n weights, which arises due to the limited statistics available for the determination of the  $\gamma\gamma \rightarrow \mu^+\mu^-$  0n0n fractions, is included as a systematic uncertainty. An alternate fit to the  $\gamma\gamma \rightarrow \mu^+\mu^-$  0n0n fractions is used to determine a variation of the weights due to the choice of fit function (see Sec. 5.3.2). The effect of the 1% ZDC inefficiency [209], was also included by varying the normalization parameters of the fitted functions by 1%. Finally, the variation in the 0n0n weights due to the choice of alternate  $m_{\text{inv}}(\mu, \mu)$  and  $|y(\mu, \mu)|$  binning, was also included as a systematic uncertainty.

### Tau decay

The uncertainty on the modeling of tau decays is taken as the full difference between the predictions of the Tauola and Pythia8 samples, both at reconstruction- and truth-level. The uncertainty per unfolded bin is typically at the 5% level, but it is found to exceed 10% in a few  $\mu e$ -FR bins, possibly due limited statistics.

<sup>8</sup>A comprehensive study of the survival factor modeling was recently performed within the gammaUPC framework, resulting in uncertainties on the photon flux below 1% (unpublished work as of writing this thesis, Ref. [237]). Thus, the quoted 2.5% uncertainty is most likely still conservative.

## 5.8.4 Other

### Photonuclear background estimate

Two systematic uncertainties related to the estimation of the photonuclear background are considered in the analysis. First, the statistical uncertainty from the normalization of the templates, due to the limited statistics in the  $4 \leq N_{\text{topocluster}}^{\text{unmatched}} \leq 8$  region, is included as a systematic uncertainty. Then, alternate templates are derived by varying the definitions of the control regions. In the  $\mu 2\text{T-CR}$  region, the two tracks are allowed to have the same charge sign, as opposed to the opposite sign requirement in the nominal definition. In the  $\mu 4\text{T-CR}$  region, a variation of the background template is constructed by only considering four-track combinations with a non-zero net charge. The uncertainty per unfolded bin is then defined by the absolute change in the photonuclear background estimate due to these selection variations.

### Luminosity

The uncertainty on the integrated luminosity of the 2015 and 2018 Pb+Pb datasets was determined in a similar manner as the preliminary calibration of the 2023 Pb+Pb dataset presented in Chapter 4. The fitting procedure that was used was manifestly two-dimensional, unlike the factorized one-dimensional analysis described for the 2023 Pb+Pb dataset. The following sources of systematic uncertainties were considered as correlated between the two data-taking years, as they have similar/identical origins: DCCT calibration, ghost and satellite charge fractions, beam-beam effects, absolute Inner Detector length scale, and fit model. The non-factorization and emittance evolution uncertainties were considered as partially (20%) correlated between the two years. The uncertainties on the 2015 and 2018 integrated luminosities are 1.5% and 1.9% respectively. Including correlations, the uncertainty on the combined Run 2 integrated luminosity was determined to be 1.5% by the ATLAS luminosity group.

### Signal Monte Carlo statistics

According to the basic unfolding equation, i.e. Eq. 5.12 for the bin-by-bin unfolding method, the statistical uncertainties of each of the components that appear in the equation – data, background, signal truth, and signal reconstructed histograms – contribute to the statistical uncertainty of the unfolded histogram. The effect of the data statistical uncertainty is treated as *genuinely* statistical in nature, while the effects of statistical uncertainties in the remaining components are treated as systematic uncertainties.

For a given unfolded bin  $k$ , the signal Monte Carlo statistical uncertainty is evaluated as the uncertainty  $\Delta w_k$  on the bin-by-bin correction factor  $w_k$ . To derive  $\Delta w_k$ , the following quantities are defined:  $N_k^{\text{rec}}$ , the number of events passing the reconstruction selections of the bin  $k$ ;  $N_k^{\text{tr}}$ , the number of events passing the truth selections of the bin  $k$ ;  $N_k^{\text{rec,tr}}$ , the number of events passing both reconstruction and truth selections for the bin  $k$ . The statistical uncertainties of these quantities are  $\Delta N_k^{\text{rec}}$ ,  $\Delta N_k^{\text{tr}}$ , and  $\Delta N_k^{\text{rec,tr}}$  respectively.  $N_k^{\text{rec}}$  and  $N_k^{\text{tr}}$  are not independent variables, as a non-zero  $N_k^{\text{rec,tr}}$  implies a partial correlation between them.

Thus, the quantities  $r_k = N_k^{\text{rec}} - N_k^{\text{rec,tr}}$  and  $t_k = N_k^{\text{tr}} - N_k^{\text{rec,tr}}$  are also defined, with which  $w_k$  can be written using three independent variables like

$$w_k = \frac{N_k^{\text{tr}}}{N_k^{\text{rec}}} = \frac{t_k + N_k^{\text{rec,tr}}}{r_k + N_k^{\text{rec,tr}}}. \quad (5.24)$$

The (squared) uncertainties of  $r_k$  and  $t_k$  are given by  $\Delta r_k^2 = (\Delta N_k^{\text{rec}})^2 - (\Delta N_k^{\text{rec,tr}})^2$  and  $\Delta t_k^2 = (\Delta N_k^{\text{tr}})^2 - (\Delta N_k^{\text{rec,tr}})^2$  since their defining variables are fully correlated.

The statistical uncertainty of  $w_k$  is then derived using Gaussian error propagation,

$$\begin{aligned} \Delta w_k^2 = & \frac{(\Delta N_k^{\text{tr}})^2 - (\Delta N_k^{\text{rec,tr}})^2}{(N_k^{\text{rec}})^2} + \frac{(N_k^{\text{tr}})^2}{(N_k^{\text{rec}})^4} \left( (\Delta N_k^{\text{rec}})^2 - (\Delta N_k^{\text{rec,tr}})^2 \right) \\ & + \frac{(\Delta N_k^{\text{rec,tr}})^2}{(N_k^{\text{rec}})^4} (N_k^{\text{rec}} - N_k^{\text{tr}})^2. \end{aligned} \quad (5.25)$$

The ratio  $\Delta w_k / w_k$  defines a systematic uncertainty on the unfolded distributions, due to the statistical uncertainty of the signal Monte Carlo sample. It is at the level of a few percent for the  $\mu 1\text{T-FR}$  distributions, while it is larger for the  $\mu 3\text{T-FR}$  and  $\mu e\text{-FR}$  variables due to the lower statistics in the Monte Carlo samples for these final states.

### Background statistics

For the same reason as the statistical uncertainty of the signal Monte Carlo sample, the statistical uncertainty of the total background estimate must also be propagated through the unfolding procedure.

The derivation of the background statistical uncertainty uses a set of *pseudo-experiments*, i.e. Gaussian fluctuations of the bin contents of the background histogram within their statistical uncertainties. A total of  $N_{\text{ps}} = 10,000$  pseudo-experiments were considered. The unfolding procedure was repeated for each pseudo-experiment, yielding a set of unfolded histograms with bin contents  $U_{i,k}$ . The uncertainty on the unfolded histogram due to the background statistics,  $\delta U_k|_{\text{bkg.stat.}}$ , is then defined as the standard deviation of the bin contents,

$$\delta U_k|_{\text{bkg.stat.}} = \left( \frac{1}{N_{\text{ps}}} \sum_{i=1}^{N_{\text{ps}}} (U_{i,k} - E[U_{i,k}])^2 \right)^{1/2} \quad (5.26)$$

Generally, this uncertainty is at the level of a few percent for the  $\mu 1\text{T-FR}$  distributions, while it is larger for the  $\mu 3\text{T-FR}$  and  $\mu e\text{-FR}$  variables due to the lower statistics.

### Unfolding data-driven closure

The result of the unfolding procedure using the IBU method may be biased, due to the choice of  $N_{\text{iter}}$ , bin edges, initial prior etc. Any bias, if present, is treated as a systematic uncertainty on the unfolded distributions. The bias on the unfolded distributions due to the unfolding proce-

ture is estimated using a stress test called the *data-driven closure test*. In the test, a reweighted version of the reconstructed and truth signal Monte Carlo histograms are constructed, which essentially makes the signal truth distribution resemble the data. The reweighted reconstructed distribution is unfolded using the original (i.e. un-reweighted) prior and response matrix, and compared to the reweighted truth distribution.

In the reweighting procedure, the truth signal histogram is multiplied by the factor  $m_k = \frac{D_k - B_k}{R_k}$  for each bin  $k$ . Then, the reconstructed signal histogram and response matrix are reweighted in a self-consistent manner, such that the acceptance and efficiency before and after reweighting are identical. In order to study the impact of the reweighting on the estimated unfolding bias, multiple versions of the reweighting factors are created by smoothing the  $m_k$  using the `TH1::Smooth()` function in ROOT<sup>9</sup> using 1, 2 and 3 iterations. Additionally, three more reweighting factors are created by performing Gaussian fluctuations of the  $m_k$  within their statistical uncertainties before smoothing. The six smoothing strategies are called `SmoothZ` and `SmoothZRandom` respectively, where  $Z = 1, 2, 3$ .

The uncertainty on the unfolded histogram due to the data-driven closure,  $\delta U_k|_{\text{DDC}}$ , is given by the average bias over all smoothing strategies, i.e.

$$\delta U_k|_{\text{DDC}} = \frac{1}{6} \sum_{i \in \text{smoothing strategies}} \left( N_{i,k}^{\text{rwt,rec,unf}} - N_{i,k}^{\text{rwt,tr}} \right), \quad (5.27)$$

where for each strategy  $i$ ,  $N_{i,k}^{\text{rwt,tr}}$  is the  $k^{\text{th}}$  bin content of the reweighted truth histogram, and  $N_{i,k}^{\text{rwt,rec,unf}}$  is the  $k^{\text{th}}$  bin content of the unfolded reweighted reconstructed histogram.

The results of the data-driven closure test for the  $p_T^\mu$  variable in the  $\mu\text{1T-FR}$  region are shown in Fig. 5.17 as an example. The reweighting factors for all smoothing strategies, shown in Fig. 5.17a, are within  $\pm 20\%$  of unity, indicating good Monte Carlo modeling. The data-driven closure systematic, defined in Eq. 5.27, is shown in Fig. 5.17b, along with the unfolding bias for each smoothing strategy. Due to the good unfolding closure, the data-driven closure systematic is found to be  $\lesssim 0.1\%$  for  $p_T^\mu$  in  $\mu\text{1T-FR}$  region. The results of the closure test for all other kinematic observables are shown in App. A.5. Across all unfolded variables, the data-driven closure systematic uncertainty is found to be  $\lesssim 1\%$  per bin, indicating that there is minimal bias in the unfolding procedure implemented in this analysis.

## 5.8.5 Impact of systematic uncertainties

The impact of the systematic uncertainties on the measured particle-level cross-sections is determined by re-running the unfolding procedure with the systematically varied set of inputs wherever appropriate. The uncertainty per bin due to a single systematic source is defined as the difference in the bin content between the nominal and varied unfolded distributions.

<sup>9</sup>The `TH1::Smooth()` function uses a non-linear, robust smoother with running medians of adjacent bin contents in the 3-5-3 sequence. See Sec. 4.2 of Ref. [238].

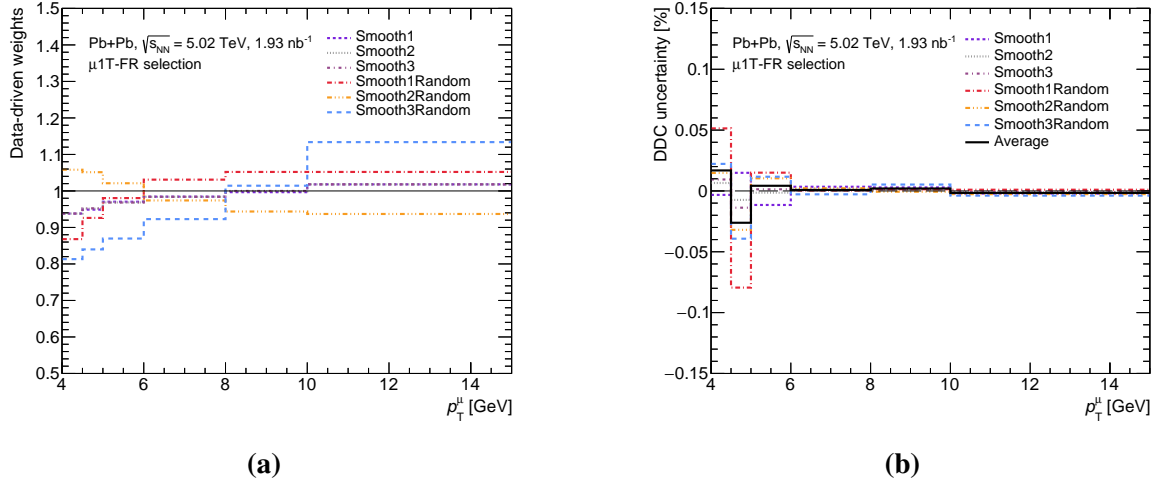


**Figure 5.17:** Results of the data-driven closure test for the  $p_T^\mu$  variable in the  $\mu 1T\text{-FR}$  region: (a) reweighting factors per bin for all smoothing strategies, (b) unfolding bias (in percent) for all smoothing strategies, and the average bias per bin.

The uncertainties on the unfolded cross-sections due to individual sources are symmetrized using two procedures:

- **Symm:** refers to simple symmetrization of up and down systematic uncertainties. Here, the average of the (absolute) up and down uncertainties (before symmetrization) is taken as both the up and down uncertainty. This strategy is adopted for systematic uncertainties that have up and down varied versions in their definitions at reconstruction-level.
- **Envl:** refers to the envelope. Here, the maximum of the (absolute) up or down uncertainties (before symmetrization) is taken as both the up and down uncertainty. This strategy is adopted for systematic uncertainties that are defined as one-sided at reconstruction-level, i.e. not as a up- and down-varied pair.

The systematic uncertainties are grouped into the following categories: *Track* (for tracking uncertainties), *EGamma* (for topocluster, electron and photon uncertainties), *Muon* uncertainties, *Trigger* uncertainties, *Modeling* uncertainties, and *Other* uncertainties (for those that do not fall into the previous groups). The combined uncertainty due to a group of sources is computed as the sum-in-quadrature of the uncertainties due to the individual sources. A complete list of the systematic uncertainties considered in the analysis, including the grouping and symmetrization strategies considered, is shown in Tab. 5.7.

The per-bin impact of the grouped systematic uncertainties for all measured kinematic observables of interest is shown in Figs. 5.18 to 5.20. In general, each group results in an uncertainty on the level of 5-10%.

Group	Systematic uncertainty	Strategy	Explanation
Track	TRK_EFF_OverallIDmat	Envl	Overall ID material
	TRK_EFF_IBLmat	Envl	IBL material
	TRK_EFF_PP0mat	Envl	Patch Panel 0 material
	TRK_EFF_QGSP_BIC	Envl	Alternate physics list
EGamma	EG_RES	Symm	Resolution
	EG_SCALE	Symm	Scale
	EL_EFF0_STAT	Symm	Electron reco+id efficiency, stat
	EL_EFF0_SYS	Symm	Electron reco+id efficiency, syst
	PH_EFF	Envl	Photon efficiency
	TC_EFF	Envl	Topocluster efficiency
	TC_CALIB	Envl	Topocluster calibration
Muon	muon_ID	Symm	ID track resolution
	muon_MS	Symm	MS track resolution
	muon_SCALE	Symm	Momentum scale
	muon_SAGITTA_RESBIAS	Symm	Momentum scale charge dependence
	muon_SAGITTA_RHO	Symm	Momentum scale charge dependence
	MUON_EFF0_STAT	Symm	Muon reco+id efficiency, stat
	MUON_EFF0_SYS	Symm	Muon reco+id efficiency, syst
Trigger	L1MU4_STAT	Symm	L1 trigger, stat
	L1MU4_SYS	Symm	L1 trigger, syst
	HLT MU4_STAT	Symm	HLT trigger, stat
	HLT MU4_SYS	Symm	HLT trigger, syst
Modeling	photon_flux_syst_WS	Symm	Photon flux, Woods-Saxon params
	photon_flux_syst_SurvFactor	Envl	Photon flux, survival factor
	0n0n_flux	Envl	0n0n weights, alt fit
	0n0n_bins_flux	Envl	0n0n weights, alt binning
	0n0n_flux_stat	Symm	0n0n weights, stat
	0n0n_flux_zdc_syst	Symm	0n0n weights, ZDC efficiency
	TAUOLA	Envl	Tau decay
Other	LUMI	Symm	Luminosity
	photonuclear_stat	Symm	Photonuclear bkg, stat
	photonuclear_syst	Envl	Photonuclear bkg, syst
	DDC	Envl	Data-driven closure
	BkgStat	Symm	Background statistics
	MCStatErr	Symm	Monte Carlo statistics

**Table 5.7:** List of systematic uncertainties considered in the analysis, grouped according to common origins. The symmetrization strategies are also listed for each source.

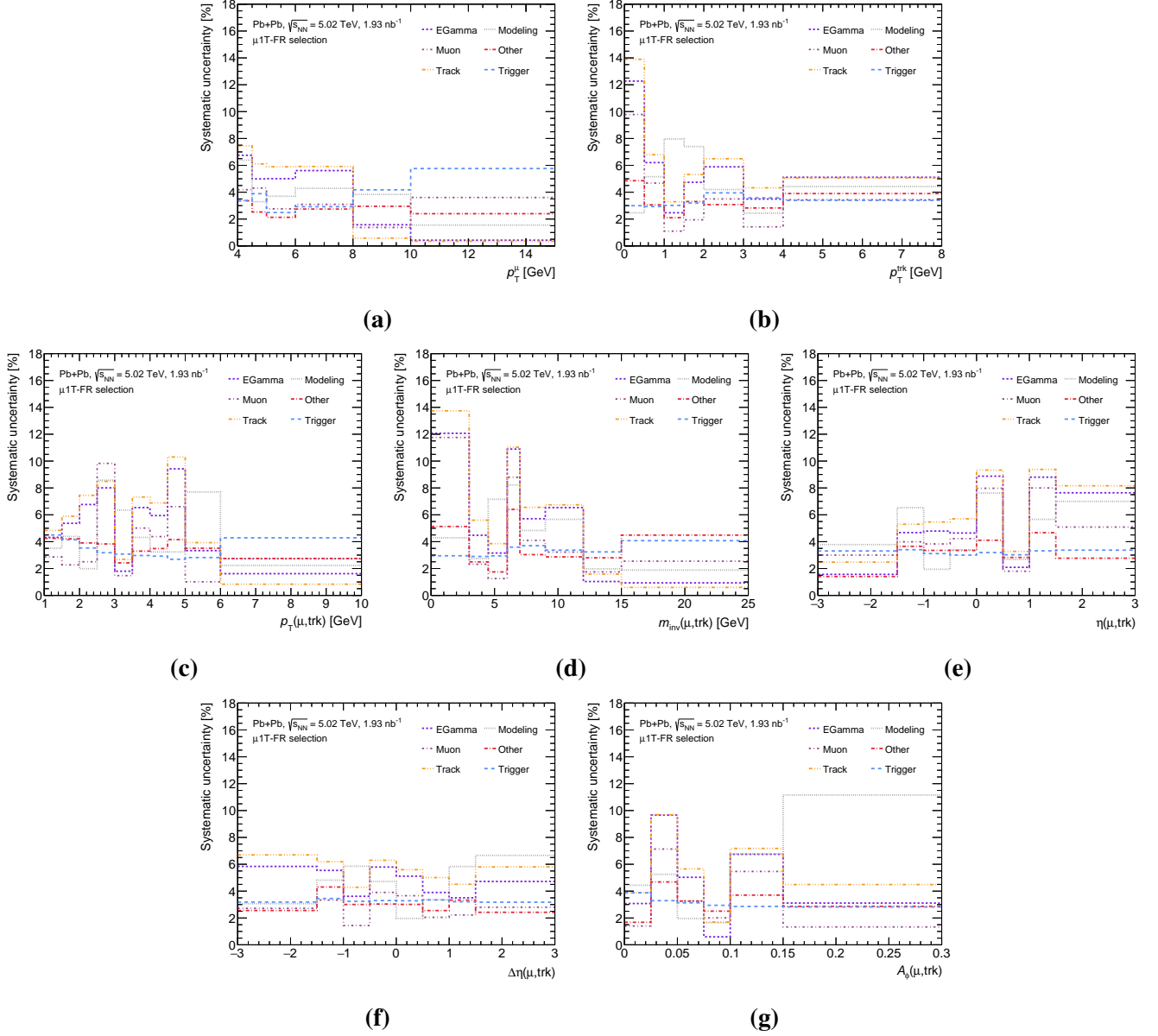


**Figure 5.18:** Grouped systematic uncertainty per bin for all kinematic observables in the  $\mu 1\text{T-FR}$  region: (a)  $p_T^\mu$ , (b)  $p_T^{\text{trk}}$ , (c)  $p_T(\mu, \text{trk})$ , (d)  $m_{\text{inv}}(\mu, \text{trk})$ , (e)  $\eta(\mu, \text{trk})$ , (f)  $\Delta\eta(\mu, \text{trk})$ , and (g)  $A_\phi(\mu, \text{trk})$



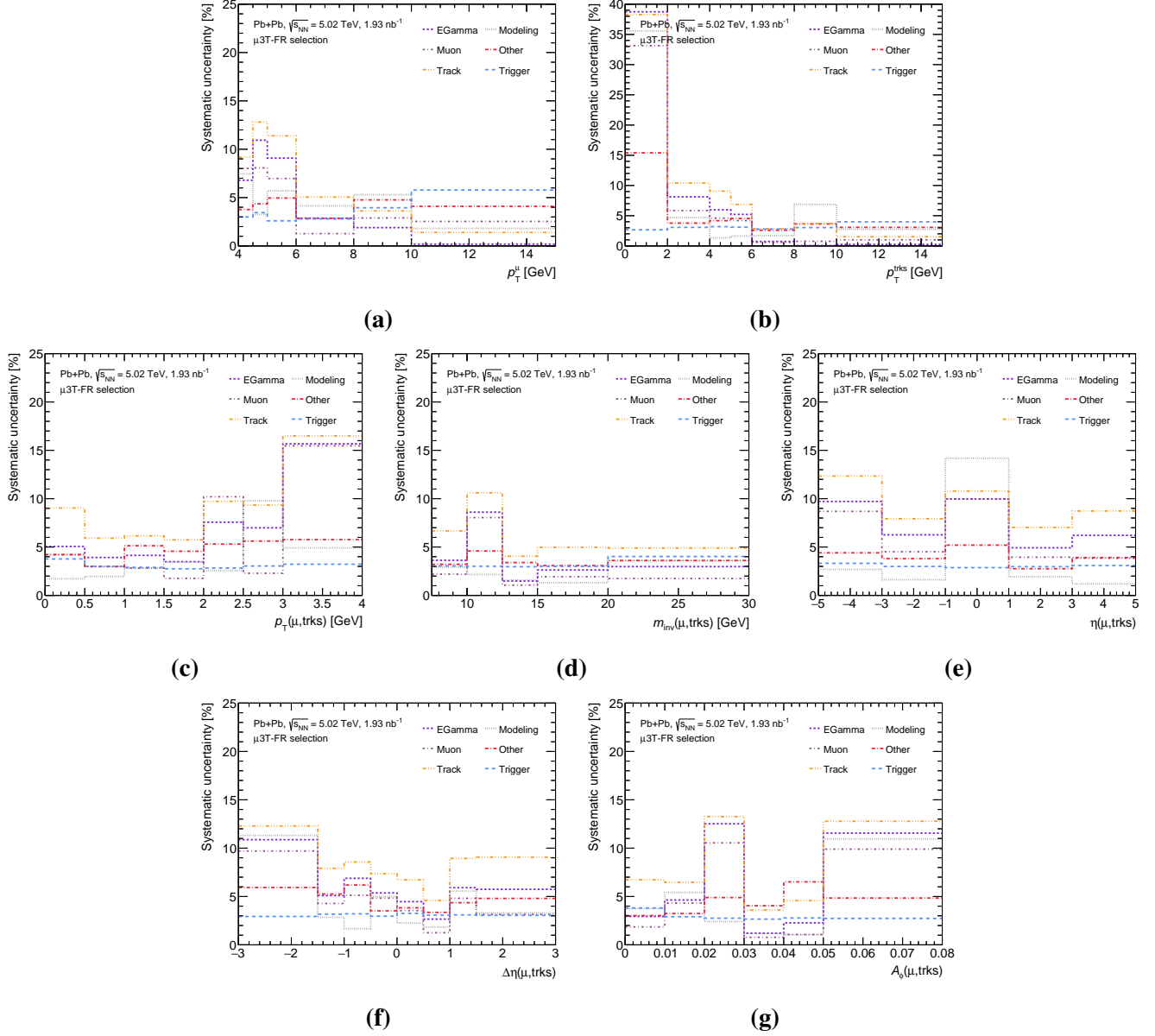


**Figure 5.19:** Grouped systematic uncertainty per bin for all kinematic observables in the  $\mu 3\text{T-FR}$  region: (a)  $p_T^\mu$ , (b)  $p_T^{\text{trks}}$ , (c)  $p_T(\mu, \text{trks})$ , (d)  $m_{\text{inv}}(\mu, \text{trks})$ , (e)  $\eta(\mu, \text{trks})$ , (f)  $\Delta\eta(\mu, \text{trks})$ , and (g)  $A_\phi(\mu, \text{trks})$ .

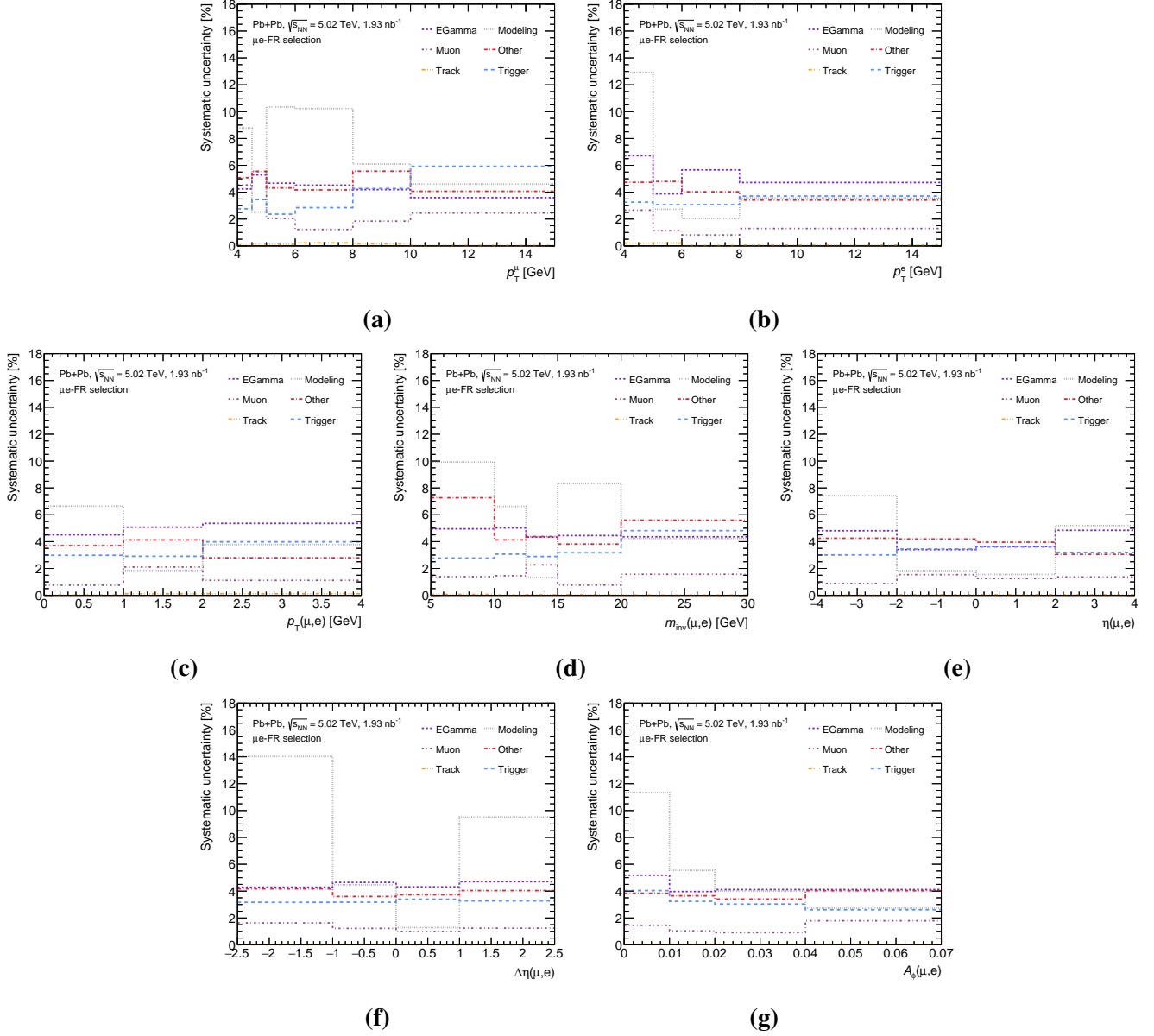


**Figure 5.20:** Grouped systematic uncertainty per bin for all kinematic observables in the  $\mu e$ -FR region: (a)  $p_T^\mu$ , (b)  $p_T^e$ , (c)  $p_T(\mu, e)$ , (d)  $m_{\text{inv}}(\mu, e)$ , (e)  $\eta(\mu, e)$ , (f)  $\Delta\eta(\mu, e)$ , and (g)  $A_\phi(\mu, e)$ .

## 5.9 Measured differential fiducial cross-sections

The result of the unfolding procedure for a kinematic observable  $x$ , is the number of fiducial events  $N_i$  for each fiducial bin  $i$ . Suppose  $\Delta x_i$  is the corresponding bin width. The differential cross-section is then obtained using

$$\frac{d\sigma}{d\Delta x_i} = \frac{N_i}{\mathcal{L}_{\text{int}}\Delta x_i}, \quad (5.28)$$

where  $\mathcal{L}_{\text{int}} = 1.93 \text{ nb}^{-1}$  is the central value of the luminosity of the 2015+2018 dataset.

The measured differential fiducial cross-sections for all kinematic observables of interest are presented in Figs. 5.21 to 5.23. The statistical uncertainties on the data points correspond to the square root of the diagonal entries of the statistical covariance matrices (see Sec. 5.7.7). The total uncertainty per bin is given by the sum-in-quadrature of the statistical and total systematic uncertainties. The precision of the measured cross-sections is between 10% and 50% depending on the observable and region, which is overwhelmingly dominated by the statistical uncertainties. The measured cross-sections are compared to the following predictions:

- **SL/SC+Py8+T**, shown with blue up-facing triangle markers: Nominal  $\gamma\gamma \rightarrow \tau^+\tau^-$  signal sample, where STARlight was used for the hard scattering (denoted by “SL”), Pythia8 for photon radiation by the taus before decay (denoted by “Py8”), and Tauola was used for the tau decays (denoted by “T”). The “/SC” indicates that the  $w_{\gamma\text{-flux}}$  was included in the Monte Carlo weights, to convert the STARlight photon flux into the SuperChic (i.e. “SC”) version.
- **SL/SC+Py8**, shown with red down-facing triangle markers: Alternate  $\gamma\gamma \rightarrow \tau^+\tau^-$  signal sample, where Pythia8 is used for the tau decays as well as the pre-decay photon radiation.
- **SL/SC+Py8+T+S-corr**, shown with green cross markers: Same as the SL/SC+Py8+T prediction, but with the bin-by-bin corrections for spin correlation effects included, as denoted by “S-corr”. This prediction is only shown for the  $\mu\text{1T-FR}$  region, as the spin correlation correction is neglected for the  $\mu\text{3T-FR}$  and  $\mu e\text{-FR}$  regions (see Sec. 5.3.4).
- **SL+Py8+T**, shown with violet plus markers: Same as the SL/SC+Py8+T prediction, but the  $w_{\gamma\text{-flux}}$  reweighting is omitted, i.e. the photon flux corresponds to the native STARlight version.

Overall, reasonable agreement is observed between the data and predictions. The agreement is better for the SL/SC+Py8+T prediction than for the SL+Py8+T prediction, indicating that the data favors the SuperChic photon flux over the STARlight photon flux. This observation is in line with the trends observed in  $\gamma\gamma \rightarrow e^+e^-$  and  $\gamma\gamma \rightarrow \mu^+\mu^-$  scattering [208, 209]. There

	$\mu 1\text{T-SR}$	$\mu 3\text{T-SR}$	$\mu e\text{-SR}$	Global
SL/SC+Py8+T	1.35	1.10	1.95	1.40
SL/SC+Py8	1.10	1.18	1.73	1.27
SL/SC+Py8+T+S-corr	1.10	1.10	1.95	1.30
SL+Py8+T	1.53	0.97	2.26	1.51

**Table 5.8:** Average  $\chi^2$  per bin, obtained when comparing the measured differential cross-sections to various theoretical predictions. The comparisons are done for the measured bins in all three fiducial regions, as well as for a *Global* combination of all measured bins.

are small visible differences between the SL/SC+Py8+T and SL/SC+Py8 predictions. The inclusion of the spin correlation corrections in the SL/SC+Py8+T+S-corr prediction slightly improves the data-theory agreement in the  $p_T(\mu, \text{trk})$  observable, but it does not fully resolve the observed differences.

The level of agreement between the data and predictions is quantified by the average  $\chi^2$  per unfolded bin,  $\bar{\chi}^2$ , which is defined as

$$\bar{\chi}^2 = \frac{1}{N_{\text{bins}}} \sum_{i,j=1}^{N_{\text{bins}}} (D_i - T_i) (V^{-1})_{ij} (D_j - T_j). \quad (5.29)$$

Here,  $D$  and  $T$  are the data and prediction respectively,  $i$  and  $j$  run over all  $N_{\text{bins}}$  bins, and  $V$  is the covariance matrix of the measured cross-sections. The diagonal entries of  $V$  correspond to the total uncertainty per bin (i.e. statistical and systematic uncertainties combined), while the off-diagonal entries correspond to the statistical covariance alone.

The results of the  $\chi^2$ -based comparisons are shown in Tab. 5.8 for all available truth predictions, when comparing to the measured cross-sections in the three fiducial regions. Additionally, a global comparison obtained by the sum of the  $\chi^2$ 's of the individual fiducial regions is also shown. Generally, the  $\bar{\chi}^2$  values are close to one, indicating that the predictions agree well with the data. The SL/SC+Py8 prediction has the smallest  $\bar{\chi}^2$  value for all comparisons, but the results are comparable to the SL/SC+Py8+T+S-corr prediction. Notably, the  $\bar{\chi}^2$  for the SL+Py8+T prediction is larger than for the other predictions by 0.2-0.5 units depending on the combination of bins, which further confirms the qualitative observation that the data favors the SuperChic photon flux.

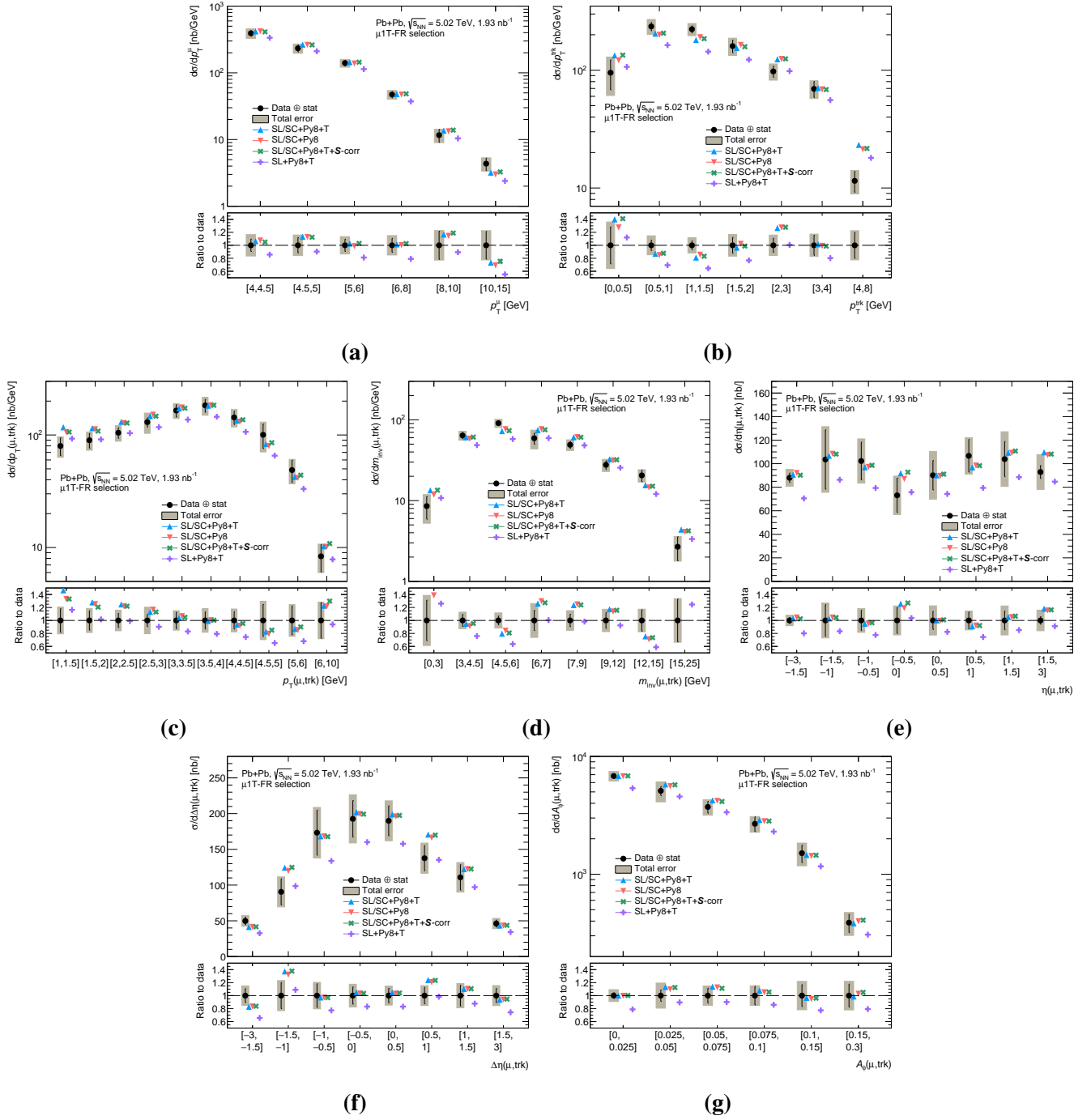


**Figure 5.21:** Differential fiducial cross-sections in units of nb, for all kinematic observables of interest in the  $\mu$ 1T-FR region: (a)  $p_T^\mu$ , (b)  $p_T^{\text{trk}}$ , (c)  $p_T(\mu, \text{trk})$ , (d)  $m_{\text{inv}}(\mu, \text{trk})$ , (e)  $\eta(\mu, \text{trk})$ , (f)  $\Delta\eta(\mu, \text{trk})$ , and (g)  $A_\phi(\mu, \text{trk})$ . For the data points, the solid lines and shaded region correspond to the (uncorrelated) statistical and total uncertainties respectively. For the predictions, the error bars correspond to the statistical uncertainties only. The lower panels show the ratios of the predictions to the data. See Sec. 5.9 for the nomenclature for Monte Carlo predictions.

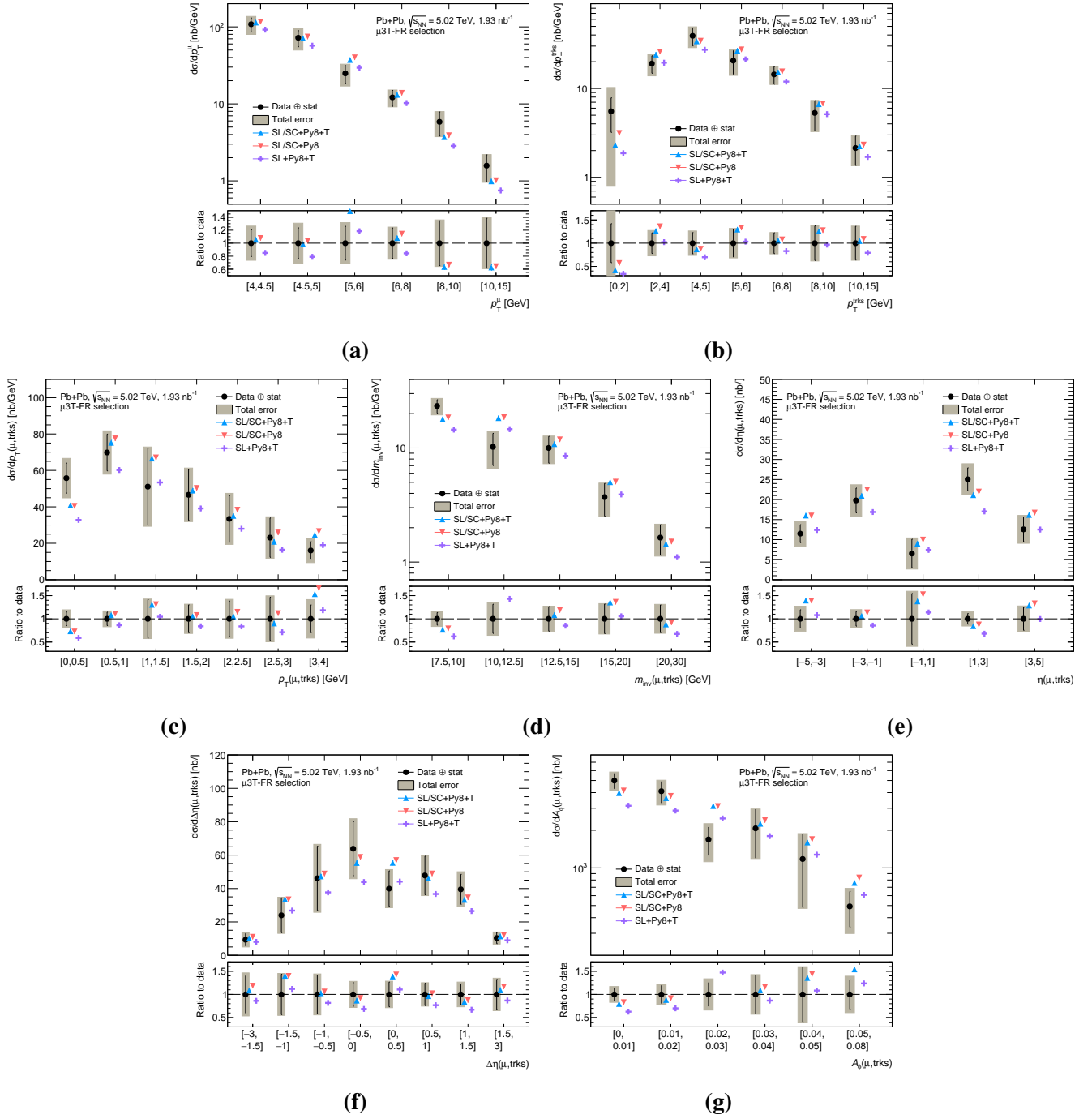


**Figure 5.22:** Differential fiducial cross-sections in units of nb, for all kinematic observables of interest in the  $\mu 3T$ -FR region: (a)  $p_T^\mu$ , (b)  $p_T^{\text{trks}}$ , (c)  $p_T(\mu, \text{trks})$ , (d)  $m_{\text{inv}}(\mu, \text{trks})$ , (e)  $\eta(\mu, \text{trks})$ , (f)  $\Delta\eta(\mu, \text{trks})$ , and (g)  $A_\phi(\mu, \text{trks})$ . For the data points, the solid lines and shaded region correspond to the (uncorrelated) statistical and total uncertainties respectively. For the predictions, the error bars correspond to the statistical uncertainties only. The lower panels show the ratios of the predictions to the data. See Sec. 5.9 for the nomenclature for Monte Carlo predictions.

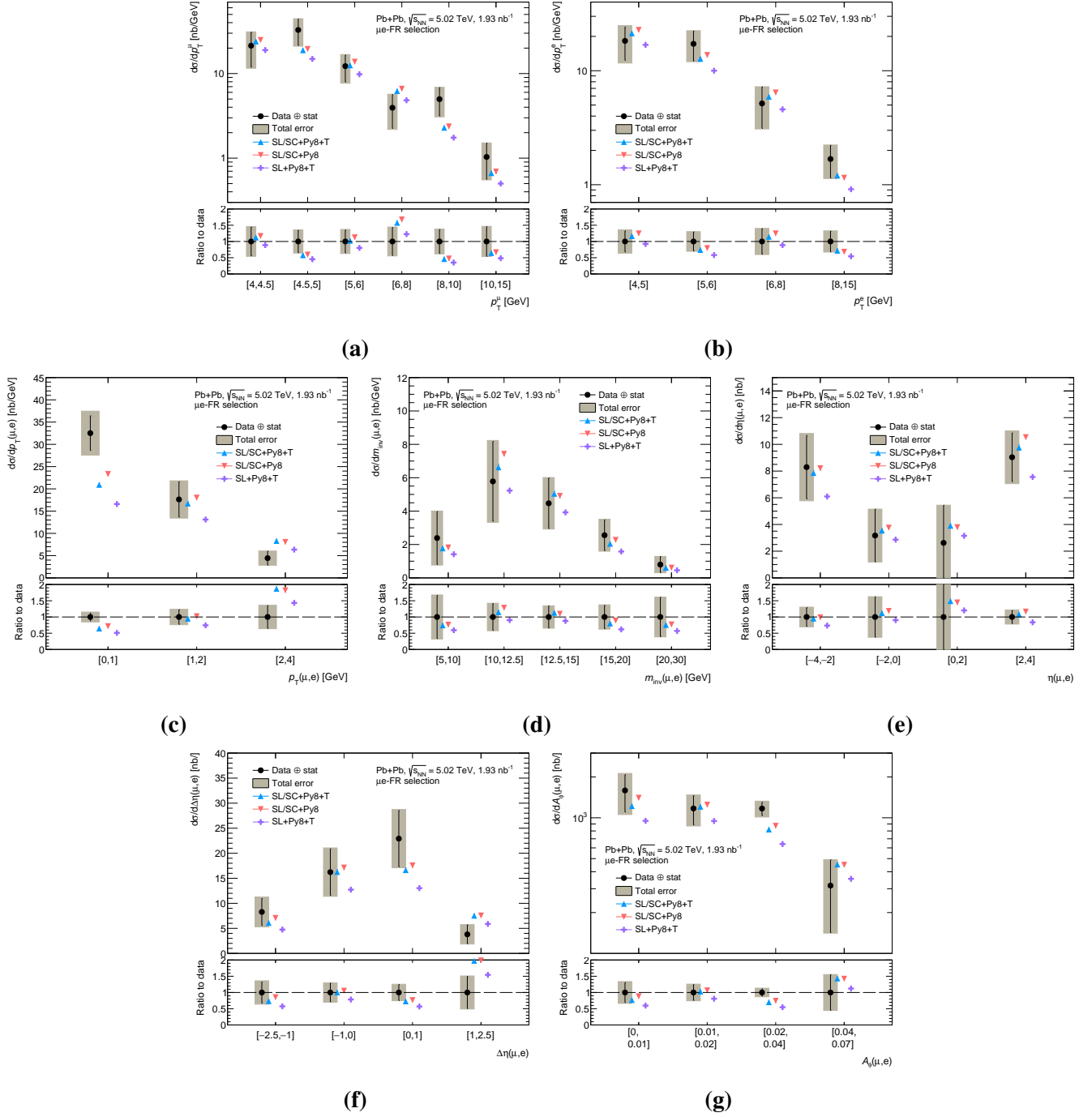


**Figure 5.23:** Differential fiducial cross-sections in units of nb, for all kinematic observables of interest in the  $\mu e$ -FR region: (a)  $p_T^\mu$ , (b)  $p_T^e$ , (c)  $p_T(\mu, e)$ , (d)  $m_{\text{inv}}(\mu, e)$ , (e)  $\eta(\mu, e)$ , (f)  $\Delta\eta(\mu, e)$ , and (g)  $A_\phi(\mu, e)$ . For the data points, the solid lines and shaded region correspond to the (uncorrelated) statistical and total uncertainties respectively. For the predictions, the error bars correspond to the statistical uncertainties only. The lower panels show the ratios of the predictions to the data. See Sec. 5.9 for the nomenclature for Monte Carlo predictions.

## 5.10 Constraints on tau lepton electromagnetic dipole moments

### 5.10.1 Modeling of non-zero dipole moments

The effect of the tau lepton EMDMs on the  $\gamma\gamma \rightarrow \tau^+\tau^-$  cross-section is captured in the  $\gamma\tau^+\tau^-$  vertex function defined in Eq. 2.41. Since the initial state photons in UPCs have virtualities of  $\mathcal{O}(10^{-3}) \text{ GeV}^2$ , it is reasonable to assume that the photons are on-shell. Thus, the  $q^2$ 's in Eq. 2.41 are set to zero, which results in the simplified vertex function,

$$i\Gamma^\mu(p_1, p_2) = -ie \left[ \gamma^\mu + \frac{i\sigma^{\mu\nu}q_\nu}{2m} F_2^0 + \frac{\gamma^5 \sigma^{\mu\nu}q_\nu}{2m} F_3^0 \right]. \quad (5.30)$$

Here,  $F_1(0) = 1$  is used, while  $F_2(0) \equiv F_2^0$  and  $F_3(0) \equiv F_3^0$  are introduced for brevity. As described in Sec. 2.2, the anomalous magnetic dipole moment of the tau lepton is given by  $a_\tau = F_2^0$ , and the electric dipole moment of the tau lepton is given by  $d_\tau = \frac{e}{2m_\tau} F_3^0$ .

Since the tau lepton EMDMs appear at the level of the hard scattering, their impact is determined by computing the variation in the squared matrix element of  $\gamma\gamma \rightarrow \tau^+\tau^-$  scattering due to non-zero values of the EMDMs. The  $\gamma\gamma \rightarrow \tau^+\tau^-$  matrix element (see Eq. 2.78), with the simplified  $\gamma\tau^+\tau^-$  vertex function, was calculated using `FeynCalc` [239], which uses the standard spin-polarization sums. The calculation was done in the center of mass frame of the two tau leptons. The center of mass energy is  $2E$ , and the photons are assumed to be on-shell. The calculation was done with the following kinematics:  $p_{\gamma_1}^\mu = (E, E\mathbf{z})$ ,  $p_{\gamma_2}^\mu = (E, -E\mathbf{z})$ ,  $p_{\tau^+}^\mu = (E, \mathbf{p})$ , and  $p_{\tau^-}^\mu = (E, -\mathbf{p})$ . Here,  $\mathbf{p} = (0, \beta E \sin \theta, \beta E \cos \theta)$  is the three-momentum of the tau leptons with  $\beta = \sqrt{1 - \frac{m_\tau^2}{E^2}}$  being the boost, and  $\theta$  being the polar angle.

Since the EMDMs appear in the  $\gamma\tau^+\tau^-$  vertex function as multiplicative constants, the squared matrix element can be factorized in  $F_2^0$  and  $F_3^0$ , i.e.

$$|\mathcal{M}(\beta, \theta, F_2^0, F_3^0)|^2 = \sum_{i,j=0}^4 (F_2^0)^i (F_3^0)^j C_{ij}, \quad (5.31)$$

where non-zero  $C_{ij}$  are

$$\begin{aligned} C_{00} &= \frac{1 + 2\beta^2 \sin^2 \theta - \beta^4 (\sin^4 \theta + 1)}{(1 - \beta^2 \cos^2 \theta)^2}, \\ C_{10} &= \frac{4}{1 - \beta^2 \cos^2 \theta}, \\ C_{20} &= \frac{5 - 3\beta^2 - 2\beta^2 \cos 2\theta}{(1 - \beta^2)(1 - \beta^2 \cos^2 \theta)}, \\ C_{30} &= \frac{2(1 - \beta^2 \cos 2\theta)}{(1 - \beta^2)(1 - \beta^2 \cos^2 \theta)}, \\ C_{40} &= \frac{1 - 2\beta^2 \cos 2\theta - \beta^4 (2 - 2\cos^2 \theta - \cos^4 \theta)}{4(1 - \beta^2)^2 (1 - \beta^2 \cos^2 \theta)}, \end{aligned}$$



$$\begin{aligned}
C_{02} &= \frac{3 - \beta^2 - 2\beta^2 \cos 2\theta}{(1 - \beta^2)(1 - \beta^2 \cos^2 \theta)}, \\
C_{12} &= C_{30}, \\
C_{22} &= 2C_{40}, \\
C_{04} &= C_{40}.
\end{aligned} \tag{5.32}$$

The first term  $C_{00}$  corresponds to the Standard Model squared matrix element. There are no  $C_{ij}$  with  $j = 1, 3$  due to the  $\mathcal{CP}$  even-ness of  $|\mathcal{M}|^2$ . Thus, the squared matrix element is sensitive only to the absolute value of  $F_3^0$ , and not its sign.

In this analysis, non-zero tau lepton EMDMs are included in the Monte Carlo predictions using an event-by-event reweighting procedure [240], that is applied to the existing Standard Model  $\gamma\gamma \rightarrow \tau^+\tau^-$  Monte Carlo samples. For a given value of  $F_2^0$  and  $F_3^0$ , the weight

$$w(\beta, \theta, F_2^0, F_3^0) = \frac{|\mathcal{M}(\beta, \theta, F_2^0, F_3^0)|^2}{|\mathcal{M}(\beta, \theta, 0, 0)|^2} \tag{5.33}$$

is included in the theoretical modeling. In the denominator, the tree-level Standard Model values (i.e. zero) are used for  $F_{2,3}^0$ . The kinematic variables  $\beta$  and  $\theta$  are computed at truth-level from the  $2 \rightarrow 2$  scattering process (i.e. before tau lepton decay) in the center of mass frame.

As an example, the impact of non-zero  $F_2^0$  and  $F_3^0$  on the predicted truth-level  $p_T^\mu$  cross-section in the  $\mu 1\text{T-FR}$  region is shown in Fig. 5.24. The same comparisons for all kinematic observables of interest are shown in App. A.6. Generally, the effect of non-zero EMDMs is to increase the overall cross-section. Certain observables like  $p_T^\mu$  and the system  $p_T$  and invariant mass variables show enhanced sensitivity to the EMDMs, particularly towards higher values. This is due to the fact that those phase space regions correspond to  $\gamma\gamma \rightarrow \tau^+\tau^-$  events with high  $m_{\text{inv}}(\tau, \tau)$ , where the sensitivity to the tau lepton EMDMs is expected to be higher.

The matrix elements presented above were computed with the standard spin-polarization sums, and are therefore *un-polarized*. The impact of spin correlations on the Standard Model cross-sections has already been investigated in Sec. 5.3.4, but it is important to investigate the interplay between spin correlations and the modeling of non-zero EMDMs. In two recent TauSpinner papers, the  $\gamma\gamma \rightarrow \tau^+\tau^-$  matrix element was computed with full spin correlation and non-zero EMDM effects: in Ref. [90] the linear dependence of  $|\mathcal{M}|^2$  on  $F_2^0$  and  $F_3^0$  was presented, while in Ref. [91], the full quartic dependence was shown. It is worth noting that Eq. 5.32 appears in the results of Ref. [91], thereby validating the calculations shown here.

At the time of writing this thesis, only the calculations in Ref. [90] were publicly available, so they were used in a spin correlation sensitivity study similar to Sec. 5.3.4. By investigating the double ratio of cross-sections,

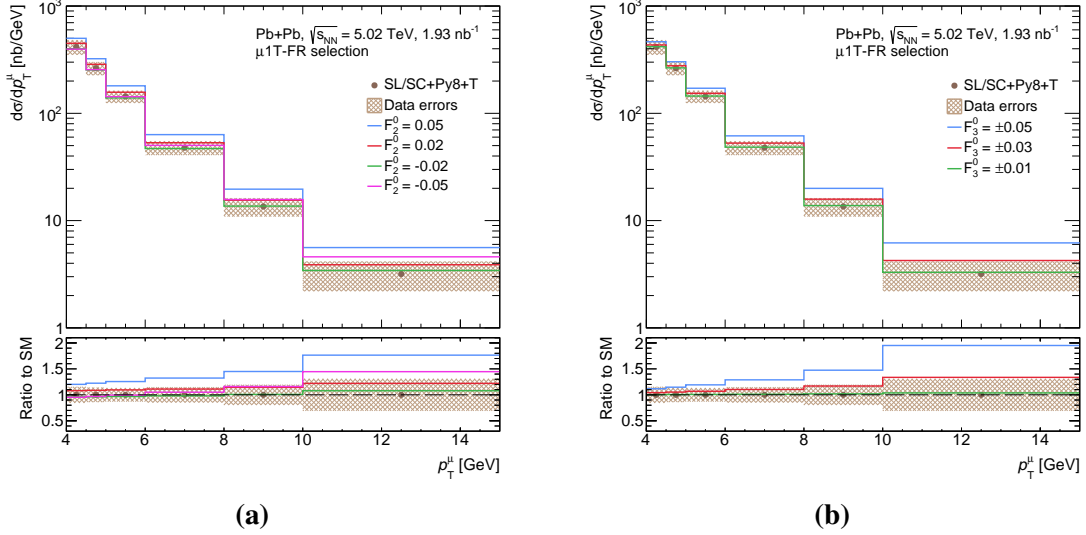


**Figure 5.24:** Sensitivity of the  $p_T^\mu$  observable in the  $\mu 1T$ -FR region to (a)  $F_2^0$  and (b)  $F_3^0$ . The SM prediction corresponding to the SL/SC+Py8+T sample is shown with brown markers, with the total uncertainty of the measured cross-sections in the shaded bands. Predictions are shown for  $F_2^0 = \pm 0.02, \pm 0.05$  and  $F_3^0 = \pm 0.01, \pm 0.03, \pm 0.05$ , along with the corresponding ratios to the SM predictions in the lower panels. The predictions are shown together with the data errors, as the analysis is blinded.

$$\frac{\left( \frac{d\sigma^{\text{pol}}(F_2^0, F_3^0 \neq 0)}{dx} \right)}{\left( \frac{d\sigma^{\text{pol}}(F_2^0, F_3^0 = 0)}{dx} \right)} \bigg/ \frac{\left( \frac{d\sigma^{\text{unpol}}(F_2^0, F_3^0 \neq 0)}{dx} \right)}{\left( \frac{d\sigma^{\text{unpol}}(F_2^0, F_3^0 = 0)}{dx} \right)}, \quad (5.34)$$

it is possible to isolate the effect of the interplay between spin correlations and the tau lepton EMDMs, on the fiducial cross-sections of interest. The quantities appearing in this equation are the same as in Eq. 5.9, but with the dependence of the spin weights on  $F_2^0$  and  $F_3^0$  included. It was found that this double ratio is consistent with unity for all kinematic observables of interest. This does not imply that there is no interplay between spin correlations and the tau lepton EMDMs. It is entirely possible that other observables not investigated in this analysis (e.g.  $\mathcal{CP}$ -odd observables), will be sensitive to this interplay. Based on the results of this study, it was concluded that the un-polarized matrix element calculations of Eq. 5.32 are sufficient for the modeling of the tau lepton EMDMs.

### 5.10.2 Statistical framework

#### Likelihood model

The goal of a statistical analysis is to quantify the compatibility between the prediction of a theoretical model and measured experimental data. This is achieved using a *likelihood* function, which gives the probability to measure the data, given a certain model. Typically, statistical

analyses using LHC collision data employ likelihood functions which are constructed using Poisson distributions, since the data entering the analyses (counts of reconstruction-level observables) are Poisson-distributed [241]. Such Poisson-based likelihood functions implicitly assume that the data are statistically uncorrelated. In the case of the analysis presented in this thesis, the data are the unfolded cross-sections measurements per fiducial bin, which have significant statistical correlations, so a Poisson-based likelihood is not the optimal approach<sup>10</sup>. The likelihood function used in this analysis is inspired by those defined in the extraction of parton distribution functions (PDFs) by ATLAS and by the H1 experiment [243], due to the fact that those extractions [244, 245], and others like it, often use data that are statistically correlated with each other.

The construction of the likelihood function proceeds as follows. Consider a cross-section measurement performed over  $N_{\text{bins}}$  bins, where  $\mathbf{n} = \{n_1, n_2, \dots, n_{N_{\text{bins}}}\}$  are the measured values per bin, with  $V$  be the statistical covariance between them. Suppose the analysis includes  $N_{\text{syst}}$  systematic uncertainties (modeling uncertainties, detector performance uncertainties etc.), such that  $\gamma_{ij}$  is the change of the cross-section in the  $i^{\text{th}}$  bin due to the  $j^{\text{th}}$  systematic uncertainty, with  $j = 1, 2, \dots, N_{\text{syst}}$ . Let  $T_i(\boldsymbol{\mu})$  be the cross-section predicted by a given model, which depends on a set of physical *parameters of interest* (POIs)  $\boldsymbol{\mu} = \{\mu_1, \mu_2, \dots, \mu_{N_{\text{POI}}}\}$ . The predictions are assumed to be affected by modeling uncertainties, whose impacts are quantified by  $\tilde{\gamma}_{im}$ , i.e. the change of the predicted cross-section in the  $i^{\text{th}}$  bin due to the  $m^{\text{th}}$  modeling uncertainty.

With these definitions, the likelihood function is given by

$$\mathcal{L}(\boldsymbol{\mu}, \mathbf{b}) = \exp \left[ -\frac{1}{2} \sum_{i,k=1}^{N_{\text{bins}}} \Delta_i (V^{-1})_{ik} \Delta_k \right] \prod_{j=1}^{N_{\text{syst}}} e^{-\frac{b_j^2}{2}}, \quad (5.35)$$

where  $\mathbf{b} = \{b_1, b_2, \dots, b_{N_{\text{syst}}}\}$  are a set of *nuisance parameters* (NPs), which include the effect of systematic uncertainties in the likelihood. The product over  $e^{-\frac{b_j^2}{2}}$  constrains the nuisance parameters to small values. The terms  $\Delta_i$  are the difference between the measurement and the model prediction,

$$\Delta_i = n_i \left( 1 - \sum_{j=1}^{N_{\text{syst}}} \gamma_{ij} b_j \right) - T_i(\boldsymbol{\mu}) \left( 1 - \sum_{m=1}^{N_{\text{syst}}} \tilde{\gamma}_{im} b_m \right). \quad (5.36)$$

Here, the terms in the brackets quantify the impact of the systematic uncertainties. The same set of nuisance parameters appears in both brackets. The non-zero terms in  $\sum_{m=1}^{N_{\text{syst}}} \tilde{\gamma}_{im} b_m$  are related to the modeling uncertainties only, since  $\tilde{\gamma}_{im} = 0$  otherwise.

To first order in  $\mathbf{b}$ , the likelihood function given by Eq. 5.35 allows the systematic uncer-

<sup>10</sup>Technically, it is possible to construct a correlated multi-dimensional Poisson-based likelihood (see Sec. 2.1 of Ref. [242]). However, such a likelihood function can only include one “global” correlation parameter, which is not applicable in this analysis, since every measured bin is uniquely correlated with every other bin.

tainties to be correlated between bins. Uncorrelated systematic uncertainties are summed-in-quadrature into the diagonal entries of the covariance matrix  $V$ . In this analysis, the background and response matrix statistical uncertainties are treated as uncorrelated. Additionally, the statistical uncertainty of the predictions  $T_i(\mu)$  are also treated as uncorrelated.

### Best-fit values and constraints

The likelihood function can be maximized with respect to the free parameters  $\mu$  and  $b$  in a statistical *fit* to the measurements  $n$ . This, by definition, maximizes the compatibility of the data and theoretical predictions. The values of  $\mu$  and  $b$  at which this occurs are denoted by  $\hat{\mu}$  and  $\hat{b}$ , and are called the *best-fit* values. In practice, the best-fit values of the free parameters are obtained by minimizing the (twice) negative log likelihood (NLL) function, i.e.

$$\{\hat{\mu}, \hat{b}\} \equiv \underset{\mu, b}{\operatorname{argmin}} [-2\text{NLL}(\mu, b)] = \underset{\mu, b}{\operatorname{argmin}} [-2 \ln \mathcal{L}(\mu, b)]. \quad (5.37)$$

Here, the factor of 2 ensures that  $-2\text{NLL}(\mu, b)$  for the likelihood function given by Eq. 5.35 takes the form of a  $\chi^2$  function between the data and prediction, i.e.

$$\chi^2(\mu, b) = -2 \ln \mathcal{L}(\mu, b). \quad (5.38)$$

In this analysis, the  $\chi^2$  minimization is performed using a framework based on the `Minuit2` library [246]. It makes use of the `Migrad` algorithm, which is based on the BFGS algorithm [247]. The approach follows Newton's method of minimization, where the inverse Hessian matrix is approximated at each iteration, rather than being computed exactly.

The likelihood function can also be used to set *constraints* or *limits* on the POIs. This can be achieved using the test statistic  $t(\mu)$ , also referred to as the *profile likelihood ratio* [241],

$$t(\mu) = -2 \ln \frac{\mathcal{L}(\mu, \hat{b})}{\mathcal{L}(\hat{\mu}, \hat{b})}, \quad (5.39)$$

where  $\hat{b}$  are the nuisance parameter values that maximize the likelihood at the given  $\mu$ . Using the  $\chi^2$  notation, the test statistic can also be written as

$$t(\mu) = \Delta\chi^2(\mu) = \chi^2(\mu, \hat{b}) - \chi^2(\hat{\mu}, \hat{b}). \quad (5.40)$$

Confidence intervals on the parameters of interest are extracted when  $\Delta\chi^2(\mu)$  crosses a given threshold. The 68% confidence level (CL) intervals are given by the  $\mu$  values that satisfy  $\Delta\chi^2(\mu) = 1.0$ , while the 95% CL intervals are defined by  $\Delta\chi^2(\mu) = 3.92$ . In this analysis, the confidence intervals are obtained by fitting the  $\Delta\chi^2(\mu)$  curves with 12<sup>th</sup> order polynomials, and extracting the values of those polynomials at 1.0 and 3.92.

### Linear template morphing

Using the reweighting procedure described in Sec. 5.10.1, a total of 76 templates were created for non-zero values of  $F_2^0$  and  $F_3^0$ . For each POI, the templates were created with the other POI fixed to its tree-level Standard Model value of zero. The scan over  $F_2^0$  and  $F_3^0$  values was performed between  $-0.1$  and  $+0.1$ , with a step size of  $0.002$  in the range  $[-0.06, +0.06]$ , and with a step size of  $0.005$  in the ranges  $[-0.1, -0.06]$  and  $[+0.06, +0.1]$ . This scan was chosen as it provides sufficient granularity in the POIs around the expected constraints.

During the  $\chi^2$  minimization procedure, the minimizer can request the predicted cross-sections for arbitrary POI values. The predictions for such cases are computed using a linear template morphing approach. Suppose the minimizer requests the predicted cross-section in a certain bin, for a POI value of  $\mu'$ , which lies between two POI values  $\mu_{1,2}$  that are in the known POI scan. Let  $y_{1,2}$  be the predicted cross-sections for  $\mu_{1,2}$ . The predicted cross-section for  $\mu'$ , called  $y'$ , is given by

$$y' = y_1 + (\mu' - \mu_1) \frac{(y_2 - y_1)}{(\mu_2 - \mu_1)}. \quad (5.41)$$

### Fit diagnostics

The first diagnostic of the robustness of the statistical analysis is the *pull* of the nuisance parameters  $b_i$ , defined as

$$\text{Pull}_i = \frac{\hat{b}_i - b_{i,0}}{\Delta b_i}, \quad (5.42)$$

where  $b_{i,0}$  is the initial value of the nuisance parameter (set to zero by default),  $\hat{b}_i$  is the best-fit value, and  $\Delta b_i = \left( \frac{d^2\chi^2(\mu, b)}{db_i^2} \right)^{-1}$  is uncertainty of  $b_i$ , obtained from the inverse Hessian along the  $b_i$  direction. The pulls are typically assigned an error bar of the size of  $\Delta b_i$ .

Ideally, the pulls should be  $0 \pm 1$ , since the pre-fit errors of  $b_i$  are unity in Eq. 5.35. If the pulls are non-zero, it could imply that the associated systematic uncertainty is overestimated, and that the data favors a non-zero value of the nuisance parameter. If  $\Delta b_i < 1$ , the size of the associated systematic uncertainty is constrained by the data. On the other hand, if  $\Delta b_i > 1$ , the associated systematic uncertainty may be underestimated.

The second diagnostic of the statistical analysis is the *impact* of the nuisance parameters on  $\hat{\mu}$ , which is defined as the change in  $\hat{\mu}$  when the nuisance parameters are fixed to certain values. For each nuisance parameter in the fit, the following impacts are considered:

- Pre-fit\_\_1up, where  $b_i = +1$  is set.
- Pre-fit\_\_1down, where  $b_i = -1$  is set.
- Post-fit\_\_1up, where  $b_i = \hat{b}_i + \Delta b_i$  is set.
- Post-fit\_\_1down, where  $b_i = \hat{b}_i - \Delta b_i$  is set.

If the post-fit impact is smaller than the pre-fit impact, the associated systematic uncertainty is likely constrained in the fit. Conversely, a post-fit impact that is larger than the pre-fit impact may imply that the systematic uncertainty was underestimated. Further, the sizes of the impacts are related to the size of the coupling between  $\mu$  and  $b$  in  $\chi^2(\mu, b)$ , which gives a measure of the “correlation” between the nuisance parameters and the POIs. In particular, large couplings between  $\mu$  and  $b$  can result in large impacts, and vice versa.

### Fit strategy

The parameter of interest for the anomalous magnetic dipole moment is  $F_2^0$ , which is numerically the same as  $a_\tau$ . Since the electric dipole moment  $d_\tau$  carries units of electric charge times centimeter, current limits place it numerically in the  $10^{-16} - 10^{-17}$  range. In order to avoid numerical issues in the statistical analysis, the form factor  $F_3^0$  is extracted rather than  $d_\tau$ . The fit results for the electric dipole moment are presented in terms of  $d_\tau$ , using the relation  $d_\tau = 5.5925 \times 10^{-15} F_3^0 e \cdot \text{cm}$ , which is obtained after converting  $\frac{1}{2m_\tau}$  to cm.

In principle, it is possible to perform a simultaneous extraction of  $F_2^0$  and  $F_3^0$ , by allowing both dipole moments to be non-zero in the likelihood. Such a *two-dimensional* fit without systematic uncertainties was performed as a preliminary check of this approach. The corresponding error ellipses (two-dimensional generalizations of the one-dimensional confidence intervals) had no discernable rotation, implying that the likelihood contains minimal coupling between the two dipole moments. This is not surprising, since the couplings induced by  $C_{12}$  and  $C_{22}$  in Eq. 5.32 are highly suppressed with respect to the leading modifications to the squared matrix element, i.e.  $C_{10}$  and  $C_{02}$ . Thus, the fits to the EMDMs are performed separately for  $F_2^0$  and  $F_3^0$ , by setting the dipole moment that is not being fitted to zero.

The fits presented in this thesis are *blinded*, i.e. they are performed without directly considering the measured  $\gamma\gamma \rightarrow \tau^+\tau^-$  cross-section values. Instead,  $n$  are taken to be the Standard Model predictions, i.e.  $T_i(a_\tau = 0, d_\tau = 0)$ . The statistical covariance matrix  $V$  and the impacts due to systematic uncertainties  $\gamma_{ik}$  and  $\tilde{\gamma}_{im}$ , are used from the measured cross-sections. By construction, the best-fit values of  $a_\tau$ ,  $d_\tau$  and all nuisance parameters are zero. The constraints on  $a_\tau$  and  $d_\tau$  obtained in this setup are called the *expected* constraints, as opposed to the *observed* constraints that would be obtained if  $n$  were taken to be the measured cross-sections.

### 5.10.3 Effect of statistical combination

The effect of the statistical combination of unfolded bins from several distributions, in the extraction of constraints on the tau lepton EMDMs, is demonstrated using a fit without systematic uncertainties. In this setup, the nuisance parameters  $b$  are set to zero in Eq. 5.35, and are not treated as free parameters in the fit. The 68% and 95% confidence intervals are obtained for:

- **Single-variable fits:** the bins from a single fiducial cross-section are combined in the likelihood. Here, only the intra-variable statistical correlations are considered, i.e. the relevant square matrix along the main block diagonal in Fig. 5.15.

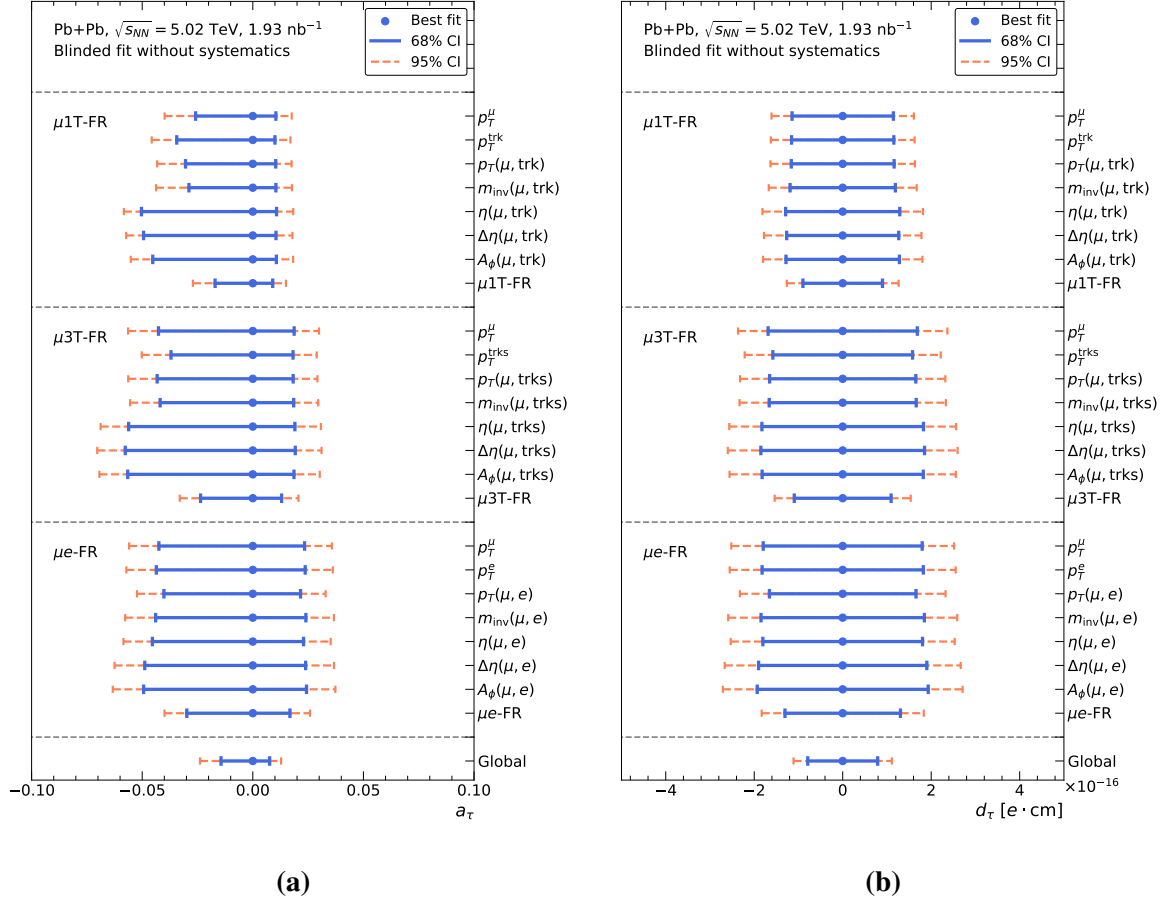


**Figure 5.25:** 68% and 95% confidence intervals (CIs) obtained for (a)  $a_\tau$  and (b)  $d_\tau$ , in a blinded fit without systematic uncertainties. The CIs are shown for each observable in the three fiducial regions, for combinations of all bins in a given region (last entry on the  $y$ -axis in each section), and for a global combination of all measured bins (final entry).

- **Full-region fits:** all cross-section bins in a given fiducial region (i.e. bins from seven kinematic observables) are combined in the likelihood. In this case, the entire covariance matrices are considered in the likelihood.
- **Global fits:** all cross-section bins across the three fiducial regions (i.e. bins from 21 kinematic observables) are combined in the likelihood. Since the fiducial regions themselves are uncorrelated, the global  $\chi^2$  is obtained using

$$\chi^2(\boldsymbol{\mu})_{\text{Global}} = \chi^2(\boldsymbol{\mu})_{\mu\text{1T-FR}} + \chi^2(\boldsymbol{\mu})_{\mu\text{3T-FR}} + \chi^2(\boldsymbol{\mu})_{\mu\text{e-FR}}. \quad (5.43)$$

The confidence intervals (CIs) for  $a_\tau$  and  $d_\tau$  obtained in these fits are shown in Fig. 5.25. Within each fiducial region, the full-region fits yield CIs that are smaller than those obtained using any single variable alone. Further, the global fits yields CIs that are smaller than those obtained from both single-variable and full-region fits. These results highlight the benefit of combining all measured cross-section bins in setting constraints on the tau lepton EMDMs.



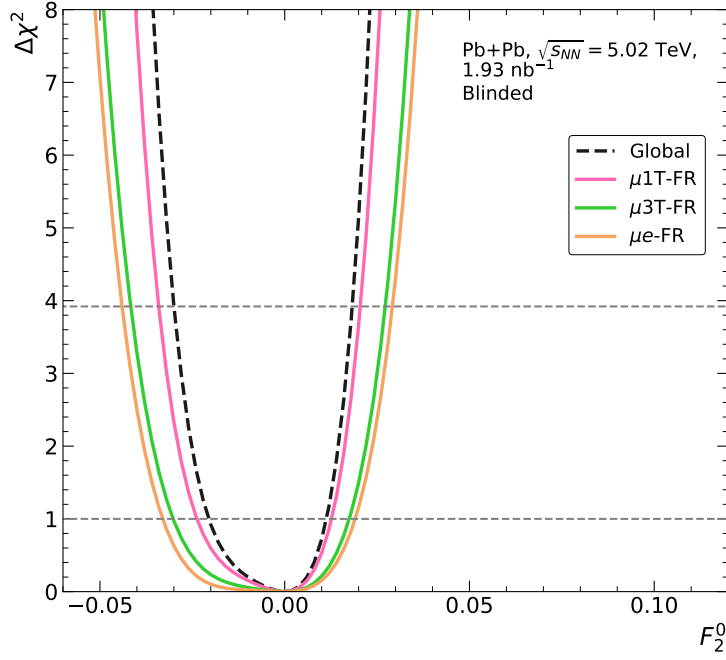


**Figure 5.26:**  $\Delta\chi^2$  curves obtained in the blinded full region and global fits to  $F_2^0$ .

Region	68% CI	95% CI
$\mu e$ -FR	$[-0.03302, +0.01909]$	$[-0.04402, +0.02916]$
$\mu 3T$ -FR	$[-0.03020, +0.01747]$	$[-0.04166, +0.02722]$
$\mu 1T$ -FR	$[-0.02376, +0.01270]$	$[-0.03410, +0.02047]$
Global	$[-0.02058, +0.01136]$	$[-0.03001, +0.01828]$

**Table 5.9:** Expected 68% and 95% confidence intervals (CIs) obtained for  $a_\tau$ , in the full region and global fits to  $F_2^0$ .

#### 5.10.4 Constraints on anomalous magnetic dipole moment

The  $\Delta\chi^2$  vs.  $F_2^0$  curves, i.e. *likelihood curves*, obtained in the fits to the differential cross-sections are shown in Fig. 5.26. The fits include nuisance parameters associated with all systematics given in Tab. 5.7. The likelihood curves are found to be parabolic, smooth, and minimized at  $F_2^0 = 0$  as expected for the blinded fit setup. Further, the likelihood curves are slightly “tilted” towards negative values of  $F_2^0$ , as the total  $\gamma\gamma \rightarrow \tau^+\tau^-$  cross-section is minimized at a small negative value ( $F_2^0 \approx -0.02$ ) in the phase space of the selected fiducial regions. The nuisance parameter impacts and pulls are given in App. A.7. All pulls are exactly at zero, and with errors that are very close to the pre-fit errors of  $\pm 1$ . The pre-fit and post-fit impacts are very similar, indicating that the fit does not strongly constrain any of the nuisance parameters.

The expected confidence intervals for  $a_\tau$  extracted from the likelihood curves are shown in Tab. 5.9. They are compared to previously published results, and to the Standard Model prediction, in Fig. 5.27. The expected statistical ordering, i.e. the length of the confidence interval being inversely related to the available statistics, is preserved even after including all



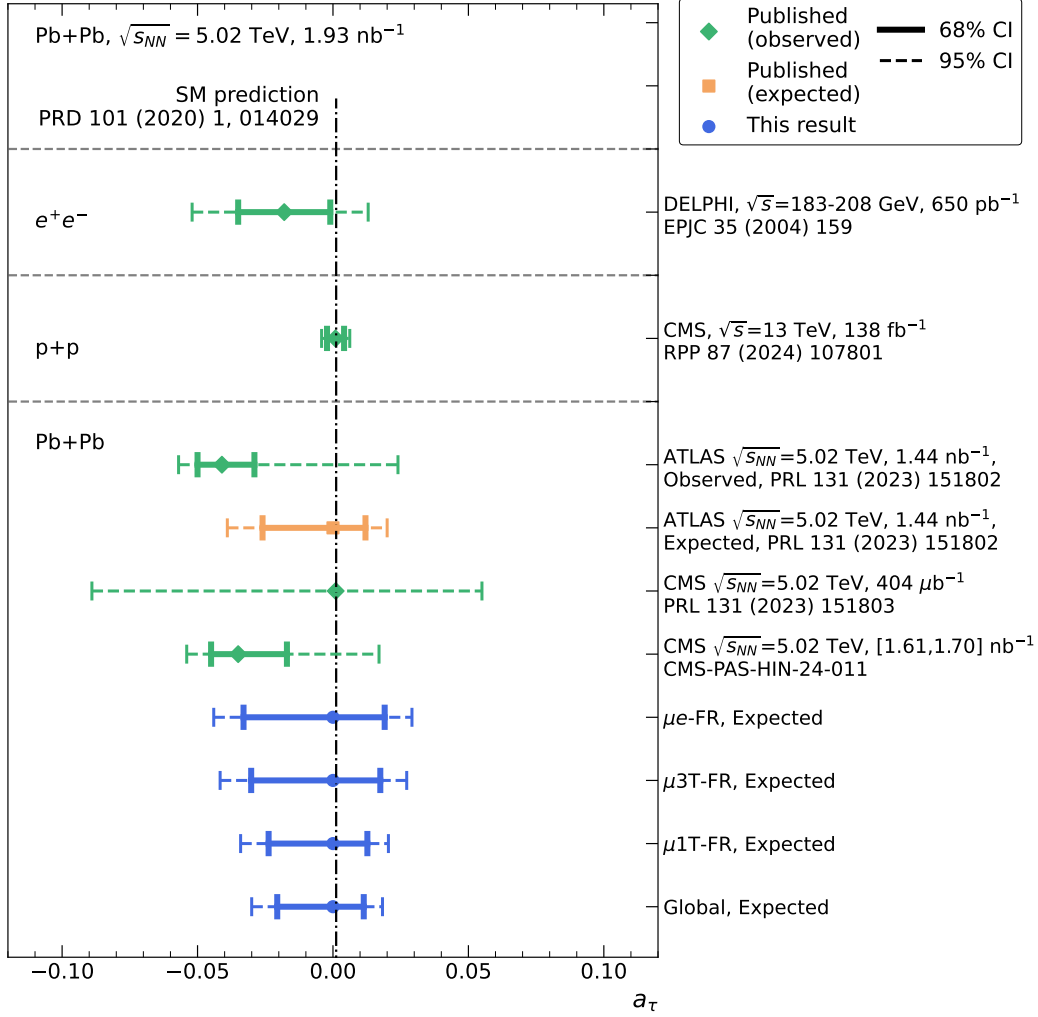


**Figure 5.27:** Expected 68% and 95% confidence intervals (CIs) for  $a_\tau$  obtained in this analysis (blue circles), compared to observed published results (green diamonds) and expected published results (orange squares). The CIs are compared to the Standard Model prediction, shown with a dash-dot line. The various collision systems are labelled.

systematic uncertainties. The current best constraint on  $a_\tau$  obtained by the CMS experiment in proton-proton collisions [63] is approximately one order of magnitude stricter than the expected global constraint obtained in this analysis. However, the expected global constraint is better than both the previous ATLAS result [3], and a recent CMS result [248], both of which performed the fits using 2018 Pb+Pb data at reconstruction-level. The ATLAS result used only the  $p_T^\mu$  distribution in the three signal regions described in Sec. 5.4.6, while the CMS result used the  $p_T^\mu$  observable in similar signal regions, as well as the  $p_T^e$  observable in an electron+3 track signal region. Further, the results of this analysis are expected to be better than the DELPHI measurement in  $e^+e^-$  collisions [60].

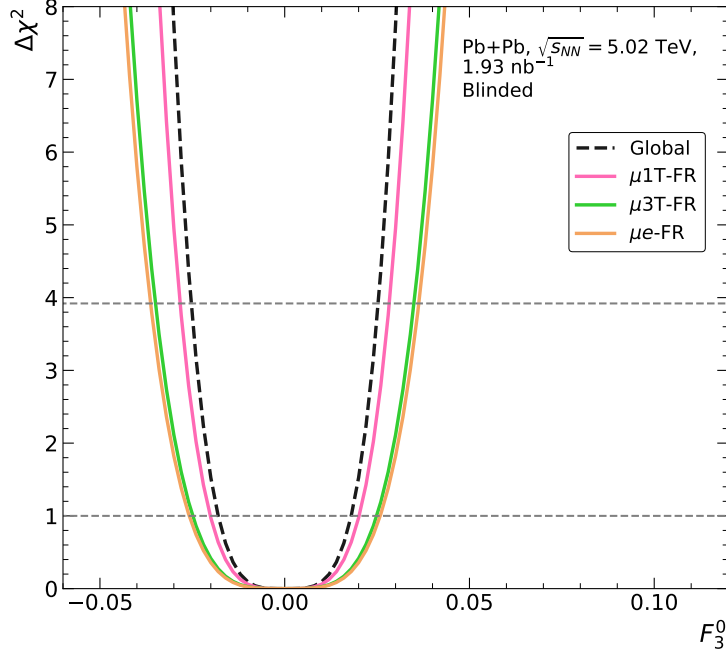


**Figure 5.28:**  $\Delta\chi^2$  curves obtained in the blinded full region and global fits to  $F_3^0$ .

Region	68% CI	95% CI
$\mu e$ -FR	$[-1.445 \times 10^{-16}, +1.445 \times 10^{-16}]$	$[-2.030 \times 10^{-16}, +2.030 \times 10^{-16}]$
$\mu 3T$ -FR	$[-1.393 \times 10^{-16}, +1.393 \times 10^{-16}]$	$[-1.957 \times 10^{-16}, +1.957 \times 10^{-16}]$
$\mu 1T$ -FR	$[-1.126 \times 10^{-16}, +1.126 \times 10^{-16}]$	$[-1.583 \times 10^{-16}, +1.583 \times 10^{-16}]$
Global	$[-1.009 \times 10^{-16}, +1.009 \times 10^{-16}]$	$[-1.416 \times 10^{-16}, +1.416 \times 10^{-16}]$

**Table 5.10:** Expected 68% and 95% confidence intervals (CIs) obtained for  $d_\tau$  (units of  $e \cdot \text{cm}$ ), in the full region and global fits to  $F_3^0$ .

### 5.10.5 Constraints on electric dipole moment

The  $\Delta\chi^2$  vs.  $F_3^0$  curves, i.e. likelihood curves, obtained in the fits to the differential cross-sections are shown in Fig. 5.28. The fits include nuisance parameters associated with all systematics given in Tab. 5.7. The likelihood curves are found to be parabolic, smooth, and minimized at  $F_3^0 = 0$  as expected for the blinded fit setup. Further, the likelihood curves are symmetric in  $F_3^0$ , since the differential cross-sections are only sensitive to the magnitude of  $F_3^0$ . The nuisance parameter impacts and pulls are given in App. A.8. All pulls are exactly at zero, and with errors that are very close to the pre-fit errors of  $\pm 1$ . The pre-fit and post-fit impacts are very similar, indicating that the fit does not strongly constrain any of the nuisance parameters. The impacts are observed to be one-sided, which is a consequence of the  $\gamma\gamma \rightarrow \tau^+\tau^-$  cross-section being symmetric in  $F_3^0$ . Due to inconsequential numerical precision issues, the impacts also sometimes carry the “wrong” sign, e.g. the down-variations of the nuisance parameters have negative impacts, as opposed to the expectation of positive impacts.

The expected confidence intervals for  $d_\tau$  extracted from the likelihood curves are shown

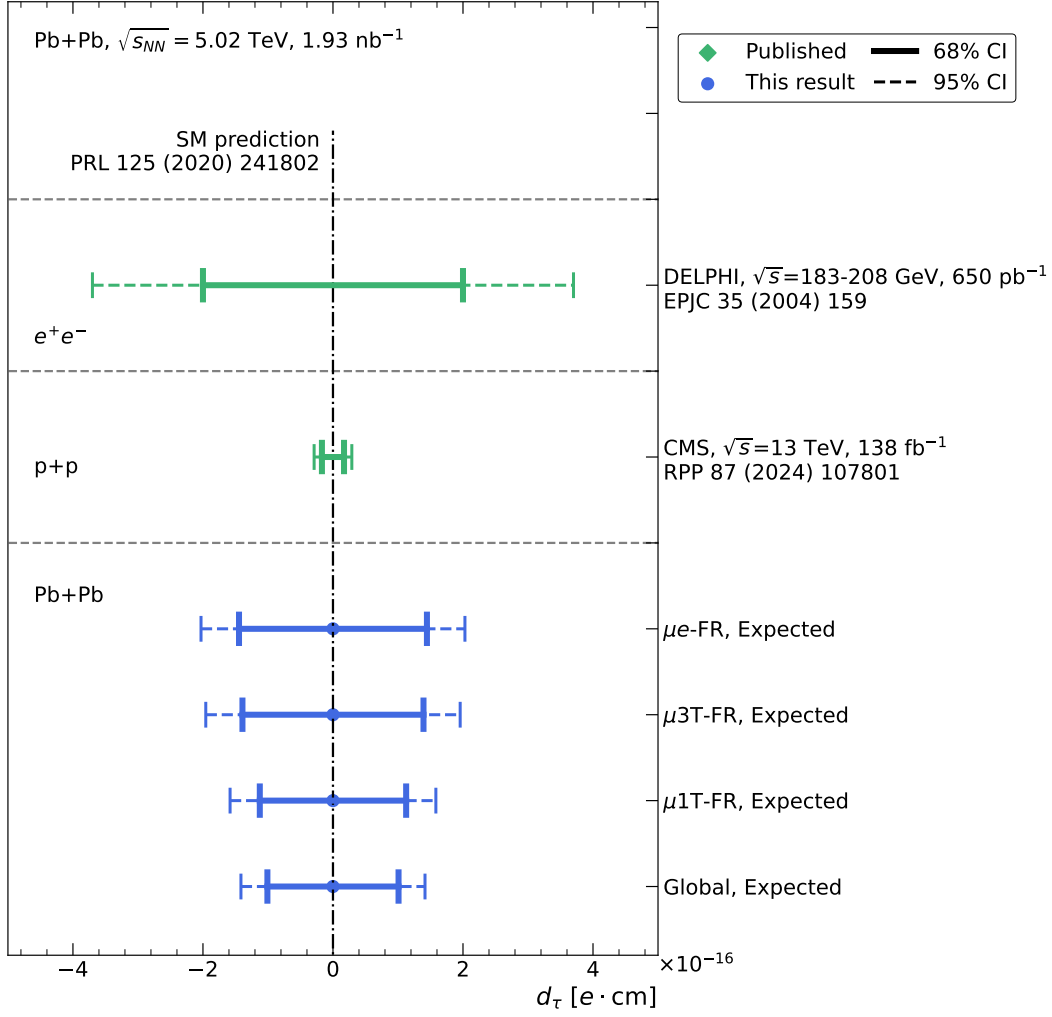


**Figure 5.29:** Expected 68% and 95% confidence intervals (CIs) for  $d_\tau$  (units of  $e \cdot \text{cm}$ ) obtained in this analysis (blue circles), compared to published results (green diamonds). The CIs are compared to the Standard Model prediction, shown with a dash-dot line. The various collision systems are labelled.

in Tab. 5.10. They are compared to previously published results, and to the Standard Model prediction, in Fig. 5.29. Like with the confidence intervals for  $a_\tau$ , the expected statistical ordering is preserved in the  $d_\tau$  confidence intervals as well. The current best constraints on  $d_\tau$  by the CMS experiment in proton-proton collisions [63] is approximately one order of magnitude stricter than the expected global constraint obtained in this analysis. However, the results of this analysis are expected to be better than the DELPHI result in  $e^+e^-$  collisions [60].

# Chapter 6

## Summary and outlook

The goal of this thesis is to study the interaction between the photon and the tau lepton. This is achieved by investigating the  $\gamma\gamma \rightarrow \tau^+\tau^-$  scattering process in ultra-peripheral Pb+Pb collisions recorded by the ATLAS detector in Run 2 of the Large Hadron Collider.

The differential cross-section of  $\gamma\gamma \rightarrow \tau^+\tau^-$  scattering in Pb+Pb UPCs was measured in three fiducial regions, defined based on the presence of one muon and either one track, three tracks, or one electron, in the final state of the  $\tau\tau$  decays. Within each fiducial region, seven kinematic observables of the tau decay products, chosen so as to access the  $\tau\tau$  kinematics through various angles, were considered for the measurement. The iterative Bayesian unfolding method was used to correct the data for detector effects like smearing and migration. The effects of systematic uncertainties on the results of the unfolding were included. The statistical correlations between the cross-section bins were evaluated using a bootstrap procedure.

Overall, good agreement was found between the measured cross-sections, and the predictions of four different theoretical models. The data is seen to favor the photon flux (or two-photon luminosity) predicted by the `SuperChic` generator over that of the `STARlight` generator. In the  $\mu$ 1T-FR region, the inclusion of spin correlation effects in the tau pair production and decay improves the data-prediction agreement. The measurements are statistically limited, with uncertainties of around 10-50%, depending on the fiducial region and bin.

The measured differential fiducial cross-sections were used to set constraints on the electromagnetic dipole moments of the tau lepton. A statistical analysis framework based on a Gaussian likelihood model was developed for this purpose. The analysis was blinded, i.e. it replaced the data with the predicted cross-sections, and used the measured statistical and systematic uncertainties of the data.

Through a global combination of the cross-sections, the expected confidence intervals (CIs) obtained for  $a_\tau$  are

$$\begin{aligned} 68\% \text{ CI} : a_\tau &\in [-0.02058, +0.01136] \\ 95\% \text{ CI} : a_\tau &\in [-0.03001, +0.01828], \end{aligned} \tag{6.1}$$

and the expected confidence intervals obtained for  $d_\tau$  are

$$\begin{aligned} 68\% \text{ CI} : d_\tau &\in [-1.009 \times 10^{-16}, +1.009 \times 10^{-16}] e \cdot \text{cm} \\ 95\% \text{ CI} : d_\tau &\in [-1.416 \times 10^{-16}, +1.416 \times 10^{-16}] e \cdot \text{cm}. \end{aligned} \quad (6.2)$$

The  $a_\tau$  and  $d_\tau$  constraints obtained in this thesis are expected to be the best results using  $\sqrt{s_{\text{NN}}} = 5.02$  TeV Pb+Pb collisions at the LHC. The expected  $a_\tau$  results are an improvement over the previous ATLAS extraction of  $a_\tau$  using 2018 Pb+Pb collision data, as well as the legacy results obtained by the DELPHI experiment using  $\gamma\gamma \rightarrow \tau^+\tau^-$  scattering in  $e^+e^-$  collisions. Moreover, the expected  $d_\tau$  constraints are the first ever obtained by the ATLAS experiment using Pb+Pb collisions.

The results of this thesis are one order of magnitude away from the constraints obtained by the CMS experiment using  $\gamma\gamma \rightarrow \tau^+\tau^-$  scattering in proton-proton collisions, which are currently the best available measurements of the tau lepton EMDMs. That being said, the  $\gamma\gamma \rightarrow \tau^+\tau^-$  phase space regions covered by the two collision systems are complementary, i.e. the Pb+Pb measurement lies in the  $m_{\text{inv}}(\tau, \tau) \lesssim 50$  GeV region, while the proton-proton measurement lies in the  $m_{\text{inv}}(\tau, \tau) \gtrsim 100$  GeV. Thus, the two measurements could be combined in a future cross-experiment and cross-collision system combination, to obtain even tighter constraints on the tau lepton EMDMs, than those obtained from a single analysis alone.

Given that the results of this thesis are statistically limited, the measurements will benefit from recording more Pb+Pb collision data. Since 2023, the LHC has delivered Pb+Pb collisions at  $\sqrt{s_{\text{NN}}} = 5.36$  TeV, as part of the LHC Run 3 (2022-2026). About  $1.7 \text{ nb}^{-1}$  of integrated luminosity was delivered to, and recorded by, ATLAS in both 2023 and 2024. It is expected that the total Run 3 Pb+Pb dataset would correspond to about 6-7  $\text{nb}^{-1}$  of integrated luminosity. Adding the  $\gamma\gamma \rightarrow \tau^+\tau^-$  scattering events from the Run 3 dataset to the fiducial regions defined in this thesis, would effectively quadruple the available statistics, and would significantly improve the constraints on the tau lepton EMDMs.

During Run 3 Pb+Pb data-taking, a new track-based trigger using signals in the Transition Radiation Tracker was introduced, which has already been used to observe and measure coherent exclusive  $J/\psi$  production in UPCs [249]. This trigger could be used to select  $\gamma\gamma \rightarrow \tau^+\tau^-$  events where the tau leptons decay to electrons and muons with  $1 < p_{\text{T}} < 4$  GeV, i.e. lower than the minimum  $p_{\text{T}}$  thresholds used in this thesis. In this  $p_{\text{T}}$  range, the leptons are reconstructed and identified only as Inner Detector tracks, rather than full electron and muon objects. The TRT trigger could also be used to define new  $\gamma\gamma \rightarrow \tau^+\tau^-$  signal regions with hadronic decays of both taus. Measuring the differential fiducial  $\gamma\gamma \rightarrow \tau^+\tau^-$  cross-sections in these *fully-hadronic* final states is interesting in its own right, as there could be enhanced spin correlation effects. The  $\gamma\gamma \rightarrow \tau^+\tau^-$  events that could be selected by the TRT trigger might provide more statistics for the extraction of the tau lepton EMDMs.

This thesis also presented a preliminary calibration of the luminosity of the 2023 Pb+Pb

---

dataset recorded by the ATLAS experiment. The calibration was performed for the LUCID BiEvtOR luminosity algorithm through an analysis of van der Meer scans, using a factorized one-dimensional approach. The effects of several systematic uncertainties were considered, related to the bunch charge measurement, the performance of the LHC instrumentation used in the calibration, and related to the calibration strategy itself. The visible cross-section of the LUCID BiEvtOR algorithm was determined to be

$$\sigma_{\text{vis}}(\text{LUCID BiEvtOR}) = 22.50 \pm 0.61 \text{ b } (2.71\%), \quad (6.3)$$

where the dominant uncertainties are due to non-factorization effects, and due to the measurement of the ghost and satellite charge fractions.

Although the 2023 Pb+Pb luminosity calibration is not at the same level of precision as previous ATLAS results, future improvements to the analysis could close the gap between them. In particular, there is scope for improving the study of non-factorization effects through the luminous region evolution analysis. Additionally, the uncertainty on the ghost and satellite fractions, assumed to be 1% for this preliminary result, can be expected to become available in the future. Alternate fitting procedures, such as likelihood based techniques, may alleviate the issues related to limited statistics that have afflicted this calibration. Optimistically, the uncertainty of a future *final* luminosity calibration of the 2023 Pb+Pb dataset could be below 2%, which is comparable to the 2015 and 2018 Pb+Pb luminosity calibrations.



# Bibliography

- [1] Martin L. Perl et al. “Evidence for Anomalous Lepton Production in  $e^+ - e^-$  Annihilation”. In: *Phys. Rev. Lett.* 35 (1975), pp. 1489–1492. DOI: 10.1103/PhysRevLett.35.1489.
- [2] Martin L. Perl. “The Discovery of the tau lepton”. In: *3rd International Symposium on the History of Particle Physics: The Rise of the Standard Model*. Sept. 1992, pp. 79–100.
- [3] ATLAS Collaboration. “Observation of the  $\gamma\gamma \rightarrow \tau\tau$  Process in Pb+Pb Collisions and Constraints on the  $\tau$ -Lepton Anomalous Magnetic Moment with the ATLAS Detector”. In: *Phys. Rev. Lett.* 131.15 (2023), p. 151802. DOI: 10.1103/PhysRevLett.131.151802. arXiv: 2204.13478 [hep-ex].
- [4] ATLAS Collaboration. *Differential measurements of  $\gamma\gamma \rightarrow \tau\tau$  using  $\sqrt{s_{NN}} = 5.02$  TeV Pb+Pb collisions with the ATLAS detector*. Tech. rep. All figures including auxiliary figures are available at <https://atlas.web.cern.ch/Atlas/GROUPS/PHYSICS/CONFNOTES/ATLAS-CONF-2025-004>. Geneva: CERN, 2025. URL: <http://cds.cern.ch/record/2929691>.
- [5] ATLAS Collaboration. *Performance studies of track counting and track-based event counting algorithms for luminosity measurement in PbPb collisions using 2018 and 2022 data*. <https://atlas.web.cern.ch/Atlas/GROUPS/PHYSICS/PLOTS/LUMI-2023-07/>.
- [6] ATLAS Collaboration. *Heavy Ion vdM Calibration Summary Plots for Run 2 and Run 3*. <https://atlas.web.cern.ch/Atlas/GROUPS/PHYSICS/PLOTS/LUMI-2025-04/>.
- [7] Matthew D. Schwartz. *Quantum Field Theory and the Standard Model*. Cambridge University Press, Mar. 2014. ISBN: 978-1-107-03473-0, 978-1-107-03473-0.
- [8] Carsten Burgard. *Example: Standard model of physics*. <https://texample.net/model-physics/>.
- [9] F. Englert and R. Brout. “Broken Symmetry and the Mass of Gauge Vector Mesons”. In: *Phys. Rev. Lett.* 13 (1964). Ed. by J. C. Taylor, pp. 321–323. DOI: 10.1103/PhysRevLett.13.321.
- [10] Peter W. Higgs. “Broken Symmetries and the Masses of Gauge Bosons”. In: *Phys. Rev. Lett.* 13 (1964). Ed. by J. C. Taylor, pp. 508–509. DOI: 10.1103/PhysRevLett.13.508.
- [11] M. Gell-Mann. “The interpretation of the new particles as displaced charge multiplets”. In: *Nuovo Cim.* 4.S2 (1956), pp. 848–866. DOI: 10.1007/BF02748000.
- [12] Kazuhiko Nishijima. “Charge Independence Theory of V Particles”. In: *Prog. Theor. Phys.* 13.3 (1955), pp. 285–304. DOI: 10.1143/PTP.13.285.
- [13] Nicola Cabibbo. “Unitary Symmetry and Leptonic Decays”. In: *Phys. Rev. Lett.* 10 (1963), pp. 531–533. DOI: 10.1103/PhysRevLett.10.531.
- [14] Makoto Kobayashi and Toshihide Maskawa. “CP Violation in the Renormalizable Theory of Weak Interaction”. In: *Prog. Theor. Phys.* 49 (1973), pp. 652–657. DOI: 10.1143/PTP.49.652.



- [15] David J. Gross and Frank Wilczek. “Ultraviolet Behavior of Nonabelian Gauge Theories”. In: *Phys. Rev. Lett.* 30 (1973). Ed. by J. C. Taylor, pp. 1343–1346. DOI: 10.1103/PhysRevLett.30.1343.
- [16] H. David Politzer. “Reliable Perturbative Results for Strong Interactions?”. In: *Phys. Rev. Lett.* 30 (1973). Ed. by J. C. Taylor, pp. 1346–1349. DOI: 10.1103/PhysRevLett.30.1346.
- [17] Super-Kamiokande Collaboration. “Evidence for oscillation of atmospheric neutrinos”. In: *Phys. Rev. Lett.* 81 (1998), pp. 1562–1567. DOI: 10.1103/PhysRevLett.81.1562. arXiv: hep-ex/9807003.
- [18] SNO Collaboration. “Direct evidence for neutrino flavor transformation from neutral current interactions in the Sudbury Neutrino Observatory”. In: *Phys. Rev. Lett.* 89 (2002), p. 011301. DOI: 10.1103/PhysRevLett.89.011301. arXiv: nucl-ex/0204008.
- [19] Kenath Arun, S. B. Gudennavar, and C. Sivaram. “Dark matter, dark energy, and alternate models: A review”. In: *Adv. Space Res.* 60 (2017), pp. 166–186. DOI: 10.1016/j.asr.2017.03.043. arXiv: 1704.06155 [physics.gen-ph].
- [20] Laurent Canetti, Marco Drewes, and Mikhail Shaposhnikov. “Matter and Antimatter in the Universe”. In: *New J. Phys.* 14 (2012), p. 095012. DOI: 10.1088/1367-2630/14/9/095012. arXiv: 1204.4186 [hep-ph].
- [21] A. D. Sakharov. “Violation of CP Invariance, C asymmetry, and baryon asymmetry of the universe”. In: *Pisma Zh. Eksp. Teor. Fiz.* 5 (1967), pp. 32–35. DOI: 10.1070/PU1991v034n05ABEH002497.
- [22] ATLAS Collaboration. *Standard Model Summary Plots June 2024*. Tech. rep. All figures including auxiliary figures are available at <https://atlas.web.cern.ch/Atlas/GROUPS/PHYSICS/PUBNOTES/ATL-PHYS-PUB-2024-011>. Geneva: CERN, 2024. URL: <https://cds.cern.ch/record/2903866>.
- [23] Ilaria Brivio and Michael Trott. “The Standard Model as an Effective Field Theory”. In: *Phys. Rept.* 793 (2019), pp. 1–98. DOI: 10.1016/j.physrep.2018.11.002. arXiv: 1706.08945 [hep-ph].
- [24] Peter Mohr et al. “CODATA Recommended Values of the Fundamental Physical Constants: 2022”. In: (Aug. 2024). arXiv: 2409.03787 [hep-ph].
- [25] Julian S. Schwinger. “On Quantum electrodynamics and the magnetic moment of the electron”. In: *Phys. Rev.* 73 (1948), pp. 416–417. DOI: 10.1103/PhysRev.73.416.
- [26] B. Grzadkowski et al. “Dimension-Six Terms in the Standard Model Lagrangian”. In: *JHEP* 10 (2010), p. 085. DOI: 10.1007/JHEP10(2010)085. arXiv: 1008.4884 [hep-ph].
- [27] D. Atwood and A. Soni. “Analysis for magnetic moment and electric dipole moment form-factors of the top quark via  $e^+ e^- \rightarrow t \text{ anti-}t$ ”. In: *Phys. Rev. D* 45 (1992), pp. 2405–2413. DOI: 10.1103/PhysRevD.45.2405.
- [28] A. Cordero-Cid et al. “Bounding the top and bottom electric dipole moments from neutron experimental data”. In: *J. Phys. G* 35 (2008), p. 025004. DOI: 10.1088/0954-3899/35/2/025004. arXiv: 0712.0154 [hep-ph].

- [29] A. S. Fomin et al. “The prospect of charm quark magnetic moment determination”.  
In: *Eur. Phys. J. C* 80.5 (2020), p. 358. DOI: 10.1140/epjc/s10052-020-7891-0.  
arXiv: 1909.04654 [hep-ph].
- [30] X. Fan et al. “Measurement of the Electron Magnetic Moment”.  
In: *Phys. Rev. Lett.* 130.7 (2023), p. 071801. DOI: 10.1103/PhysRevLett.130.071801.  
arXiv: 2209.13084 [physics.atom-ph].
- [31] Alexander Keshavarzi, Daisuke Nomura, and Thomas Teubner.  
“ $g - 2$  of charged leptons,  $\alpha(M_Z^2)$ , and the hyperfine splitting of muonium”.  
In: *Phys. Rev. D* 101.1 (2020), p. 014029. DOI: 10.1103/PhysRevD.101.014029.  
arXiv: 1911.00367 [hep-ph].
- [32] Timo Fleig. “ $\mathcal{P}$ ,  $\mathcal{T}$ -odd and magnetic hyperfine-interaction constants and excited-state lifetime for  $HfF^+$ ”. In: *Phys. Rev. A* 96.4 (2017), p. 040502. DOI: 10.1103/PhysRevA.96.040502.  
arXiv: 1706.02893 [physics.atom-ph].
- [33] Tanya S. Roussy et al. “An improved bound on the electron’s electric dipole moment”.  
In: *Science* 381.6653 (2023), adg4084. DOI: 10.1126/science.adg4084.  
arXiv: 2212.11841 [physics.atom-ph].
- [34] Luke Caldwell et al. “Systematic and statistical uncertainty evaluation of the  $HfF^+$  electron electric dipole moment experiment”. In: *Phys. Rev. A* 108.1 (2023), p. 012804.  
DOI: 10.1103/PhysRevA.108.012804. arXiv: 2212.11837 [physics.atom-ph].
- [35] Yasuhiro Yamaguchi and Nodoka Yamanaka. “Large long-distance contributions to the electric dipole moments of charged leptons in the standard model”.  
In: *Phys. Rev. Lett.* 125 (2020), p. 241802. DOI: 10.1103/PhysRevLett.125.241802.  
arXiv: 2003.08195 [hep-ph].
- [36] A. C. Vutha, M. Horbatsch, and E. A. Hessels. “Oriented polar molecules in a solid inert-gas matrix: a proposed method for measuring the electric dipole moment of the electron”.  
In: *Atoms* 6.1 (2018), p. 3. DOI: 10.3390/atoms6010003.  
arXiv: 1710.08785 [physics.atom-ph].
- [37] Particle Data Group. “Review of particle physics”. In: *Phys. Rev. D* 110.3 (2024), p. 030001.  
DOI: 10.1103/PhysRevD.110.030001.
- [38] Muon  $g-2$  Collaboration.  
“Measurement of the Positive Muon Anomalous Magnetic Moment to 0.20 ppm”.  
In: *Phys. Rev. Lett.* 131.16 (2023), p. 161802. DOI: 10.1103/PhysRevLett.131.161802.  
arXiv: 2308.06230 [hep-ex].
- [39] Muon  $g-2$  collaboration.  
“Measurement of the Positive Muon Anomalous Magnetic Moment to 127 ppb”.  
In: (June 2025). arXiv: 2506.03069 [hep-ex].
- [40] Muon  $g-2$  Collaboration.  
“Final Report of the Muon E821 Anomalous Magnetic Moment Measurement at BNL”.  
In: *Phys. Rev. D* 73 (2006), p. 072003. DOI: 10.1103/PhysRevD.73.072003.  
arXiv: hep-ex/0602035.
- [41] R. Aliberti et al.  
“The anomalous magnetic moment of the muon in the Standard Model: an update”.  
In: (May 2025). arXiv: 2505.21476 [hep-ph].
- [42] T. Aoyama et al. “The anomalous magnetic moment of the muon in the Standard Model”.  
In: *Phys. Rept.* 887 (2020), pp. 1–166. DOI: 10.1016/j.physrep.2020.07.006.  
arXiv: 2006.04822 [hep-ph].

- [43] Peter Athron et al.  
“New physics explanations of  $a_\mu$  in light of the FNAL muon  $g-2$  measurement”.  
In: *JHEP* 09 (2021), p. 080. DOI: 10.1007/JHEP09(2021)080. arXiv: 2104.03691 [hep-ph].
- [44] Muon  $g-2$  Collaboration. “An Improved Limit on the Muon Electric Dipole Moment”.  
In: *Phys. Rev. D* 80 (2009), p. 052008. DOI: 10.1103/PhysRevD.80.052008.  
arXiv: 0811.1207 [hep-ex].
- [45] F. del Aguila, F. Cornet, and Jose I. Illana. “The possibility of using a large heavy-ion collider for measuring the electromagnetic properties of the tau lepton”.  
In: *Phys. Lett. B* 271 (1991), pp. 256–260. DOI: 10.1016/0370-2693(91)91309-J.
- [46] Fernando Cornet and Jose I. Illana. “Tau pair production via photon-photon collisions at LEP”.  
In: *Phys. Rev. D* 53 (1996), pp. 1181–1184. DOI: 10.1103/PhysRevD.53.1181.  
arXiv: hep-ph/9503466.
- [47] S. Atag and A. A. Billur. “Possibility of Determining  $\tau$  Lepton Electromagnetic Moments in  $\gamma\gamma \rightarrow \tau^+\tau^-$  Process at the CERN-LHC”. In: *JHEP* 11 (2010), p. 060.  
DOI: 10.1007/JHEP11(2010)060. arXiv: 1005.2841 [hep-ph].
- [48] Iftah Galon, Arvind Rajaraman, and Tim M. P. Tait.  
“ $H \rightarrow \tau^+\tau^-\gamma$  as a probe of the  $\tau$  magnetic dipole moment”. In: *JHEP* 12 (2016), p. 111.  
DOI: 10.1007/JHEP12(2016)111. arXiv: 1610.01601 [hep-ph].
- [49] M. Köksal et al. “Model-independent sensitivity estimates for the electromagnetic dipole moments of the  $\tau$ -lepton at the CLIC”. In: *Phys. Rev. D* 98.1 (2018), p. 015017.  
DOI: 10.1103/PhysRevD.98.015017. arXiv: 1804.02373 [hep-ph].
- [50] M. Köksal. “Search for the electromagnetic moments of the  $\tau$  lepton in photon–photon collisions at the LHeC and the FCC-he”. In: *J. Phys. G* 46 (2019), p. 065003.  
DOI: 10.1088/1361-6471/ab0b53. arXiv: 1809.01963 [hep-ph].
- [51] A. Gutiérrez-Rodríguez et al. “Feasibility at the LHC, FCC-he and CLIC for sensitivity estimates on anomalous  $\tau$ -lepton couplings”. In: (Mar. 2019). arXiv: 1903.04135 [hep-ph].
- [52] Lydia Beresford and Jesse Liu. “New physics and tau  $g - 2$  using LHC heavy ion collisions”.  
In: *Phys. Rev. D* 102.11 (2020). [Erratum: *Phys.Rev.D* 106, 039902 (2022)], p. 113008.  
DOI: 10.1103/PhysRevD.102.113008. arXiv: 1908.05180 [hep-ph].
- [53] Mateusz Dyndal et al. “Anomalous electromagnetic moments of  $\tau$  lepton in  $\gamma\gamma \rightarrow \tau^+\tau^-$  reaction in Pb+Pb collisions at the LHC”. In: *Phys. Lett. B* 809 (2020), p. 135682.  
DOI: 10.1016/j.physletb.2020.135682. arXiv: 2002.05503 [hep-ph].
- [54] Xin Chen and Yongcheng Wu. “Search for the Electric Dipole Moment and anomalous magnetic moment of the tau lepton at tau factories”. In: *JHEP* 10 (2019), p. 089.  
DOI: 10.1007/JHEP10(2019)089. arXiv: 1803.00501 [hep-ph].
- [55] Andreas Crivellin, Martin Hoferichter, and J. Michael Roney.  
“Toward testing the magnetic moment of the tau at one part per million”.  
In: *Phys. Rev. D* 106.9 (2022), p. 093007. DOI: 10.1103/PhysRevD.106.093007.  
arXiv: 2111.10378 [hep-ph].
- [56] D. M. Asner et al. “Snowmass 2021 White Paper on Upgrading SuperKEKB with a Polarized Electron Beam: Discovery Potential and Proposed Implementation”. In: *Snowmass 2021*.  
May 2022. arXiv: 2205.12847 [physics.acc-ph].
- [57] M. Fabbrichesi and L. Marzola.  
“Dipole momenta and compositeness of the  $\tau$  lepton at Belle II”.  
In: *Phys. Rev. D* 109.9 (2024), p. 095026. DOI: 10.1103/PhysRevD.109.095026.  
arXiv: 2401.04449 [hep-ph].

- [58] Kartik Bhide and Valerie Lang.  
“Probing optimal measurements of the electromagnetic dipole moments of the  $\tau$  lepton”.  
In: (Oct. 2024). arXiv: 2410.23070 [hep-ph].
- [59] L. A. Harland-Lang. “Higher precision constraints on the tau  $g - 2$  in LHC photon-initiated production: a full account of hadron dissociation and soft survival effects”.  
In: *Eur. Phys. J. C* 84.12 (2024), p. 1332. DOI: 10.1140/epjc/s10052-024-13685-7.  
arXiv: 2410.10978 [hep-ph].
- [60] DELPHI Collaboration. “Study of tau-pair production in photon-photon collisions at LEP and limits on the anomalous electromagnetic moments of the tau lepton”.  
In: *Eur. Phys. J. C* 35 (2004), pp. 159–170. DOI: 10.1140/epjc/s2004-01852-y.  
arXiv: hep-ex/0406010.
- [61] L3 Collaboration.  
“Production of e, mu and tau pairs in untagged two photon collisions at LEP”.  
In: *Phys. Lett. B* 407 (1997), pp. 341–350. DOI: 10.1016/S0370-2693(97)00731-4.
- [62] OPAL Collaboration. “A Study of muon pair production and evidence for tau pair production in photon-photon collisions at LEP”. In: *Z. Phys. C* 60 (1993), pp. 593–600.  
DOI: 10.1007/BF01558388.
- [63] CMS Collaboration. “Observation of  $\gamma\gamma \rightarrow \tau\tau$  in proton-proton collisions and limits on the anomalous electromagnetic moments of the  $\tau$  lepton”.  
In: *Rept. Prog. Phys.* 87.10 (2024), p. 107801. DOI: 10.1088/1361-6633/ad6fcb.  
arXiv: 2406.03975 [hep-ex].
- [64] CMS Collaboration. “Observation of  $\tau$  lepton pair production in ultraperipheral lead-lead collisions at  $\sqrt{s_{NN}} = 5.02$  TeV”. In: *Phys. Rev. Lett.* 131 (2023), p. 151803.  
DOI: 10.1103/PhysRevLett.131.151803. arXiv: 2206.05192 [nucl-ex].
- [65] L3 Collaboration.  
“Measurement of the anomalous magnetic and electric dipole moments of the tau lepton”.  
In: *Phys. Lett. B* 434 (1998), pp. 169–179. DOI: 10.1016/S0370-2693(98)00736-9.
- [66] OPAL Collaboration. “An Upper limit on the anomalous magnetic moment of the tau lepton”.  
In: *Phys. Lett. B* 431 (1998), pp. 188–198. DOI: 10.1016/S0370-2693(98)00520-6.  
arXiv: hep-ex/9803020.
- [67] A. S. Fomin et al. “Feasibility of  $\tau$  -lepton electromagnetic dipole moments measurement using bent crystal at the LHC”. In: *JHEP* 03 (2019), p. 156. DOI: 10.1007/JHEP03(2019)156.  
arXiv: 1810.06699 [hep-ph].
- [68] J. Fu et al. “Novel Method for the Direct Measurement of the  $\tau$  Lepton Dipole Moments”.  
In: *Phys. Rev. Lett.* 123.1 (2019), p. 011801. DOI: 10.1103/PhysRevLett.123.011801.  
arXiv: 1901.04003 [hep-ex].
- [69] K. Inami et al. “An improved search for the electric dipole moment of the  $\tau$  lepton”.  
In: *JHEP* 04 (2022), p. 110. DOI: 10.1007/JHEP04(2022)110. arXiv: 2108.11543 [hep-ex].
- [70] Stephen P. Martin and James D. Wells.  
“Muon Anomalous Magnetic Dipole Moment in Supersymmetric Theories”.  
In: *Phys. Rev. D* 64 (2001), p. 035003. DOI: 10.1103/PhysRevD.64.035003.  
arXiv: hep-ph/0103067.
- [71] E. Fermi. “On the Theory of the impact between atoms and electrically charged particles”.  
In: *Z. Phys.* 29 (1924), pp. 315–327. DOI: 10.1007/BF03184853.
- [72] C. F. von Weizsacker. “Radiation emitted in collisions of very fast electrons”.  
In: *Z. Phys.* 88 (1934), pp. 612–625. DOI: 10.1007/BF01333110.

- [73] E. J. Williams. “Correlation of certain collision problems with radiation theory”. In: *Kong. Dan. Vid. Sel. Mat. Fys. Med.* 13N4.4 (1935), pp. 1–50.
- [74] M. Vidovic et al. “Impact parameter dependence of the electromagnetic particle production in ultrarelativistic heavy ion collisions”. In: *Phys. Rev. C* 47 (1993), pp. 2308–2319. DOI: 10.1103/PhysRevC.47.2308.
- [75] Mariola Klusek-Gawenda. “Production of pairs of mesons, leptons and quarks in ultraperipheral ultrarelativistic heavy ion collisions”. PhD thesis. Cracow, INP, Krakow University, 2015.
- [76] C. W. De Jager, H. De Vries, and C. De Vries. “Nuclear charge and magnetization density distribution parameters from elastic electron scattering”. In: *Atom. Data Nucl. Data Tabl.* 14 (1974). [Erratum: *Atom. Data Nucl. Data Tabl.* 16, 580–580 (1975)], pp. 479–508. DOI: 10.1016/S0092-640X(74)80002-1.
- [77] L. A. Harland-Lang, V. A. Khoze, and M. G. Ryskin. “Exclusive LHC physics with heavy ions: SuperChic 3”. In: *Eur. Phys. J. C* 79.1 (2019), p. 39. DOI: 10.1140/epjc/s10052-018-6530-5. arXiv: 1810.06567 [hep-ph].
- [78] Hua-Sheng Shao and David d’Enterria. “gamma-UPC: automated generation of exclusive photon-photon processes in ultraperipheral proton and nuclear collisions with varying form factors”. In: *JHEP* 09 (2022), p. 248. DOI: 10.1007/JHEP09(2022)248. arXiv: 2207.03012 [hep-ph].
- [79] Spencer R. Klein et al. “STARlight: A Monte Carlo simulation program for ultra-peripheral collisions of relativistic ions”. In: *Comput. Phys. Commun.* 212 (2017), pp. 258–268. DOI: 10.1016/j.cpc.2016.10.016. arXiv: 1607.03838 [hep-ph].
- [80] Anthony J. Baltz et al. “Two-Photon Interactions with Nuclear Breakup in Relativistic Heavy Ion Collisions”. In: *Phys. Rev. C* 80 (2009), p. 044902. DOI: 10.1103/PhysRevC.80.044902. arXiv: 0907.1214 [nucl-ex].
- [81] R. J. Glauber and G. Matthiae. “High-energy scattering of protons by nuclei”. In: *Nucl. Phys. B* 21 (1970), pp. 135–157. DOI: 10.1016/0550-3213(70)90511-0.
- [82] A. D. Martin, M. G. Ryskin, and V. A. Khoze. “Forward Physics at the LHC”. In: *Acta Phys. Polon. B* 40 (2009). Ed. by Krzysztof Golec-Biernat and Michal Praszalowicz, pp. 1841–1876. arXiv: 0903.2980 [hep-ph].
- [83] Stanley J. Brodsky, Toichiro Kinoshita, and Hidezumi Terazawa. “Two Photon Mechanism of Particle Production by High-Energy Colliding Beams”. In: *Phys. Rev. D* 4 (1971), pp. 1532–1557. DOI: 10.1103/PhysRevD.4.1532.
- [84] Johan Alwall et al. “MadGraph 5 : Going Beyond”. In: *JHEP* 06 (2011), p. 128. DOI: 10.1007/JHEP06(2011)128. arXiv: 1106.0522 [hep-ph].
- [85] Yung-Su Tsai. “Decay Correlations of Heavy Leptons in  $e^+ e^- \rightarrow \text{Lepton} + \text{Lepton}^-$ ”. In: *Phys. Rev. D* 4 (1971). [Erratum: *Phys. Rev. D* 13, 771 (1976)], p. 2821. DOI: 10.1103/PhysRevD.13.771.
- [86] S. Jadach et al. “The tau decay library TAUOLA: Version 2.4”. In: *Comput. Phys. Commun.* 76 (1993), pp. 361–380. DOI: 10.1016/0010-4655(93)90061-G.
- [87] T. Przedzinski, E. Richter-Was, and Z. Was. “Documentation of *TauSpinner* algorithms: program for simulating spin effects in  $\tau$ -lepton production at LHC”. In: *Eur. Phys. J. C* 79.2 (2019), p. 91. DOI: 10.1140/epjc/s10052-018-6527-0. arXiv: 1802.05459 [hep-ph].

- [88] Christian Bierlich et al. “A comprehensive guide to the physics and usage of PYTHIA 8.3”. In: *SciPost Phys. Codeb.* 2022 (2022), p. 8. DOI: 10.21468/SciPostPhysCodeb.8. arXiv: 2203.11601 [hep-ph].
- [89] Z. Czyzula, T. Przedzinski, and Z. Was. “TauSpinner Program for Studies on Spin Effect in tau Production at the LHC”. In: *Eur. Phys. J. C* 72 (2012), p. 1988. DOI: 10.1140/epjc/s10052-012-1988-z. arXiv: 1201.0117 [hep-ph].
- [90] Sw. Banerjee et al. “Electron-positron, parton-parton, and photon-photon production of  $\tau$ -lepton pairs: Anomalous magnetic and electric dipole moments spin effects”. In: *Phys. Rev. D* 109.1 (2024), p. 013002. DOI: 10.1103/PhysRevD.109.013002. arXiv: 2307.03526 [hep-ph].
- [91] A. Yu. Korchin, E. Richter-Was, and Z. Was. “TauSpinner algorithms for including spin and New Physics effects in  $\gamma\gamma \rightarrow \tau\tau$  process”. In: (June 2025). arXiv: 2506.15213 [hep-ph].
- [92] P. Gomes et al. “The control system for the cryogenics in the LHC tunnel”. In: *22nd International Cryogenic Engineering Conference and 2008 International Cryogenic Materials Conference*. 2009, pp. 45–50.
- [93] “LHC Design Report Vol.1: The LHC Main Ring”. In: (June 2004). Ed. by Oliver S. Bruning et al. DOI: 10.5170/CERN-2004-003-V-1.
- [94] ATLAS Collaboration. “The ATLAS Experiment at the CERN Large Hadron Collider”. In: *JINST* 3 (2008), S08003. DOI: 10.1088/1748-0221/3/08/S08003.
- [95] CMS Collaboration. “The CMS Experiment at the CERN LHC”. In: *JINST* 3 (2008), S08004. DOI: 10.1088/1748-0221/3/08/S08004.
- [96] ALICE Collaboration. “The ALICE experiment at the CERN LHC”. In: *JINST* 3 (2008), S08002. DOI: 10.1088/1748-0221/3/08/S08002.
- [97] LHCb Collaboration. “The LHCb Detector at the LHC”. In: *JINST* 3 (2008), S08005. DOI: 10.1088/1748-0221/3/08/S08005.
- [98] A Alici et al. “Study of the LHC ghost charge and satellite bunches for luminosity calibration.” In: (2012). URL: <https://cds.cern.ch/record/1427728>.
- [99] Shyh-yuan Lee. *Accelerator Physics (Fourth Edition)*. World Scientific Publishing Company, 2018. ISBN: 978-981-327-468-6, 978-981-327-467-9. DOI: 10.1142/11111.
- [100] C A Salgado. “Lectures on high-energy heavy-ion collisions at the LHC”. In: (2009). DOI: 10.5170/CERN-2009-002.239. URL: <https://cds.cern.ch/record/1183649>.
- [101] P. Grafström and W. Kozanecki. “Luminosity determination at proton colliders”. In: *Prog. Part. Nucl. Phys.* 81 (2015), pp. 97–148. DOI: 10.1016/j.ppnp.2014.11.002.
- [102] *The CERN accelerator complex, layout in 2022*. <https://cds.cern.ch/record/2800984>.
- [103] ATLAS Collaboration. “Observation of a new particle in the search for the Standard Model Higgs boson with the ATLAS detector at the LHC”. In: *Phys. Lett. B* 716 (2012), pp. 1–29. DOI: 10.1016/j.physletb.2012.08.020. arXiv: 1207.7214 [hep-ex].
- [104] CMS Collaboration. “Observation of a New Boson at a Mass of 125 GeV with the CMS Experiment at the LHC”. In: *Phys. Lett. B* 716 (2012), pp. 30–61. DOI: 10.1016/j.physletb.2012.08.021. arXiv: 1207.7235 [hep-ex].

- [105] D Manglunki. *LEIR operations for the LHC and future plans*.  
<https://cds.cern.ch/record/1702922>.
- [106] John Jowett et al. “The 2018 heavy-ion run of the LHC”.  
In: *10th International Particle Accelerator Conference*. 2019, WEYYPLM2.  
DOI: 10.18429/JACoW-IPAC2019-WEYYPLM2.
- [107] Adam Jeff. “A Longitudinal Density Monitor for the LHC”.  
PhD thesis. Liverpool U., Dec. 2012.
- [108] Alexander Nicholas Jury.  
*LHC bunch-population measurements in Run III and beyond: a status report*.  
<https://indico.cern.ch/event/1502802/contributions/6336764/>.
- [109] P Odier, S Thoulet, and M Ludwig. *The DCCT for the LHC beam intensity measurement*.  
Tech. rep. 2009.
- [110] D Belohrad et al. *Implementation of the electronics chain for the Bunch by Bunch Intensity Measurement devices for the LHC*. Tech. rep. 2009.
- [111] D Belohrad et al.  
*The LHC fast BCT system: a comparison of design parameters with initial performance*.  
Tech. rep. 2010.
- [112] C. Ohm and T. Pauly. “The ATLAS beam pick-up based timing system”.  
In: *Nucl. Instrum. Meth. A* 623 (2010). Ed. by Hiroyuki Iwasaki, Takeshi K. Komatsubara, and Yasuhiro Sugimoto, pp. 558–560. DOI: 10.1016/j.nima.2010.03.069.  
arXiv: 0905.3648 [physics.ins-det].
- [113] Jean-Pierre Koutchouk.  
*MEASUREMENT OF THE BEAM POSITION IN THE LHC MAIN RINGS*.  
<https://cds.cern.ch/record/1068133>.
- [114] O. R. Jones. “LHC beam instrumentation”.  
In: *2007 IEEE Particle Accelerator Conference (PAC)*. 2007, pp. 2630–2634.  
DOI: 10.1109/PAC.2007.4440723.
- [115] Marek Gasior et al.  
“First operational experience with the LHC Diode ORbit and OScillation (DOROS) system”.  
In: (2016).
- [116] ATLAS Collaboration. “The ATLAS experiment at the CERN Large Hadron Collider: a description of the detector configuration for Run 3”. In: *JINST* 19.05 (2024), P05063.  
DOI: 10.1088/1748-0221/19/05/P05063. arXiv: 2305.16623 [physics.ins-det].
- [117] *ATLAS inner detector: Technical design report. Vol. 1*. CERN-LHCC-97-16, ATLAS-TDR-4. Apr. 1997.
- [118] *ATLAS inner detector: Technical design report. Vol. 2*. CERN-LHCC-97-17. Apr. 1997.
- [119] ATLAS Collaboration. *ATLAS pixel detector: Technical design report*. CERN-LHCC-98-13. May 1998.
- [120] H. Pernegger. “The Pixel Detector of the ATLAS experiment for LHC Run-2”.  
In: *JINST* 10.06 (2015), p. C06012. DOI: 10.1088/1748-0221/10/06/C06012.
- [121] M. Capeans et al. “ATLAS Insertable B-Layer Technical Design Report”. In: (Sept. 2010).
- [122] Cinzia Da Via et al. “3D silicon sensors: Design, large area production and quality assurance for the ATLAS IBL pixel detector upgrade”.  
In: *Nucl. Instrum. Meth. A* 694 (2012), pp. 321–330. DOI: 10.1016/j.nima.2012.07.058.

- [123] A. Abdesselam et al. “The barrel modules of the ATLAS semiconductor tracker”. In: *Nucl. Instrum. Meth. A* 568 (2006), pp. 642–671. DOI: 10.1016/j.nima.2006.08.036.
- [124] A. Abdesselam et al. “The ATLAS semiconductor tracker end-cap module”. In: *Nucl. Instrum. Meth. A* 575 (2007), pp. 353–389. DOI: 10.1016/j.nima.2007.02.019.
- [125] A. Ahmad et al. “The Silicon microstrip sensors of the ATLAS semiconductor tracker”. In: *Nucl. Instrum. Meth. A* 578 (2007), pp. 98–118. DOI: 10.1016/j.nima.2007.04.157.
- [126] E. Abat et al. “The ATLAS TRT barrel detector”. In: *JINST* 3 (2008), P02014. DOI: 10.1088/1748-0221/3/02/P02014.
- [127] E. Abat et al. “The ATLAS TRT end-cap detectors”. In: *JINST* 3 (2008), P10003. DOI: 10.1088/1748-0221/3/10/P10003.
- [128] E. Abat et al. “The ATLAS Transition Radiation Tracker (TRT) proportional drift tube: Design and performance”. In: *JINST* 3 (2008), P02013. DOI: 10.1088/1748-0221/3/02/P02013.
- [129] V. Cindro et al. “The ATLAS beam conditions monitor”. In: *JINST* 3 (2008), P02004. DOI: 10.1088/1748-0221/3/02/P02004.
- [130] ATLAS Collaboration. *ATLAS calorimeter performance Technical Design Report*. CERN-LHCC-96-40. Dec. 1996.
- [131] ATLAS Collaboration. *ATLAS liquid argon calorimeter: Technical design report*. CERN-LHCC-96-41. Dec. 1996.
- [132] ATLAS Collaboration. *ATLAS tile calorimeter: Technical design report*. CERN-LHCC-96-42. Dec. 1996.
- [133] A. Artamonov et al. “The ATLAS forward calorimeters”. In: *JINST* 3 (2008), P02010. DOI: 10.1088/1748-0221/3/02/P02010.
- [134] ATLAS Collaboration. *Minimum Bias Trigger Scintillators in ATLAS Run II (ATL-COM-DAQ-2014-056)*. <https://cds.cern.ch/record/1708408>.
- [135] ATLAS Collaboration. *ATLAS muon spectrometer: Technical design report*. CERN-LHCC-97-22, ATLAS-TDR-10. June 1997.
- [136] L. Adamczyk et al. *Technical Design Report for the ATLAS Forward Proton Detector*. May 2015.
- [137] Peter Jenni et al. “ATLAS Forward Detectors for Measurement of Elastic Scattering and Luminosity”. In: (2008). DOI: 10.17181/CERN-LHCC-2008-004.
- [138] G. Avoni et al. “The new LUCID-2 detector for luminosity measurement and monitoring in ATLAS”. In: *JINST* 13.07 (2018), P07017. DOI: 10.1088/1748-0221/13/07/P07017.
- [139] *The LUCID-2 detector*. <https://lucid3.web.cern.ch/>.
- [140] Howard S. Matis et al. “The BRAN luminosity detectors for the LHC”. In: *Nucl. Instrum. Meth. A* 848 (2017), pp. 114–126. DOI: 10.1016/j.nima.2016.12.019. arXiv: 1612.01238 [physics.acc-ph].
- [141] ATLAS Collaboration. *Zero degree calorimeters for ATLAS*. CERN-LHCC-2007-01. Jan. 2007.
- [142] ATLAS Collaboration. *ATLAS central solenoid: Technical design report*. CERN-LHCC-97-21. Apr. 1997.



- [143] ATLAS Collaboration. *ATLAS barrel toroid: Technical design report*. CERN-LHCC-97-19. Apr. 1997.
- [144] ATLAS Collaboration. *ATLAS endcap toroids: Technical design report*. CERN-LHCC-97-20. Apr. 1997.
- [145] ATLAS Collaboration. *ATLAS level-1 trigger: Technical Design Report*. ATLAS-TDR-12, CERN-LHCC-98-014. June 1998.
- [146] ATLAS Collaboration. *ATLAS high-level trigger, data acquisition and controls: Technical design report*. CERN-LHCC-2003-022, ATLAS-TRD-016. July 2003.
- [147] R. Achenbach et al. “The ATLAS level-1 calorimeter trigger”. In: *JINST* 3 (2008), P03001. DOI: 10.1088/1748-0221/3/03/P03001.
- [148] ATLAS Collaboration. “Performance of the ATLAS muon triggers in Run 2”. In: *JINST* 15.09 (2020), P09015. DOI: 10.1088/1748-0221/15/09/p09015. arXiv: 2004.13447 [physics.ins-det].
- [149] H. Bertelsen et al. “Operation of the upgraded ATLAS Central Trigger Processor during the LHC Run 2”. In: *JINST* 11.02 (2016), p. C02020. DOI: 10.1088/1748-0221/11/02/C02020.
- [150] ATLAS Collaboration. “Operation of the ATLAS trigger system in Run 2”. In: *JINST* 15.10 (2020), P10004. DOI: 10.1088/1748-0221/15/10/P10004. arXiv: 2007.12539 [physics.ins-det].
- [151] ATLAS Collaboration. *Trigger menu in 2018 (ATL-DAQ-PUB-2019-001)*. <https://cds.cern.ch/record/2693402>.
- [152] Markus Elsing et al. “The ATLAS Tier-0: Overview and operational experience”. In: *J. Phys. Conf. Ser.* 219 (2010). Ed. by Jan Gruntorad and Milos Lokajicek, p. 072011. DOI: 10.1088/1742-6596/219/7/072011.
- [153] Sascha Mehlhase. “ATLAS detector slice (and particle visualisations)”. In: (2021). URL: <https://cds.cern.ch/record/2770815>.
- [154] *ATLAS Tracking Software Tutorial*. <https://atlassoftwaredocs.web.cern.ch/internal-links/tracking-tutorial/>.
- [155] T. Cornelissen et al. “Concepts, Design and Implementation of the ATLAS New Tracking (NEWT)”. In: (Mar. 2007). Ed. by A. Salzburger.
- [156] T. Cornelissen et al. “The new ATLAS track reconstruction (NEWT)”. In: *J. Phys. Conf. Ser.* 119 (2008). Ed. by Randall Sobie, Reda Tafirout, and Jana Thomson, p. 032014. DOI: 10.1088/1742-6596/119/3/032014.
- [157] ATLAS Collaboration. “Performance of the ATLAS Track Reconstruction Algorithms in Dense Environments in LHC Run 2”. In: *Eur. Phys. J. C* 77.10 (2017), p. 673. DOI: 10.1140/epjc/s10052-017-5225-7. arXiv: 1704.07983 [hep-ex].
- [158] Azriel Rosenfeld and John L Pfaltz. “Sequential operations in digital picture processing”. In: *Journal of the ACM (JACM)* 13.4 (1966), pp. 471–494.
- [159] R. Fruhwirth. “Application of Kalman filtering to track and vertex fitting”. In: *Nucl. Instrum. Meth. A* 262 (1987), pp. 444–450. DOI: 10.1016/0168-9002(87)90887-4.
- [160] ATLAS Collaboration. *Improved electron reconstruction in ATLAS using the Gaussian Sum Filter-based model for bremsstrahlung*. ATLAS-CONF-2012-047, ATLAS-CONF-2012-047. May 2012.

- [161] ATLAS Collaboration. *Heavy Ion Track Reconstruction Efficiency (IDTR-2016-008)*.  
<https://atlas.web.cern.ch/Atlas/GROUPS/PHYSICS/PLOTS/IDTR-2016-008/>.
- [162] Andrew Haas. “ATLAS simulation using real data: Embedding and overlay”.  
In: *J. Phys. Conf. Ser.* 898.4 (2017). Ed. by Richard Mount and Craig Tull, p. 042004.  
DOI: 10.1088/1742-6596/898/4/042004.
- [163] G. Piacquadio, Kirill Prokofiev, and A. Wildauer.  
“Primary vertex reconstruction in the ATLAS experiment at LHC”. In: *J. Phys. Conf. Ser.* 119 (2008). Ed. by Randall Sobie, Reda Tafiout, and Jana Thomson, p. 032033.  
DOI: 10.1088/1742-6596/119/3/032033.
- [164] ATLAS Collaboration. “Reconstruction of primary vertices at the ATLAS experiment in Run 1 proton–proton collisions at the LHC”. In: *Eur. Phys. J. C* 77.5 (2017), p. 332.  
DOI: 10.1140/epjc/s10052-017-4887-5. arXiv: 1611.10235 [physics.ins-det].
- [165] ATLAS Collaboration.  
“Topological cell clustering in the ATLAS calorimeters and its performance in LHC Run 1”.  
In: *Eur. Phys. J. C* 77 (2017), p. 490. DOI: 10.1140/epjc/s10052-017-5004-5.  
arXiv: 1603.02934 [hep-ex].
- [166] ATLAS Collaboration. “Electron reconstruction and identification in the ATLAS experiment using the 2015 and 2016 LHC proton-proton collision data at  $\sqrt{s} = 13$  TeV”.  
In: *Eur. Phys. J. C* 79.8 (2019), p. 639. DOI: 10.1140/epjc/s10052-019-7140-6.  
arXiv: 1902.04655 [physics.ins-det].
- [167] ATLAS Collaboration. “Measurement of the photon identification efficiencies with the ATLAS detector using LHC Run 2 data collected in 2015 and 2016”.  
In: *Eur. Phys. J. C* 79.3 (2019), p. 205. DOI: 10.1140/epjc/s10052-019-6650-6.  
arXiv: 1810.05087 [hep-ex].
- [168] ATLAS Collaboration. “Electron and photon performance measurements with the ATLAS detector using the 2015–2017 LHC proton-proton collision data”.  
In: *JINST* 14.12 (2019), P12006. DOI: 10.1088/1748-0221/14/12/P12006.  
arXiv: 1908.00005 [hep-ex].
- [169] ATLAS Collaboration. “Electron and photon energy calibration with the ATLAS detector using 2015–2016 LHC proton-proton collision data”. In: *JINST* 14.03 (2019), P03017.  
DOI: 10.1088/1748-0221/14/03/P03017. arXiv: 1812.03848 [hep-ex].
- [170] ATLAS Collaboration. “Measurement of light-by-light scattering and search for axion-like particles with 2.2 nb<sup>-1</sup> of Pb+Pb data with the ATLAS detector”.  
In: *JHEP* 03 (2021). [Erratum: *JHEP* 11, 050 (2021)], p. 243.  
DOI: 10.1007/JHEP03(2021)243. arXiv: 2008.05355 [hep-ex].
- [171] ATLAS Collaboration. “Muon reconstruction performance of the ATLAS detector in proton–proton collision data at  $\sqrt{s} = 13$  TeV”. In: *Eur. Phys. J. C* 76.5 (2016), p. 292.  
DOI: 10.1140/epjc/s10052-016-4120-y. arXiv: 1603.05598 [hep-ex].
- [172] ATLAS Collaboration. “Muon reconstruction and identification efficiency in ATLAS using the full Run 2 *pp* collision data set at  $\sqrt{s} = 13$  TeV”. In: *Eur. Phys. J. C* 81.7 (2021), p. 578.  
DOI: 10.1140/epjc/s10052-021-09233-2. arXiv: 2012.00578 [hep-ex].
- [173] Sébastien Rettie. “Muon identification and performance in the ATLAS experiment”.  
In: *PoS DIS2018* (2018), p. 097. DOI: 10.22323/1.316.0097.
- [174] Bo Andersson et al. “Parton Fragmentation and String Dynamics”.  
In: *Phys. Rept.* 97 (1983), pp. 31–145. DOI: 10.1016/0370-1573(83)90080-7.

- [175] B. R. Webber. “A QCD Model for Jet Fragmentation Including Soft Gluon Interference”. In: *Nucl. Phys. B* 238 (1984), pp. 492–528. DOI: 10.1016/0550-3213(84)90333-X.
- [176] ATLAS Collaboration. “Jet reconstruction and performance using particle flow with the ATLAS Detector”. In: *Eur. Phys. J. C* 77.7 (2017), p. 466. DOI: 10.1140/epjc/s10052-017-5031-2. arXiv: 1703.10485 [hep-ex].
- [177] Matteo Cacciari, Gavin P. Salam, and Gregory Soyez. “The anti- $k_t$  jet clustering algorithm”. In: *JHEP* 04 (2008), p. 063. DOI: 10.1088/1126-6708/2008/04/063. arXiv: 0802.1189 [hep-ph].
- [178] ATLAS Collaboration. “Jet energy scale and resolution measured in proton–proton collisions at  $\sqrt{s} = 13$  TeV with the ATLAS detector”. In: *Eur. Phys. J. C* 81.8 (2021), p. 689. DOI: 10.1140/epjc/s10052-021-09402-3. arXiv: 2007.02645 [hep-ex].
- [179] ATLAS Collaboration. “ATLAS flavour-tagging algorithms for the LHC Run 2 pp collision dataset”. In: *Eur. Phys. J. C* 83.7 (2023), p. 681. DOI: 10.1140/epjc/s10052-023-11699-1. arXiv: 2211.16345 [physics.data-an].
- [180] ATLAS Collaboration. “Identification and energy calibration of hadronically decaying tau leptons with the ATLAS experiment in  $pp$  collisions at  $\sqrt{s}=8$  TeV”. In: *Eur. Phys. J. C* 75.7 (2015), p. 303. DOI: 10.1140/epjc/s10052-015-3500-z. arXiv: 1412.7086 [hep-ex].
- [181] ATLAS Collaboration. *Identification of hadronic tau lepton decays using neural networks in the ATLAS experiment*. ATL-PHYS-PUB-2019-033. 2019.
- [182] ATLAS Collaboration. “Performance of missing transverse momentum reconstruction with the ATLAS detector using proton-proton collisions at  $\sqrt{s} = 13$  TeV”. In: *Eur. Phys. J. C* 78.11 (2018), p. 903. DOI: 10.1140/epjc/s10052-018-6288-9. arXiv: 1802.08168 [hep-ex].
- [183] C Moller. “GENERAL PROPERTIES OF THE CHARACTERISTIC MATRIX IN THE THEORY OF ELEMENTARY PARTICLES. 1.” In: *Matematisk-fysiske Meddelelser Kongelige Danske Videnskabernes Selskab* 23.1 (1945), pp. 1–48.
- [184] ATLAS Collaboration. “Luminosity Determination in  $pp$  Collisions at  $\sqrt{s} = 7$  TeV Using the ATLAS Detector at the LHC”. In: *Eur. Phys. J. C* 71 (2011), p. 1630. DOI: 10.1140/epjc/s10052-011-1630-5. arXiv: 1101.2185 [hep-ex].
- [185] CMS Collaboration. “Luminosity determination using Z boson production at the CMS experiment”. In: *Eur. Phys. J. C* 84.1 (2024), p. 26. DOI: 10.1140/epjc/s10052-023-12268-2. arXiv: 2309.01008 [hep-ex].
- [186] TOTEM Collaboration. “First measurement of elastic, inelastic and total cross-section at  $\sqrt{s} = 13$  TeV by TOTEM and overview of cross-section data at LHC energies”. In: *Eur. Phys. J. C* 79.2 (2019), p. 103. DOI: 10.1140/epjc/s10052-019-6567-0. arXiv: 1712.06153 [hep-ex].
- [187] ALICE Collaboration. “ALICE luminosity determination for Pb–Pb collisions at  $\sqrt{s_{NN}} = 5.02$  TeV”. In: *JINST* 19.02 (2024), P02039. DOI: 10.1088/1748-0221/19/02/P02039. arXiv: 2204.10148 [nucl-ex].
- [188] S. van der Meer. *Calibration of the Effective Beam Height in the ISR*. CERN-ISR-PO-68-31. June 1968.

- [189] Carlo Rubbia. *Measurement of the luminosity of  $p$ – $\overline{p}$  collider with a (generalized) Van der Meer Method*. Tech. rep. Geneva: CERN, 1977.  
URL: <https://cds.cern.ch/record/1025746>.
- [190] ATLAS Collaboration. “Luminosity determination in  $pp$  collisions at  $\sqrt{s} = 13$  TeV using the ATLAS detector at the LHC”. In: *Eur. Phys. J. C* 83.10 (2023), p. 982.  
DOI: 10.1140/epjc/s10052-023-11747-w. arXiv: 2212.09379 [hep-ex].
- [191] CMS Collaboration. “Precision luminosity measurement in proton-proton collisions at  $\sqrt{s} = 13$  TeV in 2015 and 2016 at CMS”. In: *Eur. Phys. J. C* 81.9 (2021), p. 800.  
DOI: 10.1140/epjc/s10052-021-09538-2. arXiv: 2104.01927 [hep-ex].
- [192] CMS Collaboration. “Luminosity measurement for lead-lead collisions at  $\sqrt{s_{NN}} = 5.02$  TeV in 2015 and 2018 at CMS”. In: (Mar. 2025). arXiv: 2503.03946 [hep-ex].
- [193] ALICE luminosity determination for  $pp$  collisions at  $\sqrt{s} = 13$  TeV.  
ALICE-PUBLIC-2016-002. 2016.
- [194] LHCb Collaboration. “Precision luminosity measurements at LHCb”.  
In: *JINST* 9.12 (2014), P12005. DOI: 10.1088/1748-0221/9/12/P12005.  
arXiv: 1410.0149 [hep-ex].
- [195] ATLAS Collaboration.  
*Early Inner Detector Tracking Performance in the 2015 data at  $\sqrt{s} = 13$  TeV*.  
ATL-PHYS-PUB-2015-051. 2015.
- [196] ALICE Collaboration. “Transverse momentum spectra and nuclear modification factors of charged particles in  $pp$ ,  $p$ -Pb and Pb-Pb collisions at the LHC”. In: *JHEP* 11 (2018), p. 013.  
DOI: 10.1007/JHEP11(2018)013. arXiv: 1802.09145 [nucl-ex].
- [197] ATLAS Collaboration. *Preliminary analysis of the luminosity calibration for the ATLAS 13.6 TeV data recorded in 2023*. Tech. rep. All figures including auxiliary figures are available at <https://atlas.web.cern.ch/Atlas/GROUPS/PHYSICS/PUBNOTES/ATL-DAPR-PUB-2024-001>.  
Geneva: CERN, 2024. URL: <https://cds.cern.ch/record/2900949>.
- [198] C Barschel et al. *Results of the LHC DCCT Calibration Studies*.  
<https://cds.cern.ch/record/1425904>. 2012.
- [199] Matthias Danninger and Anthony Keith Morley.  
*Alignment uncertainty in absolute Inner Detector length scale*. Tech. rep.  
Geneva: CERN, 2018. URL: <https://cds.cern.ch/record/2625293>.
- [200] A. Babaev et al. “Impact of beam–beam effects on absolute luminosity calibrations at the CERN Large Hadron Collider”. In: *Eur. Phys. J. C* 84.1 (2024), p. 17.  
DOI: 10.1140/epjc/s10052-023-12192-5. arXiv: 2306.10394 [physics.acc-ph].
- [201] Alexander Wu Chao et al., eds.  
*Handbook of accelerator physics and engineering: 2nd Edition*. 2nd ed.  
Hackensack, USA: World Scientific, 2013. ISBN: 978-981-4415-84-2. DOI: 10.1142/8543.
- [202] R. Bruce et al. “Performance and luminosity models for heavy-ion operation at the CERN Large Hadron Collider”. In: *Eur. Phys. J. Plus* 136.7 (2021), p. 745.  
DOI: 10.1140/epjp/s13360-021-01685-5. arXiv: 2107.09560 [physics.acc-ph].
- [203] Foteini Asvesta. *Sources and mitigation of non-factorization in the injectors and the LHC*.  
<https://indico.cern.ch/event/1502802/contributions/6326634/>.
- [204] ATLAS Collaboration. “Improved luminosity determination in  $pp$  collisions at  $\sqrt{s} = 7$  TeV using the ATLAS detector at the LHC”. In: *Eur. Phys. J. C* 73.8 (2013), p. 2518.  
DOI: 10.1140/epjc/s10052-013-2518-3. arXiv: 1302.4393 [hep-ex].

- [205] W. Adam et al. “Radiation hard diamond sensors for future tracking applications”. In: *Nucl. Instrum. Meth. A* 565 (2006). Ed. by J. Grosse-Knetter, H. Krueger, and N. Vermes, pp. 278–283. DOI: 10.1016/j.nima.2006.05.127.
- [206] ATLAS Collaboration. “ATLAS data quality operations and performance for 2015–2018 data-taking”. In: *JINST* 15.04 (2020), P04003. DOI: 10.1088/1748-0221/15/04/P04003. arXiv: 1911.04632 [physics.ins-det].
- [207] S. Donnachie et al. *Pomeron physics and QCD*. Vol. 19. Cambridge University Press, Dec. 2004. ISBN: 978-0-511-06050-2, 978-0-521-78039-1, 978-0-521-67570-3.
- [208] ATLAS Collaboration. “Exclusive dielectron production in ultraperipheral Pb+Pb collisions at  $\sqrt{s_{NN}} = 5.02$  TeV with ATLAS”. In: *JHEP* 2306 (2023), p. 182. DOI: 10.1007/JHEP06(2023)182. arXiv: 2207.12781 [nucl-ex].
- [209] ATLAS Collaboration. “Exclusive dimuon production in ultraperipheral Pb+Pb collisions at  $\sqrt{s_{NN}} = 5.02$  TeV with ATLAS”. In: *Phys. Rev. C* 104 (2021), p. 024906. DOI: 10.1103/PhysRevC.104.024906. arXiv: 2011.12211 [nucl-ex].
- [210] N. Davidson, T. Przedzinski, and Z. Was. “PHOTOS interface in C++: Technical and Physics Documentation”. In: *Comput. Phys. Commun.* 199 (2016), pp. 86–101. DOI: 10.1016/j.cpc.2015.09.013. arXiv: 1011.0937 [hep-ph].
- [211] J. Allison et al. “Recent developments in Geant4”. In: *Nucl. Instrum. Meth. A* 835 (2016), pp. 186–225. DOI: 10.1016/j.nima.2016.06.125.
- [212] Constantin Loizides, Jason Kamin, and David d’Enterria. “Improved Monte Carlo Glauber predictions at present and future nuclear colliders”. In: *Phys. Rev. C* 97.5 (2018). [Erratum: *Phys.Rev.C* 99, 019901 (2019)], p. 054910. DOI: 10.1103/PhysRevC.97.054910. arXiv: 1710.07098 [nucl-ex].
- [213] ALICE Collaboration. “Measurement of the Cross Section for Electromagnetic Dissociation with Neutron Emission in Pb-Pb Collisions at  $\sqrt{s_{NN}} = 2.76$  TeV”. In: *Phys. Rev. Lett.* 109 (2012), p. 252302. DOI: 10.1103/PhysRevLett.109.252302. arXiv: 1203.2436 [nucl-ex].
- [214] I. A. Pshenichnov et al. “Mutual heavy ion dissociation in peripheral collisions at ultrarelativistic energies”. In: *Phys. Rev. C* 64 (2001), p. 024903. DOI: 10.1103/PhysRevC.64.024903. arXiv: nucl-th/0101035.
- [215] Nathan Isgur, Colin Morningstar, and Cathy Reader. “The  $a_1$  in tau Decay”. In: *Phys. Rev. D* 39 (1989), p. 1357. DOI: 10.1103/PhysRevD.39.1357.
- [216] Stanislaw Jadach, Johann H. Kuhn, and Zbigniew Was. “TAUOLA: A Library of Monte Carlo programs to simulate decays of polarized tau leptons”. In: *Comput. Phys. Commun.* 64 (1990), pp. 275–299. DOI: 10.1016/0010-4655(91)90038-M.
- [217] ATLAS Collaboration. “Rapidity gap cross sections measured with the ATLAS detector in  $pp$  collisions at  $\sqrt{s} = 7$  TeV”. In: *Eur. Phys. J. C* 72 (2012), p. 1926. DOI: 10.1140/epjc/s10052-012-1926-0. arXiv: 1201.2808 [hep-ex].
- [218] ATLAS Collaboration. “Monitoring and data quality assessment of the ATLAS liquid argon calorimeter”. In: *JINST* 9 (2014), P07024. DOI: 10.1088/1748-0221/9/07/P07024. arXiv: 1405.3768 [hep-ex].

- [219] ATLAS Collaboration. *Charged particle multiplicities in pp interactions at  $\sqrt{s} = 2.36$  TeV measured with the ATLAS detector at the LHC*. Tech. rep. All figures including auxiliary figures are available at <https://atlas.web.cern.ch/Atlas/GROUPS/PHYSICS/CONFNOTES/ATLAS-CONF-2010-047>. Geneva: CERN, 2010. URL: <https://cds.cern.ch/record/1281299>.
- [220] François Chollet et al. *Keras*. <https://keras.io>. 2015.
- [221] Ilkka Helenius and Christine O. Rasmussen. “Hard diffraction in photoproduction with Pythia 8”. In: *Eur. Phys. J. C* 79.5 (2019), p. 413. DOI: 10.1140/epjc/s10052-019-6914-1. arXiv: 1901.05261 [hep-ph].
- [222] ATLAS Collaboration. “Measurement of coincident photon-initiated processes in ultra-peripheral Pb+Pb collisions with the ATLAS detector”. In: (Apr. 2025). arXiv: 2504.07795 [nucl-ex].
- [223] L. A. Harland-Lang. “Modelling Coincident Particle Production in Ultraperipheral Heavy Ion Collisions”. In: (June 2025). arXiv: 2506.03264 [hep-ph].
- [224] Francesco Spano. “Unfolding in particle physics: a window on solving inverse problems”. In: *EPJ Web Conf.* 55 (2013). Ed. by T. Delemontex and Arnaud Lucotte, p. 03002. DOI: 10.1051/epjconf/20135503002.
- [225] HEP ML Living Review. *A Living Review of Machine Learning for Particle Physics*. <https://iml-wg.github.io/HEPML-LivingReview/#unfolding>.
- [226] Anders Andreassen et al. “OmniFold: A Method to Simultaneously Unfold All Observables”. In: *Phys. Rev. Lett.* 124.18 (2020), p. 182001. DOI: 10.1103/PhysRevLett.124.182001. arXiv: 1911.09107 [hep-ph].
- [227] ATLAS Collaboration. “Simultaneous Unbinned Differential Cross-Section Measurement of Twenty-Four Z+jets Kinematic Observables with the ATLAS Detector”. In: *Phys. Rev. Lett.* 133.26 (2024), p. 261803. DOI: 10.1103/PhysRevLett.133.261803. arXiv: 2405.20041 [hep-ex].
- [228] Lydia Brenner et al. “Comparison of unfolding methods using RooFitUnfold”. In: *Int. J. Mod. Phys. A* 35.24 (2020), p. 2050145. DOI: 10.1142/S0217751X20501456. arXiv: 1910.14654 [physics.data-an].
- [229] Andreas Hocker and Vakhtang Kartvelishvili. “SVD approach to data unfolding”. In: *Nucl. Instrum. Meth. A* 372 (1996), pp. 469–481. DOI: 10.1016/0168-9002(95)01478-0. arXiv: hep-ph/9509307.
- [230] G. D’Agostini. “A Multidimensional unfolding method based on Bayes’ theorem”. In: *Nucl. Instrum. Meth. A* 362 (1995), pp. 487–498. DOI: 10.1016/0168-9002(95)00274-X.
- [231] G. D’Agostini. “Improved iterative Bayesian unfolding”. In: *Alliance Workshop on Unfolding and Data Correction*. Oct. 2010. arXiv: 1010.0632 [physics.data-an].
- [232] Bradley Efron and Robert J Tibshirani. *An introduction to the bootstrap*. Chapman and Hall/CRC, 1994.
- [233] ATLAS Collaboration. *Evaluating statistical uncertainties and correlations using the bootstrap method*. Tech. rep. All figures including auxiliary figures are available at <https://atlas.web.cern.ch/Atlas/GROUPS/PHYSICS/PUBNOTES/ATL-PHYS-PUB-2021-011>. Geneva: CERN, 2021. URL: <https://cds.cern.ch/record/2759945>.

- [234] B. Klos et al. “Neutron density distributions from antiprotonic Pb-208 and Bi-209 atoms”. In: *Phys. Rev. C* 76 (2007), p. 014311. DOI: 10.1103/PhysRevC.76.014311. arXiv: nucl-ex/0702016.
- [235] C. M. Tarbert et al. “Neutron skin of  $^{208}\text{Pb}$  from Coherent Pion Photoproduction”. In: *Phys. Rev. Lett.* 112.24 (2014), p. 242502. DOI: 10.1103/PhysRevLett.112.242502. arXiv: 1311.0168 [nucl-ex].
- [236] L. A. Harland-Lang, V. A. Khoze, and M. G. Ryskin. “Elastic photon-initiated production at the LHC: the role of hadron-hadron interactions”. In: *SciPost Phys.* 11 (2021), p. 064. DOI: 10.21468/SciPostPhys.11.3.064. arXiv: 2104.13392 [hep-ph].
- [237] Nicolas Crepet. *Recent development on gamma gamma collisions at hadron colliders*. <https://indico.global/event/9992/timetable/?view=standard#23-recent-development-on-gamma>.
- [238] Jerome H. Friedman. “Data Analysis Techniques for High-Energy Particle Physics”. In: *3rd CERN School of Computing*. Oct. 1974, p. 271.
- [239] Vladyslav Shtabovenko, Rolf Mertig, and Frederik Orellana. “FeynCalc 10: Do multiloop integrals dream of computer codes?”. In: *Comput. Phys. Commun.* 306 (2025), p. 109357. DOI: 10.1016/j.cpc.2024.109357. arXiv: 2312.14089 [hep-ph].
- [240] Olivier Mattelaer. “On the maximal use of Monte Carlo samples: re-weighting events at NLO accuracy”. In: *Eur. Phys. J. C* 76.12 (2016), p. 674. DOI: 10.1140/epjc/s10052-016-4533-7. arXiv: 1607.00763 [hep-ph].
- [241] Glen Cowan et al. “Asymptotic formulae for likelihood-based tests of new physics”. In: *Eur. Phys. J. C* 71 (2011). [Erratum: *Eur.Phys.J.C* 73, 2501 (2013)], p. 1554. DOI: 10.1140/epjc/s10052-011-1554-0. arXiv: 1007.1727 [physics.data-an].
- [242] David I. Inouye et al. *A Review of Multivariate Distributions for Count Data Derived from the Poisson Distribution*. 2016. arXiv: 1609.00066 [stat.ME]. URL: <https://arxiv.org/abs/1609.00066>.
- [243] H1 Collaboration. “The H1 detector at HERA”. In: *Nucl. Instrum. Meth. A* 386 (1997), pp. 310–347. DOI: 10.1016/S0168-9002(96)00893-5.
- [244] ATLAS Collaboration. “Determination of the parton distribution functions of the proton from ATLAS measurements of differential  $W^\pm$  and Z boson production in association with jets”. In: *JHEP* 07 (2021), p. 223. DOI: 10.1007/JHEP07(2021)223. arXiv: 2101.05095 [hep-ex].
- [245] H1 and ZEUS Collaborations. “Combination of measurements of inclusive deep inelastic  $e^\pm p$  scattering cross sections and QCD analysis of HERA data”. In: *Eur. Phys. J. C* 75.12 (2015), p. 580. DOI: 10.1140/epjc/s10052-015-3710-4. arXiv: 1506.06042 [hep-ex].
- [246] F. James and M. Roos. “Minuit: A System for Function Minimization and Analysis of the Parameter Errors and Correlations”. In: *Comput. Phys. Commun.* 10 (1975), pp. 343–367. DOI: 10.1016/0010-4655(75)90039-9.
- [247] Roger Fletcher. *Practical methods of optimization*. John Wiley & Sons, 2000.
- [248] CMS Collaboration. *Measurement of the tau g-2 factor in ultraperipheral PbPb collisions recorded by the CMS experiment*. CMS-PAS-HIN-24-011, CMS-PAS-HIN-24-011. 2024.

- [249] ATLAS Collaboration. *Measurement of coherent exclusive  $J/\psi \rightarrow \mu^+\mu^-$  production in ultraperipheral Pb+Pb collisions at  $\sqrt{s_{NN}} = 5.36$  TeV with the ATLAS detector*. Tech. rep. All figures including auxiliary figures are available at <https://atlas.web.cern.ch/Atlas/GROUPS/PHYSICS/CONFNOTES/ATLAS-CONF-2025-003>. Geneva: CERN, 2025. URL: <https://cds.cern.ch/record/2929557>.





# **Appendices**



# Appendix A

## Supplementary material for Chapter 5

### A.1 Monte Carlo samples

A summary of the key parameters of the Monte Carlo samples generated for the analysis presented in Chapter 5 is given in Tab. [A.1](#).

Process	Generator	Mass slice (GeV)	$\sigma_{\text{gen}}$ (nb)	$\epsilon_{\text{filt}}$	$N_{\text{gen}}$ (2015)	$N_{\text{gen}}$ (2018)
$\gamma\gamma \rightarrow \tau^+\tau^-$	SL+Py8+Tauola+PHOTOS	$m_{\text{inv}}(\tau, \tau) \in [4, 200]$	244.869e3	0.080539	921.2e3	999.5e3
	SL+Py8+PHOTOS	$m_{\text{inv}}(\tau, \tau) \in [4, 200]$	244.869e3	0.079817	1.0e6	2.0e6
$\gamma\gamma \rightarrow \mu^+\mu^-$	SL+Py8	$m_{\text{inv}}(\mu, \mu) \in [7, 20]$	76.64e3	–	1.1e6	4.1e6
	SL+Py8	$m_{\text{inv}}(\mu, \mu) \in [20, 200]$	7.12e3	–	5.0e5	1.1e5
$\gamma\gamma \rightarrow \mu^+\mu^- + \gamma$	MG5+Py8 ( $p + p$ )	–	389.0e-6	–	2.0e4	2.0e4
$\gamma\gamma \rightarrow e^+e^-$	SL+Py8	$m_{\text{inv}}(e, e) \in [4.5, 7]$	156.55e3	–	1.0e6	4.0e6
	SL+Py8	$m_{\text{inv}}(e, e) \in [7, 15]$	121.77e3	–	5.0e5	4.0e6
	SL+Py8	$m_{\text{inv}}(e, e) \in [15, 200]$	17.83e3	–	5.0e5	1.0e6

**Table A.1:** Summary of Monte Carlo samples generated for  $\gamma\gamma \rightarrow \ell^+\ell^-$  scattering, where  $\ell = e, \mu, \tau$ . Here,  $\sigma_{\text{gen}}$  is the generated cross-section,  $\epsilon_{\text{filter}}$  is the efficiency of the charged particle filter, and  $N_{\text{gen}}$  is the number of generated events, shown for both the 2015 and 2018 samples.  $m_{\ell\ell}$  refers to the dilepton invariant mass. The nomenclature for generators is: SL for STARlight v2.0, Py8 for Pythia8 v8.245, Tauola for Tauola++ v1.1.6, PHOTOS for Photos++ v3.61, and MG5 for MadGraph5\_aMC@NLO v2.9.2. The ( $p + p$ ) for the  $\gamma\gamma \rightarrow \mu^+\mu^- + \gamma$  sample denotes that the photon flux associated with the proton was used, instead of the Pb ion as for the other samples.

## A.2 Unfolding inputs

The reconstructed and truth  $\gamma\gamma \rightarrow \tau^+\tau^-$  signal histograms are shown for all kinematic observables (except for  $p_T^\mu$ ) in Figs. [A.1](#) to [A.3](#). The corresponding response matrices are shown in Figs. [A.4](#) to [A.6](#). The acceptance and efficiency factors for all kinematic observables of interest are shown in Figs. [A.7](#) to [A.9](#).

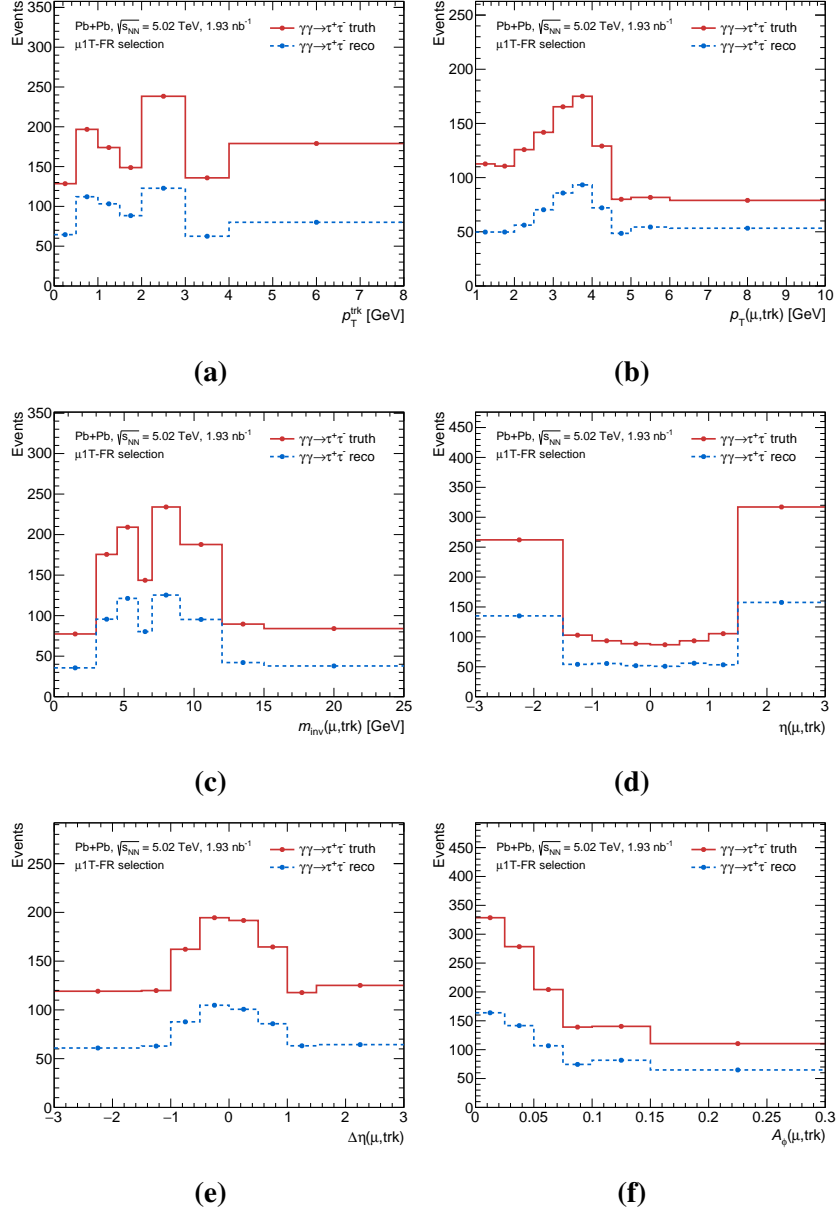


**Figure A.1:** Reconstructed and truth  $\gamma\gamma \rightarrow \tau^+\tau^-$  distributions for the following kinematic observables in the  $\mu 1T\text{-FR}$  region: (a)  $p_T^{\text{trk}}$ , (b)  $p_T(\mu, \text{trk})$ , (c)  $m_{\text{inv}}(\mu, \text{trk})$ , (d)  $\eta(\mu, \text{trk})$ , (e)  $\Delta\eta(\mu, \text{trk})$ , and (f)  $A_\phi(\mu, \text{trk})$ .

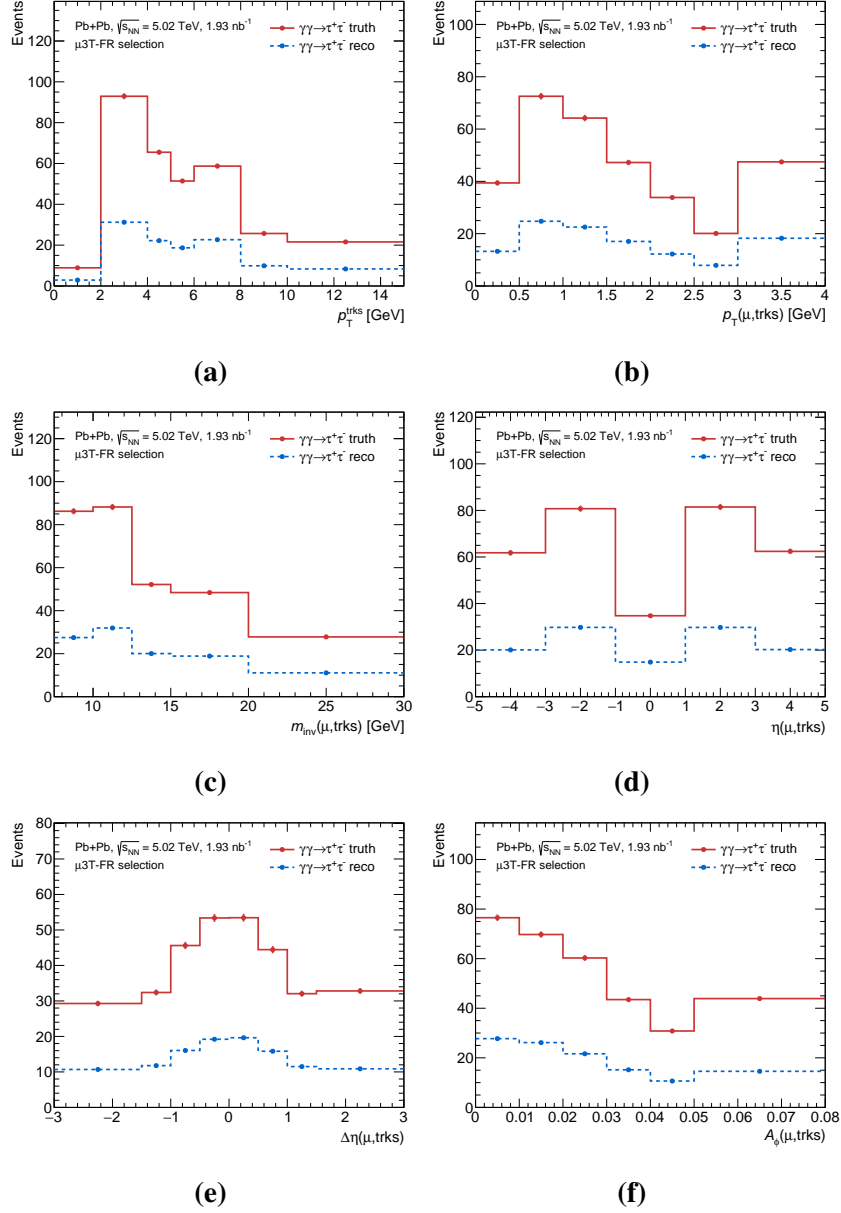


**Figure A.2:** Reconstructed and truth  $\gamma\gamma \rightarrow \tau^+\tau^-$  distributions for the following kinematic observables in the  $\mu 3T$ -FR region: (a)  $p_T^{\text{trks}}$ , (b)  $p_T(\mu, \text{trks})$ , (c)  $m_{\text{inv}}(\mu, \text{trks})$ , (d)  $\eta(\mu, \text{trks})$ , (e)  $\Delta\eta(\mu, \text{trks})$ , and (f)  $A_\phi(\mu, \text{trks})$ .



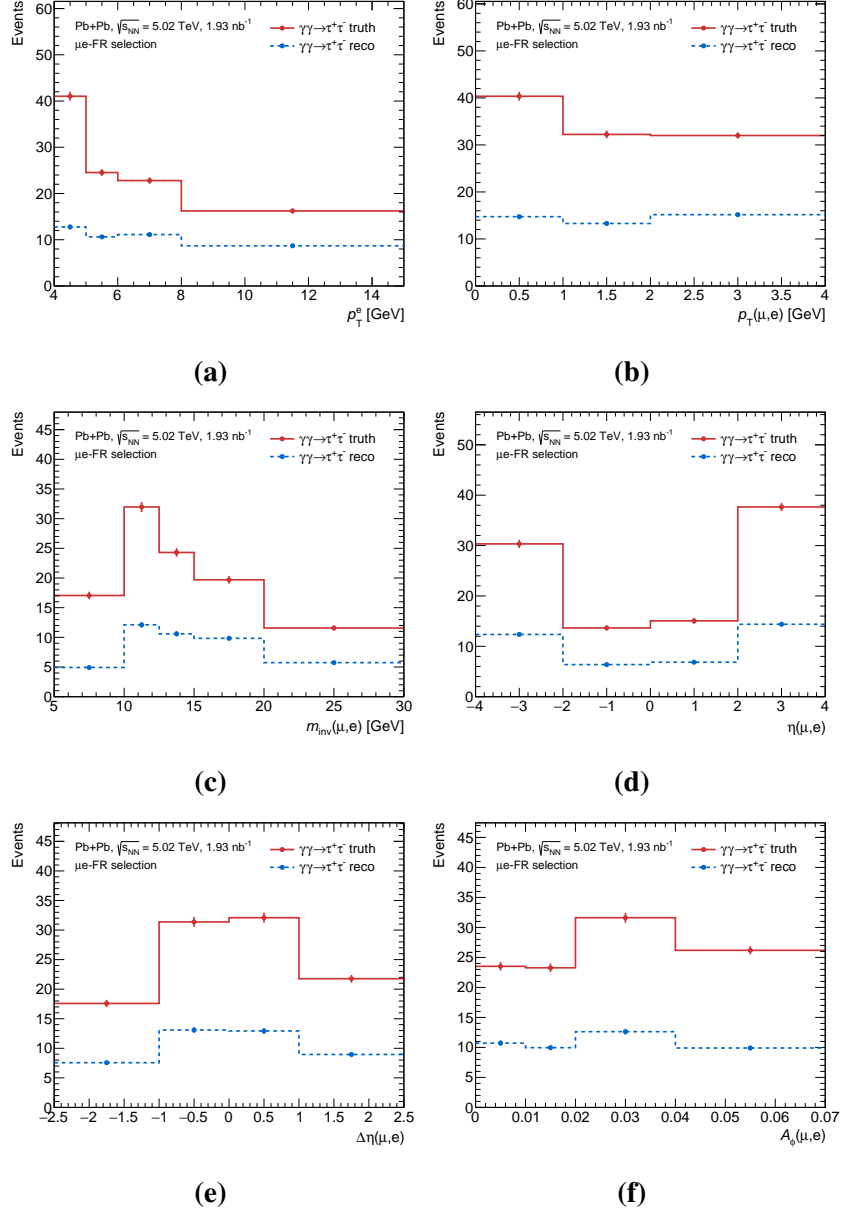


**Figure A.3:** Reconstructed and truth  $\gamma\gamma \rightarrow \tau^+\tau^-$  distributions for the following kinematic observables in the  $\mu e$ -FR region: (a)  $p_T^e$ , (b)  $p_T(\mu, e)$ , (c)  $m_{\text{inv}}(\mu, e)$ , (d)  $\eta(\mu, e)$ , (e)  $\Delta\eta(\mu, e)$ , and (f)  $A_\phi(\mu, e)$ .

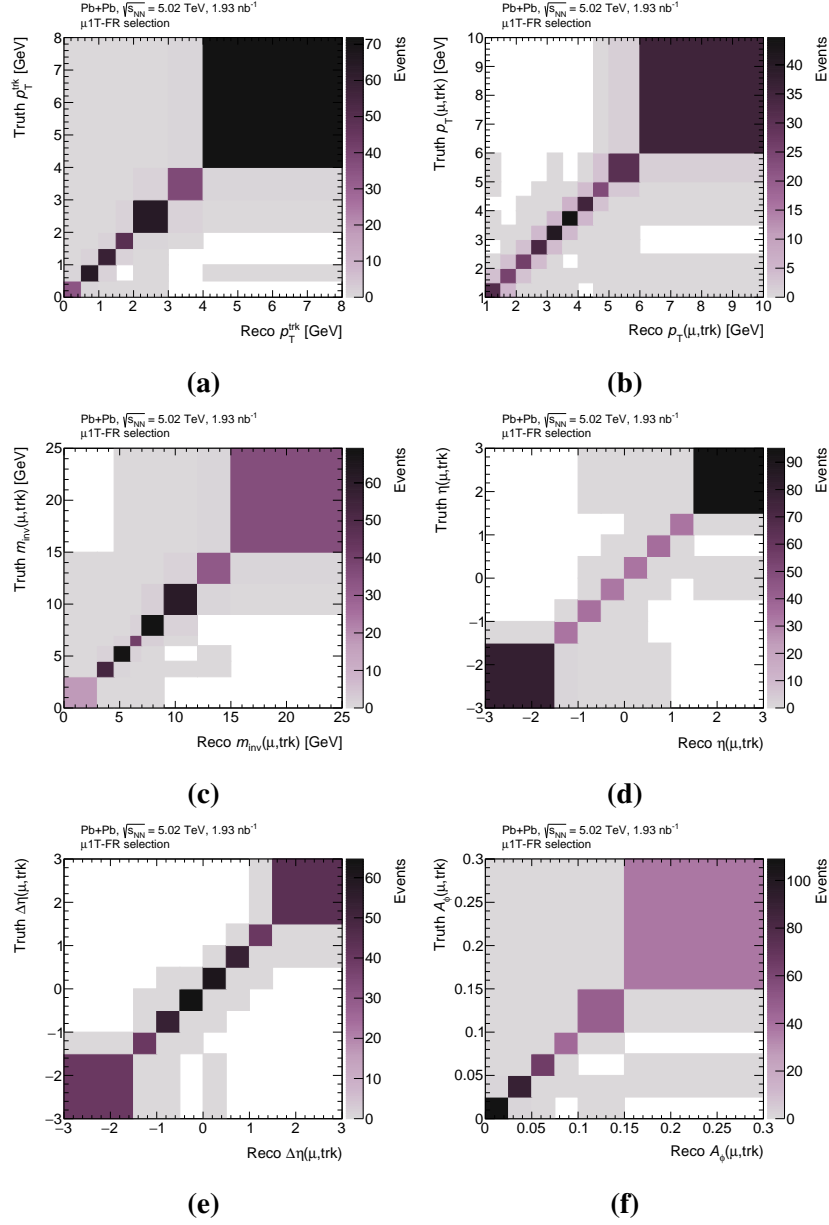


**Figure A.4:** Response matrices for the following kinematic observables in the  $\mu 1T\text{-FR}$  region: (a)  $p_T^{\text{trk}}$ , (b)  $p_T(\mu, \text{trk})$ , (c)  $m_{\text{inv}}(\mu, \text{trk})$ , (d)  $\eta(\mu, \text{trk})$ , (e)  $\Delta\eta(\mu, \text{trk})$ , and (f)  $A_\phi(\mu, \text{trk})$ .

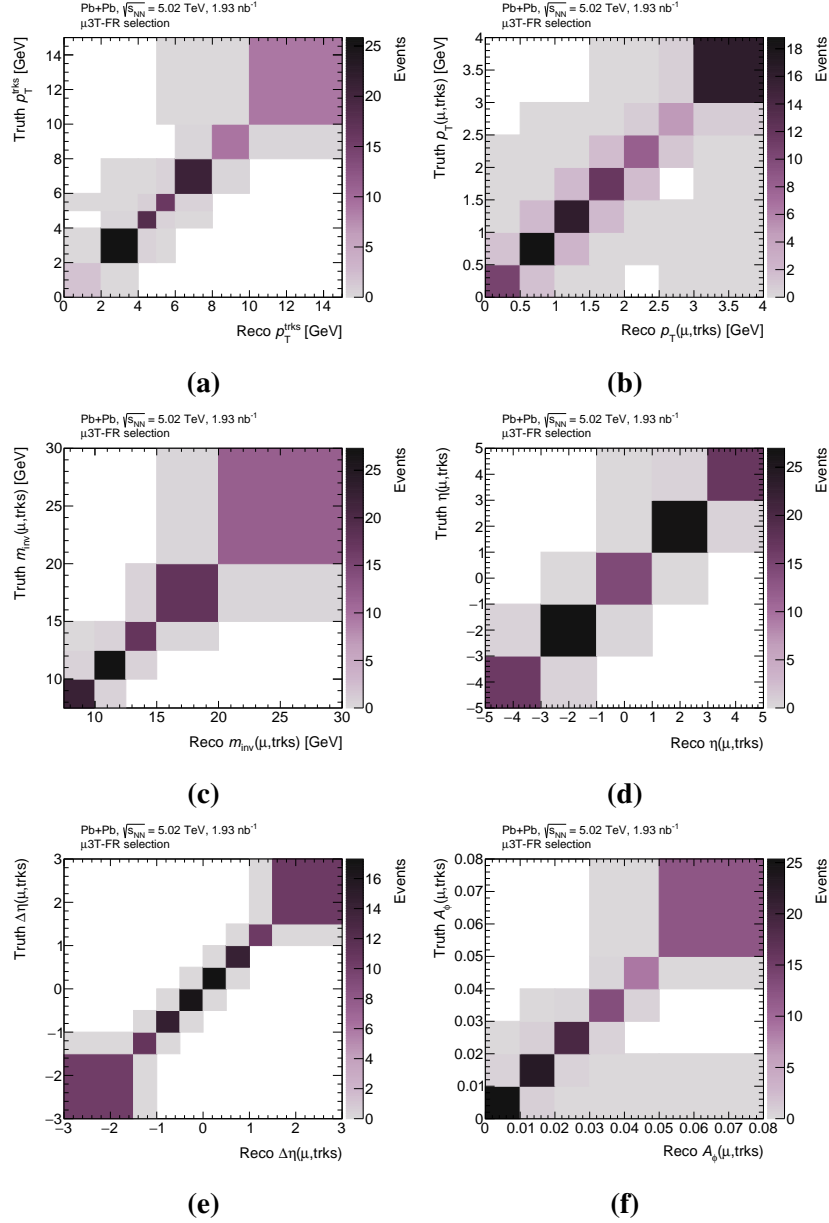


**Figure A.5:** Response matrices for the following kinematic observables in the  $\mu 3T\text{-FR}$  region: (a)  $p_T^{\text{trks}}$ , (b)  $p_T(\mu, \text{trks})$ , (c)  $m_{\text{inv}}(\mu, \text{trks})$ , (d)  $\eta(\mu, \text{trks})$ , (e)  $\Delta\eta(\mu, \text{trks})$ , and (f)  $A_\phi(\mu, \text{trks})$ .

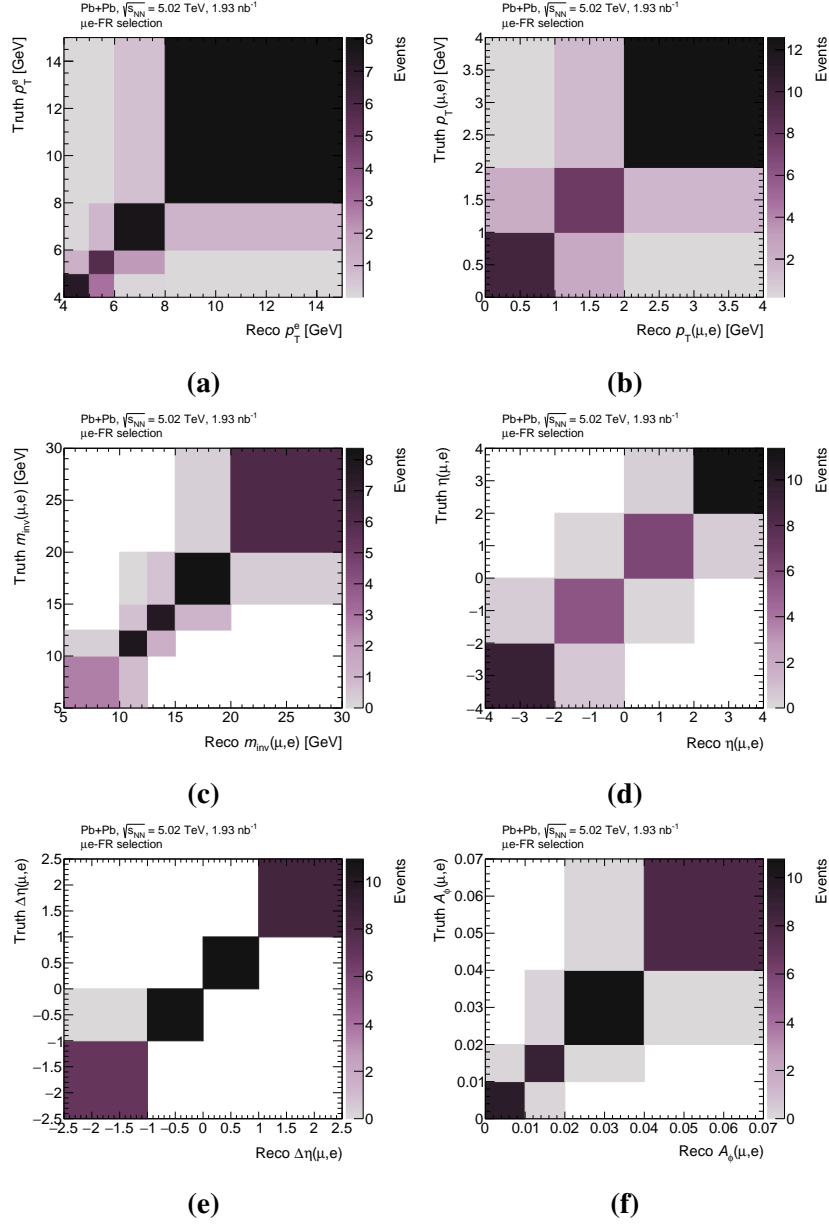


**Figure A.6:** Response matrices for the following kinematic observables in the  $\mu e$ -FR region: (a)  $p_T^e$ , (b)  $p_T(\mu, e)$ , (c)  $m_{\text{inv}}(\mu, e)$ , (d)  $\eta(\mu, e)$ , (e)  $\Delta\eta(\mu, e)$ , and (f)  $A_\phi(\mu, e)$ .

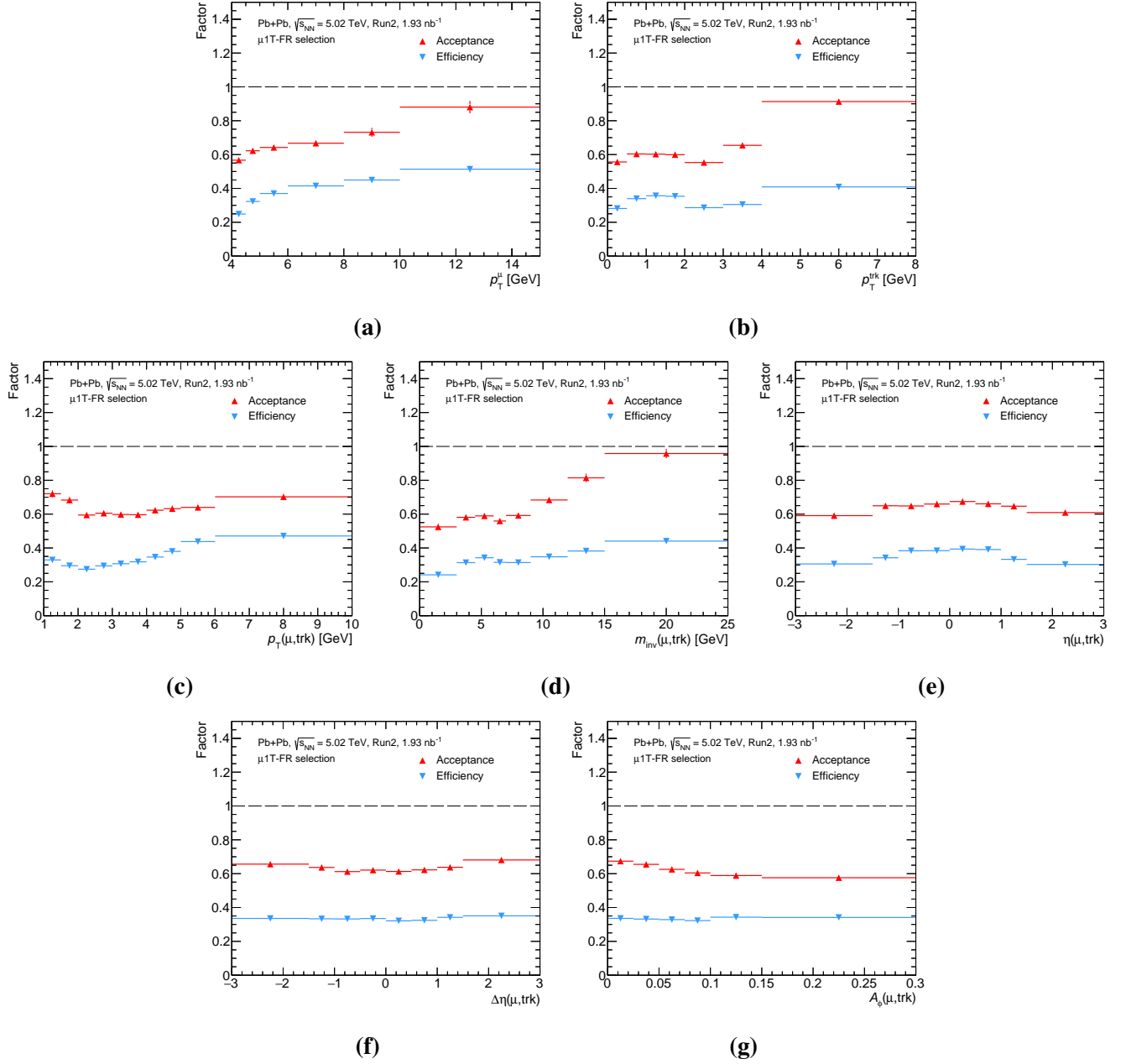


**Figure A.7:** Acceptance and efficiency factors, for all kinematic observables in the  $\mu 1T\text{-FR}$  region: (a)  $p_T^\mu$ , (b)  $p_T^{\text{trk}}$ , (c)  $p_T(\mu, \text{trk})$ , (d)  $m_{\text{inv}}(\mu, \text{trk})$ , (e)  $\eta(\mu, \text{trk})$ , (f)  $\Delta\eta(\mu, \text{trk})$ , and (g)  $A_\phi(\mu, \text{trk})$ .

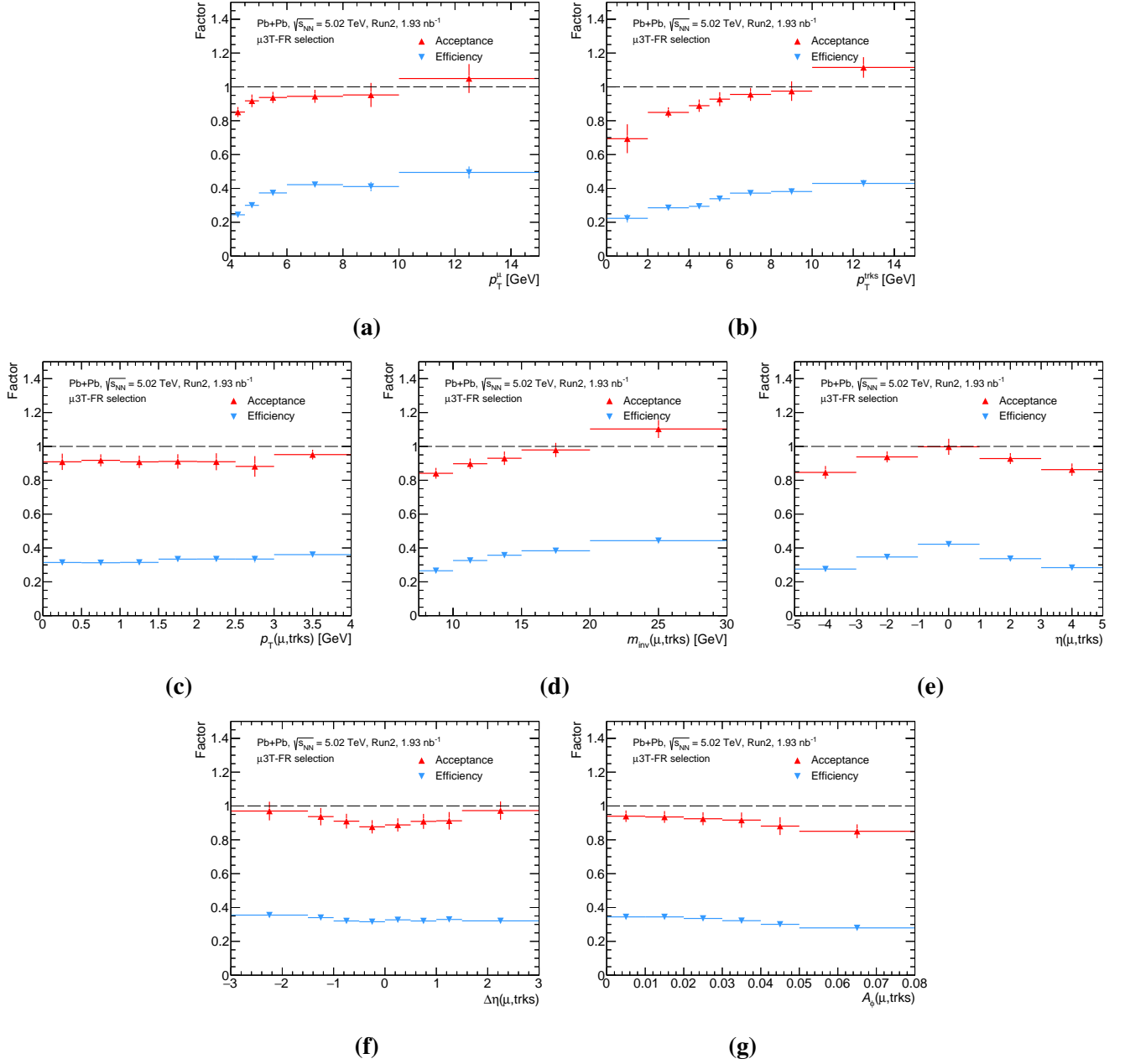


**Figure A.8:** Acceptance and efficiency factors, for all kinematic observables in the  $\mu 3T$ -FR region: (a)  $p_T^\mu$ , (b)  $p_T^{\text{trks}}$ , (c)  $p_T(\mu, \text{trks})$ , (d)  $m_{\text{inv}}(\mu, \text{trks})$ , (e)  $\eta(\mu, \text{trks})$ , (f)  $\Delta\eta(\mu, \text{trks})$ , and (g)  $A_\phi(\mu, \text{trks})$ .

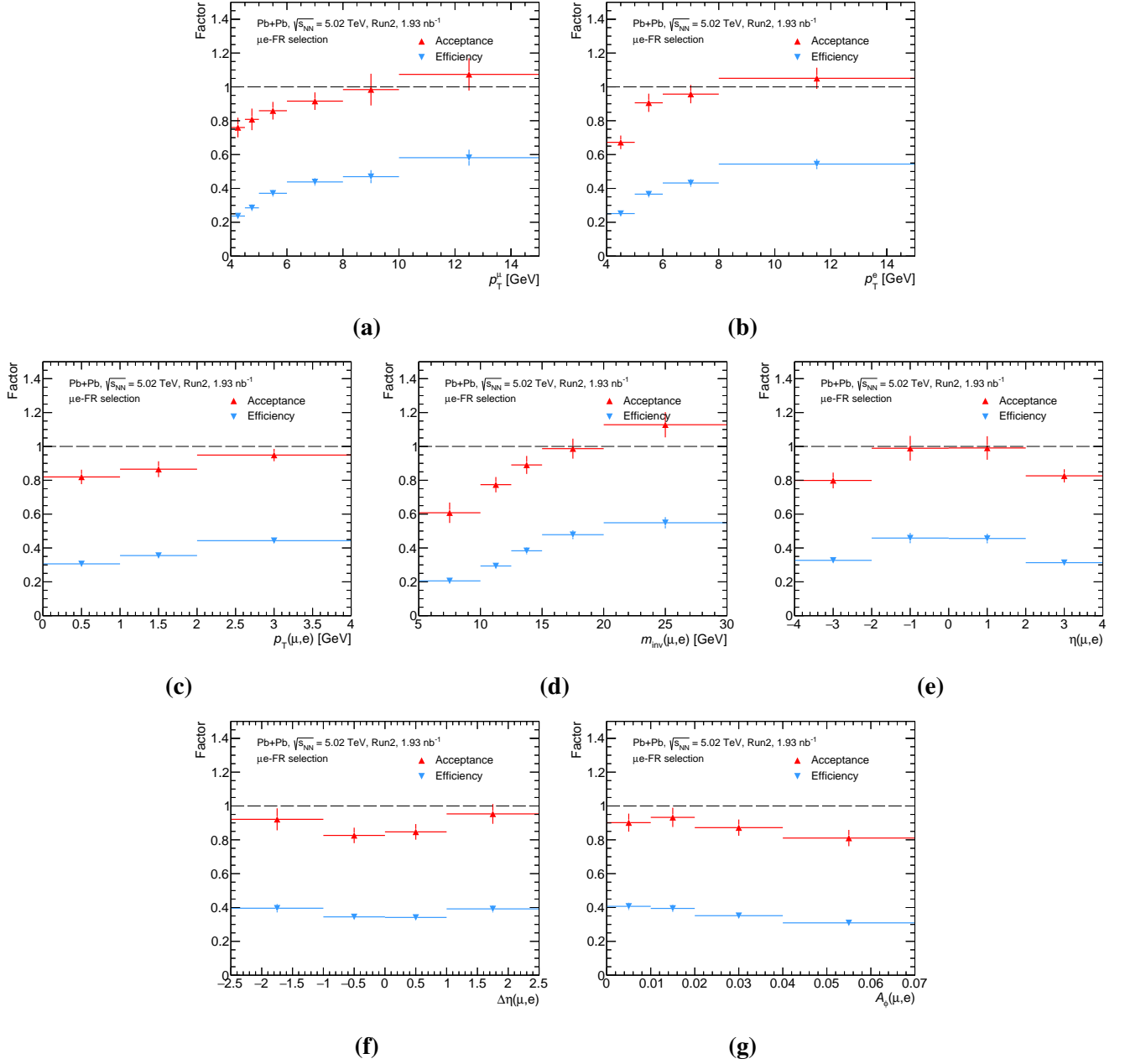


**Figure A.9:** Acceptance and efficiency factors, for all kinematic observables in the  $\mu e$ -FR region: (a)  $p_T^\mu$ , (b)  $p_T^e$ , (c)  $p_T(\mu, e)$ , (d)  $m_{\text{inv}}(\mu, e)$ , (e)  $\eta(\mu, e)$ , (f)  $\Delta\eta(\mu, e)$ , and (g)  $A_\phi(\mu, e)$ .

### A.3 Monte Carlo closure test

The results of the Monte Carlo closure test are shown in Figs. [A.10](#) to [A.12](#) for all kinematic observables (except for  $p_T^\mu$ ) in the three fiducial regions. The results for the  $p_T^\mu$  observable are shown in Fig. [5.14](#). For each of the unfolding methods, the unfolded reconstructed signal distribution is identical to the truth signal distribution, as indicated by the ratios in the lower panels of the figures being at unity. This implies that the procedure has been set up correctly.



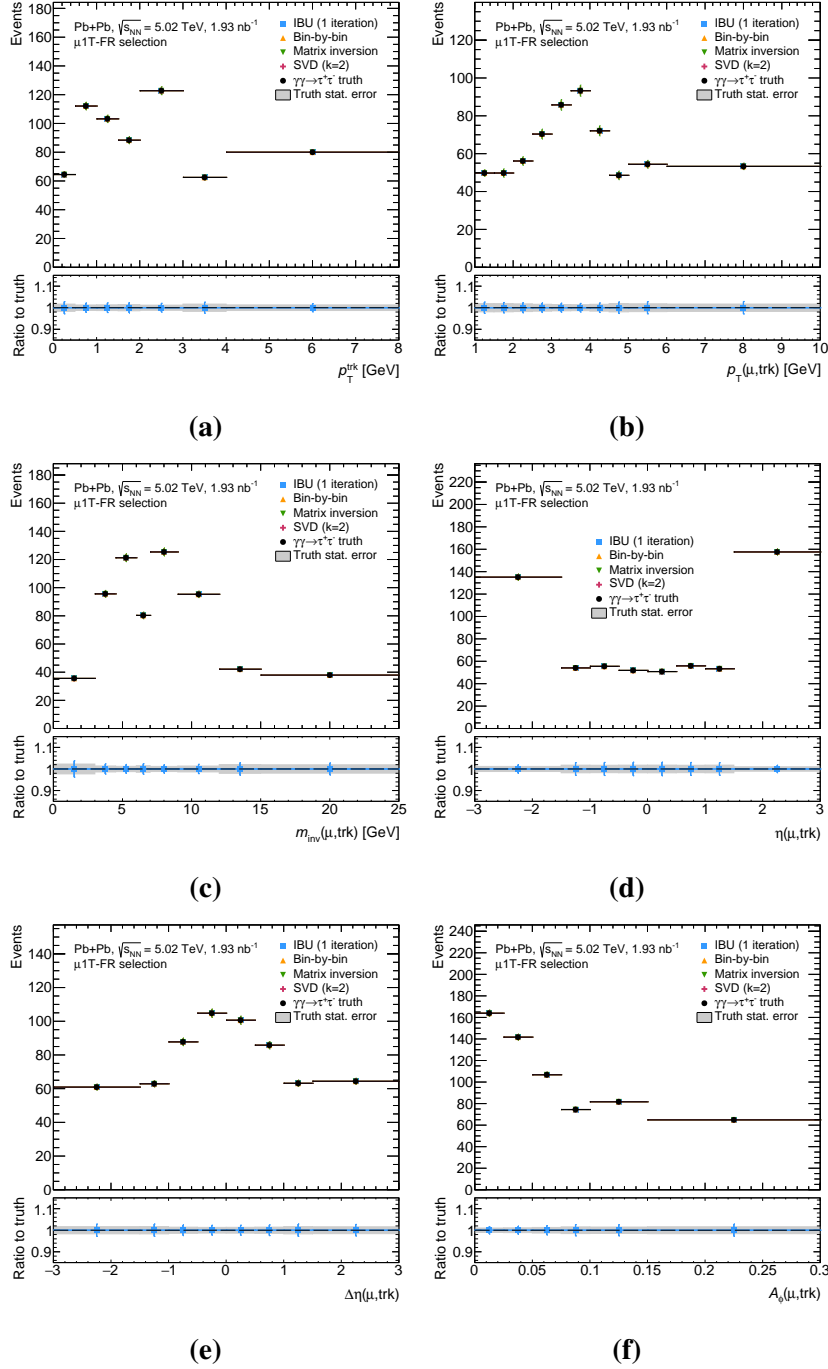


**Figure A.10:** Results of the Monte Carlo closure test for the following kinematic observables in the  $\mu 1\text{T-FR}$  region: (a)  $p_T^{\text{trk}}$ , (b)  $p_T(\mu, \text{trk})$ , (c)  $m_{\text{inv}}(\mu, \text{trk})$ , (d)  $\eta(\mu, \text{trk})$ , (e)  $\Delta\eta(\mu, \text{trk})$ , and (f)  $A_\phi(\mu, \text{trk})$ . Several unfolding methods are shown. For the Iterative Bayesian Unfolding (IBU) method, only one iteration is used. For the Singular Value Decomposition (SVD) method, the second singular value is used for  $\tau$ . Ratios of the unfolded distributions to the signal truth are shown in the lower panels. The shaded band shows the statistical uncertainty of the  $\gamma\gamma \rightarrow \tau^+\tau^-$  truth sample.

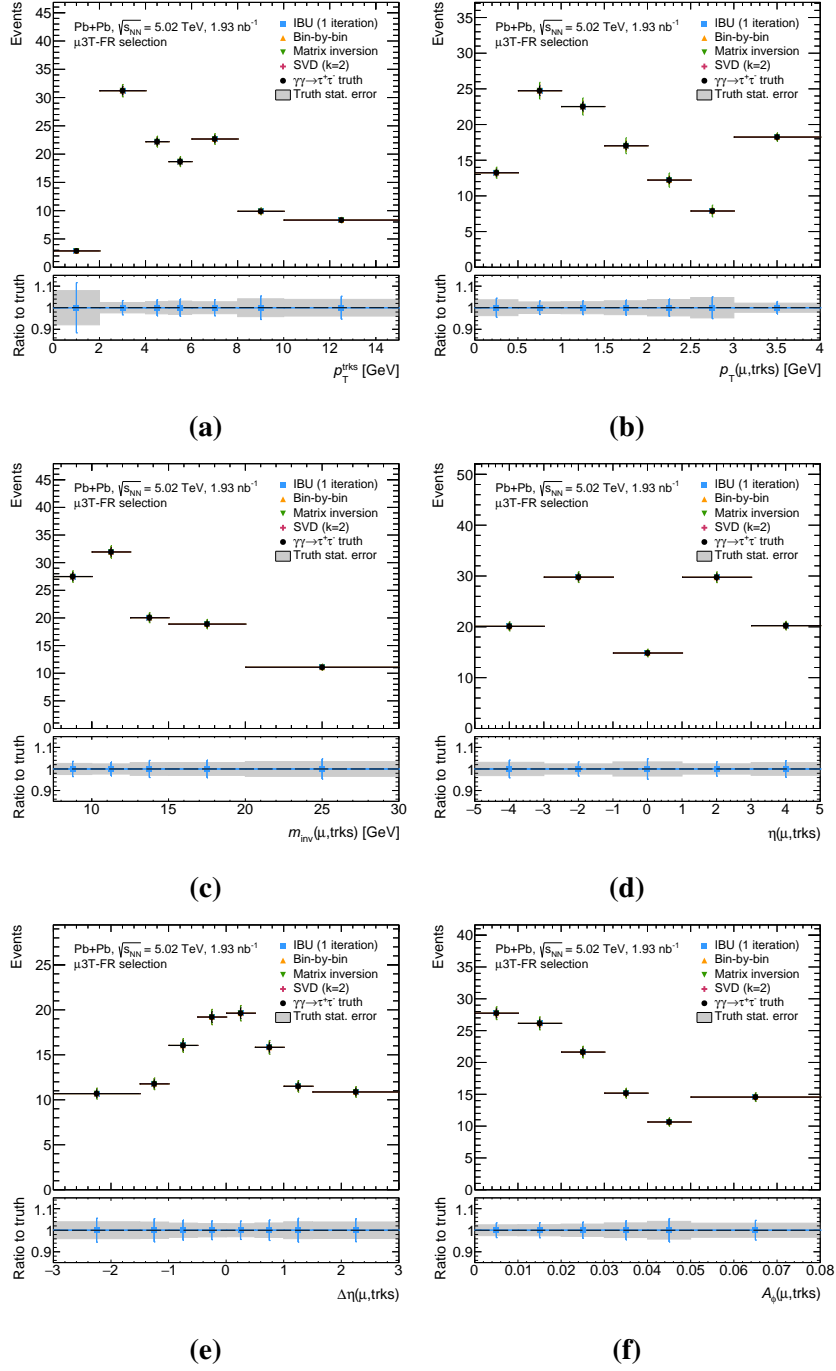


**Figure A.11:** Results of the Monte Carlo closure test for the following kinematic observables in the  $\mu 3T$ -FR region:  $\mu 3T$ -SR region: (a)  $p_T^{\text{trks}}$ , (b)  $p_T(\mu, \text{trks})$ , (c)  $m_{\text{inv}}(\mu, \text{trks})$ , (d)  $\eta(\mu, \text{trks})$ , (e)  $\Delta\eta(\mu, \text{trks})$ , and (f)  $A_\phi(\mu, \text{trks})$ . Several unfolding methods are shown. For the Iterative Bayesian Unfolding (IBU) method, only one iteration is used. For the Singular Value Decomposition (SVD) method, the second singular value is used for  $\tau$ . Ratios of the unfolded distributions to the signal truth are shown in the lower panels. The shaded band shows the statistical uncertainty of the  $\gamma\gamma \rightarrow \tau^+\tau^-$  truth sample.

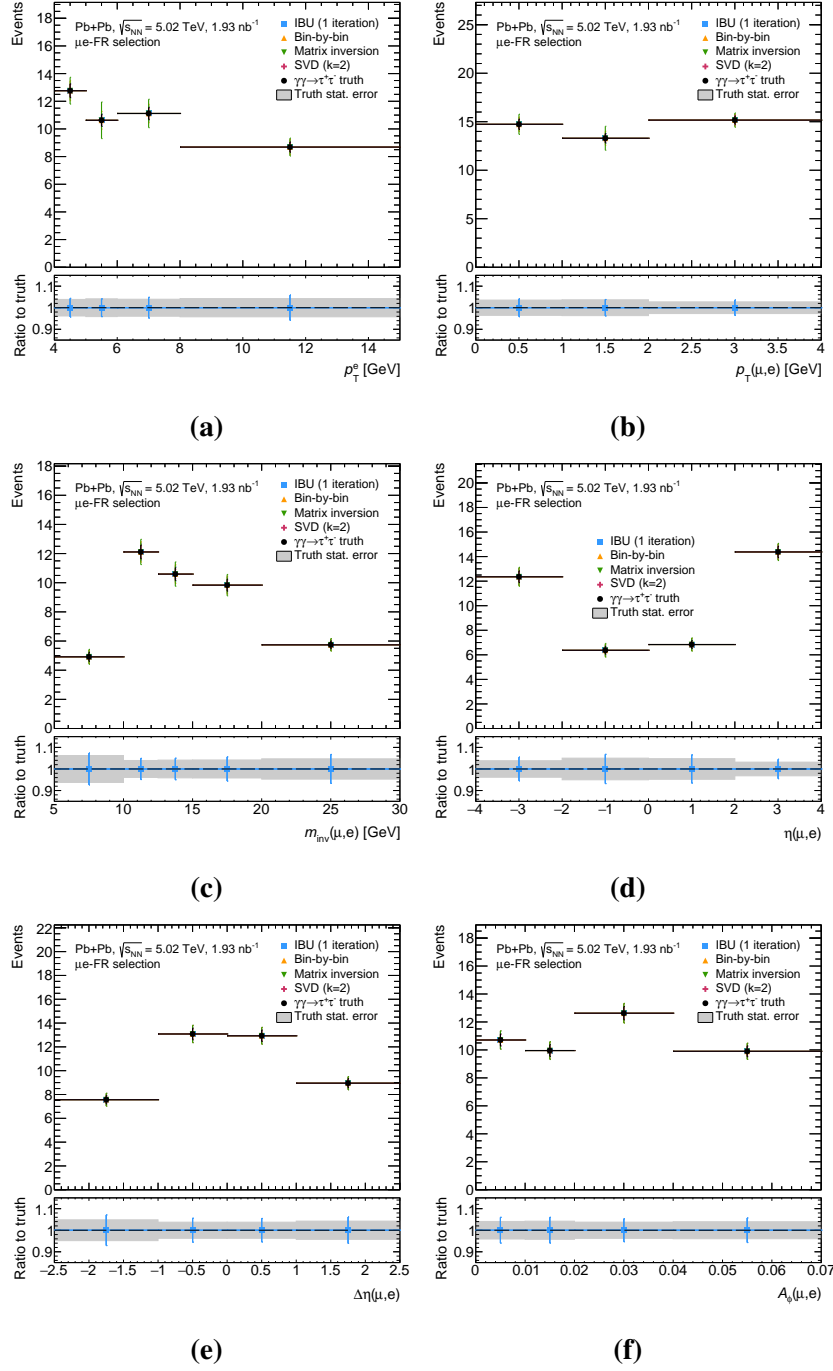


**Figure A.12:** Results of the Monte Carlo closure test for the following kinematic observables in the  $\mu e$ -FR region:  $\mu e$ -SR region: (a)  $p_T^e$ , (b)  $p_T(\mu, e)$ , (c)  $m_{\text{inv}}(\mu, e)$ , (d)  $\eta(\mu, e)$ , (e)  $\Delta\eta(\mu, e)$ , and (f)  $A_\phi(\mu, e)$ . Several unfolding methods are shown. For the Iterative Bayesian Unfolding (IBU) method, only one iteration is used. For the Singular Value Decomposition (SVD) method, the second singular value is used for  $\tau$ . Ratios of the unfolded distributions to the signal truth are shown in the lower panels. The shaded band shows the statistical uncertainty of the  $\gamma\gamma \rightarrow \tau^+\tau^-$  truth sample.

## A.4 Number of iterations for unfolding

The results of the test performed to determine the optimal number of iterations for the unfolding of all kinematic observables of interest are shown in Figs. [A.13](#) to [A.15](#). The test is described in Sec. [5.7.6](#). For ease of presentation, the two types of  $\chi^2$ 's are normalized to their values for  $N_{\text{iter}} = 1$ . The optimal number of iterations for each kinematic observables is marked with an arrow.

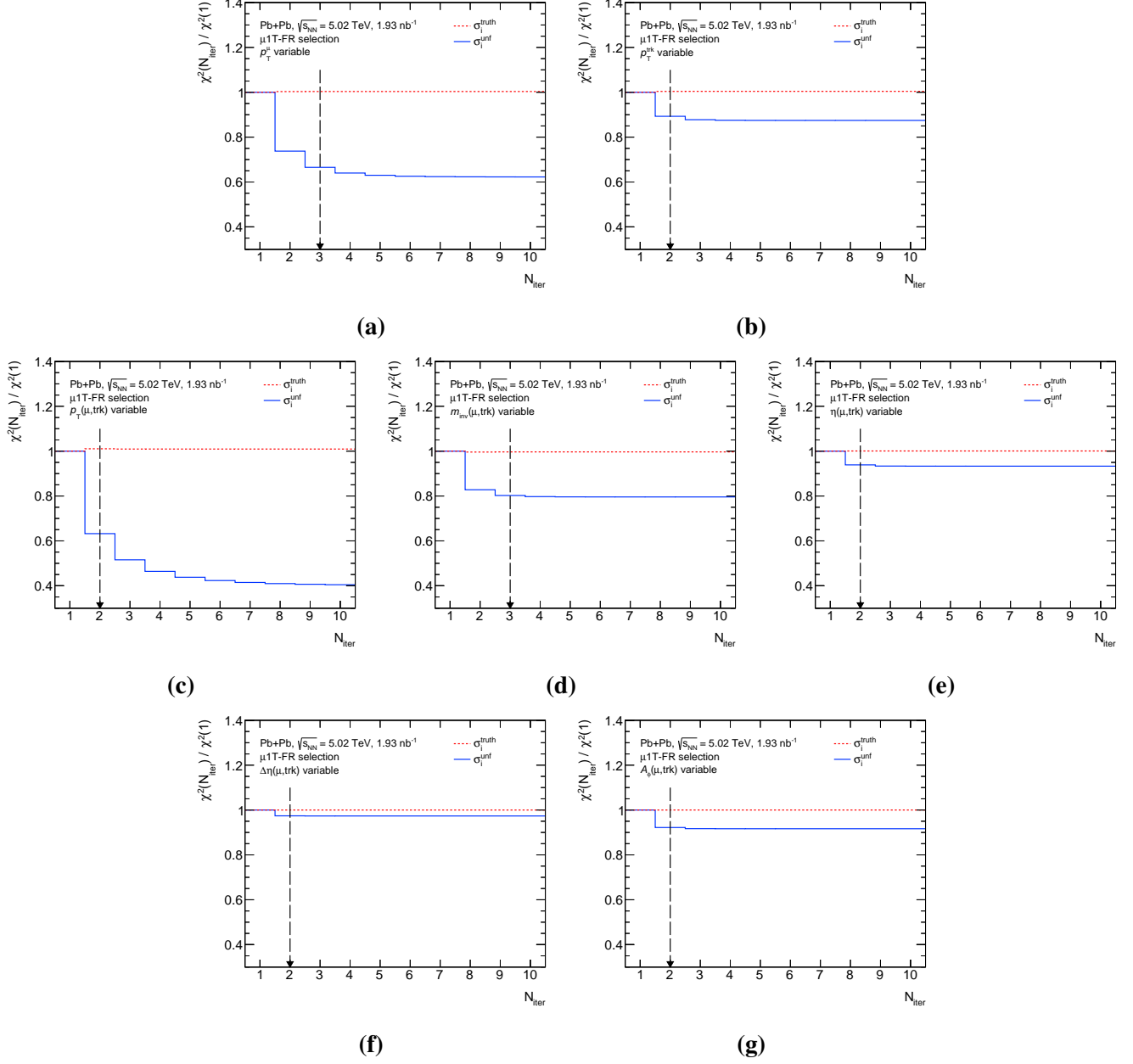


**Figure A.13:** Results of the test performed to determine the optimal number of iterations required for the IBU method, for all kinematic observables in the  $\mu\text{1T-FR}$  region: (a)  $p_T^\mu$ , (b)  $p_T^{\text{trk}}$ , (c)  $p_T(\mu, \text{trk})$ , (d)  $m_{\text{inv}}(\mu, \text{trk})$ , (e)  $\eta(\mu, \text{trk})$ , (f)  $\Delta\eta(\mu, \text{trk})$ , and (g)  $A_\phi(\mu, \text{trk})$ . The two types of  $\chi^2$ 's are shown based on the errors they use, i.e.  $\sigma_i^{\text{truth}}$  vs.  $\sigma_i^{\text{unf}}$ . The optimal number of iterations is marked with an arrow.

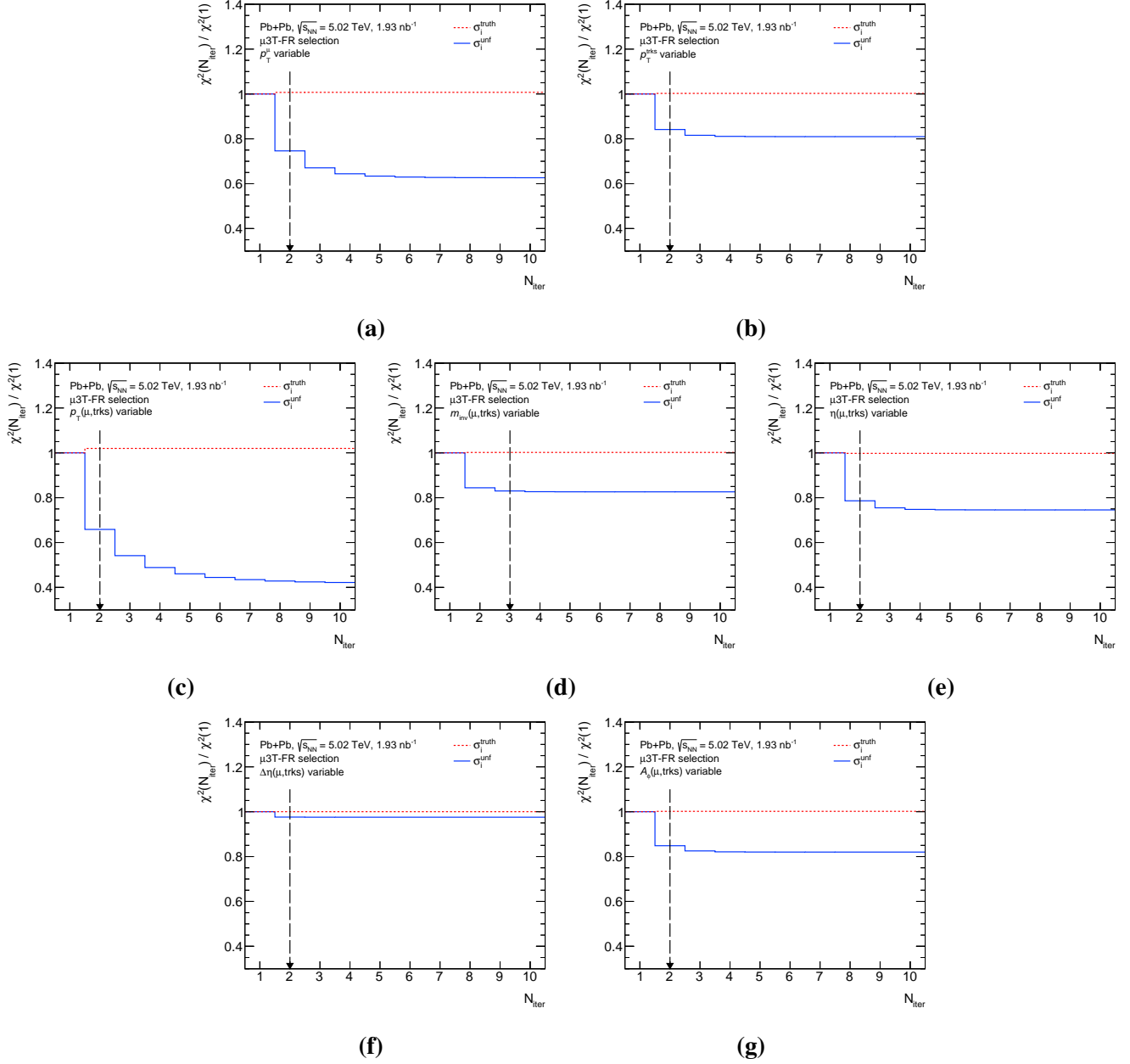


**Figure A.14:** Results of the test performed to determine the optimal number of iterations required for the IBU method, for all kinematic observables in the  $\mu\text{3T-FR}$  region: (a)  $p_T^\mu$ , (b)  $p_T^{\text{trks}}$ , (c)  $p_T(\mu, \text{trks})$ , (d)  $m_{\text{inv}}(\mu, \text{trks})$ , (e)  $\eta(\mu, \text{trks})$ , (f)  $\Delta\eta(\mu, \text{trks})$ , and (g)  $A_\phi(\mu, \text{trks})$ . The two types of  $\chi^2$ 's are shown based on the errors they use, i.e.  $\sigma_i^{\text{truth}}$  vs.  $\sigma_i^{\text{unf}}$ . The optimal number of iterations is marked with an arrow.

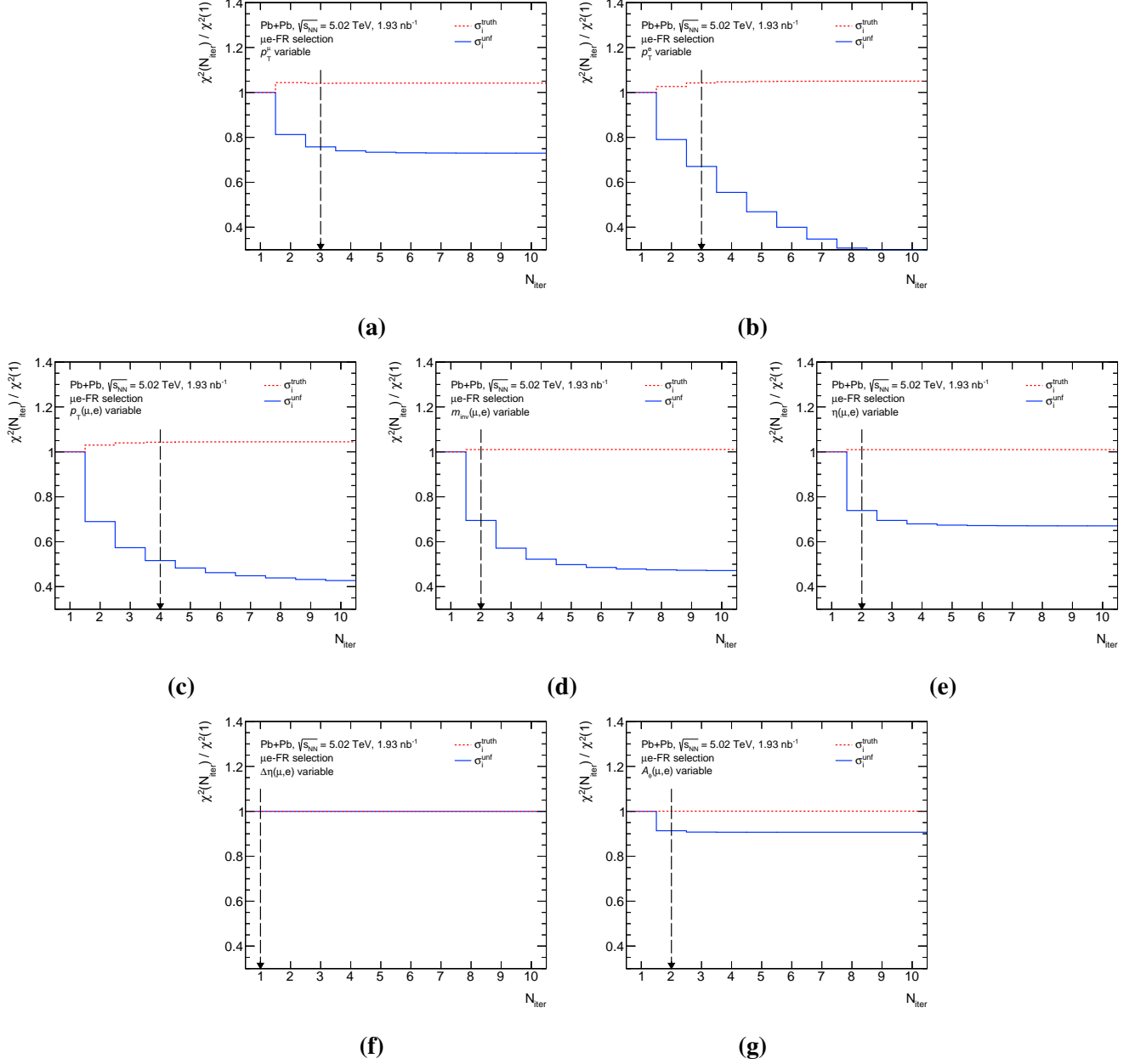


**Figure A.15:** Results of the test performed to determine the optimal number of iterations required for the IBU method, for all kinematic observables in the  $\mu e$ -FR region: (a)  $p_T^\mu$ , (b)  $p_T^e$ , (c)  $p_T(\mu, e)$ , (d)  $m_{\text{inv}}(\mu, e)$ , (e)  $\eta(\mu, e)$ , (f)  $\Delta\eta(\mu, e)$ , and (g)  $A_\phi(\mu, e)$ . The two types of  $\chi^2$ 's are shown based on the errors they use, i.e.  $\sigma_i^{\text{truth}}$  vs.  $\sigma_i^{\text{unf}}$ . The optimal number of iterations is marked with an arrow.

## A.5 Data-driven closure test

The bin-by-bin reweighting factors used in the data-driven closure test, are shown for all kinematic observables in Figs. [A.16](#) to [A.18](#). The bin-by-bin unfolding bias for all kinematic observables are shown in Figs. [A.19](#) to [A.21](#).



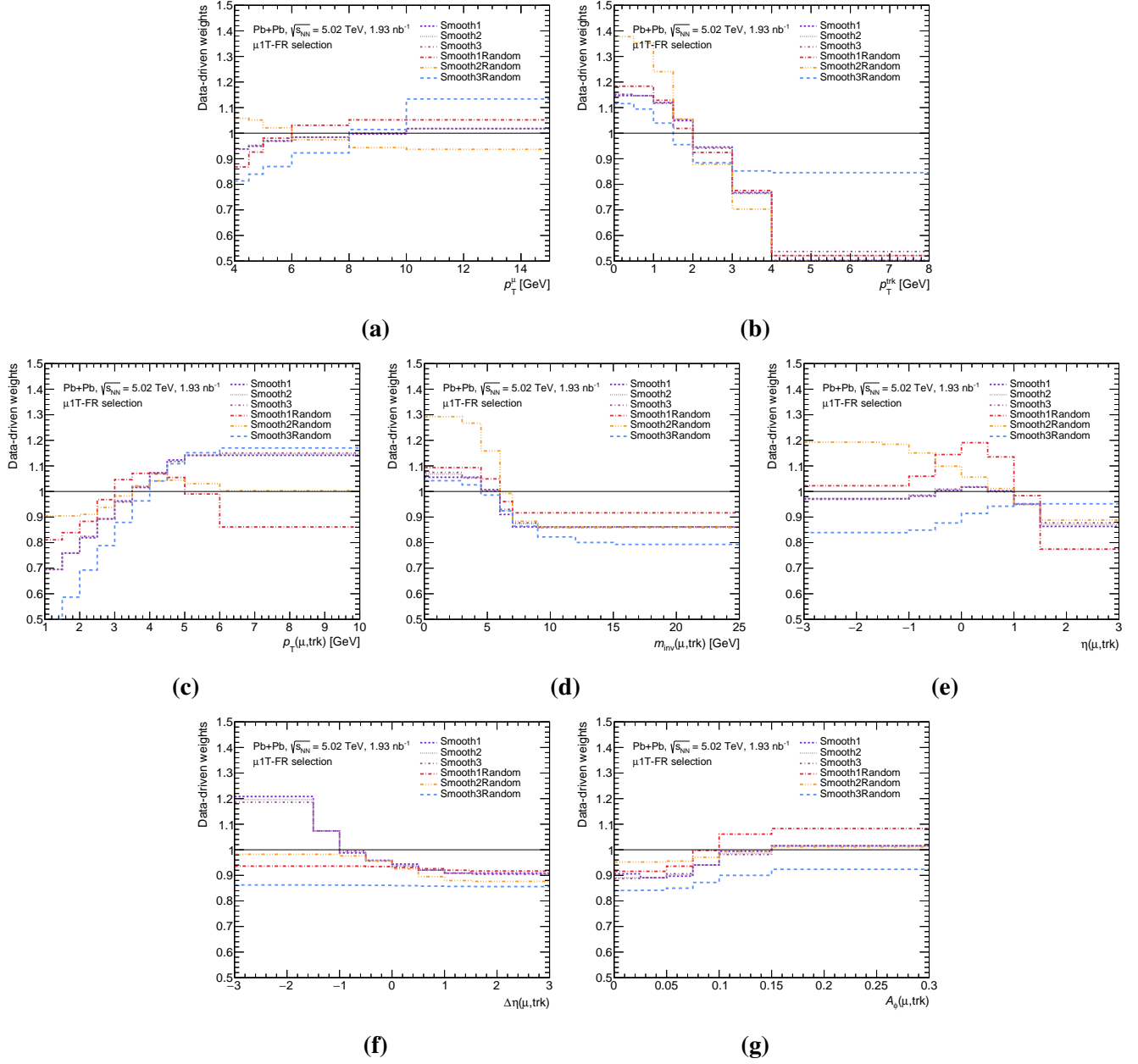


**Figure A.16:** Reweighting factor per unfolded bin, for all kinematic observables in the  $\mu 1\text{T-FR}$  region: (a)  $p_T^\mu$ , (b)  $p_T^{\text{trk}}$ , (c)  $p_T(\mu, \text{trk})$ , (d)  $m_{\text{inv}}(\mu, \text{trk})$ , (e)  $\eta(\mu, \text{trk})$ , (f)  $\Delta\eta(\mu, \text{trk})$ , and (g)  $A_\phi(\mu, \text{trk})$ . The weights are shown for all smoothing strategies.

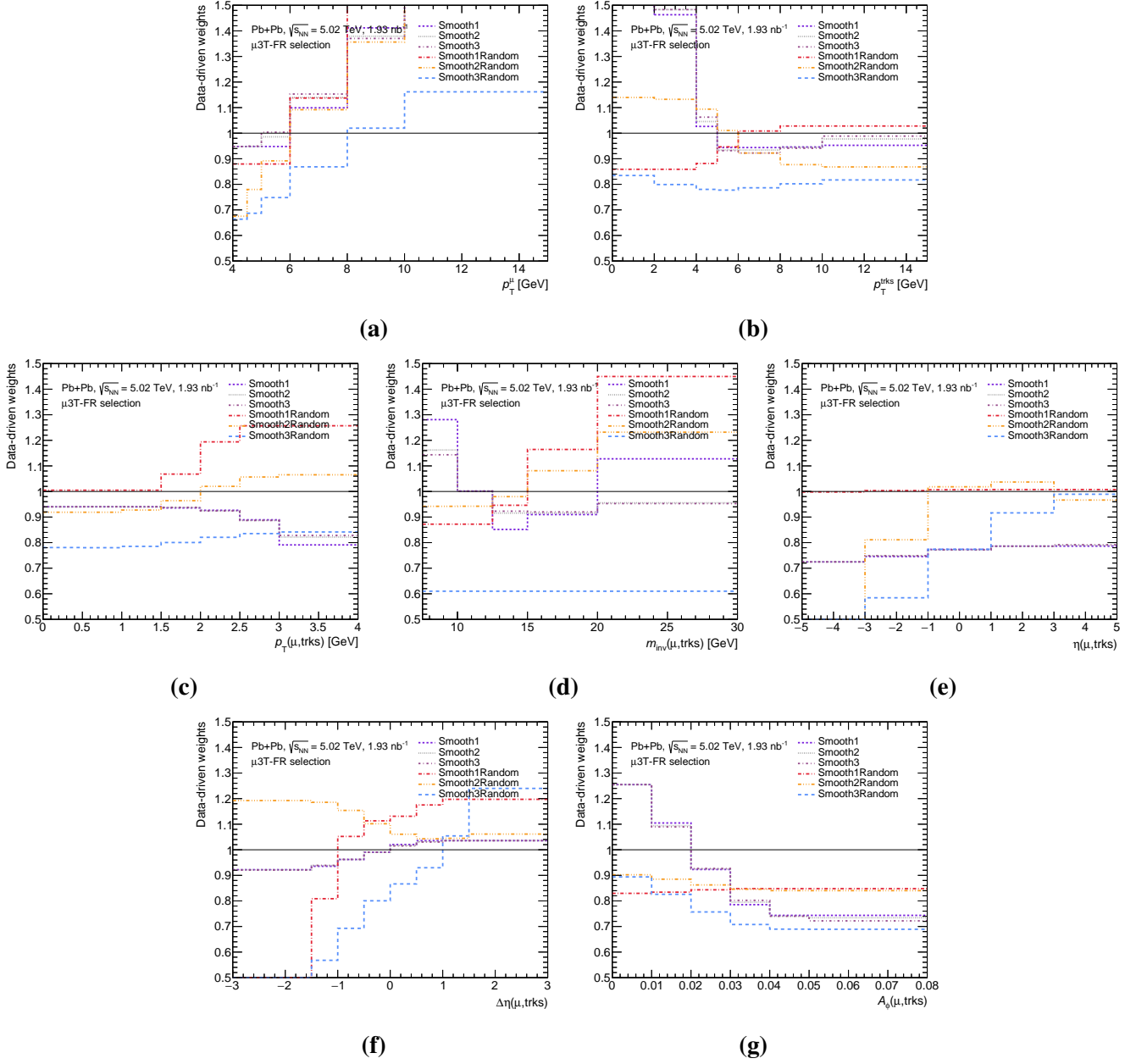


**Figure A.17:** Reweighting factor per unfolded bin, for all kinematic observables in the  $\mu 3\text{T-FR}$  region: (a)  $p_T^\mu$ , (b)  $p_T^{\text{trks}}$ , (c)  $p_T(\mu, \text{trks})$ , (d)  $m_{\text{inv}}(\mu, \text{trks})$ , (e)  $\eta(\mu, \text{trks})$ , (f)  $\Delta\eta(\mu, \text{trks})$ , and (g)  $A_\phi(\mu, \text{trks})$ . The weights are shown for all smoothing strategies.

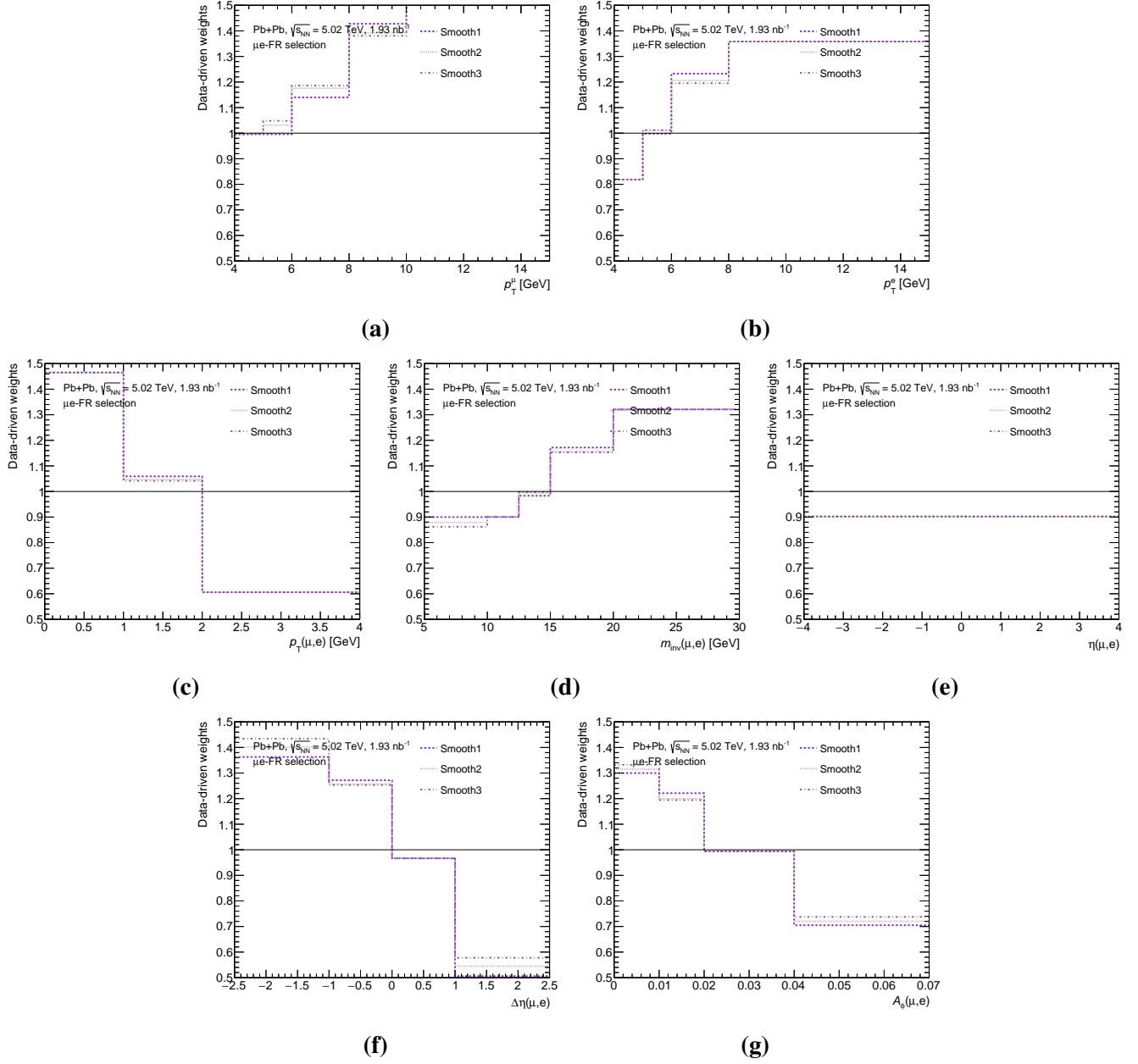


**Figure A.18:** Reweighting factor per unfolded bin, for all kinematic observables in the  $\mu e$ -FR region: (a)  $p_T^\mu$ , (b)  $p_T^e$ , (c)  $p_T(\mu, e)$ , (d)  $m_{\text{inv}}(\mu, e)$ , (e)  $\eta(\mu, e)$ , (f)  $\Delta\eta(\mu, e)$ , and (g)  $A_\phi(\mu, e)$ . The weights are shown for all smoothing strategies.

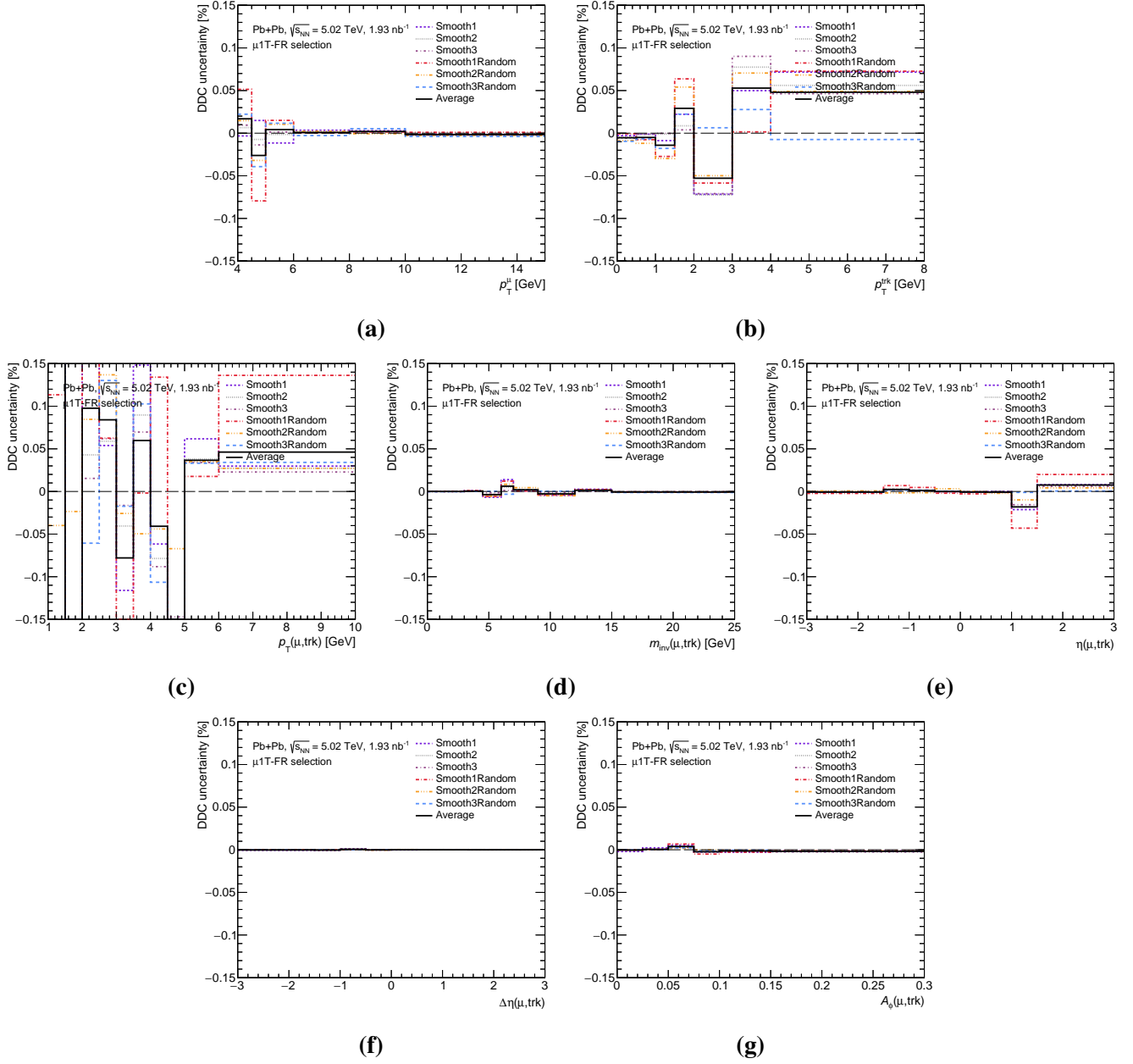


**Figure A.19:** Unfolding bias (in percent) for all kinematic observables in the  $\mu$ 1T-FR region: (a)  $p_T^\mu$ , (b)  $p_T^{\text{trk}}$ , (c)  $p_T(\mu, \text{trk})$ , (d)  $m_{\text{inv}}(\mu, \text{trk})$ , (e)  $\eta(\mu, \text{trk})$ , (f)  $\Delta\eta(\mu, \text{trk})$ , and (g)  $A_\phi(\mu, \text{trk})$ . The bias for all smoothing strategies is shown, along with the average over all strategies.

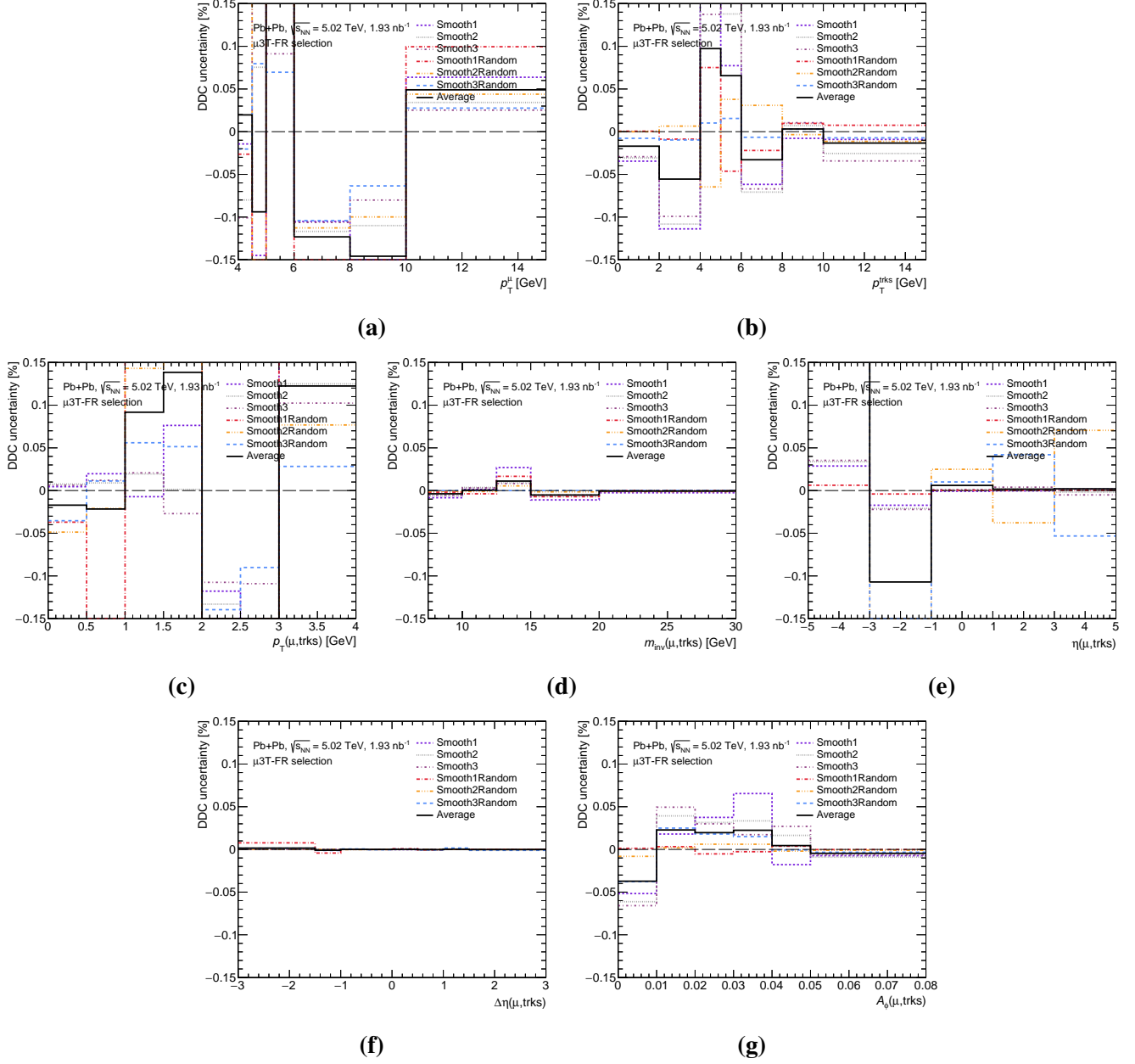


**Figure A.20:** Unfolding bias (in percent) for all kinematic observables in the  $\mu 3\text{T-FR}$  region: (a)  $p_T^\mu$ , (b)  $p_T^{\text{trks}}$ , (c)  $p_T(\mu, \text{trks})$ , (d)  $m_{\text{inv}}(\mu, \text{trks})$ , (e)  $\eta(\mu, \text{trks})$ , (f)  $\Delta\eta(\mu, \text{trks})$ , and (g)  $A_\phi(\mu, \text{trks})$ . The bias for all smoothing strategies is shown, along with the average over all strategies.

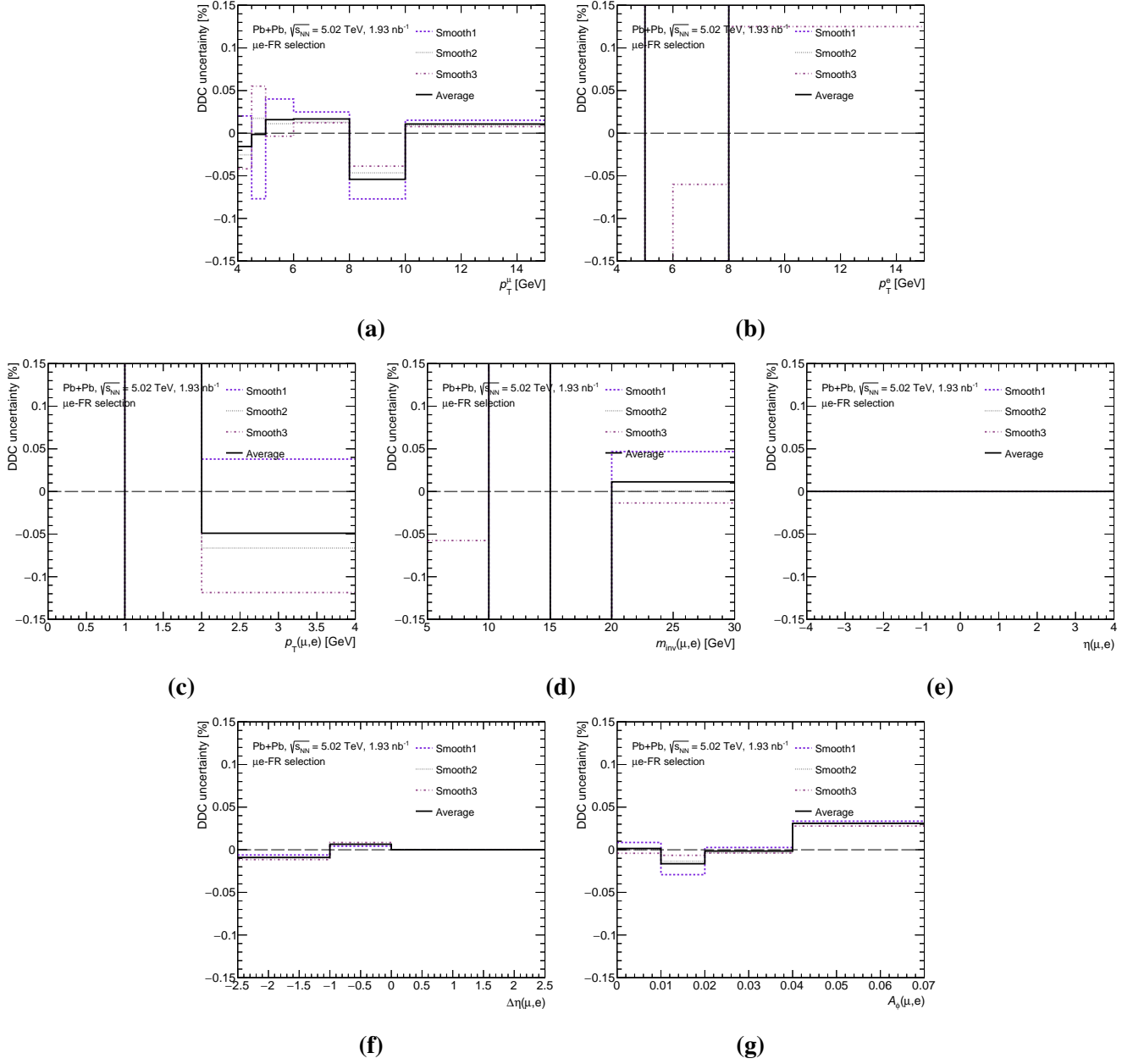


**Figure A.21:** Unfolding bias (in percent) for all kinematic observables in the  $\mu e$ -FR region: (a)  $p_T^\mu$ , (b)  $p_T^e$ , (c)  $p_T(\mu, e)$ , (d)  $m_{inv}(\mu, e)$ , (e)  $\eta(\mu, e)$ , (f)  $\Delta\eta(\mu, e)$ , and (g)  $A_\phi(\mu, e)$ . The bias for all smoothing strategies is shown, along with the average over all strategies.

## A.6 Impact of tau lepton EMDM's on truth-level observables

The impact of  $F_2^0$  (i.e. the tau lepton anomalous magnetic dipole moment) on the truth-level cross-sections for all kinematic observables of interest are shown in Figs. [A.22](#) to [A.24](#). The impact of  $F_3^0$  (i.e. the tau lepton electric dipole moment) are shown in Figs. [A.25](#) to [A.27](#). In these figures, the predictions are shown together with the data errors, as the analysis is blinded.

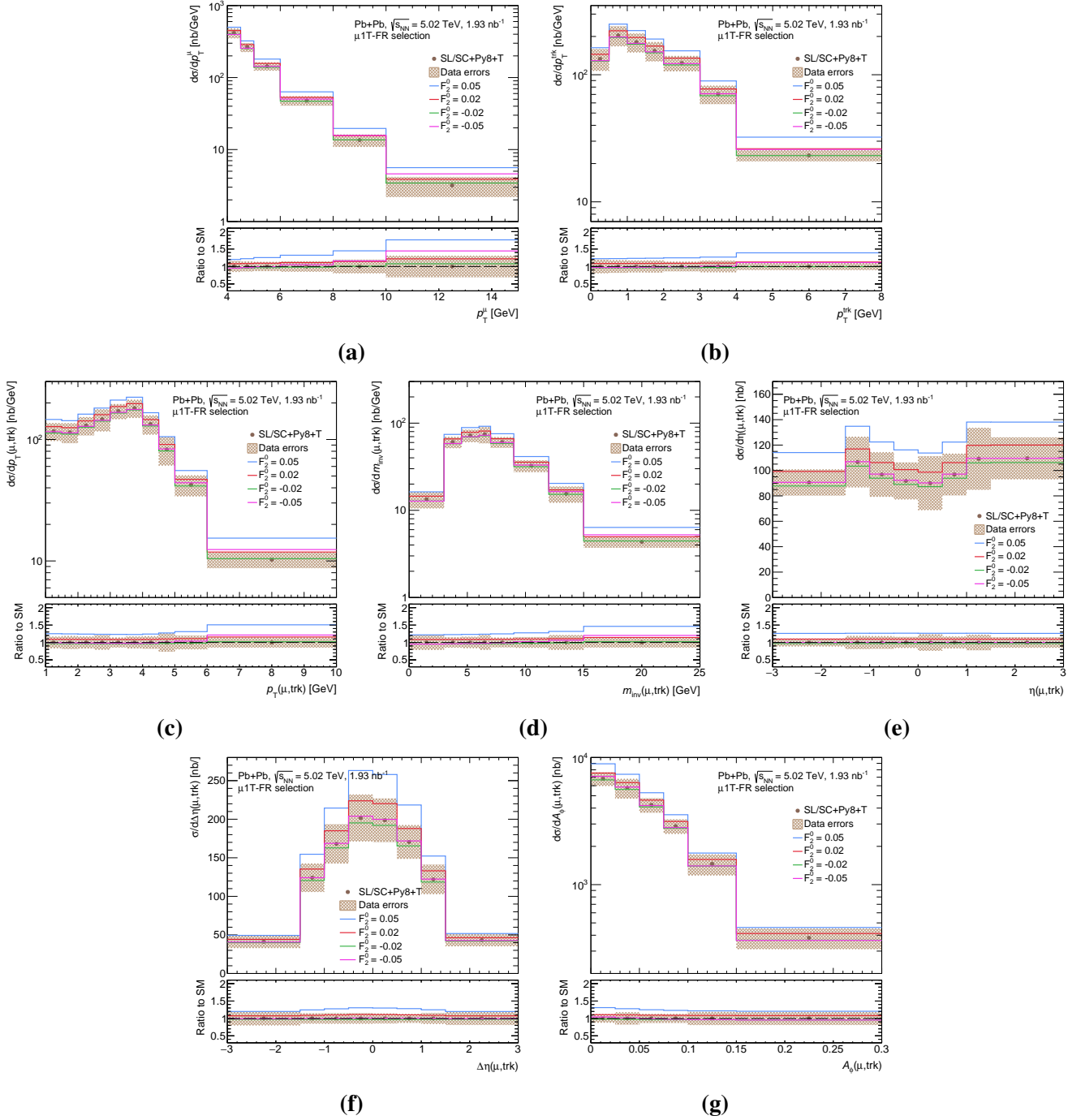


**Figure A.22:** Sensitivity to  $F_2^0$  for all kinematic observables in the  $\mu 1\text{T-FR}$  region: (a)  $p_T^\mu$ , (b)  $p_T^{\text{trk}}$ , (c)  $p_T(\mu, \text{trk})$ , (d)  $m_{\text{inv}}(\mu, \text{trk})$ , (e)  $\eta(\mu, \text{trk})$ , (f)  $\Delta\eta(\mu, \text{trk})$ , and (g)  $A_\phi(\mu, \text{trk})$ . The SM prediction corresponding to the SL/SC+Py8+T sample is shown with brown markers, with the total systematic uncertainty of the measured cross-sections in the shaded bands. Predictions are shown for  $F_2^0 = \pm 0.02, \pm 0.05$ , along with the corresponding ratios to the SM predictions in the lower panels.



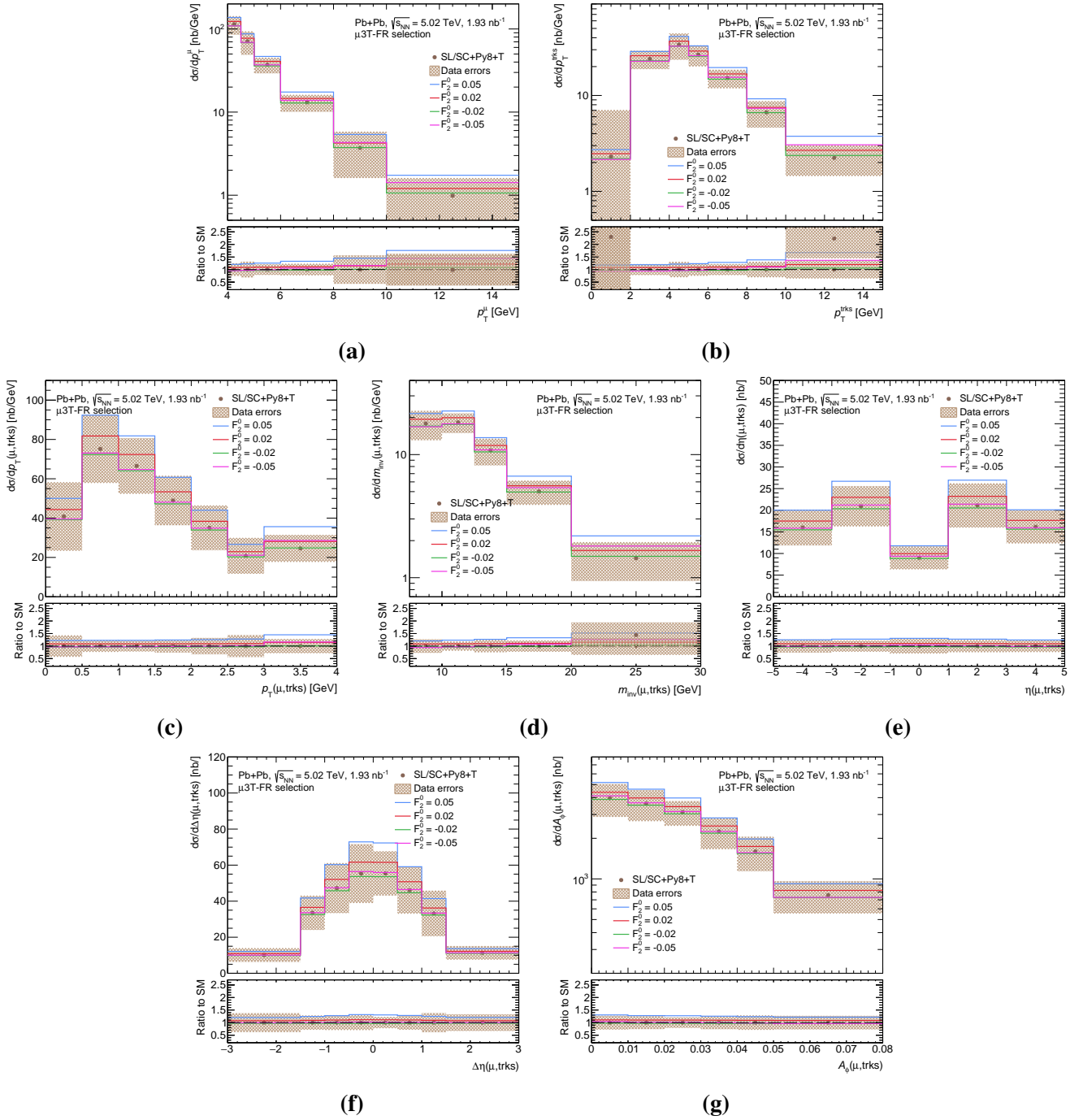


**Figure A.23:** Sensitivity to  $F_2^0$  for all kinematic observables in the  $\mu 3T$ -FR region: (a)  $p_T^\mu$ , (b)  $p_T^{\text{trks}}$ , (c)  $p_T(\mu, \text{trks})$ , (d)  $m_{\text{inv}}(\mu, \text{trks})$ , (e)  $\eta(\mu, \text{trks})$ , (f)  $\Delta\eta(\mu, \text{trks})$ , and (g)  $A_\phi(\mu, \text{trks})$ . The SM prediction corresponding to the SL/SC+Py8+T sample is shown with brown markers, with the total systematic uncertainty of the measured cross-sections in the shaded bands. Predictions are shown for  $F_2^0 = \pm 0.02, \pm 0.05$ , along with the corresponding ratios to the SM predictions in the lower panels.

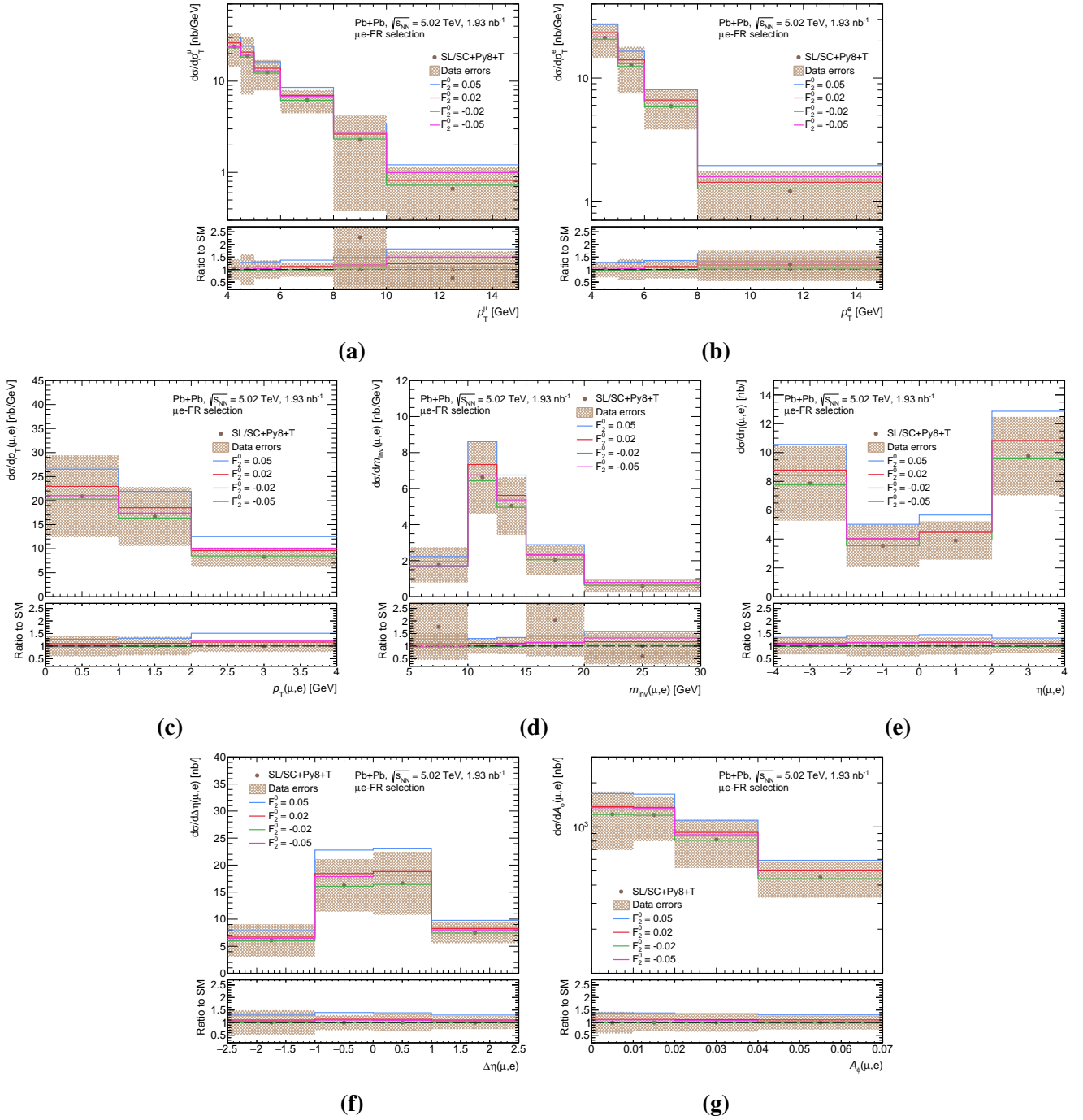


**Figure A.24:** Sensitivity to  $F_2^0$  for all kinematic observables in the  $\mu e$ -FR region: (a)  $p_T^\mu$ , (b)  $p_T^e$ , (c)  $p_T(\mu, e)$ , (d)  $m_{\text{inv}}(\mu, e)$ , (e)  $\eta(\mu, e)$ , (f)  $\Delta\eta(\mu, e)$ , and (g)  $A_\phi(\mu, e)$ . The SM prediction corresponding to the SL/SC+Py8+T sample is shown with brown markers, with the total systematic uncertainty of the measured cross-sections in the shaded bands. Predictions are shown for  $F_2^0 = \pm 0.02, \pm 0.05$ , along with the corresponding ratios to the SM predictions in the lower panels.

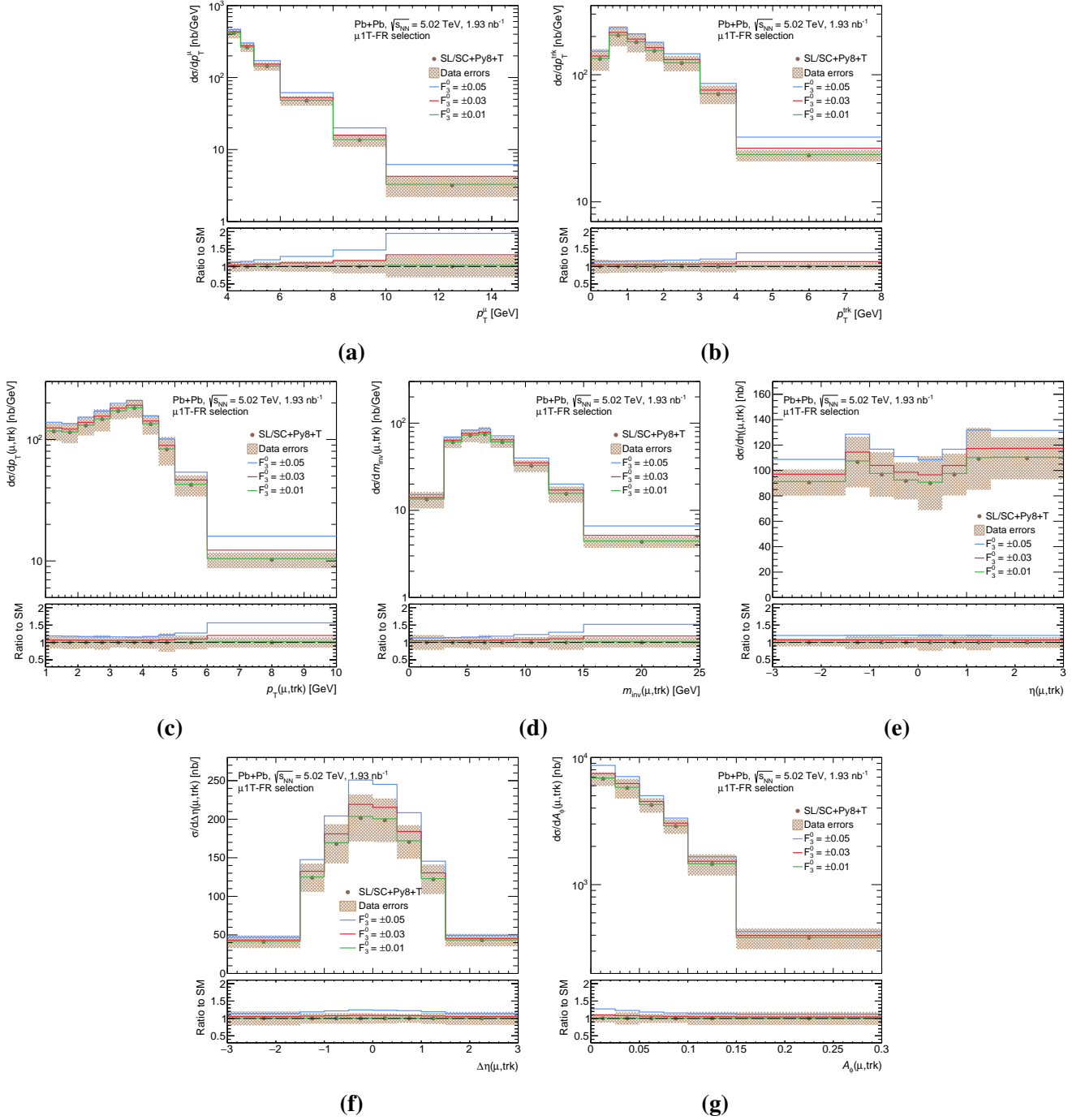


**Figure A.25:** Sensitivity to  $F_3^0$  for all kinematic observables in the  $\mu 1\text{T-FR}$  region: (a)  $p_T^\mu$ , (b)  $p_T^{\text{trk}}$ , (c)  $p_T(\mu, \text{trk})$ , (d)  $m_{\text{inv}}(\mu, \text{trk})$ , (e)  $\eta(\mu, \text{trk})$ , (f)  $\Delta\eta(\mu, \text{trk})$ , and (g)  $A_\phi(\mu, \text{trk})$ . The SM prediction corresponding to the SL/SC+Py8+T sample is shown with brown markers, with the total systematic uncertainty of the measured cross-sections in the shaded bands. Predictions are shown for  $F_3^0 = \pm 0.01, \pm 0.03, \pm 0.05$ , along with the corresponding ratios to the SM predictions in the lower panels.

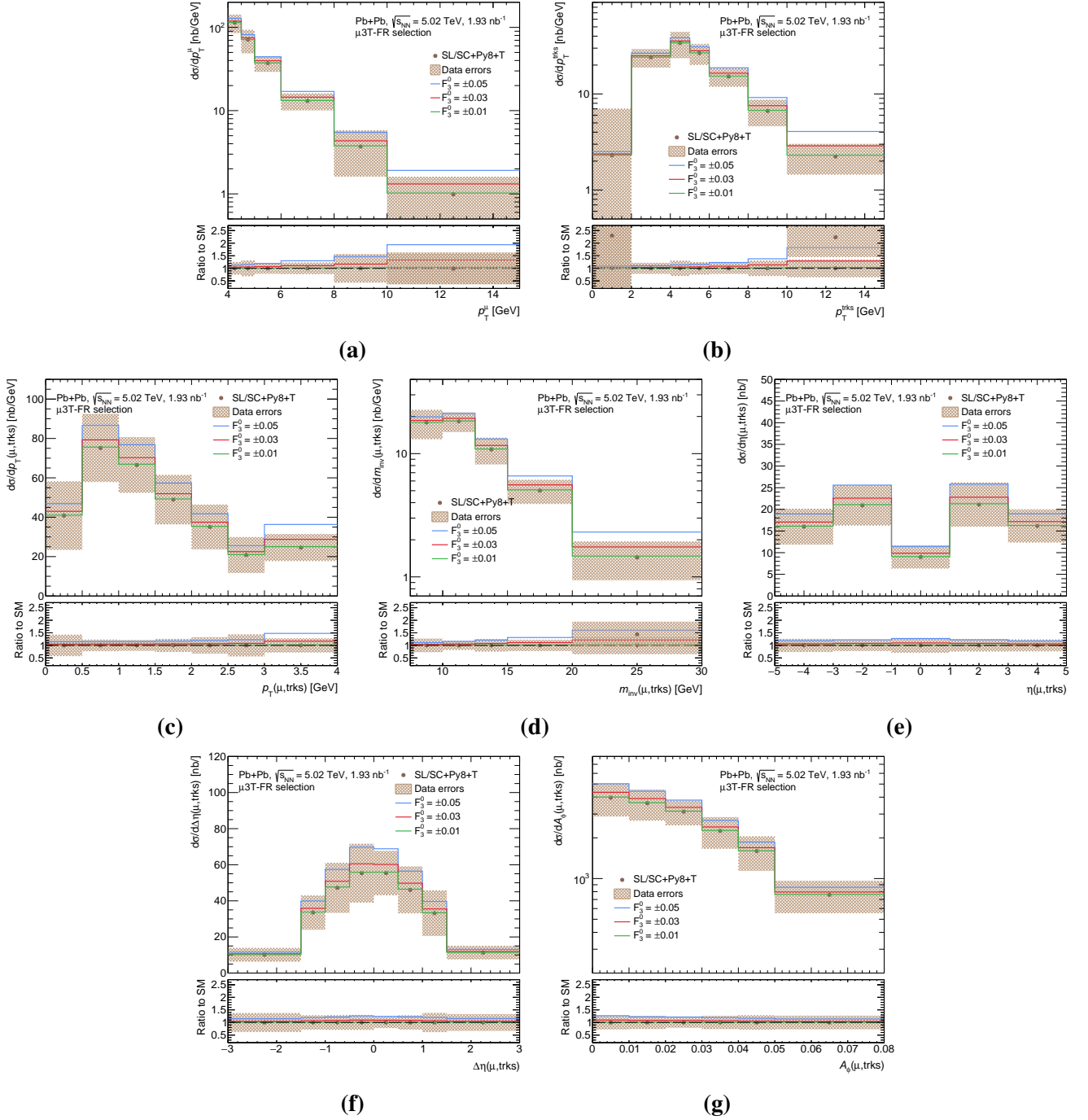


**Figure A.26:** Sensitivity to  $F_3^0$  for all kinematic observables in the  $\mu 3T$ -FR region: (a)  $p_T^\mu$ , (b)  $p_T^{\text{trks}}$ , (c)  $p_T(\mu, \text{trks})$ , (d)  $m_{\text{inv}}(\mu, \text{trks})$ , (e)  $\eta(\mu, \text{trks})$ , (f)  $\Delta\eta(\mu, \text{trks})$ , and (g)  $A_\phi(\mu, \text{trks})$ . The SM prediction corresponding to the SL/SC+Py8+T sample is shown with brown markers, with the total systematic uncertainty of the measured cross-sections in the shaded bands. Predictions are shown for  $F_3^0 = \pm 0.01, \pm 0.03, \pm 0.05$ , along with the corresponding ratios to the SM predictions in the lower panels.

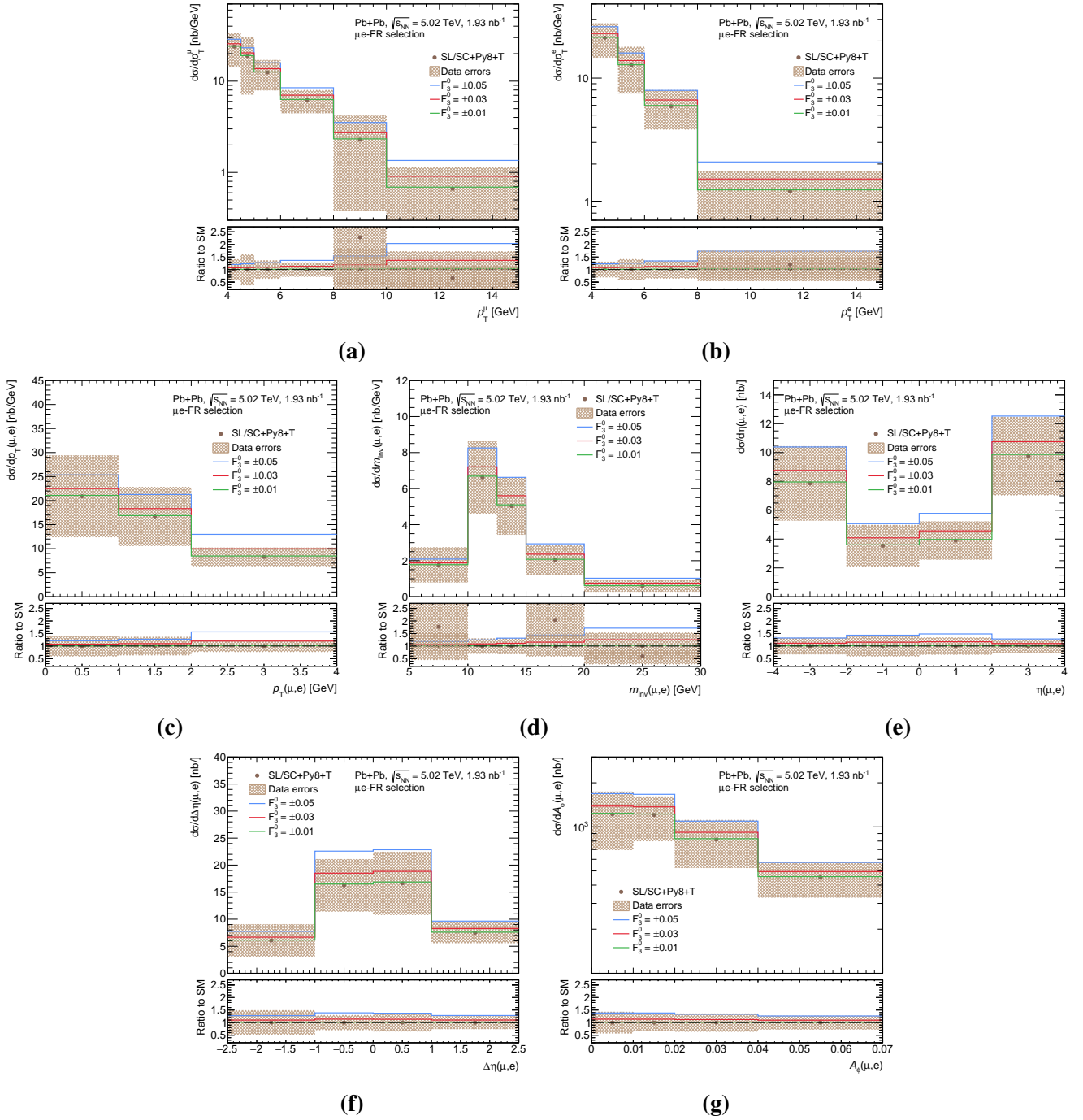


**Figure A.27:** Sensitivity to  $F_3^0$  for all kinematic observables in the  $\mu e$ -FR region: (a)  $p_T^\mu$ , (b)  $p_T^e$ , (c)  $p_T(\mu, e)$ , (d)  $m_{\text{inv}}(\mu, e)$ , (e)  $\eta(\mu, e)$ , (f)  $\Delta\eta(\mu, e)$ , and (g)  $A_\phi(\mu, e)$ . The SM prediction corresponding to the SL/SC+Py8+T sample is shown with brown markers, with the total systematic uncertainty of the measured cross-sections in the shaded bands. Predictions are shown for  $F_3^0 = \pm 0.01, \pm 0.03, \pm 0.05$ , along with the corresponding ratios to the SM predictions in the lower panels.

## A.7 Fit diagnostics for $a_\tau$ extraction

The nuisance parameter impacts and pulls obtained in the fits for  $F_2^0$  to the  $\gamma\gamma \rightarrow \tau^+\tau^-$  fiducial differential cross-sections are shown in Figs. A.28 to A.31 for the global,  $\mu 1$ T-FR,  $\mu 3$ T-FR and  $\mu e$ -FR fits respectively.

The composition of the figures is as follows. For each labelled nuisance parameter, the pre-fit and post-fit impacts are shown in open and filled bars respectively. The up- and down-variations of the impacts are shown in orange and blue respectively. The impacts correspond to the lower horizontal axis. The pulls of the nuisance parameters are shown with black markers and lines, and correspond to the upper horizontal axis. The grid lines are associated with the pulls-axis, rather than the impacts-axis. The nuisance parameters are ordered by the decreasing length of their post-fit impacts.

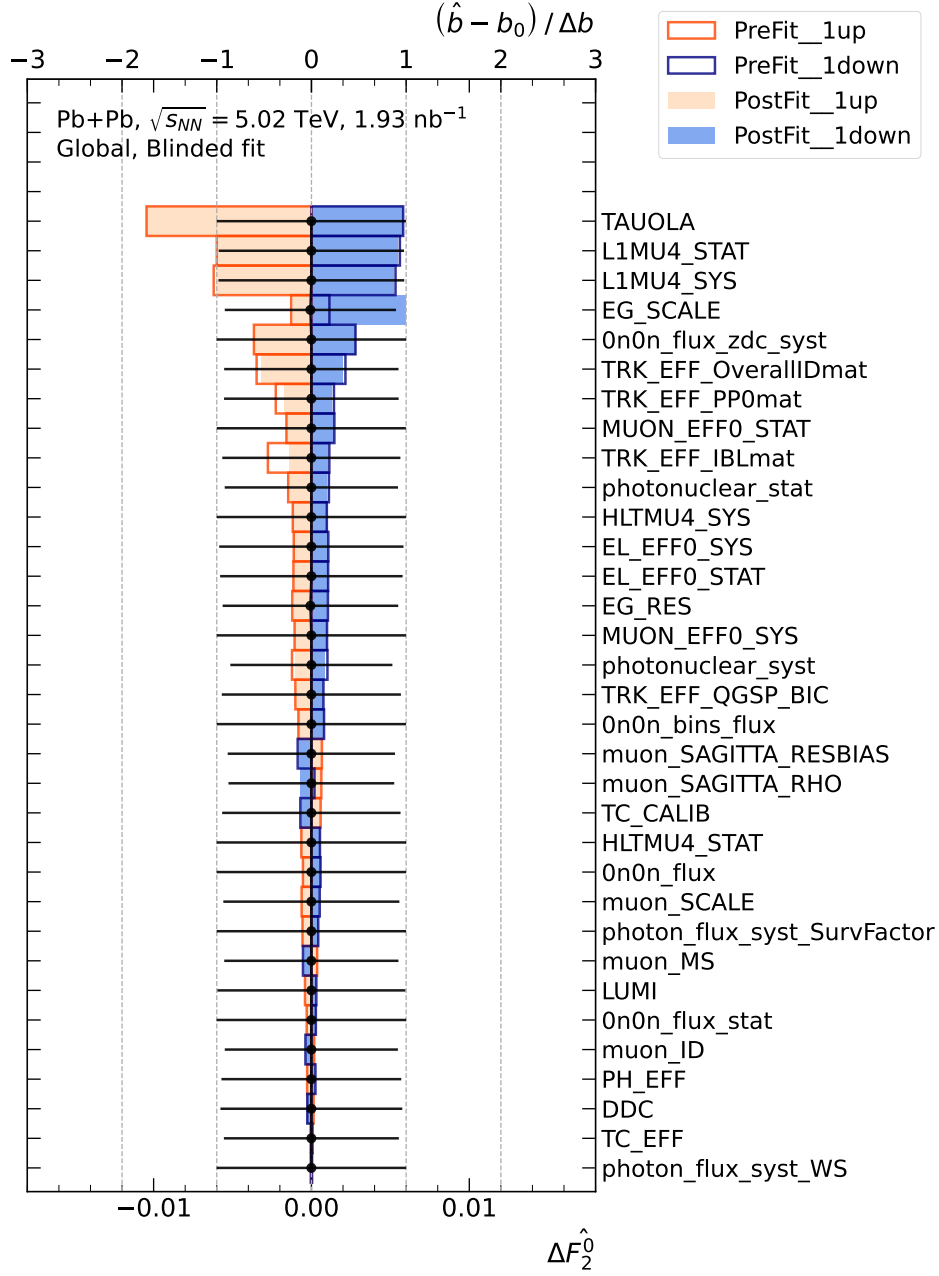


**Figure A.28:** Nuisance parameter impacts and pulls, in the fit for  $F_2^0$  using global data. The composition of the figure is explained in App. A.7.



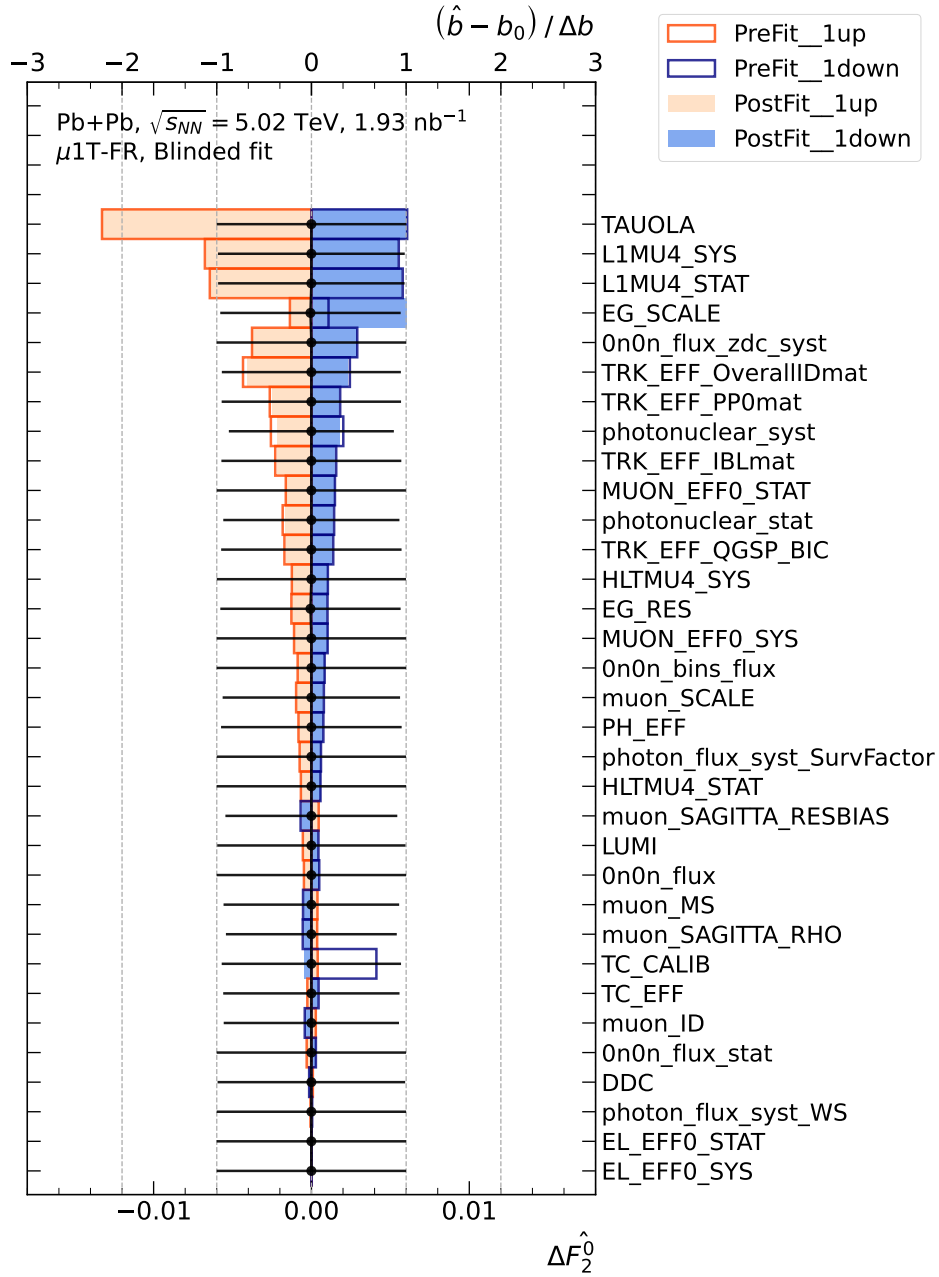


**Figure A.29:** Nuisance parameter impacts and pulls, in the fit for  $F_2^0$  using  $\mu 1T$ -FR data. The composition of the figure is explained in App. A.7.



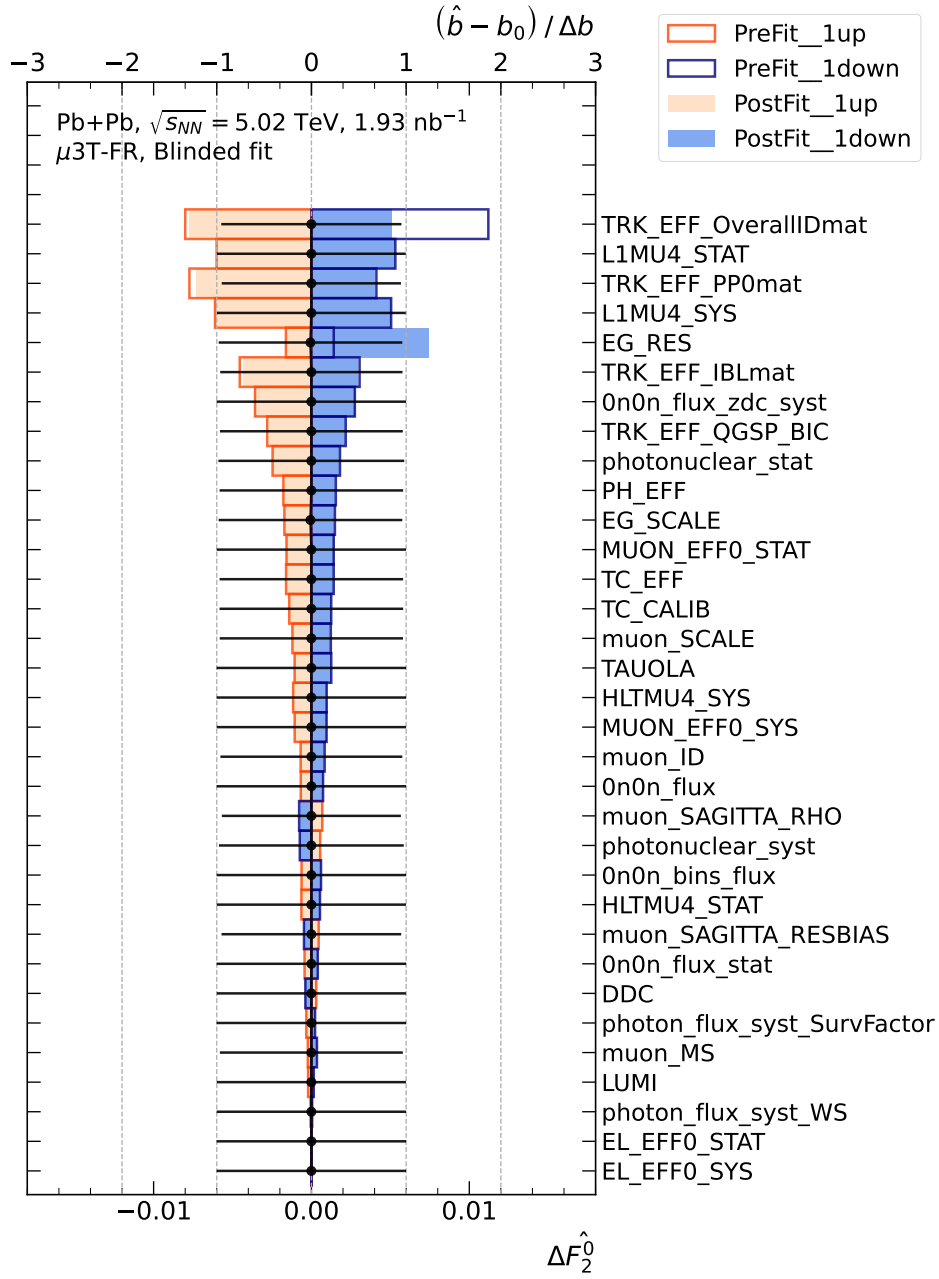


**Figure A.30:** Nuisance parameter impacts and pulls, in the fit for  $F_2^0$  using  $\mu 3\text{T-FR}$  data. The composition of the figure is explained in App. A.7.

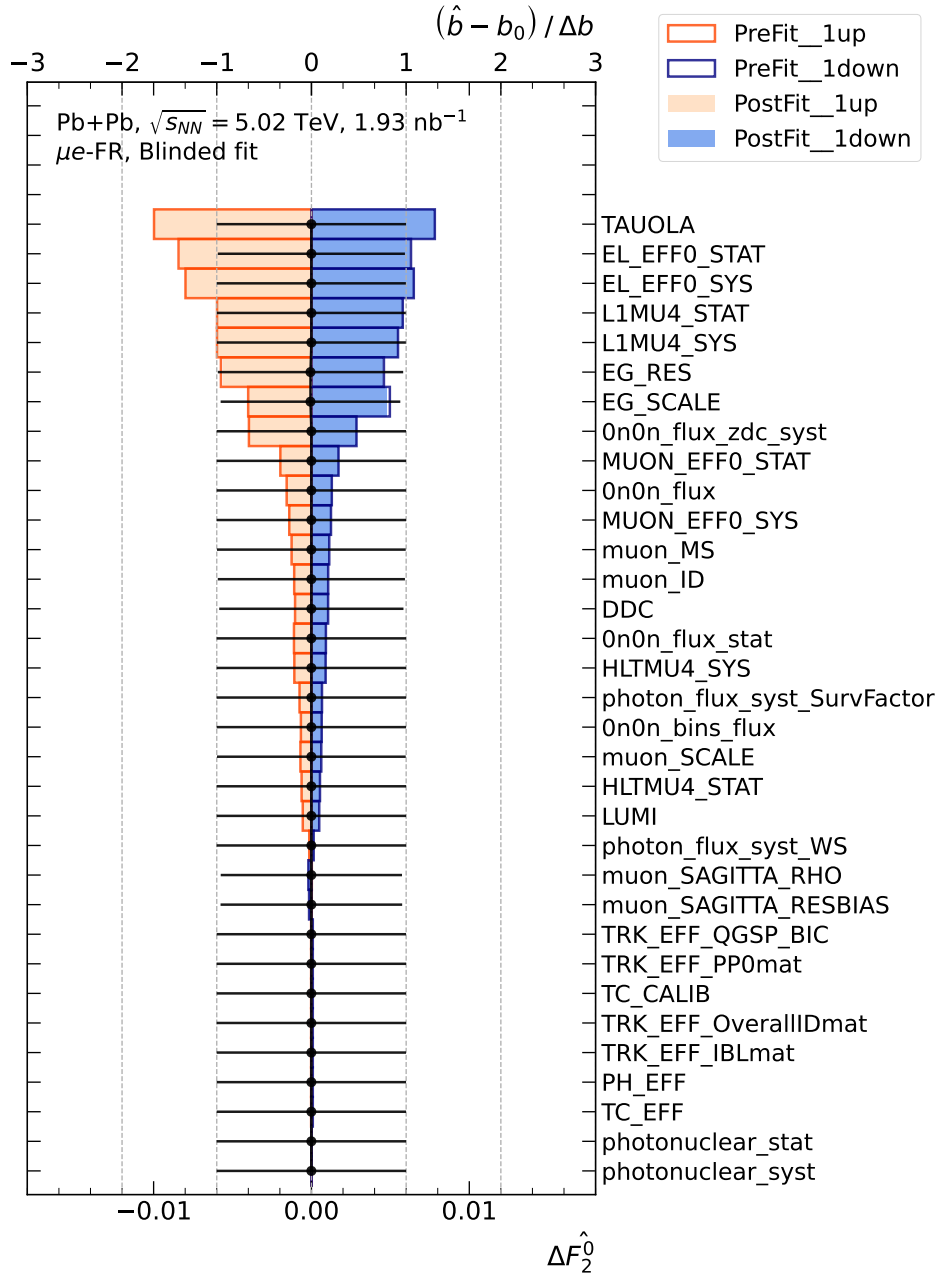


**Figure A.31:** Nuisance parameter impacts and pulls, in the fit for  $F_2^0$  using  $\mu e$ -FR data. The composition of the figure is explained in App. A.7.

## A.8 Fit diagnostics for $d_\tau$ extraction

The nuisance parameter impacts and pulls obtained in the fits for  $F_3^0$  to the  $\gamma\gamma \rightarrow \tau^+\tau^-$  fiducial differential cross-sections are shown in Figs. [A.32](#) to [A.35](#) for the global,  $\mu 1$ T-FR,  $\mu 3$ T-FR and  $\mu e$ -FR fits respectively.

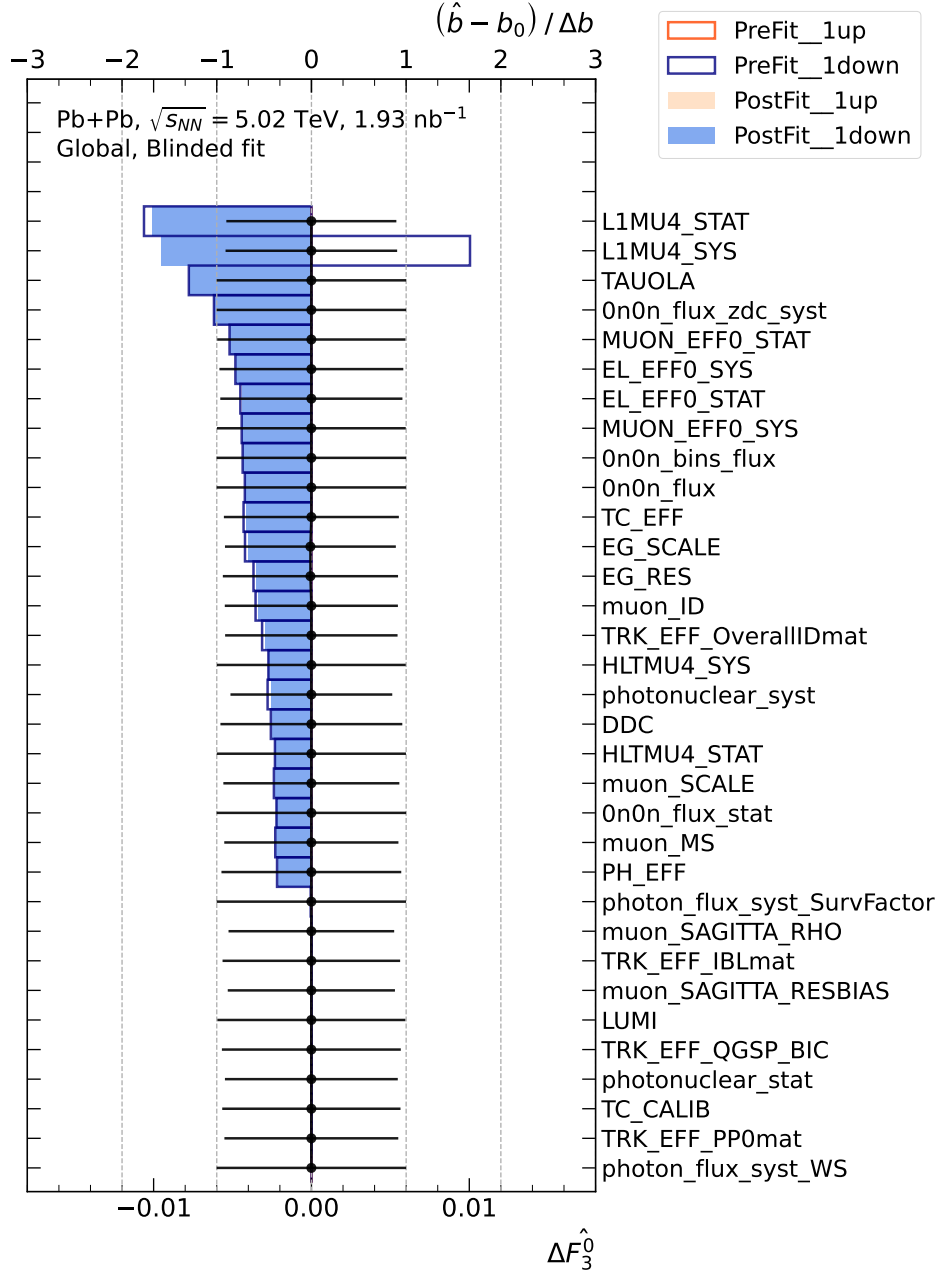


**Figure A.32:** Nuisance parameter impacts and pulls, in the fit for  $F_3^0$  using global data. The composition of the figure is explained in App. A.7.

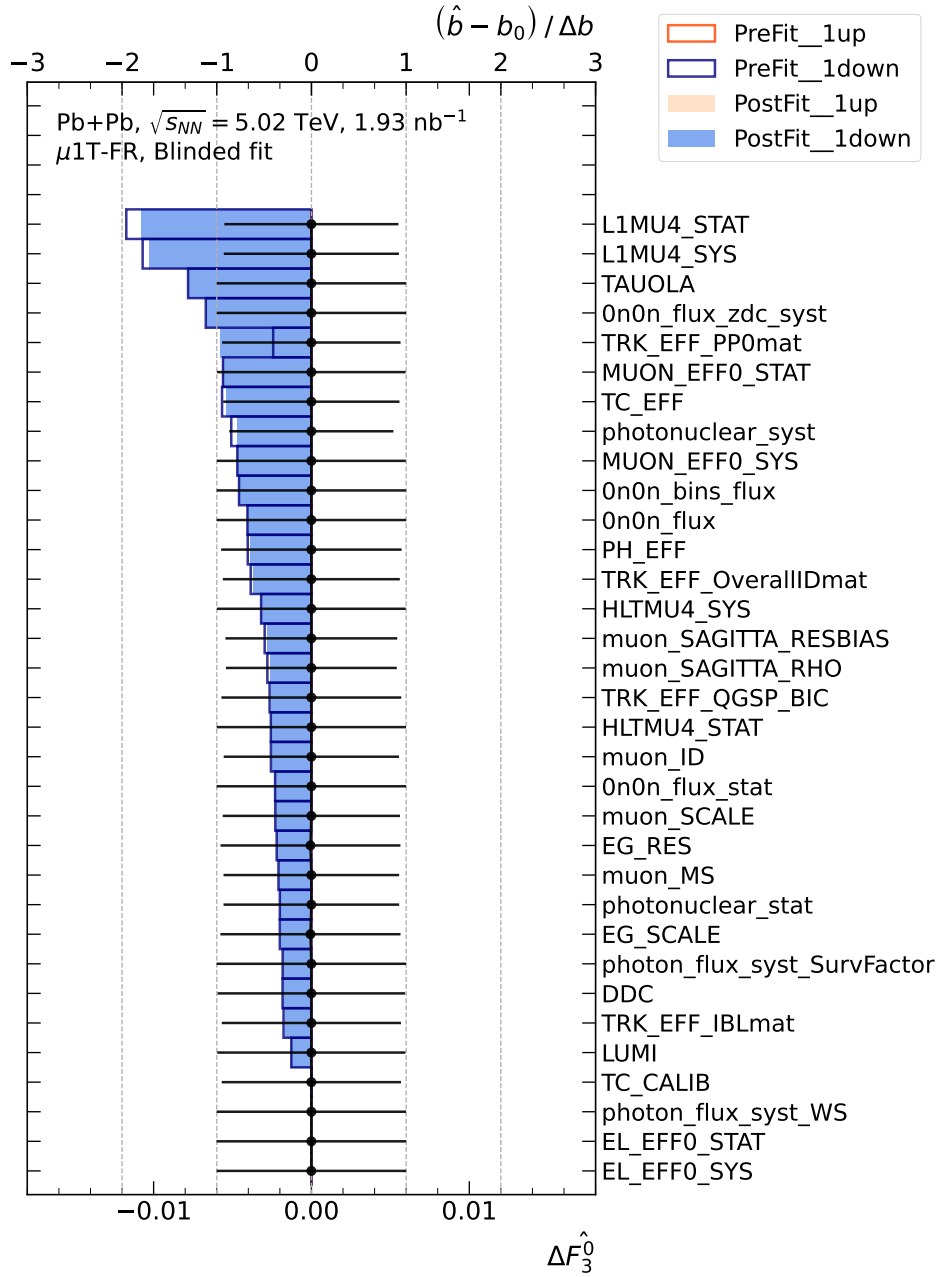


**Figure A.33:** Nuisance parameter impacts and pulls, in the fit for  $F_3^0$  using  $\mu 1\text{T-FR}$  data. The composition of the figure is explained in App. A.7.

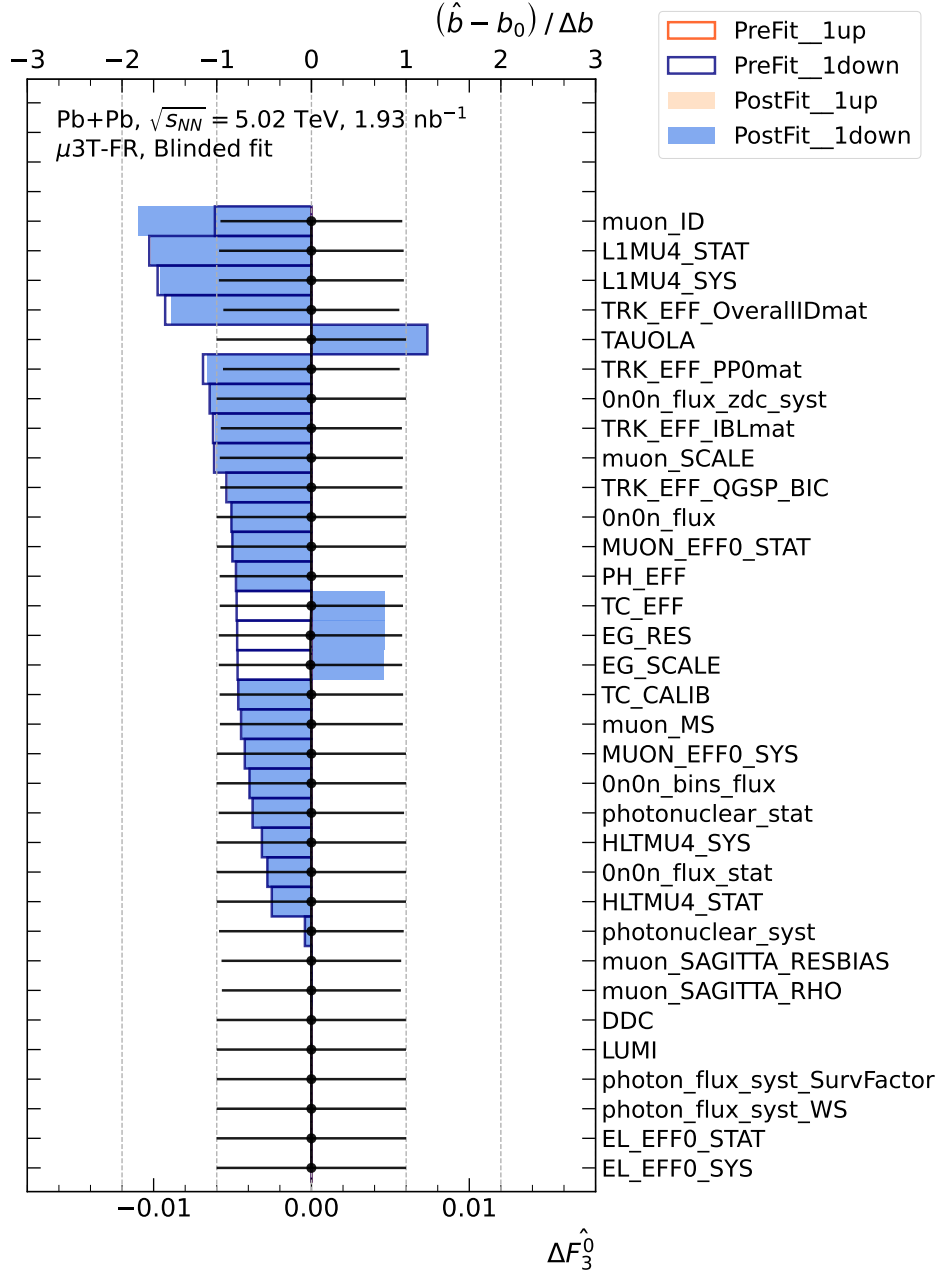


**Figure A.34:** Nuisance parameter impacts and pulls, in the fit for  $F_3^0$  using  $\mu 3\text{T-FR}$  data. The composition of the figure is explained in App. A.7.

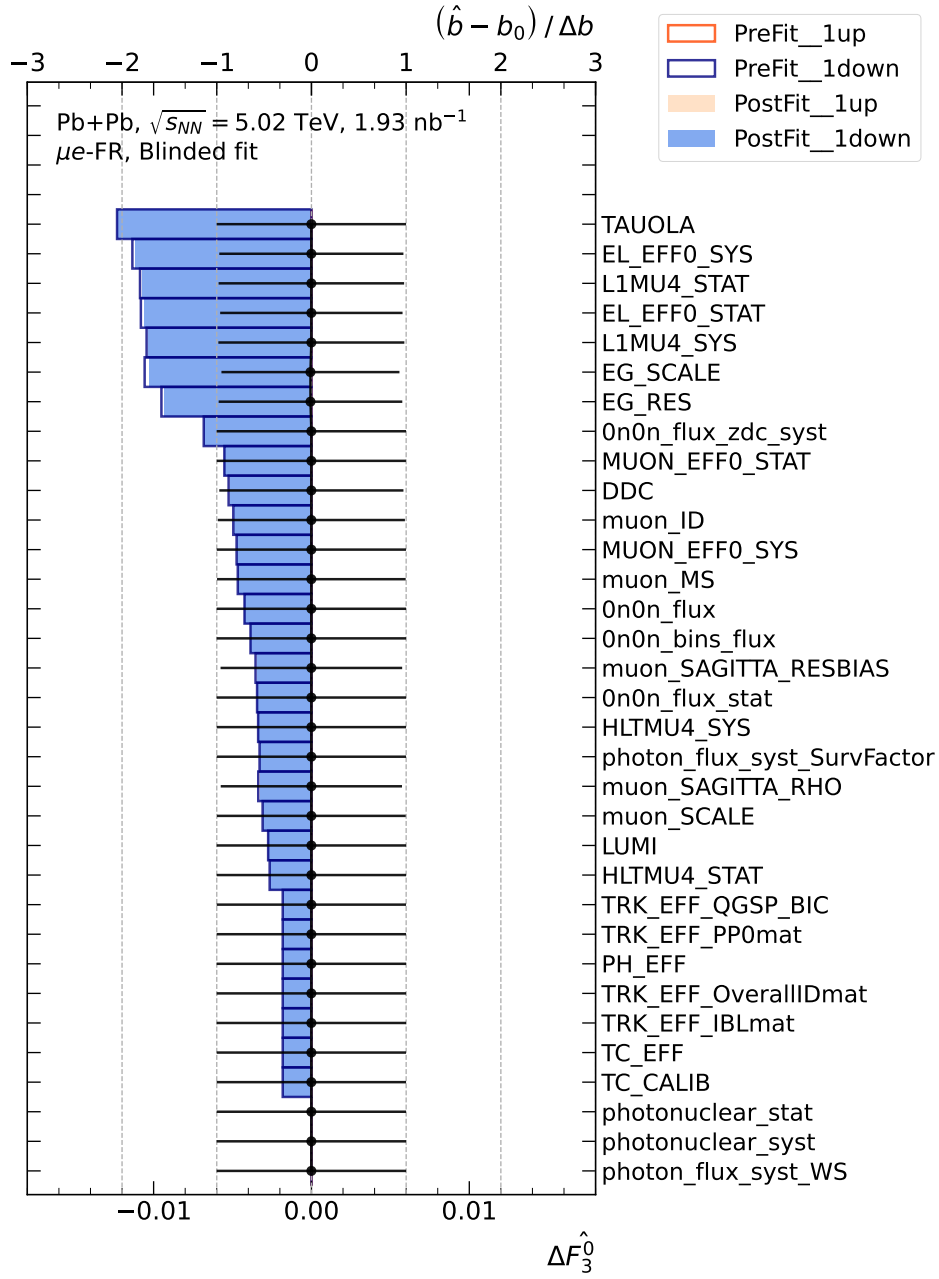


**Figure A.35:** Nuisance parameter impacts and pulls, in the fit for  $F_3^0$  using  $\mu e$ -FR data. The composition of the figure is explained in App. A.7.